Testing the Silicic Acid Leakage Hypothesis as a cause of CO_2 drawdown during Marine Isotope Stage 4

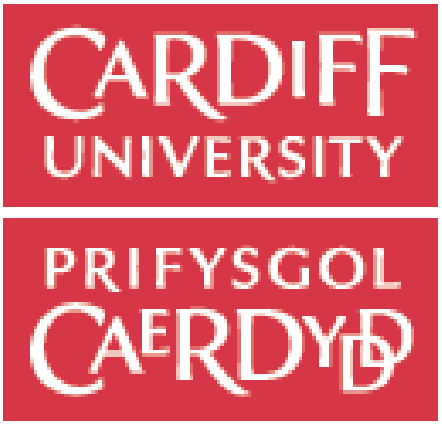

James D. Griffiths

A dissertation submitted for the Degree of Doctor of Philosophy
Cardiff University
August 2012

Declaration

This dissertation is the result of my own work and includes nothing which is the outcome of collaboration except where specifically indicated in the text. It does not exceed the word limit and is not substantially the same as any work that has been or is being submitted to any other university for any degree, diploma or other qualification.

James Griffiths
August 2012

Testing the Silicic Acid Leakage Hypothesis as a cause of CO_2 drawdown during Marine Isotope Stage 4
James D. Griffiths

The 'Silicic Acid Leakage Hypothesis' (SALH) is a mechanism by which the increased supply of silicic acid to the low latitude ocean allows diatoms (silica producers) to outcompete coccolithophorids (carbonate producers). This would result in a decrease in the export of carbonate, and drawdown of atmospheric CO_2 through changes in surface- and whole-ocean alkalinity.

Here I test the SALH as a potential cause of CO_2 drawdown during glacial Marine Isotope Stage (MIS) 4 (~70-59 ka). Firstly, I measure opal (biogenic silica) accumulation rates in a suite of cores from the equatorial Atlantic, to determine whether the export productivity of diatoms increased during MIS 4. I found that opal accumulation rates increased ~100% in MIS 4 relative to interglacial MIS 5a (~84-77 ka), in agreement with the SALH; however the timing of the changes make the SALH unlikely to be the direct cause of the CO_2 drawdown.

I then measured the calcium carbonate accumulation rates in the same suite of cores and found that carbonate accumulation decreased in MIS 4 relative to MIS 5a, also in agreement with the SALH. However, I found that this decrease may have been the result of enhanced carbonate dissolution.

I also tested the SALH directly by reconstructing changes in the silicic acid concentration of AAIW, by using neodymium and silicon isotopic ratio measurements. I found that AAIW conveyed an increased amount of silicic acid into the western tropical Atlantic during MIS 4, and that the timing of this increase was coeval with increases in both low latitude opal accumulation, and also opal accumulation in the northwest Atlantic.

Lastly, I tested the amount of atmospheric CO_2 drawdown which could have been attributed to the SALH mechanism during MIS 4 by using a box model, and I estimated that ~35-50 ppmv of CO_2 drawdown is achievable.

Table of Contents

1. Introduction 1

1.1 Carbon dioxide and the climate system 1

1.2 pCO_2 variations over geological time 3

1.3 Climatic changes during the Marine Isotope Stage 5/4 transition 7

1.4 Carbon dioxide in the oceans 8

1.5 The Silicic Acid Leakage Hypothesis (SALH) 15

1.6 Aims and objectives 20

1.7 Thesis layout 21

2. Methods **23**

2.1 Sedimentary calcium carbonate 23

2.1.1 Operational principles 23

2.1.2 Precision and accuracy of method 27

2.2 Sedimentary biogenic opal 27

2.2.1 Procedure 27

2.2.2 Calculation of dissolved silica and opal concentrations 28

2.2.3 Precision of method 29

2.2.4 Accuracy of method 30

2.2.5 Silica yield 31

2.3 Sedimentary ^{231}Pa, ^{230}Th, ^{232}Th, ^{234}U and ^{238}U 32

2.3.1 Sample weighing and addition of spikes 32

2.3.2 Total sediment digestion 33

2.3.3 Column chemistry for U, Th, Pa and Be 33

2.3.4 Final dry-down of samples 33

2.3.5 ICP-MS analysis 33

2.3.6 Calculation of U, Th and Pa abundances from raw data 34

2.4 Foraminiferal fragmentation index (core ODP 663A) 35

2.5 Determination of stable oxygen and carbon isotope ratios 36

2.6 Determination of sedimentary TOC and TN 36

2.7 Measurement of sedimentary neodymium (Nd) isotopic ratios 37

2.7.1 Carbonate leaching procedure 37

2.7.2 Fe-Mn oxide leaching procedure 37

2.7.3 Column chemistry pre-treatment 38

2.7.4 TRU-spec column chemistry 38

2.7.5 Sr-spec column chemistry 38

2.7.6 Ln-spec column chemistry 38

2.7.7 Determination of Nd isotopic ratios by MC-ICP-MS 39

2.8 Measurement of silicon (Si) isotopic ratios in sponge spicules 40

2.8.1 Picking sponge spicules 40
2.8.2 Si separation from major ions 40
2.8.3 Determination of Si isotopic ratios by MC-ICP-MS 41
2.9 Sedimentary diatom frustule counts 42
2.9.1 Preparation of slides 42
2.9.2 Diatom fragment counts 42
2.10 Determination of sedimentary biomarker ratios 42
2.10.1 Extraction 42
2.10.2 Separating the polar and apolar fractions 43
2.10.3 Standard addition and derivitisation 43
2.10.4 Gas Chromatography (GC) analysis 43
2.10.5 Gas Chromatography-Mass Spectrometry (GC-MS) analysis 43
2.10.6 Biomarker abundance ratios 43

3. Changes in equatorial Atlantic opal accumulation during MIS 5/4 transition 44
3.1 Introduction 44
3.2 Previous tests of the SALH and MIS 4 CO_2 drawdown 45
3.3 Sampling rationale, core locations and oceanographic setting 50
3.4 Thorium and protactinium proxy background 53
3.5 Core age model development 58
3.5.1 ODP 663A 58
3.5.2 VM19-296 60
3.5.3 RC24-01 62
3.5.4 VM30-40 63
3.5.5 RC16-66 64
3.6 Results 65
3.6.1 Comparison of ^{230}Th-normalised opal flux rates and $^{231}Pa_{xs}/^{230}Th_{xs}$ 65
3.6.2 Comparison of glacial (MIS 4) and interglacial (MIS 5a) opal burial 72
3.6.3 *Ethmodiscus rex* valve counts 73
3.6.4 Biomarker study 75
3.7 Discussion 78
3.7.1 Opal preservation in the EEA during the MIS 5a/4 transition 78
3.7.2 Controls of $(^{231}Pa/^{230}Th)_0$ and its use as a palaeoproductivity proxy 81
3.7.3 Comparison with other palaeoproductivity proxies 86
3.7.4 Influence of *Ethmodiscus rex* on opal and organic carbon export 93
3.7.5 Changes in brassicasterol to alkenone ratio through MIS 5a/4 94
3.7.6 Comparison to other EEA opal productivity records 96
3.7.7 Possible sources of silica in the EEA during MIS 4 96

3.7.8 Opal ballasting 98
3.7.9 Comparison of opal flux rate changes to the pCO_2 record 99
3.8 Conclusions 100

4. Changes in eq. Atl. $CaCO_3$ accumulation during MIS 5/4 transition 103
4.1 Introduction 103
4.1.1 Background 103
4.1.2 Approach to reconstructing $CaCO_3$ accum. in the EEA MIS 5a/4 104
4.1.3 Changes in $CaCO_3$ accumulation during MIS 4 106
4.2 Results 107
4.2.1 ODP 663A 107
4.2.2 VM19-296 109
4.2.3 RC24-01 110
4.2.4 VM30-40 111
4.2.5 RC16-66 112
4.2.6 Patterns of $CaCO_3$ accumulation change in the EEA MIS 5a/4 113
4.3 Discussion 116
4.4 Conclusions 124

5. Tracing silicic acid leakage in AAIW 126
5.1 Introduction 126
5.1.1 Background 126
5.1.2 Previous investigations of the SALH 129
5.1.3 Nd and Si proxy background 130
5.1.4 Study area and methods 133
5.1.5 Core age control 137
5.2 Results 140
5.2.1 Low latitude silicic acid leakage during MIS 4 140
5.2.2 Low latitude opal accumulation during MIS 4 143
5.3 Discussion 145
5.4 Conclusions 152

6. Box modelling simulation of the SALH during MIS 4 153
6.1 Introduction 153
6.1.1 Background 153
6.1.2 A previous model test of the SALH 154
6.1.3 Model equations 159
6.1.4 Test of the new model against the Matsumoto *et al*. [2002] model 166
6.2 Results 167
6.2.1 Model comparisons 167
6.2.2 Model pCO_2 sensitivity 169

6.2.3 Differences in modeling approach from new data constraints.....170
6.2.4 Glacial boundary conditions.....172
6.2.5 Modelling a glacial SALH scenario with new data constraints.....172
6.3 Discussion.....174
6.4 Conclusions.....177

7. Summary and overall conclusions.....179
References.....185
Appendix Table A1 – Pa and Th sample and spike weights.....204
Appendix Table A2 – Pa and Th gamma counts.....207
Appendix Table A3 – Nd isotopic data.....210
Appendix Table A4 – Si isotopic data.....211
Appendix Table A5 – Stable isotope data.....212
Appendix Table A6 – $CaCO_3$ data.....217
Appendix Table A7 – Percent opal and opal flux data.....225
Appendix Table A8 – Pa, Th and U radionuclide data.....233
Appendix Table A9 – TOC, TN, F(TOC), F(TN) and biomarker data.....235
Appendix Table A10 – Foraminiferal fragmentation data.....238

Acknowledgements

My sincere and grateful thanks goes to my supervisors Stephen Barker and Ian Hall for their time, effort and patience in helping me understand the complexities of reconstructing Atlantic palaeoproductivity and nutrient dynamics. I would also like to particularly thank David Thornalley for enthusiastic and extremely helpful academic discussions, and for sharing much of his own data to assist my research.

My gratitude also goes to Kate Hendry, Tina van de Flierdt and Robert Anderson for their invaluable contributions to my thesis, both in terms of assisting data production, and academic discussion. I am grateful to Julia Becker for stable isotope analysis and measurement of total organic carbon and nitrogen in my samples; Marty Fleisher, Rusty Lotti, George Lozefski and Nichole Anest for advice and assistance with radionuclide analysis and core sampling at Lamont-Doherty Earth Observatory; and Katharina Kreissig, Claire Huck and Carys Cook for laboratory assistance and running extra neodymium samples in the MAGIC Laboratories at Imperial College London.

My thanks also go to Rich Pancost and Paul Monaghan at Bristol University, for assistance in obtaining sedimentary biomarker data, and insightful discussion concerning organic geochemistry, Dirk Nürnberg for assistance with sampling core MD99-2198, Rainer Zahn and Katharina Pahnke for providing $\delta^{18}O$ data on MD99-2198, and Rebecca Pyne for sampling core ODP 1063. I am grateful to Jenny Pike for identification of diatoms in my core, Jamie Wilson for much assistance with the technical aspects of box modelling, and to Tony Oldroyd for helping me navigate around the geochemistry lab.

Lastly, thanks to my office mates (past and present): Tom, Paola, Laura, Pete W, Naomi, Margit, Pete B, Sam, Jamie, Scott and Elaine, for being there when a break was needed! And most importantly of all, I would like to thank all my family and Ellen for their continuing love and support.

Testing the Silicic Acid Leakage Hypothesis as a cause of CO_2 drawdown during Marine Isotope Stage 4

Chapter 1 – Overall thesis introduction

1.1 Carbon dioxide and the climate system

The Earth's climate system is principally driven by heat energy from the Sun. The incoming solar radiation measured at the top of the Earth's atmosphere is currently around 1360.8 ± 0.5 W m^{-2} [*Kopp and Lean*, 2011]. The Earth's atmosphere is transparent to incoming short-wavelength solar radiation, but absorbs ~95 % of the longwave back radiation, retaining the associated heat within the atmosphere (Figure 1.1). This absorption of outgoing radiation is due to the presence of so-called 'greenhouse gases' [*Mitchell*, 1989].

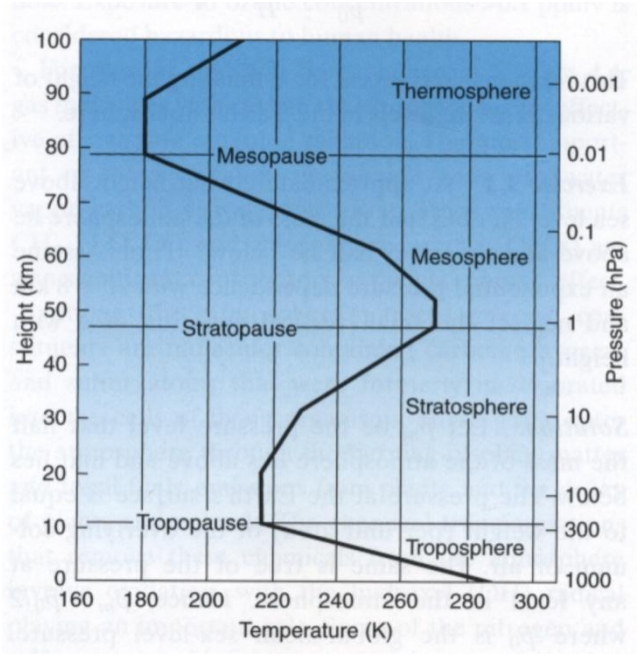

Figure 1.1 – A typical mid-latitude vertical temperature profile. The temperature increases in the stratosphere and thermosphere are due to absorption and re-radiation of longwave radiation by water vapour and other greenhouse gases above the troposphere. Reproduced from Wallace and Hobbs [2006].

One of the most important greenhouse gases (in terms of its effect on outgoing longwave back radiation) is carbon dioxide (CO_2) [*Wang et al.*, 1976; *Hansen et al.*, 1981; *Lacis et al.*, 2010]. Despite constituting only ~0.03 % of the dry atmosphere (Figure 1.2), CO_2 absorbs longwave radiation in the 7-14 μm 'atmospheric window', which leads to outgoing longwave radiation being lost from higher, colder regions of the atmosphere; and results in surface and tropospheric warming, termed the 'greenhouse effect' [*Wang et al.*, 1976]. Although water vapour constitutes ~3-4 % of the lower

atmosphere [*Barry and Chorley*, 1987], and similarly absorbs outgoing longwave radiation; CO_2 is particularly important because, unlike water vapour, it does not condense [*Lacis et al.*, 2010].

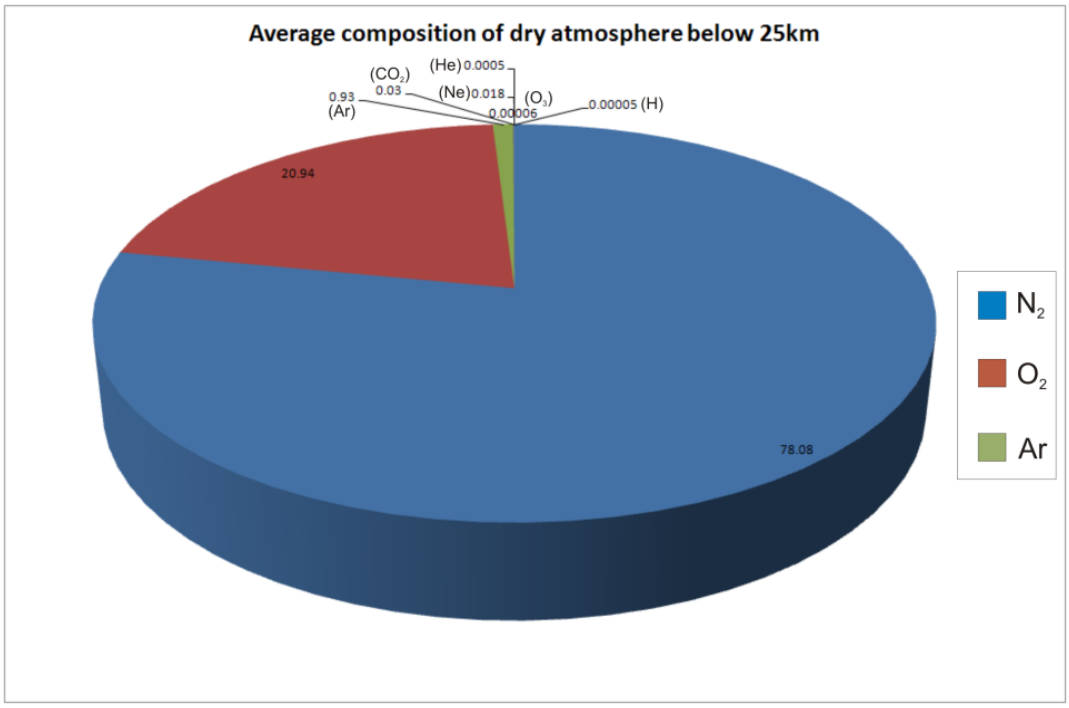

Figure 1.2 - The average composition of dry atmosphere below 25 km altitude. Carbon dioxide makes up a small but slightly variable proportion of the atmosphere (~0.03%). Data are taken from Barry and Chorley [1987].

Small changes in atmospheric temperature brought about by the absorption of outgoing longwave radiation by CO_2 have the potential to be greatly amplified, and affect other parts of the climate system; such as the biosphere [*Cox et al.*, 2000], oceans [*Roy et al.*, 2011] and polar regions [*Ridley et al.*, 2005].

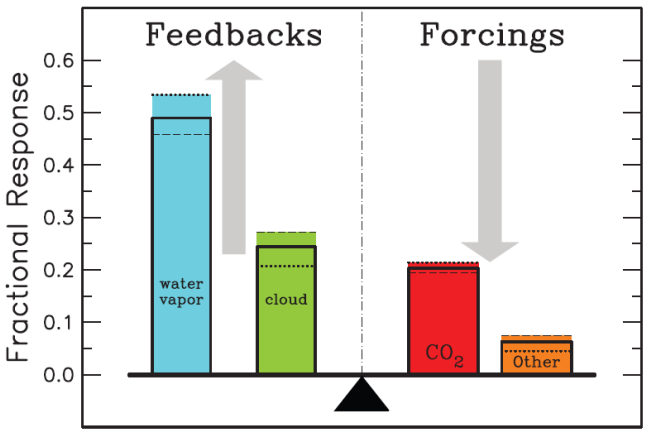

Figure 1.3 - Summary of the different contributions of individual components of the climate system to feedbacks and forcings. The reference atmosphere is from 1980. Reproduced from Lacis et al. [2010].

Although water vapour provides the strongest atmospheric feedback of the greenhouse gases, CO_2 is the main radiative forcing greenhouse gas [*Hansen et al.*, 1995; *Lacis et al.*, 2010], (see Figure 1.3). This importance of CO_2 as a potential driver of climate change has led to its effect on climate being intensely studied in recent decades. Human input of CO_2 into the atmosphere has increased through fossil fuel burning since the Industrial Revolution, and caused the atmospheric CO_2 (pCO_2) level to increase from the pre-industrial value of ~280 ppm [*Petit et al.*, 1999], to a value of 394.45 ppmv in 2012 [*Tans and Keeling*, 2012]. The effect of increasing pCO_2 on climate has implications for all of Earth's inhabitants, and it is therefore highly important to understand what factors controlled pCO_2 in the geological past, if researchers are to better comprehend future CO_2-induced climate change.

1.2 pCO_2 variations over geological time

Over geological timescales (10^6-10^7 years) the principal input source of CO_2 to the atmosphere is volcanoes [*Berner*, 2004], and the principal sink is silicate weathering [*Walker et al.*, 1981].

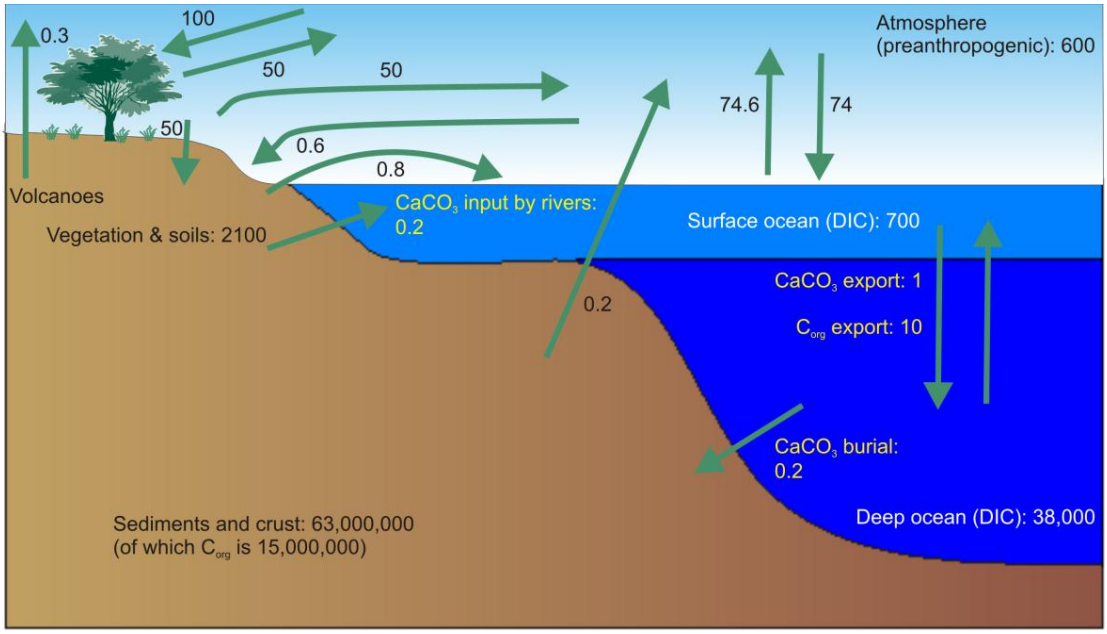

Figure 1.4 – Diagram showing the principal reservoirs and fluxes in the carbon cycle. The sizes of reservoirs are expressed in gigatonnes (Gt) of carbon. Fluxes are in Gt/yr. The fluxes marked in yellow are the principle components of the oceanic carbon cycle. Adapted from Sigman and Boyle [2000], Ruddiman [2001] and Sarmiento et al. [2002].

On shorter timescales (10^3-10^5 years), many other factors may have an influence on pCO_2, and hence on climate. The ease with which CO_2 can be stored in and released from different reservoirs, and hence how quickly it can be taken in or released define whether or not these mechanisms could have affected climate on these timescales.

The rate of carbon taken up by the hydrolysis of silicates, and released by volcanoes, are relatively small (Fig. 1.4), and thus cannot be implicated as the causes of shorter-term pCO_2 variations [*Berner et al.*, 1983]. The factors that may have affected CO_2 on timescales of 10^3-10^5 years are summarised in Figure 1.4.

One of the most important sets of interactions in the carbon cycle on the timescales relevant to this thesis is that between the oceans and the atmosphere. The ocean carbon reservoir is sufficiently large, and reactive enough to produce significant pCO_2 variations on these shorter timescales [*Broecker*, 1982]. A topic of much research in paleoclimatology is the forcings and feedbacks involved in the repeated cycle of glaciations in the Pleistocene Epoch (~ 1.8 Ma – ~10 ka before present), and the role that CO_2 may have had to play in these large climatic perturbations.

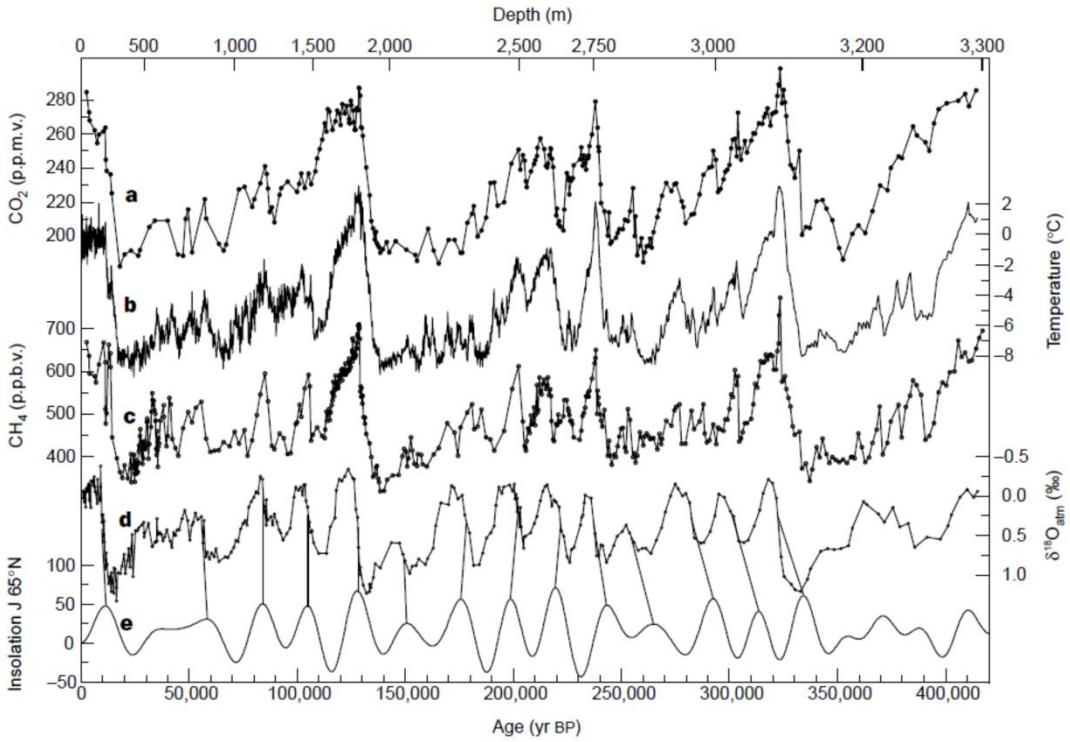

Figure 1.5 – A plot of temperature (curve b) from the Vostok ice core, East Antarctica. The $\delta^{18}O$ of snow over Antarctica is linearly related to the temperature above the inversion level, T_1, and also to the surface temperature of the precipitation site. The Antarctic temperature is highly correlated over the past 420 ka with the concentration of CO_2, as measured directly in bubbles containing samples of the past atmosphere within the ice core. Reproduced from Petit et al. [1999].

Ice cores drilled in the southern polar regions have provided a direct record of pCO_2, and show a close relationship between pCO_2 and proxies for temperature over the last 400 ka (Figure 1.5). In peak glacial periods, such as the Last Glacial Maximum (LGM), the concentration of pCO_2 was ~100 ppmv lower than the preindustrial value of ~280 ppmv [*Petit et al.*, 1999; *Ahn and Brook*, 2008]. Extensive research has recently focused on the precise timings of changes in pCO_2, Antarctic air and deep-water temperature, and ice sheet dynamics; and establishment of the cause-and-effect relationships between the mechanisms [*Blunier et al.*, 1998; *Mashiotta et al.*, 1999; *Shackleton*, 2000; *Blunier and Brook*, 2001; *Mudelsee*, 2001; *Bintanja and van de Wal*, 2008].

Ice core records have also shown that pCO_2 varies significantly on sub-orbital timescales, and that these pCO_2 variations also correlate with proxies for Antarctic temperature [*Ahn and Brook*, 2008]. These changes are not restricted to just the southern polar region, as data from a number of studies have suggested an important climatic 'teleconnection' between the northern and southern hemispheres, termed the 'bipolar see-saw' [*Blunier et al.*, 1998; *Blunier and Brook*, 2001; *Yiou and Vimeux*, 2001; *Hinnov et al.*, 2002; *Barker et al.*, 2009; *Barker et al.*, 2011].

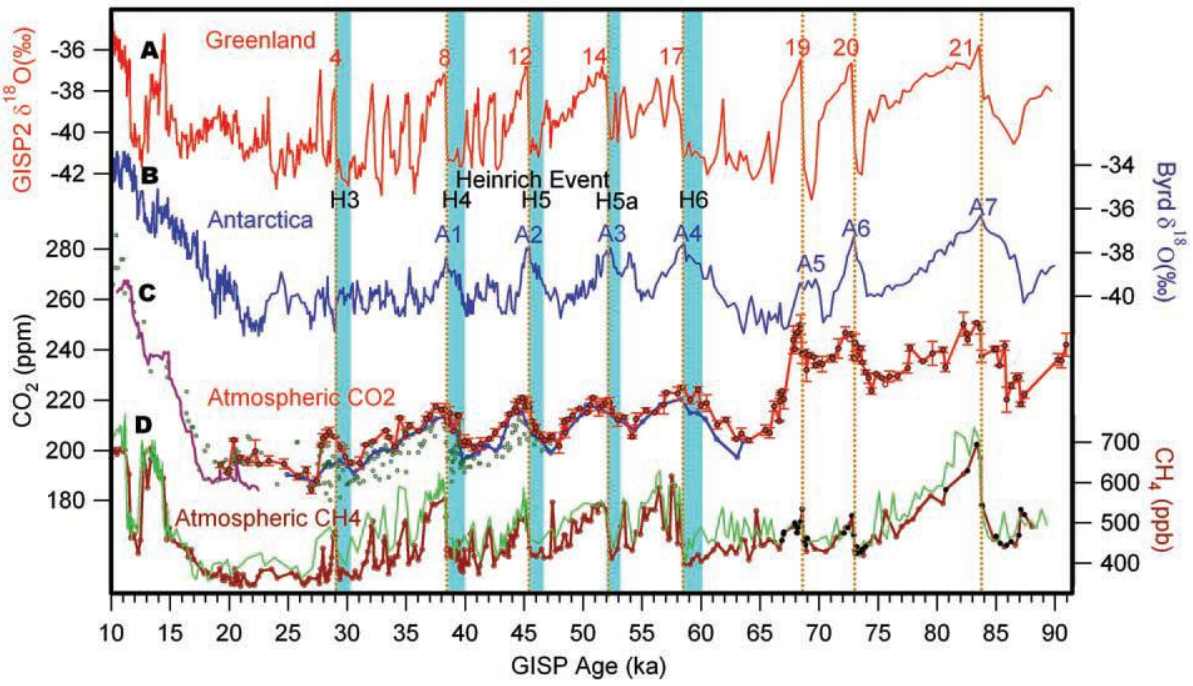

Figure 1.6 – Proxy records for temperature ($\delta^{18}O$) from the Greenland GISP2 ice core and the Antarctic Byrd ice core (red and blue curves, respectively) compared to a composite record of pCO_2 and CH_4. D/O Events are numbered from right to left in the Greenland record, and Heinrich events are marked as blue bands. Reproduced from Ahn and Brook [2008].

The proposed bipolar seesaw mechanism links large and abrupt changes in northern hemisphere climate, termed Dansgaard-Oeschger (D-O) oscillations [*Oeschger et al.*, 1984; *Dansgaard et al.*, 1993] to more gradual warming and cooling phases in Antarctica [*EPICA*, 2006]; through inter-hemispheric heat transport associated with the strength and mode of the Atlantic Meriodional Overturning Circulation (AMOC) [*Crowley*, 1992; *Broecker*, 1998].

The D-O cycles can be seen in the Greenland Ice Sheet Project (GISP2) ice core $\delta^{18}O$ record [*Ahn and Brook*, 2008] (see Figure 1.6). D-O oscillations are characterised by extremely rapid northern hemisphere warming (5 -10°C) followed by a more gradual cooling over several hundred years [*Bond et al.*, 1999]. D-O events have a number of effects; they appear to produce strong and abrupt changes in atmospheric conditions over the Greenland ice sheet, and they also appear to affect sea surface temperature and salinity in the North Atlantic circumpolar waters [*Seidov and Maslin*, 1999; *Schmidt et al.*, 2006]. At lower latitudes (and in the North Pacific Ocean) 'D-O-like' oscillations manifest as alternations between dry and humid hydrologic states, in both continental and marine proxies from a number of tropical and subtropical locations in both hemispheres [*Leuschner and Sirocko*, 2000]. Counterparts to the D-O oscillations are seen in the Antarctic temperature record, but at ~1/10th of the spectral power of those in the northern hemisphere [*Blunier et al.*, 1998; *Blunier and Brook*, 2001; *Yiou and Vimeux*, 2001; *Hinnov et al.*, 2002].

D-O oscillations are also thought to be linked to another type of abrupt, extreme northern hemisphere climatic perturbation known as Heinrich events, after their identification by Heinrich [1988] (see light blue bands in Figure 1.6). Heinrich Events are evidenced by greatly increased abundances of lithic fragments (180µm-3mm) of continental origin, which are taken as evidence of ice-rafted debris from the Laurentide ice sheet, due to sudden massive discharge of icebergs into the North Atlantic [*Heinrich*, 1988; *Bond et al.*, 1992].

Although debate surrounds the cause of Heinrich events, they appear to occur in Greenland cold periods immediately preceding the rapid warming phases associated with D-O oscillations [*Bond and Lotti*, 1995], and are thought to involve sudden changes in the North Atlantic freshwater balance, rates of North Atlantic Deep Water (NADW) formation, and meridional heat transport to the northern hemisphere [*Seidov and Maslin*, 1999; *Bard et al.*, 2000; *Ganopolski and Rahmstorf*, 2001].

To summarise, changes in pCO_2 on millennial timescales are correlated to changes in Antarctic temperature [*Petit et al.*, 1999; *Ahn and Brook*, 2008], which are

linked to the northern hemisphere through the bipolar seesaw mechanism [*Broecker*, 1998; *Barker et al.*, 2009; *Barker et al.*, 2011]. Northern hemisphere climate oscillations may then be linked to other parts of the climate system at low and mid-latitudes in both hemispheres [*Leuschner and Sirocko*, 2000; *Dannenmann et al.*, 2003; *Cruz et al.*, 2005].

As yet, the precise nature of the link between pCO_2 and glacial cycles is unknown, but growing evidence suggests that the interaction between oceanic physical and biogeochemical processes may have a significant effect on pCO_2, and subsequently on climate through the complex interactions outlined above. In particular, the marine carbon cycle is likely to have played an important role [*Archer and Maier-Reimer*, 1994; *Sigman and Boyle*, 2000; *Sigman et al.*, 2010].

1.3 Climatic changes during the Marine Isotope Stage 5/4 transition

Ice cores record a large (~47 ppmv) decrease in pCO_2 that occurred over ~4 ka, at the transition from Marine Isotope Stage (MIS) 5a to 4 [*Martinson et al.*, 1987], at around 71 ka (on the Hulu-Sanbao speleothem-tuned Greenland ice core $\delta^{18}O$ GICC05 age scale, see Chapter 3.5) [*Ahn and Brook*, 2008]. During this transition, sea level is estimated to have fallen by ~81 metres, based on coral records [*Cutler et al.*, 2003]. This would have lead to an increase in ocean salinity of around 2 % relative to modern values. In addition, tropical regions experienced cooling of ~3-5°C in the transition to glacial MIS 4 [*CLIMAP*, 1981; *Schneider et al.*, 1999], and high latitude regions experienced cooling of ~3°C inferred from deep sea temperature changes [*Shackleton*, 2000].

The MIS 5/4 transition was also a period in which major changes in oceanic circulation took place. Neodymium isotopic composition data suggests that during MIS 5, an increased proportion of North Atlantic Deep Water (NADW) reached the Indian Ocean, and that this proportion decreased at the onset of MIS 4 [*Piotrowski et al.*, 2009]. In the North Atlantic, changes in protactinium/thorium ratios from MIS 5a to MIS 4 have been interpreted as a decrease in the strength of Atlantic Meriodional Overturning Circulation (AMOC) [*Guihou et al.*, 2010].

The MIS 5/4 transition is less well studied than the LGM-Holocene transition, and the cause(s) of this prominent pCO_2 decrease remain largely unresolved. It is possible that changes in marine productivity and ocean circulation [*Sigman et al.*, 2010] may have played a major role in the initiation of the pCO_2 change and been one of the

causal mechanisms in bringing about the glacial conditions that persisted for ~8 ka during MIS 4 [*Ahn and Brook*, 2008].

1.4 Carbon dioxide in the oceans

In order to better understand the glacial-interglacial (G-IG) variations in pCO_2, we must also understand the interaction of gaseous CO_2 in the atmosphere with dissolved carbon in the ocean. The inorganic carbon content of the preindustrial atmosphere was 600 Pg (1 Pg = 1 $x10^{15}$ g). The size of the terrestrial biosphere/soil inorganic carbon reservoir is approximately 3-4 times the size of the preindustrial atmosphere, but put together these reservoirs are only ~10 % of the size of the inorganic carbon reservoir of the deep ocean (see Figure 1.4). Deep water comes into contact with the atmosphere on a timescale of approximately 1000 years. Any non-oceanic contributions to pCO_2 changes on G-IG timescales would probably be masked by the effects of dilution from the deep ocean inorganic carbon reservoir [*Sigman and Boyle*, 2000].

The mean concentration of aqueous CO_2 in the surface ocean (Equation 1.1) is closely tied to atmospheric pCO_2. When gaseous CO_2 dissolves in seawater it is first hydrated to form aqueous CO_2, which then reacts to form carbonic acid, and sets up the following thermodynamic equilibrium between the carbonate species:

Equation 1.1

$$CO_{2(g)} \leftrightarrow CO_{2\,(aq)} \leftrightarrow H_2CO_3 \leftrightarrow H^+ + HCO_3^- \leftrightarrow 2H^+ + CO_3^{2-}$$

(where $CO_{2(g)}$ is gaseous CO_2, $CO_{2(aq)}$ is aqueous CO_2, H_2CO_3 is carbonic acid, H^+ is the hydrogen ion, HCO_3^- is the bicarbonate ion, and CO_3^{2-} is the carbonate ion). The concentration of H_2CO_3 in seawater is very low and difficult to distinguish from $CO_{2\,(aq)}$, and the two species are usually considered in combination, and denoted H_2CO_3* [*Stumm and Morgan*, 1981; *Dickson and Goyet*, 1994]. The equilibrium relationship between these species is shown below (Equations 1.2-1.4):

Equation 1.2

$$K_0 = \frac{[H_2CO_3^*]}{pCO_2}$$

Equation 1.3

$$K_1 = \frac{[H^+][HCO_3^-]}{[H_2CO_3^*]}$$

Equation 1.4

$$K_2 = \frac{[H^+][CO_3^{2-}]}{[H_2CO_3^-]}$$

The equilibrium constant K_0 is the solubility coefficient of CO_2 in seawater. The CO_2 concentration in the air is sometimes expressed as its fugacity, which is related to its partial pressure, but allows for the non-ideality of CO_2 in air [*Sarmiento and Gruber*, 2006]. The equilibrium constants K_1 and K_2 depend on pressure (P), salinity (S) and Temperature (T). Under equilibrium conditions (no net exchange of CO_2 between air and sea) the fugacity of CO_2 in the atmosphere can be defined by Henry's Law:

Equation 1.5

$$CO_{2\,(g)} \overset{K_0}{=} CO_{2\,(aq)}$$

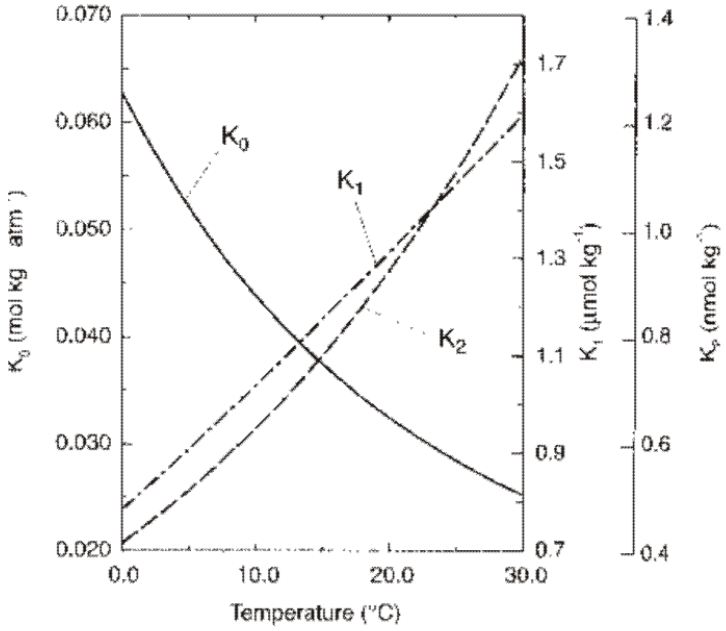

Figure 1.7 – A plot of CO_2 solubility (K_0), and the dissociation constants K_1 and K_2 as a function of temperature. Reproduced from Sarmiento and Gruber [2006].

As CO_2 is more soluble in colder water (Equations 1.2 - 1.4), the ocean must be considered as a potential store of atmospheric CO_2 during glacial periods. The temperature of the deep ocean is currently around 2°C [*Schlitzer*, 2000], and seawater freezes at around -2°C, which constrains the maximum deep sea temperature decrease to a maximum of 4°C in glacial periods [*Adkins et al.*, 2002]. As the deep ocean ventilates primarily at southern polar latitudes [*Primeau*, 2005], the temperature of the glacial polar ocean is similar to that of the deep ocean.

Estimates of temperature decreases in the glacial tropical oceans are 3-5°C [*CLIMAP*, 1976; *Guilderson et al.*, 1994]. Taking this into account, and an estimate of a glacial ocean which was ~2-3% saltier than today's ocean due to sequestration of freshwater in ice sheets [*Fairbanks*, 1989], an estimated 23.5 ppmv of pCO_2 drawdown was attributable to these mechanisms [*Sigman and Boyle*, 2000].

Other physical mechanisms thought to have contributed significantly to the lowering of pCO_2 to glacial levels include the shoaling of the Atlantic thermohaline circulation and the possible creation of a deep salty Antarctic water mass which filled the abyssal ocean [*Duplessy et al.*, 1988; *Rutberg et al.*, 2000; *Guihou et al.*, 2010]. This deep, CO_2-rich water may have caused dissolution of deep-sea $CaCO_3$ and increased whole ocean alkalinity (see below), which would have increased the CO_2 drawdown associated with the initial cooling. The amount of CO_2 drawdown attributed to this mechanism (known as carbonate compensation) in recent modelling studies is 35-43 ppmv [*Brovkin et al.*, 2007; *Hain et al.*, 2010]. Another associated mechanism is increased glacial Southern Ocean sea-ice coverage (which may have prevented direct exchange of CO_2 with the atmosphere) [*Stephens and Keeling*, 2000]. Other work suggests a link between the rate of Antarctic wind-driven upwelling and the deglacial rise in pCO_2 [*Anderson et al.*, 2009].

In addition to the physical mechanisms outlined above, which cannot themselves account for peak glacial CO_2 levels alone; biogeochemical dynamics are thought to have had the potential to affect atmospheric pCO_2 through their involvement in the oceanic carbon cycle [*Archer and Maier-Reimer*, 1994; *Brovkin et al.*, 2007; *Marinov et al.*, 2008]. In particular, the Southern Ocean is thought to be an important site for sequestration of carbon to the deep ocean, as the upwelled circumpolar deep water is high in 'preformed' (non-regenerated) nutrients, and represents a 'missed opportunity' for Southern Ocean phytoplankton to draw down CO_2 from the atmosphere [*Sigman et al.*, 2010] (see below). The Southern Ocean is termed a 'high-nutrient, low-chlorophyll' (HNLC) area. The unexpectedly low productivity seen in the Southern Ocean is possibly because phytoplankton in the Southern Ocean are limited by Fe [*Martin*, 1990; *de Baar et al.*, 1995].

Despite being able to account for up to two-thirds of the glacial-interglacial atmospheric pCO_2 variations by invoking the mechanisms above, current model studies cannot reliably account for the whole pCO_2 change [*Brovkin et al.*, 2007], implying that other, currently unquantified biogeochemical and/or physical mechanisms may have also contributed to glacial-interglacial pCO_2 drawdown. See [*Sigman and Boyle*, 2000] and [*Sigman et al.*, 2010] for an overall review.

Primary productivity by photoautotrophic organisms in the ocean's photic zone (~0-200 m) creates organic matter, containing organic carbon (C_{org}). This process increases surface seawater pH, and draws down CO_2, and is termed the 'biological pump' (Equation 1.6):

Equation 1.6

$$CO_2 + 2H_2O \rightarrow CH_2O + O_2 + H_2O$$

Organic carbon constitutes 30-40 % of the particulate biogenic matter above water depths of 100-200 m (the remainder being composed of $CaCO_3$ and opal), but decreases to <10 % at depth [*Clegg and Whitfield*, 1990]. The degradation of organic matter in sediments can also raise sedimentary pore-water CO_2 and promote the lowering of pH, and this may then lead to dissolution of calcium carbonate (see below) [*Emerson and Bender*, 1981; *Archer et al.*, 1989]. However, most sinking organic matter will eventually be respired and recycled in the deep ocean:

Equation 1.7

$$CH_2O + O_2 + H_2O \rightarrow CO_2 + 2H_2O$$

The biological pump affects pCO_2 directly by removing Dissolved Inorganic Carbon (DIC - also termed ΣCO_2) from the surface ocean (Equation 1.6), but also affects the whole alkalinity of the ocean (see below). The export production (C_{org}) of surface waters causes a moderate increase in alkalinity associated with nitrate uptake by phytoplankton [*Sigman and Boyle*, 2000]. The DIC content of the oceans is defined as the sum of the separate carbonate species (Equation 1.8):

Equation 1.8

$$DIC = [CO_2] + [HCO_3^-] + [CO_3^{2-}]$$

The distribution of DIC among the species is a function of both the total DIC concentration and the alkalinity of seawater. The Total Alkalinity (TA) of seawater is defined as the charge difference between the major conservative cations and anions (Equation 1.9), and also as a function carbonate, water and borate alkalinities (Equation 1.10) [*Barker*, 2006]:

Equation 1.9

$$TA \approx ([Na^+] + 2[Mg^{2+}] + 2[Ca^{2+}] = [K^+]) - ([Cl^-] + 2[SO_4^{2-}])$$

Figure 1.8 – A Bjerrum plot for the carbonate system in seawater. The heavy curves represent the following conditions: salinity = 35ppt, temperature = 25°C, pressure = 0 dbar. The light curves represent S = 35ppt, T = 0°C, P = 0 dbar, and the dashed curves represent S = 35ppt, T = 0°C, P = 3,000 dbar. The shaded area represents a typical range of ocean pH. Reproduced from Barker [2006].

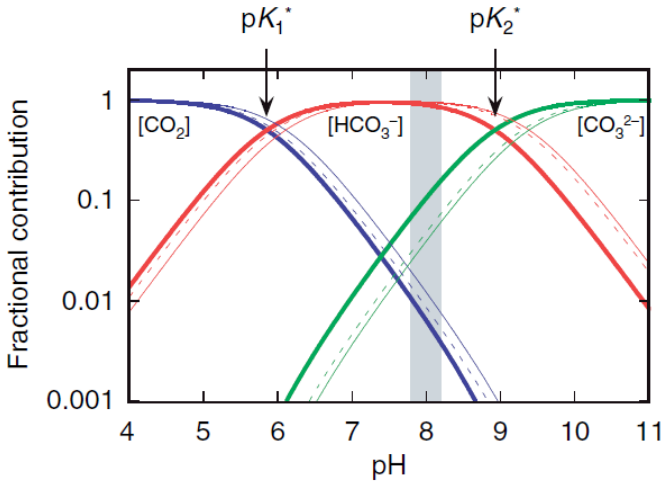

Equation 1.10

$$TA = [HCO_3^-] + 2[CO_3^{2-}] + [OH^-] - [H^+] + [B(OH)_4^-]$$

(Where $[B(OH)_4]$ is the concentration of the borate ion)

The contribution of the borate ion is only 4.2% [*Sarmiento and Gruber*, 2006], so that TA can be approximated to carbon alkalinity (CALK):

Equation 1.11

$$TA \approx CALK = [HCO_3^-] + 2[CO_3^{2-}]$$

CALK is added to the oceans primarily through weathering of terrestrial carbonate rocks, and is removed largely by precipitation and burial in sediment by oceanic biota. Nannoplankton such as coccolithophores and single-celled protozoa such as foraminifera both form calcareous external coverings (tests) by extracting calcium and carbonate ions from seawater:

Equation 1.12

$$Ca^{2+} + 2HCO_3^- \leftrightarrow CaCO_3 + CO_2 + H_2O$$

The predominant form of calcium carbonate is calcite, which reflects the abundance of the two groups of microfossil-forming organisms, foraminifera and

coccolithophores [*Honjo*, 1976; *Armstrong and Brasier*, 2005]. As calcite from the surface ocean falls through the water column, it starts to dissolve. The tendency of $CaCO_3$ to dissolve in seawater is dependent on its degree of saturation (Ω) with respect to the specific mineral phase (calcite or aragonite):

Equation 1.13

$$\Omega = [Ca^{2+}][CO_3^{2-}]/K_{sp}$$

Because $[Ca^{2+}]$ is a conservative constituent in seawater [*Wilson*, 1975], the following approximation can be made:

Equation 1.14

$$\Omega = [CO_3^{2-}]/[CO_3^{2-}]_{sat}$$

When $\Omega < 1$ the system is undersaturated with respect to $CaCO_3$, and it begins to dissolve. The saturation state is the main control on $CaCO_3$ dissolution, and may be influenced by pressure and temperature changes. In the deep ocean, pressure influences the saturation state as it pertains to the partial molar volume ΔV:

Equation 1.15

$$\Delta V = V_{Ca} + V_{CO3} - V_{CaCO3}$$

ΔV is negative for calcite and aragonite (i.e. $CaCO_3$ takes up more space than the individual ions Ca^{2+} and CO_3^{2-}). Hence, at the higher pressure found in the deep ocean, calcite and aragonite both dissolve. The crystal structure of aragonite renders it more soluble than calcite [*Mucci*, 1983; *Acker et al.*, 1987], and therefore the aragonite saturation horizon (the point at which $\Omega = 1$, see Equation 1.14) is 1-1.5 km shallower than the calcite saturation horizon. Hence, all the carbonate found at depths greater than ~2.7 km in the Atlantic and ~0.5 km in the Pacific is calcite [*Sarmiento and Gruber*, 2006].

The calcite lysocline is defined as the transition zone between the initiation of $CaCO_3$ dissolution, and the depth in the water column at which the rate of $CaCO_3$ dissolution is equal to the rate of its supply. The latter depth is termed the 'carbonate compensation depth' (CCD), above which some $CaCO_3$ will be preserved in sediments, and below which nearly all $CaCO_3$ will be dissolved [*Berger*, 1970; *Archer*, 1991]. The CCD occurs on average at 3.5 km in the worlds ocean [*Broecker and Takahashi*,

1978], although it is far deeper in the Atlantic than in the Pacific [*Sarmiento and Gruber*, 2006] (see Figure 1.9).

The CALK/DIC system responds to oceanographic changes in two ways; referred to as 'closed system responses' and 'open system responses'.

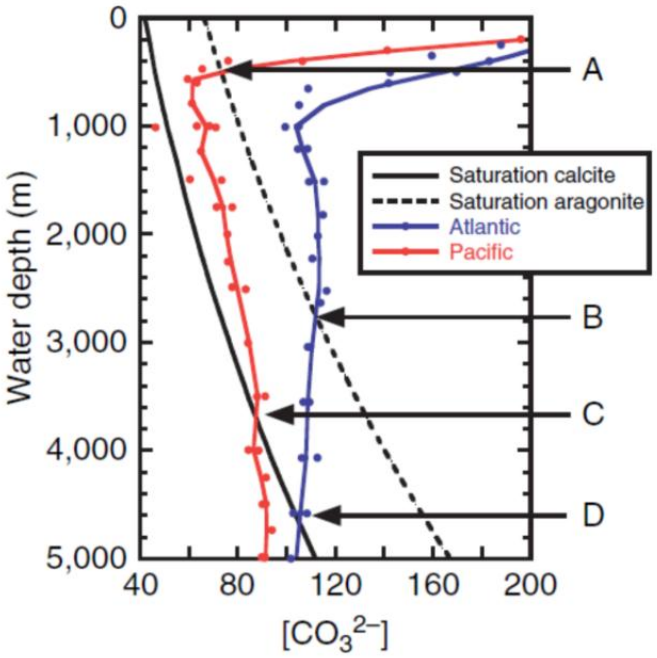

Figure 1.9 – Water column profiles of *in-situ* [CO_3^{2-}] from the Atlantic and Pacific. The saturation profile of aragonite is represented by the dashed black line, and that of calcite by a solid black line. Overall, the saturation horizons of both calcite and aragonite occur at shallower depths in the Pacific than in the Atlantic. The saturation horizons for calcite and aragonite in both oceans are labelled A-D. Reproduced from Barker [2006].

Closed system responses refer to internal redistributions of the CALK and DIC inventory within the ocean, while open system responses refer to changes in the size of the CALK and DIC reservoir by imbalances in continental input of $CaCO_3$ and its burial in the deep ocean [*Archer and Maier-Reimer*, 1994; *Archer et al.*, 2000a; *Sigman and Boyle*, 2000].

Figure 1.10 - The effect of the $CaCO_3$ budget on the DIC and CALK concentrations of surface seawater. The surface water pCO_2 (which communicates to the atmosphere) decreases as DIC decreases and/or CALK increases. The dashed blue arrow shows the effect of $CaCO_3$ burial. The solid green arrows show the effect of biogenic export production on CALK and DIC.
The salinity is 35ppt and the temperature is 20°C. Reproduced from Sigman and Boyle [2000].

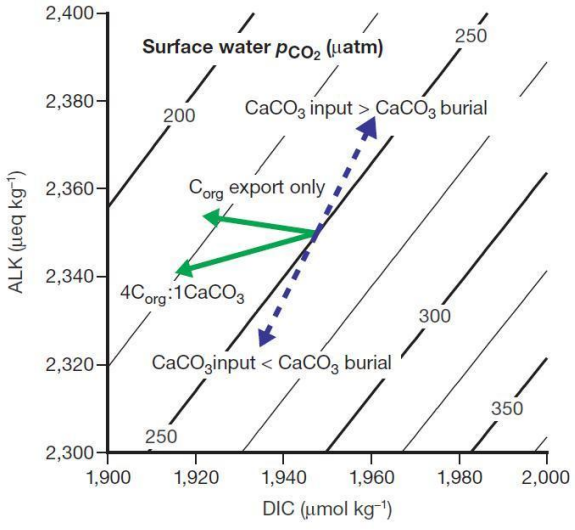

Addition of CALK to the oceans occurs through carbonate weathering and riverine transport of $CaCO_3$ into the surface ocean, and removal occurs through $CaCO_3$ burial in the deep ocean, and also in shallow water and reef environments [*Milliman and Droxler*, 1996]. The balance of inputs and removal of $CaCO_3$ is mediated by the depth of the calcite lysocline. Changing the continental input of $CaCO_3$ so that inputs exceed burial will result in an increase of CALK and DIC in the whole ocean, in a 2:1 ratio [*Sigman and Boyle*, 2000]. The burial rate of $CaCO_3$ will subsequently increase as the deep ocean CO_3^{2-} concentration increases, which, in turn causes the lysocline to deepen.

The process of balancing inputs and outputs of $CaCO_3$ causes a decrease in surface ocean pCO_2 (see Figure 1.10), which in turn causes a decrease in atmospheric pCO_2 (see Equation 1.5).

The marine carbon cycle has been the focus of much research as to the role it may have played in the glacial-interglacial climate cycles that have dominated on Earth since the Pliocene, through its effect on pCO_2. In particular, the export production of $CaCO_3$ by calcareous phytoplankton (Equation 1.12) may affect pCO_2 through its impact on the CALK and DIC inventory of the ocean [*Archer and Maier-Reimer*, 1994; *Keir*, 1995; *Archer et al.*, 2000a].

The ratio of $CaCO_3$:C_{org} exported from the surface ocean can strongly influence the relative concentrations of CALK and DIC in the surface ocean, and hence also pCO_2 [*Sigman and Boyle*, 2000]. Globally, the export ratio of $CaCO_3$:C_{org} is estimated at ~0.1 in the modern ocean [*Yamanaka and Tajika*, 1997; *Sarmiento et al.*, 2002]. Currently, the dominant region of carbonate export is the low-latitude ocean (tropical and subtropical latitudes, see Figure 1.12) [*Sarmiento et al.*, 2002; *Thurman and Trujillo*, 2002].

If some perturbation of the oceanic biogeochemical cycle caused less $CaCO_3$ to be produced, C_{org} production to increase, or both; the $CaCO_3$:C_{org} export ratio would decrease. This would have two effects, firstly a greater proportion of oceanic alkalinity would remain in the surface waters, which would have enhanced CO_2 solubility (a "closed system" effect), and also by decreasing $CaCO_3$ burial, the whole ocean alkalinity inventory would be increased (an "open system" effect).

1.5 The Silicic Acid Leakage Hypothesis (SALH)

One biogeochemical mechanism suggested as a possible contributing cause to CO_2 drawdown during glacial times proposes a major change in the oceanic silicon (Si) cycle, and is known as the Silicic Acid Leakage Hypothesis (SALH) [*Brzezinski et al.*,

2002; *Matsumoto et al.*, 2002]. The oceanic Si cycle is globally important in terms of primary productivity [*Nelson et al.*, 1995; *Ragueneau et al.*, 2000]. Silicic acid (or dissolved silica) is supplied to the oceans via three main sources:

1) Chemical weathering of silicate and aluminosilicate minerals by carbonic acid (rainwater) produces silicic acid, which is washed into rivers. Rivers also transport suspended lithogenic debris into the oceans. Rivers account for 6.1 ± 2 x 10^{12} M yr^{-1} (~80%) of the net input of Si into the oceans, assuming an average silicic acid concentration of 150 µM [*Tréguer et al.*, 1995].

2) Hydrothermal emanations through the interaction of seawater with mid-ocean ridges, and low-temperature alteration of oceanic basalts are thought to be responsible for 1-4 x 10^{11} M yr^{-1} of silicic acid input to the deep ocean [*Mortlock et al.*, 1993].

3) Approximately 0.5 x 10^{12} M yr^{-1} of silicic acid is supplied to the oceans through the dissolution of eolian lithogenic material [*Tréguer et al.*, 1995].

Silicic acid is removed from the oceans mainly by the group of unicellular algae known as diatoms, which use silicic acid to make their protective outer coatings (frustules) [*Ragueneau et al.*, 2000; *Armstrong and Brasier*, 2005]. Diatoms produce biogenic silica (variously known as opal, biogenic opal, or amorphous opaline silica), which is an amorphous metal oxide formed through organic polymerisation processes [*Coradin and Lopez*, 2003]. Globally, diatoms are estimated to remove 200 - 280 x10^{12} M yr^{-1} of silicic acid from the oceans, of which at least 50% dissolves in the euphotic zone, and 100 - 140 x10^{12} M yr^{-1} is exported to the deep ocean [*Nelson et al.*, 1995]. The major loci for modern opal deposition are the Southern Ocean, the North Pacific (NP), the equatorial divergences, and coastal upwelling regions [*Lisitzin*, 1972; *Thurman and Trujillo*, 2002]. Due to the high opal productivity in the Southern Ocean [*DeMaster*, 1981; *Tréguer et al.*, 1995], and the high rate of dissolution and recycling [*Nelson et al.*, 1995], the deep Southern Ocean has a high concentration of silicic acid (>100 µM/kg) [*Schlitzer*, 2000] (see Figure 1.11).

In the modern Southern Ocean, high diatom productivity depletes the surface waters in the subantarctic region. Because the Southern Ocean is Fe-limited, diatoms take up much more dissolved silica relative to nitrate than they would under nutrient-replete conditions [*Brzezinski*, 1985]. The uptake ratio of Si:N by diatoms in the Southern Ocean may be as high as 4:1 [*Franck et al.*, 2000]. This preferential uptake depletes Antarctic Surface Water (AASW) in Si, whilst it remains high in preformed N. Subantarctic Mode Water (SAMW) and Antarctic Intermediate Water (AAIW) are sourced from AASW in the circumpolar region [*Sarmiento et al.*, 2004].

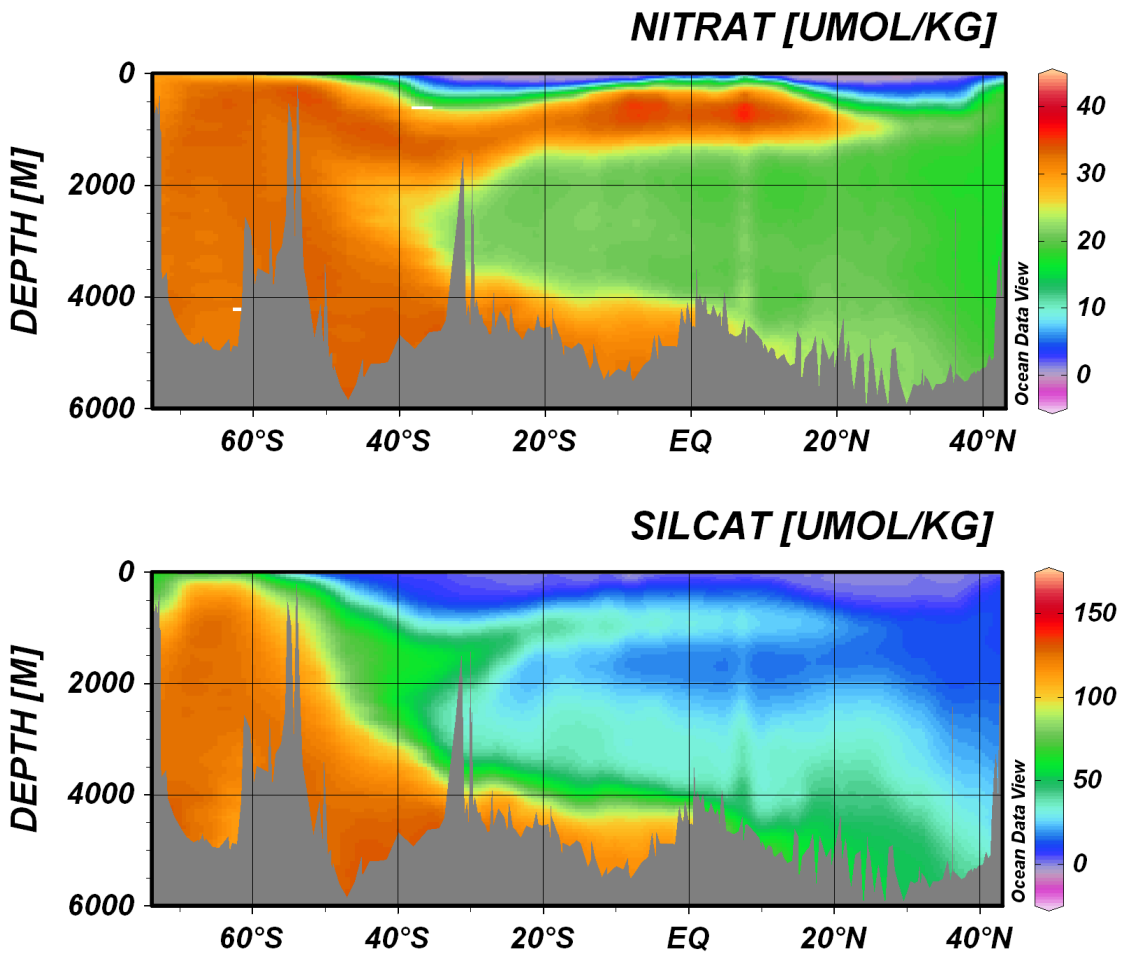

Figure 1.11 – Plots of the concentration of nitrate (NO_3^-) (top) and silicate/silicic acid ($SiOH_4$) (bottom) for an Atlantic ocean transect. A key feature is the long 'tongue' of high nitrate concentration (representing AAIW) extending from high southern latitude to low latitude in the top plot. In a SALH scenario a similar tongue of higher-silicate AAIW would influence the low latitude ocean. Reproduced from eWOCE online gallery [*Schlitzer*, 2000].

The preformed Si:N of SAMW and AAIW is an important control on low latitude primary productivity [*Matsumoto et al.*, 2002; *Sarmiento et al.*, 2004], and the low Si:N (~1:4) in modern AAIW favours the dominance of carbonate ($CaCO_3$) – producing phytoplankton over a large proportion of the oceans between ~55°S to 60°N [*Thurman and Trujillo*, 2002] (see Figure 1.12). The dominance of carbonate-producing phytoplankton across a large area of the equatorial oceans has implications for the global ratio of calcium carbonate to organic carbon export ($CaCO_3$:C_{org}) from the surface ocean, which has been estimated at ~0.1 [*Sarmiento et al.*, 2002].

If some major perturbation in the oceanic silica cycle caused the Si:N uptake ratio of diatoms in AASW to change significantly during glacial times, then the silicic acid content of AASW could have increased, leading to the creation of excess silicic acid in AASW, and hence in SAMW/AAIW. Subsequently, this would have led to an increase in the availability of dissolved silicic acid in low latitude oceans during glacial

times; and providing that the excess silicic acid reached the euphotic zone, may have allowed diatoms a competitive advantage over coccolithophorids in terms of nutrient utilisation [*Brzezinski et al.*, 2002; *Matsumoto et al.*, 2002]. This then would have led to a decrease in $CaCO_3$ production by the coccolithophorids. In a mesocosm nutrient-addition experiment it has been demonstrated that diatoms are able to outcompete a common coccolithophorid (*E. huxleyi*), when the concentration of silicic acid is >2 µM [*Egge and Aksnes*, 1992]. Any significant enhancement of diatom productivity over coccolithophorids would lead to a perturbation in the $CaCO_3$:C_{org} ratio, and reduction of surface water pCO_2 (Figure 1.10), and hence atmospheric pCO_2 (Equation 1.5), which is the most fundamental affect of the SALH [*Matsumoto and Sarmiento*, 2008]. The SALH relies on some mechanism(s) creating an excess of silicic acid in AASW which could have then been transported to low latitudes within SAMW/AAIW.

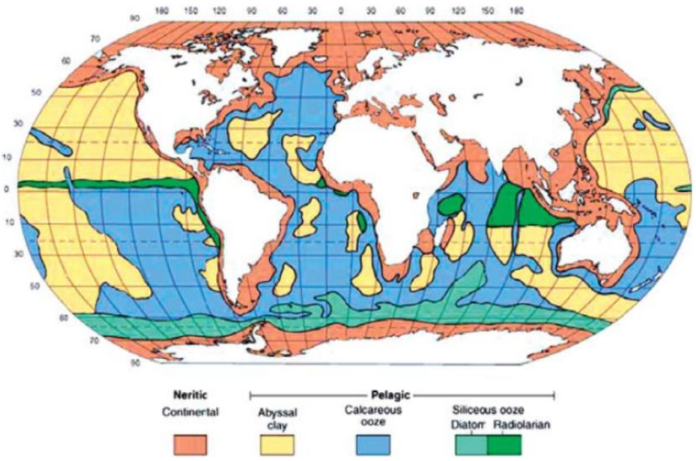

Figure 1.12 – An illustration of the dominant sediment types in the world ocean. Note the occurrence of generally calcareous sediment in the low-latitude Atlantic ocean, and the circum-Antarctic zone of dominantly siliceous sediment. Reproduced from Thurman and Trujillo [2002].

Possible mechanisms for the creation of a silicic acid excess in AASW are, firstly, a large glacial addition of Fe to the glacial Southern Ocean, which may have caused a change in the Si:N uptake ratio of the resident diatoms. A number of studies have demonstrated that the addition of Fe to Fe-depleted seawater lowers the Si:N uptake ratio of diatoms from ~4:1 to 1:1 [*Hutchins and Bruland*, 1998; *Takeda*, 1998; *Franck et al.*, 2000; *Brzezinski et al.*, 2002], and the dust content of Antarctic ice cores during glacial periods indicates that there was significant aeolian delivery of Fe to the glacial Southern Ocean [*Petit et al.*, 1999]. Stable isotope analyses of nitrogen ($\delta^{15}N$) and silicon ($\delta^{30}Si$) in Southern Ocean sediments appear to support this hypothesis [*Brzezinski et al.*, 2002].

A second alternative mechanism suggested for the creation of a silicic acid excess in the Southern Ocean is a simple reduction in diatom stock in AASW [*Martin*, 1992]. This hypothesis supposes that diatoms were largely replaced by soft-tissue phytoplankton such as the common Antarctic species *Phaeocystis*. This hypothesis has

some support; in the modern ocean *Phaeocystis* is associated with high levels of dimethylsulphide [*DiTullio and Smith Jr.*, 1995], and elevated concentrations of dimethylsulphide-related compounds have been found within the glacial intervals of the Vostok ice core, suggesting that soft-tissue primary productivity may have been enhanced in the glacial Southern Ocean [*Legrand et al.*, 1991].

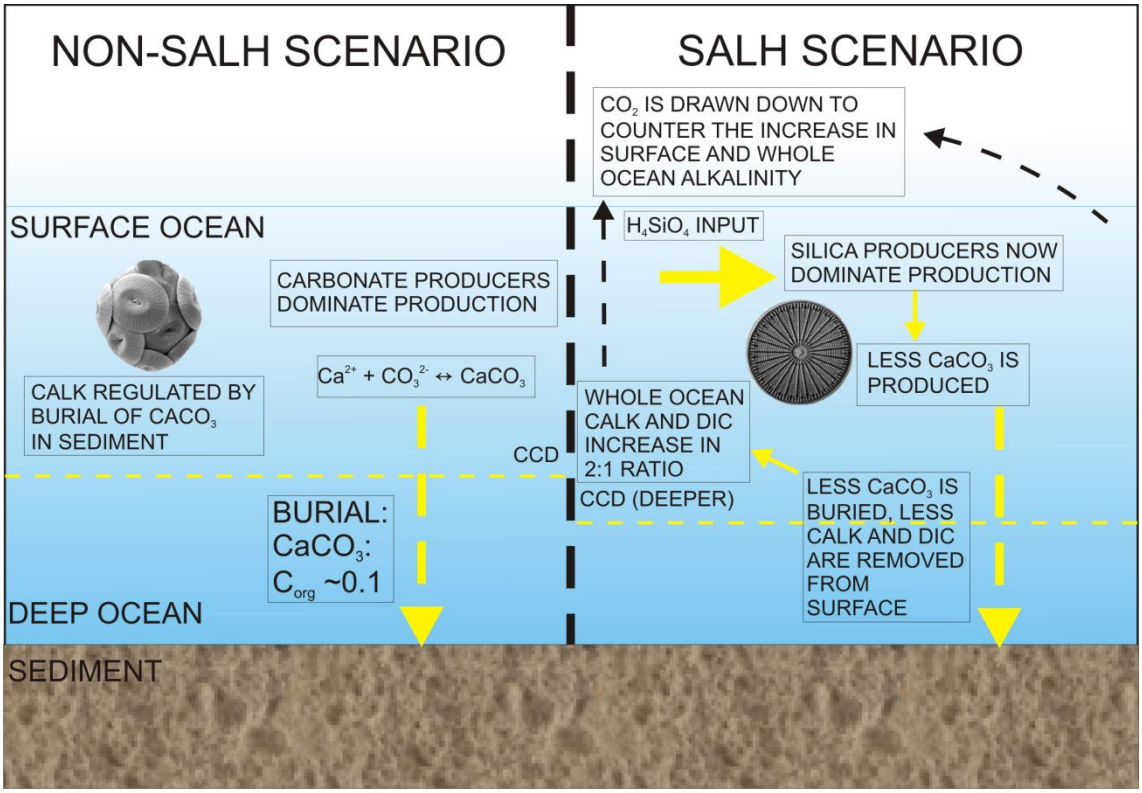

Figure 1.13 – Diagrammatic summary of the silicic acid leakage hypothesis (SALH), as it is hypothesised to occur in the low latitude ocean.

Lastly, an increase in sea ice cover could have also limited diatom productivity, and hence Si uptake north of the APF [*Charles et al.*, 1991; *Chase et al.*, 2003]. It is possible that a combination of two or three of these factors (which are not mutually exclusive) could have led to the creation of a silicic acid excess in the Southern Ocean during glacial periods.

A SALH scenario has been simulated using a simple oceanic 8-box model [*Matsumoto et al.*, 2002] (see Chapter 6), attached to a simple sedimentary $CaCO_3$ model (to simulate "open-system" conditions). The study simulated a decrease in the Si:N uptake ratio of Southern Ocean diatoms to create an excess of silicic acid in AASW, and allowed it to 'leak' to low latitudes. The result of the study was that a combination of a reduced carbonate pump and open system carbonate compensation drew down atmospheric pCO_2 by ~40-50 ppmv, depending on where the excess silicic

acid was consumed (low latitude surface ocean as opposed to the subantarctic zone). Although the drawdown predicted by the model cannot explain all of the glacial CO_2 decrease, the authors note that a more complex model such as an Atmosphere-Ocean General Circulation Model (AOGCM) that has increased low-latitude CO_2 sensitivity may draw down more CO_2 in response to a SALH scenario [*Matsumoto et al.*, 2002]. This result suggests that the SALH has at least the potential to contribute significantly to glacial-interglacial CO_2 drawdown.

1.6 Aims and Objectives

The primary aims of this thesis are to firstly, test whether the accumulation rates of biogenic opal in a range of cores spanning the equatorial Atlantic region increased during MIS 4 (glacial) relative to MIS 5a, which is an *a priori* expectation if a SALH scenario of increased diatom abundance occurred in the equatorial Atlantic. Similarly, the accumulation of sedimentary calcite ($CaCO_3$) will be measured to determine whether a decrease in $CaCO_3$ export due to reduced surface productivity took place during MIS 4 relative to MIS 5a, which would be consistent with the occurrence of a SALH scenario.

It is of key importance to distinguish the effects of variations in opal and $CaCO_3$ productivity on the sedimentary accumulation record, to those of variations in preservation of either component, dilution or sediment redistribution. To aid interpretation of the opal and $CaCO_3$ records, additional palaeoproductivity proxies (authigenic uranium, total organic carbon, total nitrogen) are reported on some of the same core intervals. All sedimentary components can be normalised to the sedimentary concentration of the thorium radionuclide ^{230}Th to account for sediment redistribution [*Bacon*, 1984; *Suman and Bacon*, 1989; *Francois et al.*, 2004] (see Chapter 3.4). Additionally, the ratios of sedimentary markers specific to diatoms and coccolithophorids (common $CaCO_3$-producers) will be measured to add further information about changes in the phytoplankton composition. The overall goal of these measurements is to reconstruct productivity patterns of diatoms and $CaCO_3$-producing phytoplankton during MIS 5a and MIS 4.

Age control will come from tuning of high-resolution $\delta^{18}O$ records generated in this study to the $\delta^{18}O$ of the Greenland (NGRIP) ice core record [*Andersen et al.*, 2007], with absolute age control from Chinese speleothem records [*Wang et al.*, 2001; *Wang et al.*, 2008] (see Chapter 3.5). Our hope is that high-resolution age control will reveal

more about cause-and-effect relationships between changes in ocean marine biogeochemistry and the Antarctic pCO_2 record [*Ahn and Brook*, 2008].

The main aim of the thesis is to examine whether the effect of any shift in the low latitude Atlantic phytoplankton composition towards being more diatom-dominated could have contributed to the large and abrupt (~ 47 ppmv in ~ 4 ka) decrease in pCO_2 [*Ahn and Brook*, 2008] that occurred at the MIS 5a/4 transition (~69 ka) [*Martinson et al.*, 1987]. The most fundamental prediction of the SALH is that it has the ability to bring about a decrease in pCO_2 through changing the export rain ratio of $CaCO_3$:C_{org} [*Sarmiento et al.*, 2002], and not its ability to affect the export of biogenic opal *per se* [*Matsumoto and Sarmiento*, 2008]. This will be investigated using the geochemical proxy data from equatorial Atlantic cores from this study, in combination with a simple MATLAB-based 8-box geochemical model based on that of [*Matsumoto et al.*, 2002].

1.7 Thesis Layout

The thesis layout is outlined below:

- Chapter 2 provides information on all laboratory methods used in data production for this thesis. Complete step-by-step details of all methods may be found in the attached electronic appendix.

- Chapter 3 details previous investigations of the SALH, and details the methodology used in creating age models for the cores used in this Chapter and in Chapter 4. Chapter 3 reconstructs biogenic opal accumulation in a suite of five cores from the equatorial Atlantic between ~95 and 40 ka, using radionuclide measurements to account for sediment redistribution, and reconstructing parallel downcore records of total organic carbon (TOC), total nitrogen (TN), authigenic uranium and sedimentary biomarker ratios to provide indications of overall changes in palaeoproductivity in the studied interval.

- Chapter 4 examines the controls on $CaCO_3$ sedimentation in the equatorial Atlantic, and goes on to reconstruct a high-resolution record of $CaCO_3$ accumulation in the same suite of equatorial Atlantic cores used in Chapter 3. In particular this chapter analyses whether the $CaCO_3$ record is controlled primarily by production or preservation. The chapter goes on to discuss the implications of this and the findings of Chapter 3 for the low latitude $CaCO_3$:C_{org} (and hence for pCO_2).

- Chapter 5 details the direct geochemical reconstruction of the silicic acid reconstruction of Antarctic Intermediate Water (AAIW) from a site in the western tropical Atlantic, using the neodymium and silicon isotopic ratios of sedimentary components as parallel proxies for silica leakage in AAIW. The Chapter then goes on to describe the effect that this leaked silicic acid may have had on low latitude diatom productivity in the Atlantic. This Chapter contains a full explanation of physical and chemical factors that may affect the supply of silicic acid to the tropical Atlantic in southern-sourced intermediate water, and the particulars of age control for all cores used in the Chapter.

- Chapter 6 describes the creation and testing of a MATLAB-based 8-box geochemical model, based closely on that of [*Matsumoto et al.*, 2002]. My intention was to use the model to produce an updated estimate of the effect of the SALH on pCO_2, given new geochemical constraints from this investigation.

- Chapter 7 is an overall synthesis of the thesis findings, and final conclusions.

Chapter 2 – Methods

2.1. Sedimentary calcium carbonate ($CaCO_3$)

2.1.1 Operational Principles

Measurements of sedimentary $CaCO_3$ were made at Cardiff University using a UIC Instruments Inc. CM5014 Coulometer connected to a CM5130 Acidification Module (see Figure 2.1 and 2.2). The Acidification Module (AM) is designed to capture the inorganic carbon produced when an acid is combined with a bulk sediment sample. The inorganic carbon evolved from the sample is transported by CO_2-free carrier air stream through a scrubbing system and into the CM5014 Coulometer (coulometer) for detection. The coulometer takes external air from its surroundings, and compresses it, before introducing it to the 'pre-scrubber'. The 'pre-scrubber' is a glass column containing a 45% potassium hydroxide (KOH) solution, which removes CO_2 from the air prior to its introduction to the acidified sample. Once the air stream has incorporated the CO_2 produced from the acidified sample, it passes through a 'post-scrubber', another reaction vessel containing a 50% potassium iodide (KI) solution, which removes hydrogen sulphide, sulphuric oxides and/or any other molecules which may result from the acidification of some materials. From here the air stream (containing only CO_2 evolved from the sample) is connected to the CM5014 Coulometer via a tube.

The coulometer provides an accurate, absolute determination of carbon in any CO_2-containing air stream. The coulometer cell (see Figure 2.1) is filled with approximately 75-100 ml of a 'cathode solution' containing monoethanolamine and a colourimetric pH indicator. A platinum cathode is positioned in the cell so that it was completely immersed in the cathode solution. Similarly, around 15-20 ml of 'anode solution' is placed into a smaller separate compartment of the coulometer cell, with a ~0.5cm-thick layer of potassium iodide (KI) placed on the bottom of the anode compartment. A silver anode is then placed into the compartment, so that the anode is completely immersed in the anode solution. The cell assembly is then placed into the coulometer cell compartment between a light source and a photodetector, so that the light source shines through the cathode solution into the main part of the cell.

An air stream containing the sample-evolved CO_2 passes via an inlet tube into the cathode solution in the main part of the coulometer cell. Once in contact with the cathode solution the CO_2 is quantitatively absorbed, and reacts with the monoethanolamine to form a titratable acid, which causes the colourimetric pH indicator to fade. The photodetector monitors the change in the colour of the solution as a percent transmittance of the light source (%T). As the % T increases, the titration current is automatically switched on to generate base at a rate proportional to the % T (approximately 1500 µg of carbon per minute). When the solution returns to its original

value of % T (original colour), the current stops. The titration current is measured continually and integrated to the units selected by the operator on the sample screen. Since the current is effectively acting as the titrant, there was no requirement for sample calibration.

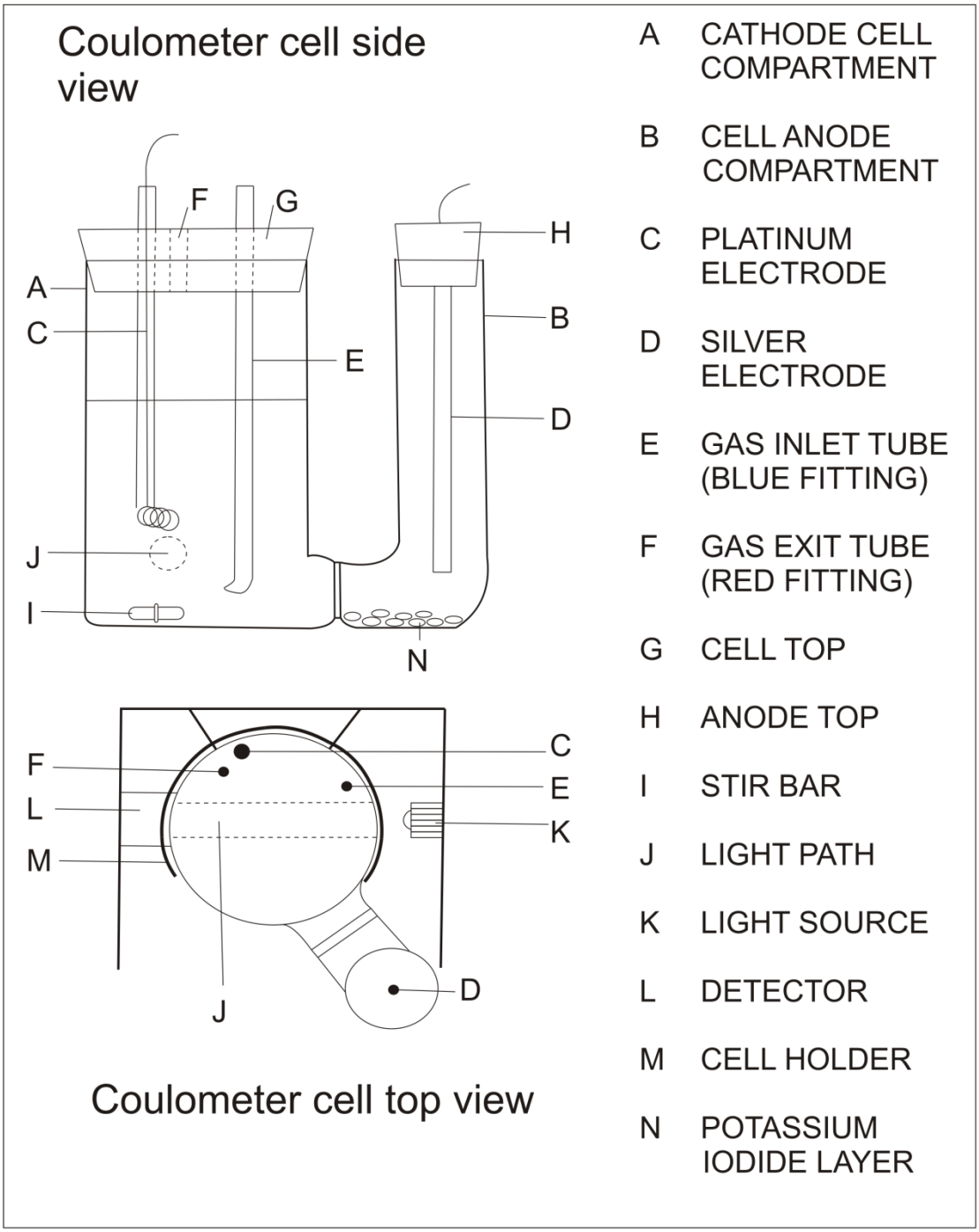

Figure 2.1 – Schematic diagram explaining the operation of the CM5014 Coulometer cell, reproduced from UIC Coulometrics Inc. instruction manual [2008a].

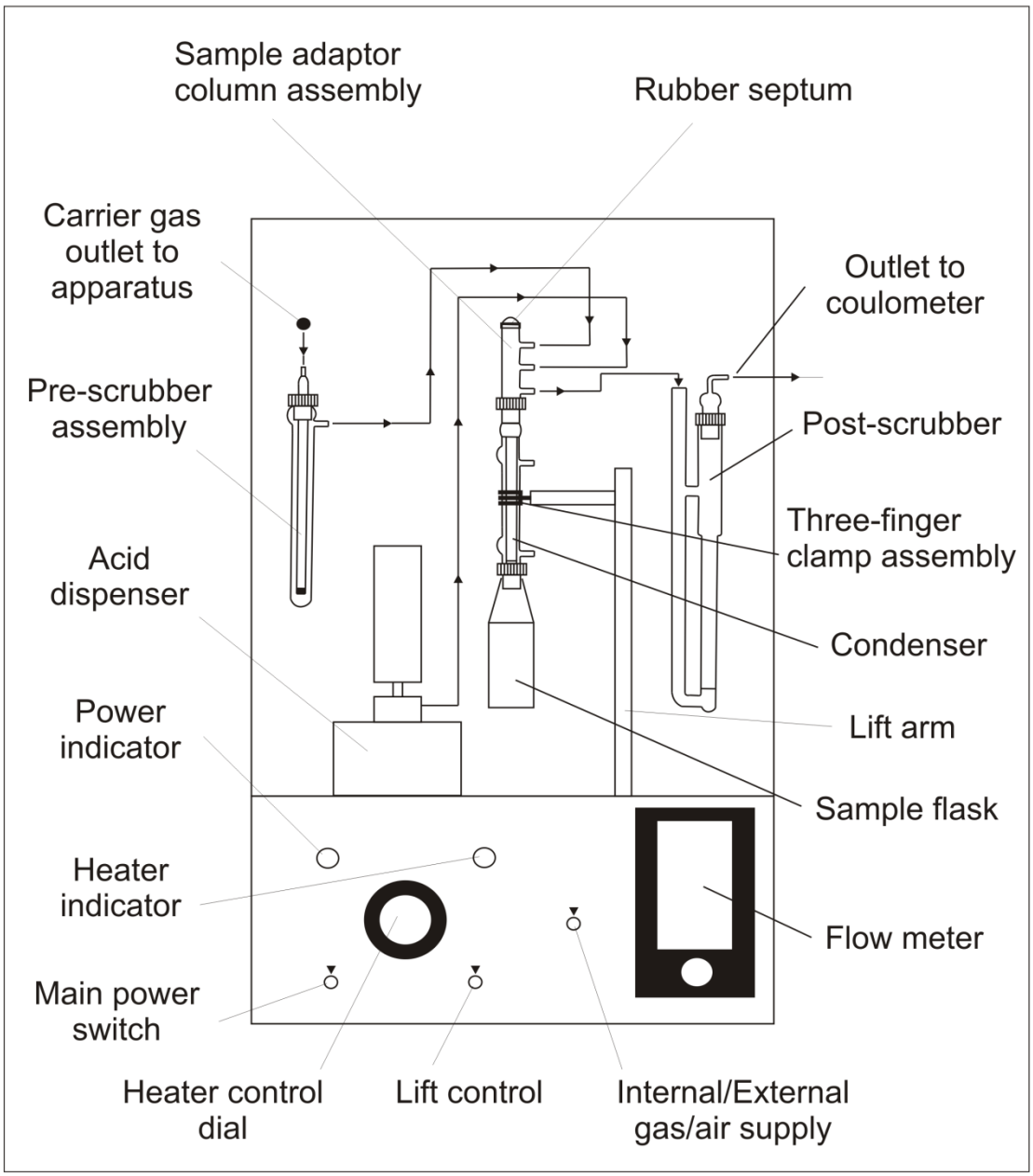

Figure 2.2 – Schematic diagram explaining the operation of the CM5130 Acidification Module, reproduced from UIC Coulometrics Inc. instruction manual [2008b].

The coulometer operates on the principles of Faraday's Law, which states that *1 faraday of electricity will result in the alteration of 1 GEW (gram equivalent weight) of a substance during electrolysis*. In the coulometer, each faraday of electricity expended is equivalent to 1 GEW of CO_2 titrated. A summary of the reactions that occurred in the coulometer cell are as follows [*UIC Coulometrics Inc.*, 2008a; 2008b]:

Absorption of CO_2 by cathode solution (cathode reaction):

Equation 2.1

$$CO_2 + HOCH_2CH_2NH_2 \rightarrow HOCH_2CH_2NHCOOH$$

monoethanolamine hydroxyethylcabamic acid

Electrochemical generation of OH^- (cathode reaction)

Equation 2.2

$$2H_2O + 2e^- \rightarrow H_2\,(g) + 2OH^-$$

Neutralisation of absorbed CO_2 reaction product by electrochemically generated OH^-

Equation 2.3

$$HOCH_2CH_2NHCOOH + OH^- \rightarrow HOCH_2CH_2NHCOO^- + H_2O$$

Anode reaction

Equation 2.4

$$Ag^0 \rightarrow Ag^+ + e^-$$

The acid used to evolve CO_2 from the samples is 2N sulphuric acid (H_2SO_4), and 10 ml is added to each sample. The weight of sample used is ~30 mg. The sample is weighed on a 5-place balance into small Teflon cups which were then placed in the sample tube. Cleaning of the tubes and cups is done in between samples with 15 MΩ distilled water and methanol. Once the 2N H_2SO_4 has been added to the sample, the evolution of CO_2 from the sample is measured continuously by the coulometer, using the input parameter of sample weight (mg). Each time the machine is set up the user runs a blank sample (acid added to sample tube with no sediment or standard added). The percentage of the total sample weight that is CO_2 is then calculated internally by the coulometer using the algorithm below:

$$\%\ CO_2 = \frac{(\text{display value of } CO_2 \text{ in mg}) - (\text{blank value of } CO_2 \text{ in mg}) \times 100}{\text{sample weight in mg}}$$

A factor of 2.272727 is then used to convert CO_2 (molecular weight 44) to $CaCO_3$ (molecular weight 100) to produce a weight percentage of $CaCO_3$ for the bulk sediment. After every 11 analyses a standard (artificial 100% $CaCO_3$) is routinely run to ensure that the coulometer continued to make accurate readings.

2.1.2 Precision and accuracy of method

Analyses of 38 standard runs using artificial 100% $CaCO_3$ standard resulted in an accuracy error of -1.32 % (yield always under 100%) and a precision of 0.39% (1 SD). Steps to ensure further accuracy of the results included firstly, initiating the coulometer's measurement sequence before the introduction of acid to the sample (to ensure no loss of sample-evolved CO_2); and secondly, when the sample tube was changed, the tube was allowed to 'purge' for 30 seconds to ensure that no CO_2 from the air in the tube was measured, along with that from the sample. Note: For all $CaCO_3$ measurements see Appendix Table A6.

2.2 Sedimentary biogenic opal

2.2.1 Procedure

Opal measurements were made at Cardiff University using the protocol of Mortlock and Froelich [1989]. Samples of bulk marine sediment were run in batches of 44, in 2 x racks of 24. Each rack contained an operational blank (a tube taken through the entire analytical procedure, with no added sediment), and a sedimentary standard of known opal concentration. In addition, a 'reagent blank' (all reagents used mixed in one bottle, minus sample) was used to determine whether any background absorbance resulted from the reagents used. The samples and standards were weighed out using a 5-place (10^{-5} g) balance and transferred to the 50 ml Nalgene centrifuge tubes. Approximately 100 mg of sediment was used for sediments that were estimated to have a low percentage of opal, for example ODP 663A, from previous work by [*deMenocal et al.*, 1993] and 30 mg was used from sediments that potentially had very high percentage opal (e.g. VM19-296, known to contain interval(s) of diatomaceous ooze, from [*Gardner and Burckle*, 1975]. The method is designed so that a sample should not contain more than 25 mg of pure opal. In each run approximately 30 mg of standard was used; in earlier runs this standard was the L-DEO OFI (Original Flow-In) sediment silica standard, but when this ran out it was not replenished due to diminishing stocks. In its place a diatomaceous sediment from the Mertz-Ninnis Trough, Southern Ocean (Jumbo Piston Core NBP01-01) was used. The laboratory protocol for sample treatment was based on that of L-DEO (L. Baker, personal communication – see appendix for full method).

Acid wash – Samples were treated with 10 % H_2O_2 to remove organic compounds, and 10 % HCl to removed carbonate. All samples were then disaggregated by placing them in an ultrasonic bath.

Extraction – Samples were extracted in 40 ml of Na_2CO_3 for 5 hours in a water bath at 85°C. Longer extraction times were tested to investigate whether this affected silica yield (see 2.2.5).

Mixing – All Si standards, procedural blanks, sediment standards and samples were mixed with 17.5 ml of molybdate working solution (5 parts 18.2 MΩ Milli–Q water, 1 part ammonium molybdate, 1 part HCl); and 7.5 ml of reducing solution (1 part metol-sulphite, 1 part oxalic acid, 1 part H_2SO_4)

Measurement – Absorbance of the Si standards, procedural blanks, sediment standards and samples were measured on a Perkin-Elmer Lambda 2 UV/VIS spectrophotometer, with the absorbency wavelength set at 815 µm (silicates). Background absorbance was corrected for using cuvettes filled with 18.2 MΩ Milli-Q water.

2.2.2 Calculation of dissolved silica and opal concentrations

Absorbency of the samples was translated into dissolved silica concentration using a series of standards containing a known concentration of silicon (see opal data in appendix for standard information). When the absorbency versus concentration of this standard series was plotted, a linear regression (R^2 >0.99) gave the relationship between absorbency and concentration and was used to calculate the silica concentration of the sample (C_s):

Equation 2.5

$$C_s = S \times (A_s - A_0)$$

Where S is the slope of regression through the standard curve, A_s is sample absorbance and A_0 is the absorbance of the operational blank. Once C_s had been calculated, the weight percentage of silicon is calculated by the equation:

$$\%Si_{opal} = 100 \times (C_s/M) \times (28.09 \text{ g mol}^{-1}) \times (0.04 \text{ l}) \times (1000 \text{ mg g}^{-1}) \times (\text{mol } 1000 \text{ mmol}^{-1})$$

Or more simply:

Equation 2.6

$$\%Si_{opal} = 112.4 \times (C_s/M)$$

Although $\%Si_{opal}$ is a more direct and unambiguous measure of the silica content of sediments, it was one of the aims of this study to reconstruct a mass accumulation rate (mass flux) of opal, hence an estimate of the formula weight of opal needed to be made, as the formula weight was uncertain and probably not constant. Mortlock and Froelich [1989] estimate from the literature and from their own analyses that most diatomaceous silica younger than 30 Ma displays a relatively constant water content of about 10 % (see Table 2.1 below).

Equation 2.7

$$\% \text{ OPAL} = 2.4 \times \%Si_{OPAL}$$

Mortlock and Froelich [1989] note that radiolarians typically display higher water contents, but in this investigation the contribution of radiolarians to biogenic opal in the eastern equatorial Atlantic was assumed to be minimal [*Lange et al.*, 1994; *Ruddiman et al.*, 1986; *Treppke et al.*, 1996].

Mortlock and Froelich [1989] cite the inhomogeneity of some opal as the possible cause of the demonstrated irreproducibility, which is a particular problem for opal-poor samples. In the course of this investigation, reproducibility of the Cardiff opal standard was found to be ~4.5 %, which was used in error estimates. Mortlock and Froelich [1989] report an average short-term precision of ±6 % for 'opal-poor' samples (<15 % opal) and ±8 % for 'opal-rich' samples (>50 % opal). Our long-term average precision for opal-rich samples was ± 4 %.

2.2.3 Precision of method

Table 2.1 (previous page) – Water contents of biogenic silica. References *1, F1-STD [*Mortlock and Froelich*, 1989] ; 2, [*Leclerc and Labeyrie*, 1987]; 3, [*Wang and Yeh*, 1984a]; 4, [*Wang and Yeh*, 1985]; 5, [*Wang and Yeh*, 1984b]; 6, [*Labeyrie*, 1979]; 7, [*Knauth and Epstein*, 1982]; 8, [*Hurd and Theyer*, 1977]† Calculated from exchangeable oxygen in Table 2 of [*Leclerc and Labeyrie*, 1987]assuming all O_{xch} is in $–OH_2$. Table reproduced from Mortlock and Froelich [1989].

H_2O loss (%)	error	n	Age	∆T (deg C)	Procedure	Reference
2.0		1	Pleistocene	25-60	Weight loss	1
8.1	0.4	3	Pleistocene	60-1000	Weight loss	1
†3.8	0.7	10	Pleistocene	25-200	6.2% ^{18}O xchnge	2
3.4 - 6.7	N/A	75	Pleistocene	110-1000	H_2O-H_2; Vol	3,4
4.6 - 5.1	N/A	3	Pleistocene	110-1000	H_2O-H_2; Vol	5
9.7	N/A	1	?	20-1000	Weight loss	6
8.1	N/A	1	Miocene	25-1000	H_2O-H_2; D/H	7
		Water content of Radiolaria				
14.5	2.0	11	10 Ma	25-1000	Weight loss	8
11.0	1.9	17	11-40 Ma	25-1000	Weight loss	8
13.0	N/A	?	Recent?	110-1000	H_2O-H_2; Vol	3,5
		Formula weight conversions as a function of water content				

	H2O content (%)	Formula	Formula wt (g mol $^{-1}$)	Theoretical $\%Si_{opal}$	Conversion OPAL%Si	
N/A	0	SiO2	60.1	46.7	2.14	N/A
N/A	8	SiO2 . 0.3H2O	65.5	42.9	2.33	N/A
N/A	10	SiO2 . 0.4H2O	67.3	41.7	2.40	N/A
N/A	14	SiO2 . 0.55H2O	70.0	40.2	2.49	N/A

2.2.4 Accuracy of method

Although there are no certified methods or standards to exemplify the accuracy of the determination of biogenic opal, cross-laboratory comparisons using a variety of extraction techniques produced excellent agreement (see Table 2.2 and Figure 2.3). Mortlock and Froelich [1989] also analyse an artificial sediment standard (AS-STD) to produce a measured silica content of 1.58 ±0.08 % Si (n = 31 separate batches):

Table 2.2 - An inter-laboratory comparison of different techniques to measure % biogenic opal. Reproduced from Mortlock and Froelich [1989]. L-DGO is Lamont-Doherty Geological Observatory, and OSU is Oregon State University.

Sample	L-DGO	error	OSU	XRD	Sequential dissolution
SX20485	1.25	0.24	0.43	N/A	N/A
SX27548	2.96	0.16	1.12	N/A	N/A
SX27549	3.16	0.29	2.98	N/A	N/A
SX27550	3.05	0.32	0.69	N/A	N/A
SX27552	5.57	0.69	6.22	N/A	N/A
SX12280	6.24	0.54	5.06	N/A	N/A
SX27553	5.21	0.25	4.36	N/A	N/A
SX21194	2.26	0.17	1.92	N/A	N/A
SX27547	6.13	0.27	5.42	N/A	N/A
SX27551	28.53	1.14	31	N/A	N/A
E49-17 (cm)					
310	15.41	0.56	16.4	N/A	N/A
350	19.11	0.87	21.1	N/A	N/A
500	17.78	0.66	14.5	N/A	N/A
880	15.67	0.64	15.3	N/A	N/A
RC14105 (cm)					
310-312	8.93	N/A	N/A	8.13	7.95
329-330	6.45	N/A	N/A	5.33	7.25
510-512	5.89	N/A	N/A	6.12	5.61
1730-1732	2.99	N/A	N/A	2.95	3.97
2190-2192	2.34	N/A	N/A	2.38	0.93
DSDP662A-18-2:100	1.47	N/A	N/A	N/A	1.36
DSDP662A-18-4:146	0.8	N/A	N/A	N/A	0.78
E49-18:110	14.69	N/A	N/A	N/A	14.57
E49-18:1000	11.65	N/A	N/A	N/A	10.38
SX27551	29.81	N/A	N/A	N/A	28.69
E17-9:2000	39.94	N/A	N/A	N/A	40.01

2.2.5 Silica yield

A small, separate methodological investigation was performed alongside the opal analyses as part of this investigation, in order to determine whether the extraction time of 5 hours prescribed by Mortlock and Froelich [1989] was sufficient to ensure that as much opal as possible within the sample was being extracted. The aim of the investigation was to see whether longer extraction times produced higher opal yields. We tested extracts from the same opal sample at 5, 10 and 15 hours in Na_2CO_3 solution in a water bath set to 85°C, designated 'normal' in Figure 2.4.

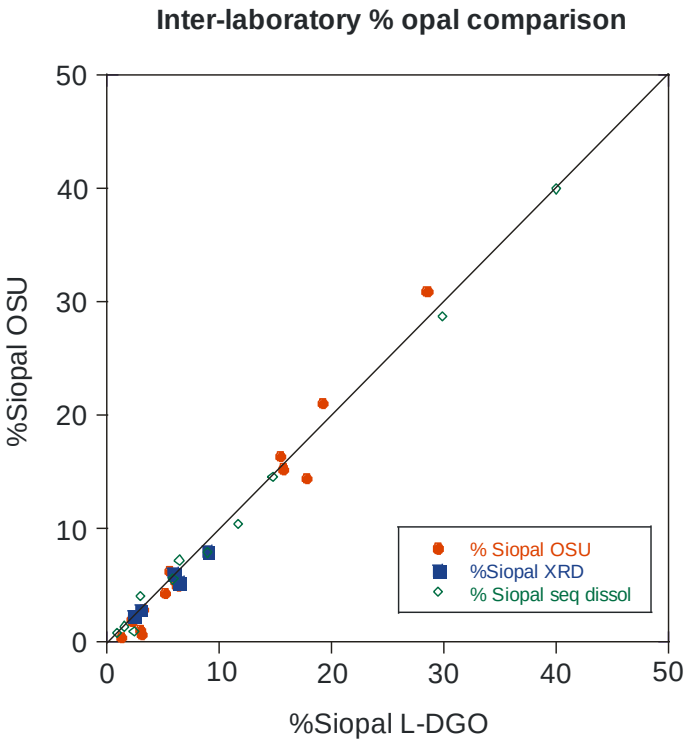

Figure 2.3 (above) – Comparisons of % silicon (opal) obtained by the alkaline extraction technique of [*Mortlock and Froelich*, 1989] (x-axis, '%Siopal L-DGO') versus other techniques performed on the same samples. Red markers represent the alkaline extraction technique of Mortlock & Froelich [1989], performed at Oregon State University (OSU), blue squares are %opal determination by XRD (URI-Leinen, 1985) and the green diamonds represent %opal determination by timed sequential dissolution. The straight line represents perfect 1:1 agreement between methods. Figure reproduced from Mortlock and Froelich [1989].

In addition, I tested the silica yield on extracts at 5 and 10 hours (designated 'mix') which had received additional mixing (by twice briefly inverting the sample tubes after vortex-mixing the tubes at 2 and 4 hours). The results in Figure 2.4 below show that the strategy of mixing is important, but that extraction times longer than 5 hours are not required provided all samples are mixed.

All values of %opal attained in the experiment were lower than those obtained by deMenocal *et al*.[1993] but in most cases were within 0.5 %. Therefore, the strategy of mixing each sample twice (at 2 and 4 hours) during the extraction step was adopted for all opal extractions, and an extraction time of 5 hours was deemed sufficient. Note: For all opal measurements see Appendix Table A7.

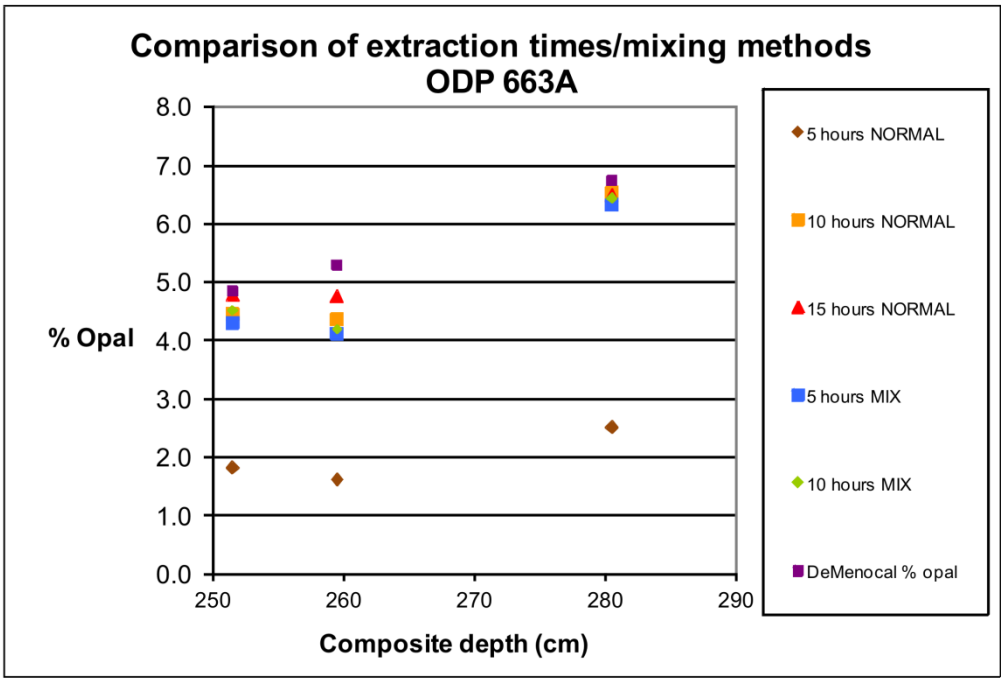

Figure 2.4 - Comparison of extraction times and the effect of mixing vs non-mixing in ODP 663A samples.

2.3 Sedimentary ^{231}Pa, ^{230}Th, ^{232}Th, ^{234}U and ^{238}U

Concentrations of radionuclides were measured in sediment to normalise the flux of sedimentary components (to ^{230}Th), to account for the sedimentary redistribution on accumulation rates [*Francois et al.*, 2004]. Measurement of ^{231}Pa also allowed the construction of an excess ^{231}Pa/^{230}Th ratio, which had previously been used in the Atlantic as a measure of diatom palaeoproductivity [*Bradtmiller et al.*, 2007]. Measurements were made at L-DEO using their protocol (see electronic appendix for full methodology).

2.3.1 Sample weighing and addition of spikes

The technique used to determine radionuclides in sediment was after *Anderson and Fleer* [1982] and *Fleisher and Anderson* [2003]. Aliquots of ^{229}Th were added to each beaker. The step was then repeated for all beakers, adding aliquots of ^{236}U spike, and then again by adding aliquots of ^{233}Pa spike. Finally, a stable Be carrier was added to all beakers. For sample and spike weights see Table A1 (printed appendix).

The bulk, freeze-dried sediment was then weighed out onto aluminium foil, and added to the slightly acidic mixture in the Teflon beaker. Approximately 0.1 grams of sediment were weighed out per sample. Samples were run in five batches of 18-20, plus one blank. One sample (JG-12) was run 5 times to test the precision of the data.

2.3.2 Total sediment digestion

The sediments were digested by heating with HNO_3, $HClO_4$ and HF. Any iron hydroxide in the samples was precipitated by raising the pH of the samples by adding ammonium hydroxide (NH_4OH); centrifuging, and then disposing of the supernatant. For more detailed information see appendix.

2.3.3 Column chemistry for U, Th, Pa and Be

Radionuclides were separated out using anion resin column chemistry. Column #1 (2ml AG1-X8 anion resin) was used to separate the U/Th fraction, and this was concentrated using $HClO_4$ and HNO_3. Column #2 (1ml AG1-X8 anion resin) was used for clean-up of the Pa fraction, and the beakers gamma-counted (see Table A2 in appendix) to ensure that Pa fraction had been cleaned adequately.

2.3.4 Final dry-down of samples

The Pa fraction from each sediment sample was heated with HF and concentrated in $HClO_4$ before being mixed into an ultra-clean 1% HNO_3/1% HF solution, and was then ready for analysis by ICP-MS. The U+Th fraction from each sediment sample was heated with HF and concentrated in $HClO_4$ before being mixed into an ultra-clean 1% HNO_3/1% HF solution, and was also ready for analysis by ICP-MS.

2.3.5 ICP-MS Analysis

Determination of the concentrations of ^{231}Pa, ^{230}Th and ^{238}U were made using a VG Axiom Multi-Collector Inductively-Coupled Plasma Mass Spectrometer (MC-ICP-MS) at L-DEO Isotope Geochemistry Lab. The Pa isotopes were measured in 'Flight Tube Scan Mode', which only monitored the masses 231 and 233. Precision on the 231/233 ratio was better than 2.5 % at the 1 sigma level, for 5 replicates. Machine sensitivity was 5-10 x 10^6 counts per second/ppb of 0.1 ppb ^{238}U solution. Concentrations of 'common' thorium (^{232}Th) in the Pa fraction were low enough to allow the MS to be run at a low resolving power (RP≈ 400).

Solutions containing U and Th were run in 'normal scan' mode, at a higher resolving power (RP≈500), which decreased the sensitivity but allowed a reduction in the correction applied on ^{229}Th, ^{230}Th, ^{234}U, ^{235}U and ^{236}U, from 'tailing' of concentrations by ^{232}Th or ^{238}U. Mass bias corrections were performed in a similar manner to those used for Pa [*Fleisher and Anderson*, 2003]. Batch 3 (some samples from ODP 663A and all samples from RC16-66) had high ^{232}Th count rates, resulting in the count rates on the mass 228.5 tail correction (Cf-229) also being high. The Th from

Batch 3 was run again using a 4:1 dilution and this data was used in the final data reduction.

2.3.6 Calculation of U, Th and Pa abundances from raw data

Note: For proxy background see Chapter 3.4. The primary aim of this analysis was to determine the activity of scavenged (or 'unsupported') ^{230}Th ($A_{Th\text{-}230}^{scav}$). This is the ^{230}Th that is adsorbed to falling particles in the water column and precipitated in sediment. Knowing $A_{Th\text{-}230}^{scav}$ would allow determination of thorium-normalised flux rates of biogenic components [*Bacon*, 1984; *Francois et al.*, 2004].

Calculation of $A_{Th\text{-}230}^{scav}$ depends on the activity contributions of detrital ($A_{Th\text{-}230}^{det}$), and/or authigenic ^{230}Th ($A_{Th\text{-}230}^{auth}$). The assumption is generally made that detrital ^{230}Th is in secular equilibrium with detrital ^{238}U. The activity of detrital ^{238}U is estimated from the activity of ^{232}Th in sediment. The isotope ^{232}Th is found almost exclusively in the lithogenic (detrital) fraction [*Brewer et al.*, 1980], and has an average crustal activity ratio of detrital ^{238}U to ^{232}Th of 0.6 ±0.1 for the Atlantic Ocean [*Henderson and Anderson*, 2003]. The contribution of ^{232}Th was assumed to be 10 ppm for the ODP 663A, VM19-296, RC24-01 and VM30-40 core sites (eastern and mid-equatorial Atlantic), and 15 ppm for RC16-66 (western equatorial Atlantic), due to the enhanced detrital input from the Amazon plume [*Vital and Stattegger*, 2000]. The same values were used to calculate $A_{Th\text{-}230}^{scav}$ in a suite of cores from the equatorial Atlantic [*Bradtmiller et al.*, 2007].

The secondary aim of the analysis was to calculate the activity of scavenged ^{231}Pa ($A_{Pa\text{-}231}^{scav}$), which also needed to be corrected for the contribution of detrital ^{232}Th to allow the calculation of excess ^{231}Pa/^{230}Th ratios as a measure of palaeoproductivity. All calculations were performed in Microsoft Excel, using the algorithms for calculating the unsupported activities of ^{231}Pa, ^{230}Th, ^{232}Th, ^{234}U and ^{238}U. Calculation of $A_{Th\text{-}230}^{scav}$ ($^{230}Th_{xs}$) used the following algorithm (Equation 2.1):

$$^{230}Th_{xs} = {}^{230}Th_{meas} - \{(0.6\pm0.1)\,{}^{232}Th_{meas}\}-$$

$$\left\{\left[{}^{238}U_{meas}-(0.6\pm0.1)\cdot{}^{232}Th_{meas}\right]\cdot\left[1-e^{-\lambda 230 t}\right)+\frac{\lambda_{230}}{\lambda_{230}-\lambda_{234}}\cdot\left(e^{-\lambda 234 t}-e^{-\lambda 230 t}\right)\cdot\left(\left(\frac{^{234}U}{^{238}U}\right)_{init}-1\right)\right]\right\}$$

Equation 2.16 - Calculation of unsupported (scavenged) ^{230}Th in sediment. All nuclide measurements are expressed in activities (A). The first term in curly brackets corrects for the influence of detrital ^{230}Th, and the second term in curly brackets corrects for the influence of authigenic uranium. Reproduced from Henderson and Anderson [2003].

Calculation of excess (unsupported) Pa, to allow the calculation of $^{231}Pa_{xs}$/$^{230}Th_{xs}$, uses the following algorithm (Equation 2.8):

$$^{231}Pa_{xs} = {}^{231}Pa_{meas} - \{0.046(0.6 \pm 0.1)^{232}Th_{meas}\} - \{[0.046^{238}U_{meas}\text{-}(0.6\pm0.1)^{232}Th_{meas}][1\text{-}e^{-\lambda 231 t}]\}$$

Equation 2.8 - Calculation of unsupported ^{231}Pa, see Chapter 2.3 for details. Reproduced from [*Henderson and Anderson*, 2003]

Thorium-normalised fluxes of preserved sedimentary components, such as opal or $CaCO_3$ (denoted i below), were calculated in the following way [*Bacon*, 1984; *Suman and Bacon*, 1989]:

$$F_i = Z(^{234}U)\lambda^{230}\frac{f_i}{^{230}Th_{xs}{}^{0}}$$

Equation 2.9 - Flux normalisation, where F_i is the normalised flux of component i (e.g. opal) to the sediment in g m^{-2} yr^{-1}; Z is the depth of the water column in metres, f_i is the weight fraction of component i in the sediment, (^{234}U) is the seawater activity of ^{234}U in dpm m^{-3}, λ^{230} is the decay constant of ^{230}Th (2.3 x 10^{-5} dpm/cm^3/ka), and $^{230}Th_{xs}{}^{0}$ is the activity of unsupported ^{230}Th. The % sedimentary content of components (e.g. opal or $CaCO_3$) was multiplied by 0.01 before it was multiplied by $^{230}Th_{xs}$. Equation 2.3 reproduced from Henderson and Anderson [2003].

Compound errors on flux estimates were made using the following algorithm (Equation 2.10):

$$\Delta z = Z \times [(\Delta x/X)^2+(\Delta y/Y)^2]^{1/2}$$

Equation 2.10 – Estimation of errors in ^{230}Th-normalised fluxes of sedimentary constituents.

Where the function Z = XY, Δx is the error in sedimentary constituent X (%) and Δy is the absolute error in the total thorium-normalised sedimentary flux, F(total). Note: For all U, Th and Pa measurements and error estimates see Appendix Table A8.

2.4 Foraminiferal fragmentation index (core ODP 663A)

Foraminiferal fragmentation in ODP 663A was measured at Cardiff University. Dried bulk sediment was sieved to <150μm, to exclude larger benthonic species. The dried bulk sample was then put through a sediment splitter, and split an appropriate number of times to leave ~300-500 individuals. Counts were based on numbers of whole, identifiable tests; and the number of fragments (less than half a test) from an identifiable foraminiferal species. The fragmentation index was defined as:

Equation 2.11

(number of fragments)/(number of fragments + number of whole tests)

To provide a measure of consistency between counts, repeats were run on both the same (saved) splits and also on new splits on the same depth interval. Repeat

values within +/- 10 % were accepted, if the repeat error was greater than this, the value of the fragmentation index was modified to reflect the new figure. The method was adapted from [*Le and Shackleton*, 1992; *Le et al.*, 1995]. Note: For all foraminiferal fragmentation measurements see Appendix Table A10.

2.5 Determination of stable oxygen and carbon isotope ratios in foraminiferal calcite

Stable oxygen isotope ratios ($\delta^{18}O$) and carbon isotope ratios ($\delta^{13}C$) were determined for the foraminifer *Globigerinoides ruber* (white) at Cardiff University. The foraminiferal tests were picked from the 250-315 µm size fraction, under a Zeiss Stemi 2000 light microscope (using 14x magnification). The tests were then transferred to plastic auto-analyser pots for analysis. Around 8-18 specimens were picked from each interval to ensure a sufficient amount of foraminiferal calcite for stable isotope analysis. The whole specimens were cleaned using a 3 % solution of hydrogen peroxide (H_2O_2) to remove organic material. Ultrasonification was used to disaggregate clays within the tests, and reagent-grade methanol was added to drive out water from the tests, and remove remaining clays.

The samples were analysed using an automated carbonate preparation device (Kiel-III) coupled online to a Thermo Finnigan MAT252 stable isotope mass spectrometer. Analytical precision was determined by repeated measurements of the Cardiff University in-house (Carrara) and international (NBS19) carbonate standards with a precision of 0.06 ‰. All results are reported relative to the PDB scale. Note: For all stable oxygen and carbon isotope measurements see Appendix Table A5.

2.6 Determination of sedimentary concentration of total organic carbon (TOC) and total nitrogen (TN)

Measurements of TOC and TN were made at Cardiff University. For each sample interval, two aliquots of approximately 2.5 mg of freeze-dried, crushed bulk sediment were weighed out into an aluminium foil cup, and a tin foil cup, respectively. The samples in the tin cups were then placed into a furnace at 500°C for 4 hours to burn off the organic carbon. The samples were then analysed in a Thermo Flash EA 1112 Series elemental analyser, which used a 2-column reduction-oxidation process to determine total carbon (TC) and total nitrogen (TN) weight percentage in the samples.

Table 2.3 – Standard precision for the analysis of TOC and TN in all cores. Averages of these errors were used in the estimation of % TOC and % TN measurement errors.

Standard	TOC error (%)	TN error (%)
Acetylinide	2.98	3.10
Urea	9.03	9.23
Cardiff marine standard	0.96	8.43
AVERAGE	4.32	6.92

After every ten samples, a blank was run, followed by three standards (acetylinide, urea and Cardiff marine sediment standard). Details of standard precision are found in Table 2.3. All of the remaining carbon in the samples after treatment in the furnace was assumed to be inorganic. The weight percentage of total organic carbon (TOC) was then found by subtracting the weight percentage of inorganic carbon from the original sample weight. Note: For all total organic carbon (TOC) and total nitrogen (TN) measurements see Appendix Table A9.

2.7 Measurement of sedimentary neodymium (Nd) isotopic ratios

2.7.1 Carbonate leaching procedure

Initial carbonate leaching steps of all Nd samples was done at Cardiff University. Between 2 and 4 grams of uncrushed fine (<63μm) sediment were weighed and placed into 50ml acid-cleaned plastic centrifuge tubes. The samples first received 25ml of buffered acetic acid, then were mixed with a vortexer, and disaggregated for 6 hours on a rocking table. The samples were then centrifuged and the excess acetic acid decanted and disposed of. This step was repeated a total of 3 times, making sure that no reaction was detectable (to ensure complete carbonate removal).

2.7.2 Fe-Mn oxide leaching procedure

The samples were washed three times in 18.2 MΩ Milli-Q water to remove traces of acetic acid. Oxides of Fe and Mn were separated from the samples by adding 2 ml of a reductive solution of hydroxylamine hydrochloride (HH) to the samples, and placing them on a rocking table for 2 hours, to avoid precipitation of the sediment and ensure maximum leaching efficiency of the HH. After 2 hours, this first leach was collected in labelled 60 ml Nalgene bottles, and would subsequently be analysed for Nd isotopic ratios.

2.7.3 Column chemistry pre-treatment

The samples were purified by heating in clean HNO_3, and treated in an ultrasonic bath, to destroy the HH. The samples were evaporated in HNO_3 several times, and refluxed for longer periods, also in HNO_3. Lastly, the samples were treated in an ultrasonic bath again, then centrifuged at very high speed (13400 rpm) to remove solid residue. Once these steps had been completed, the samples were ready to undergo column chemistry.

2.7.4 TRU-spec column chemistry

All steps from this point onwards were completed in the MAGIC Laboratories at Imperial College London. The TRU-spec columns were used to separate out the Rare Earth Element (REE) fraction. The 100 µl TRU-spec columns were prepared by injecting 300 µl of the colloidal resin suspension in to the column and allowing it to settle. The REE fraction was eluted with 3 x 200 µl 4M HCl into a new labelled beaker. The REE fraction was then evaporated on a hotplate 70°C.

2.7.5 Sr-spec column chemistry

This column was used to collect Sr to perform Sr isotope analysis. The 30 µl columns were prepared by slightly overfilling with resin suspension, and the samples from the TRU-spec columns were prepared by adding 300 µl of 3M HNO_3, and were then placed in the ultrasonic bath for 10 minutes. The REE matrix was eluted back into the REE beakers with 5 x 250 µl of 3M HNO_3, and the Sr eluted into a fresh labelled beaker with 3 full reservoirs of 18.2 MΩ Milli-Q water. The Sr beakers were then evaporated on a hotplate at 70°C.

2.7.6 Ln-spec column chemistry

Ln-spec columns were used to separate out Nd from the rest of the REE fraction. The long columns were filled with 2 x 600 µl of resin suspension (leaving ~50-100 µl of resin in the column). The samples were prepared by adding 100 µl of 0.2 M HCl, and all were placed in an ultrasonic bath for 10 minutes.

The unwanted REE fraction was eluted with 5.5 ml of 0.2 M HCl. The REE fraction was discarded, and the collection beakers were refluxed with 6 M HCl and rinsed with 18.2 MΩ Milli-Q water, to remove the last REE traces. The beaker was then placed under the columns and the Nd was eluted with 5 ml of 0.2 M HCl. The Nd fraction was then evaporated in an open beaker on a hotplate at 70°C.

2.7.7 Determination of Nd isotopic ratios by MC-ICP-MS

After column chemistry, the extracted and purified Nd fraction was analysed on a Nu-plasma Multi-Collector Inductively-Coupled Plasma Mass Spectrometer (MC-ICP-MS) in the MAGIC Laboratories at Imperial College London. The sensitivity of the MC-ICP-MS is reported as 3.4V on ^{144}Nd per 50 ppb of solution, the rate of the nebuliser was 100 µl/minute. The ^{143}Nd/^{144}Nd ratios of the sediment samples (shown below in results section) are normalised to a ^{146}Nd/^{144}Nd = 0.7219 to accomplish mass bias correction.

$$\varepsilon Nd = \left[\frac{\left[\left(\frac{^{143}Nd}{^{144}Nd}SAMPLE\right) - \left(\frac{^{143}Nd}{^{144}Nd}CHUR\right)\right]}{\frac{^{143}Nd}{^{144}Nd}CHUR}\right] 10{,}000$$

Equation 2.12 – The value of the chondritic uniform reservoir (CHUR) is currently 0.512638 [*Jacobsen and Wasserburg*, 1980].

Standard (JNdi-1) was run routinely after every one or two samples to correct for instrumental drift. More than ten standard runs were also run at the beginning of each analysis session (i.e. per day) to determine the instrumental stability. Standard runs (and associated error to the JNdi-1 reference) from the first two analysis days are shown in Figure 2.5. The corrected ^{143}Nd/^{144}Nd of the samples was converted to values of epsilon neodymium (εNd) using the Equation 2.20.

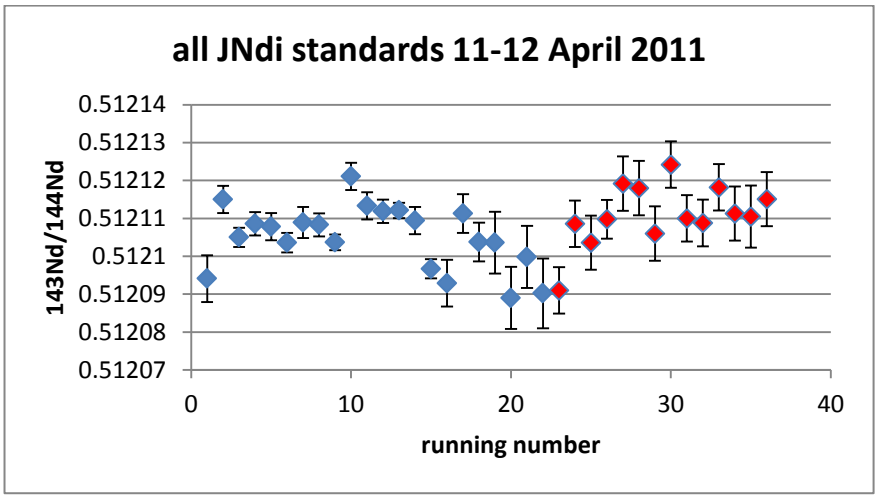

Figure 2.5 – All JNdi standard runs conducted throughout 2 days of Nd isotope analysis. Instrumental drift and errors on the standard runs were deemed to be within acceptable limits. Blue markers denote standard runs from the first day of analysis and the red markers denote standard runs from the second day of analysis.

External reproducibility from routine runs of the JNdi-1 standard was 0.512105 ± 0.000017 (2σ, n=21) for the first day of analysis, 0.512112 ± 0.000012 (2σ, n=14) for the second day, and 0.512057 ± 0.000015 (2σ, n=19). Fifteen samples were run in total, with sample number 12 having an insufficient concentration of Nd to generate an

accurate ε_{Nd}. All sample values were normalised to the recommended JNdi $^{143}Nd/^{144}Nd$ ratio of 0.512115 [*Tanaka et al.*, 2000].

Samples 9 and 14 could also not be used to determine an ε_{Nd} value due to isobaric interference from ^{144}Sm. Sample 7 was diluted with an additional 3ml of 0.15 M HNO_3^-, and sample 5 was diluted with an additional 3 ml of 0.15 M HNO_3^-, as both samples contained high enough abundances of Nd to overwhelm the detectors. External 2σ standard deviation for the ε_{Nd} of the samples was calculated by Equation 2.6:

$$\left[\frac{2\sigma \text{ SD (first 10 standard runs)}}{\text{Average } \frac{^{143}\text{Nd}}{^{144}\text{Nd}} \text{ (first ten standard runs)}}\right] . 10{,}000$$

Equation 2.13 – Calculation of 2σ standard deviation in Nd isotopic ratios

All other samples were run undiluted. The 'chemistry blank' which was run to determine any background contamination evident from the column chemistry steps was run and yielded the following results: Background on axial cup (^{144}Nd) -3 x 10^{-3} mV, signal on 50 ppb standard on axial cup (^{144} Nd) 2.1-2.5V, signal for blank on axial cup (^{144}Nd) 0.00. An additional two samples from core MD99-2198 were run at a later date by project collaborators at Imperial College London, using the same procedure described here. For all Nd isotopic data see appendix table A3.

2.8 Measurement of silicon (Si) isotopic ratios in sponge spicules

2.8.1 Picking sponge spicules (Cardiff University)

Sponge spicules were picked by hand from the 63-215 µm fraction of the coarse (<63 µm) sediment with a moist paintbrush using a Zeiss Stemi 2000 light microscope under 14x magnification. The spicules were placed in plastic auto-analyser pots in a small amount of 15 MΩ distilled water, and the pot lids sealed tightly with Parafilm for transportation to Woods Hole Oceanographic Institute (WHOI). Differences in species are not expected to affect the relationship between spicule $\delta^{30}Si$ and the concentration of H_4SiO_4 [*Hendry et al.*, 2010].

2.8.2 Si separation from major ions (WHOI)

At WHOI the analysis of the silicon isotopic signature of the sponge spicules was conducted by Kate Hendry, and proceeded according to the method of Hendry *et al.*, (2010). First the spicules were cleaned by heating in 30% reagent grade H_2O_2 for an hour, then they were dissolved in 0.4 M NaOH at 100°C for three days [*Hendry et al.*, 2010]. The solutions were then diluted and acidified to pH ~2-3.

A cation exchange resin (BioRad AG50W-X12) was used to quantitatively separate Si from other major ions [*Georg et al.*, 2006]. The standard and samples (<0.4 ml) were added to the column, which contained a quantity of wet resin at neutral pH suitable for the amount of added Na (0.8 to 1.8 ml). $Si(OH)_4$ is in equilibrium with the anionic silicate species $H_3SiO_4^-$ in the pH range 2-8 [*Georg et al.*, 2006], and can be eluted with 18.2 MΩ Milli-Q water. A recent study has shown that pH does not affect the yield of Si, or fractionation in the column [*Savage et al.*, 2010].

2.8.3 Determination of Si isotopic ratios by MC-ICP-MS

Determination of Si isotopic ratios was done by Kate Hendry at WHOI. The post-column samples were introduced into the Thermo Neptune Multi-Collector Inductively Coupled Plasma Mass Spectrometer (MC-ICP-MS) instrument at the Woods Hole Oceanographic Institution (WHOI) ICP-MS Facility. The instrument was operated in a dry plasma mode, with the sample introduced via a self-aspirating PFA micro-concentric nebuliser, plugged into an ARIDUS-II (not connected to N_2) with an uptake rate of 50-100 µl min^{-1}, in high-resolution mode. Full operating conditions are described in [*Hendry et al.*, 2010].

The solutions were run at least in duplicate. Mass bias and drift were corrected for by standard-sample bracketing, intensity matching samples and bracketing standards. Values of $\delta^{29}Si$ and $\delta^{30}Si$ were calculated offline (relative to NBS28), taking an average of the two bracketing standards for each sample. Data that did not meet strict quality control criteria were rejected, meeting guidelines described in [*Hendry et al.*, 2010]. Repeat measurements of sponge standard LMG08 show long-term reproducibility over several months is ~ 0.07‰ for $\delta^{29}Si$ and ~0.16‰ for $\delta^{30}Si$ (2SD of three replicates per run) [*Hendry et al*., 2010; *Hendry et al*., 2011]. For each sample, at least one measurement was also made using an Mg doping internal correction.

Si and Mg isotopes were measured in dual mode (peak-hopping) utilising a method adapted from Cardinal *et al*. (2003), so that $\delta^{28}Si$, $\delta^{29}Si$ and $\delta^{30}Si$ were measured in the first cycle and ^{24}Mg, ^{25}Mg and ^{26}Mg measured on the second cycle, with each cycle comprising 30 alternate measurements. Samples and bracketing standards were spiked with Mg standard (Inorganic Ventures), an intensity matched for ^{28}Si and ^{24}Mg signals within 10 % (typically within 5 %). $^{29}Si/^{28}Si$ isotope ratios were corrected using a fractionation factor calculated using the measured $^{25}Mg/^{24}Mg$ ratios, see [*Cardinal et al.*, 2003] for details. The $\delta^{29}Si$ values obtained from the standard-sample bracketing method and the Mg doping method agreed typically within ± 0.1 ‰. For all Si data see Table A4 in printed appendix.

2.9 Sedimentary diatom frustule counts

2.9.1 Preparation of slides

Diatom slides were prepared at Cardiff University using the method of [*Scherer*, 1994], which has been adapted by Claire S. Allen (British Antarctic Survey) (personal communication). See appendix for full methodology.

2.9.2 Diatom fragment counts

Diatoms were examined under a Leica DMRX microscope (Cardiff University School of Earth and Ocean Sciences, Room 1.14) using the 100x objective. Counts were made according to the method of [*Scherer*, 1994], but the samples contained insufficient valves to make a full count. Images to aid diatom identification were captured as necessary on the microscope-linked PC, using microscope imaging software.

Diatoms were grouped into the following general categories: *Ethmodiscus* (centric), *Thalassiosira* (centric), *Chaetoceros r.s.* (centric), *Thalassiothrix* (pennate), and *Rhizosolenia* (pennate). The diatom count was therefore only a qualitative measure of diatom species change. Of key importance was the identification of *Ethmodiscus rex* fragments. The identification of *Ethmodiscus rex* was made by observation and identification of the central section of a frustule by Dr. J. Pike, and the identification agrees with that of [*Gardner and Burckle*, 1975], for the MIS 4 interval from cores in this region.

2.10 Determination of sedimentary biomarker ratios

2.10.1 Extraction

All preparation and measurement was carried out at Bristol University (see appendix for full methodology). Samples were weighed out (~2-4 g of bulk, freeze-dried and crushed sediment) into glass centrifuge tubes (in groups of 3-8). Initial extraction of organic compounds proceeded by adding ~5 ml of dichloromethane (DCM) to all samples, placing in an ultrasonic bath for 20 minutes, and centrifuging. The supernatant containing the organic compounds was then siphoned off using a pipette and transferred to bulb flasks. These steps were repeated once more using DCM, then twice with a 1:1 mixture of DCM and methanol, and finally twice more with methanol. The excess solvent was removed using a rotary-evaporator, and the remaining organic

compound residue was re-dissolved in 1ml of 1:1 DCM/methanol. The samples were then dried down gently under N_2 gas (to minimise oxidation of the organic compounds).

2.10.2 Separating the polar and apolar fractions

Silica gel columns were prepared, and the samples were separated into polar and apolar molecule fractions and collected, with the apolar fraction in hexane and the polar fraction in 1:1 DCM/methanol.

2.10.3 Standard addition and derivitisation

The standard used in biomarker quantification was standard 5a-androstan-3β-ol (androstanol), which was added to the whole total lipid extract (TLE) of each sample. The TLE was then split in half, with one half stored as a sample archive.

2.10.4 Gas Chromatography (GC) analysis

Derivatised samples were analysed using a Hewlett-Packard 5890 series II GC with a flame ionisation detector, the carrier gas was hydrogen. The fused-silica column used was a Phenomenex Zebron ZB-1, 60 m length x 0.32 mm ID x 0.1 µm FT. The derivatised samples in hexane were injected into the GC (1 µl using a precision syringe). The initial temperature was 70°C, which was increased to 130°C at the rate of 20°C a minute, the temperature increased further to 300°C at a rate of 4°C a minute and was then held constant for 25 min.

2.10.5 Gas Chromatography-Mass Spectrometry (GC-MS) analysis

Quantitative analysis of biomarkers was made on a Finnigan Trace GC-MS using the same GC temperature conditions as above, the carrier gas was helium. The fused-silica column used was a Agilent HP-1, 50 m length x 0.32 mm ID x 0.17 µm FT.

2.10.6 Biomarker abundance ratios

Biomarkers abundance ratios were measured using raw abundance peaks obtained by using the analysis software Xcalibur. Simple ratios of the raw abundance peaks of brassicasterol (diatom biomarker), and the total abundance of $C_{37(2)}$, $C_{37(3)}$ and C_{38} alkenones were then calculated in Excel. For all biomarker data see Appendix Table A9.

Chapter 3 – Measuring changes in equatorial Atlantic opal burial during the MIS 5/4 transition: an initial test of the Silicic Acid Leakage Hypothesis

3. 1 Introduction

The Silicic Acid Leakage Hypothesis (SALH) involves a reorganisation of the oceans dissolved silica cycle [*Brzezinski et al.*, 2002; *Matsumoto et al.*, 2002]. Diatoms (unicellular algae) use dissolved silica (silicic acid) from seawater to build their protective outer frustules [*Armstrong and Brasier*, 2005]; which, on the death of the organism, sinks through the water column and becomes buried in sediment as biogenic silica (opal). A number of studies have linked increased levels of sedimentary opal with past episodes of increased diatom productivity [*Bradtmiller et al.*, 2006; 2007; *Anderson et al.*, 2009; *Bradtmiller et al.*, 2009].

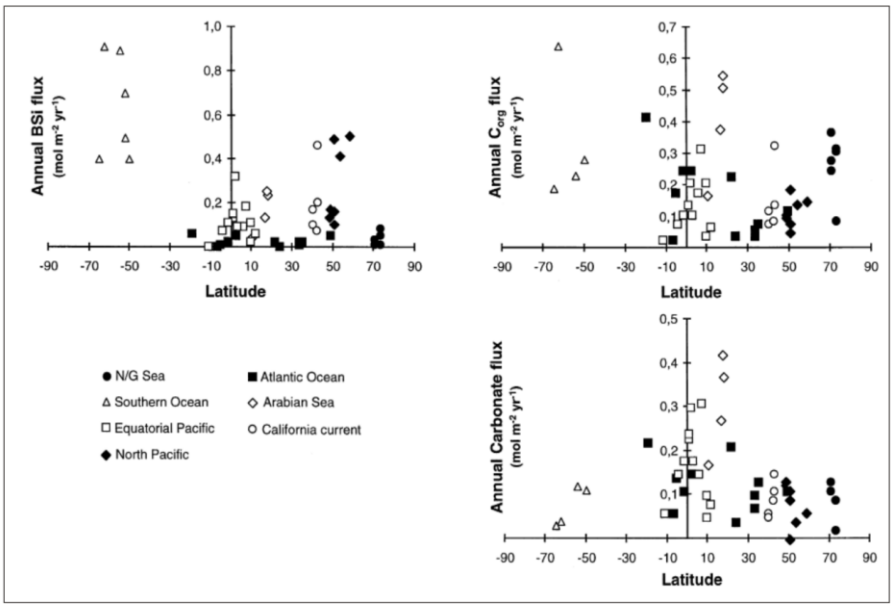

Figure 3.1 – Latitudinal variations in sediment trap-recorded fluxes of opal/biogenic silica (BSi), organic carbon (C_{org}) and calcium carbonate ($CaCO_3$). Reproduced from Ragueneau *et al*. [2000].

A central prediction of the SALH is that an increase in the availability of silicic acid, supplied by Antarctic Intermediate Water (AAIW) [*Sarmiento et al.*, 2004], to the low latitude ocean during glacial times may have allowed diatoms a competitive advantage over $CaCO_3$-producing phytoplankton (such as coccolithophorids) in terms of nutrient availability, leading to a decrease in $CaCO_3$ production, and export to the deep ocean. This then could have led to a pCO_2 decrease through changes in surface- and whole ocean alkalinity [*Matsumoto et al.*, 2002].

In the modern ocean, diatom productivity at low latitudes is limited by silicic acid availability, with <1 µM of silicic acid a typical concentration in low latitude surface waters [*Nelson et al.*, 1995]. Therefore, the prevailing pattern of primary productivity

in the oceans tends to be silica-dominated in polar regions and carbonate-dominated in the low latitude/equatorial regions (Figure 3.1). It has been shown experimentally that addition of silicic acid to Si-depleted diatoms allows them to outcompete a common coccolithophorid (*E. huxleyi*), when the silicic acid concentration exceeds a threshold of ~2 µM [*Egge and Aksnes*, 1992].

This prevailing situation in the modern ocean may have been altered in the past by the delivery of large quantities of silicic acid to the low latitude surface ocean, potentially supplied by an increase in the silicic acid content of AAIW [*Brzezinski et al.*, 2002]. Mechanisms that could have led to a change in the silicic acid content of AAIW include a change in the silicic acid uptake ratio of diatoms due to enhanced input of Fe into the Southern Ocean [*Hutchins and Bruland*, 1998; *Takeda*, 1998], an overall reduction in diatom stock in the Southern Ocean [*Martin*, 1992], or an increase in Southern Ocean sea-ice cover [*Charles et al.*, 1991; *Chase et al.*, 2003]. Each of these mechanisms may have individually or collectively contributed to the creation of a silicic acid excess in the Southern Ocean (SO), which could have then been transferred to low latitudes via AAIW/SAMW [*Sarmiento et al*., 2004]. This could then have allowed diatoms to outcompete coccolithophorids as Si-limitation was alleviated [*Egge and Aksnes*, 1992]. A study of silicon isotope ratios in diatoms (proxy for Si uptake) from RC13-259 (in the Atlantic sector of the SO), suggests that excess glacial silicic acid in the SO was a plausible possibility [*Brzezinski et al.*, 2002].

3.2 Previous tests of the SALH and MIS 4 CO_2 drawdown

Most previous tests of the SALH have used the accumulation rate of sedimentary opal in glacial and interglacial periods in order to examine the validity of the SALH. A testable prediction of the SALH is that opal productivity will be higher in glacial periods than in interglacial periods, in the 'low latitude' ocean, i.e. where the flux and preformed chemistry of AAIW is potentially able to influence export productivity [*Sarmiento et al.*, 2004]. This prediction must be tested carefully as sedimentary opal accumulation is not necessarily always related to diatom export productivity in the surface ocean [*Ragueneau et al.*, 2000; *Dubois et al.*, 2010].

The SALH has been tested as a cause of CO_2 drawdown in the Last Glacial Period (LGP), ~18-28 ka, in the equatorial Pacific [*Higginson and Altabet*, 2004; *Bradtmiller et al.*, 2006; *Richaud et al.*, 2007], and in the same region over the last 150 ka [*Kienast et al.*, 2006]. The SALH has also been tested in the Pacific sector of the SO as a cause of CO_2 drawdown during the LGP [*Bradtmiller et al.*, 2009], and also in the equatorial Atlantic [*Bradtmiller et al.*, 2007]. The results of these last two studies suggest that an excess of silicic acid was created in the SO, which is consistent with other work [*Brzezinski et al.*, 2002; *Chase et al.*, 2003]. The low

latitude Pacific was seen as a suitable location to study the SALH, given the potential that the SO has to affect low latitude diatom productivity, and that the diatom productivity in the equatorial Pacific today appears to be Si-limited [*Dugdale and Wilkerson*, 1998; *Sarmiento et al.*, 2004].

However, these studies have so far proved inconclusive as to the effect that silicic acid leakage may have had on the productivity of the low latitude oceans. All three of the studies by Bradtmiller *et al*. used thorium (^{230}Th)-normalised sedimentary opal accumulation rates to determine whether opal productivity at low latitudes was higher in the Last Glacial Period (LGP, ~18-28 ka) than in an interglacial period (the Holocene). The result of the Pacific study was that Holocene opal burial rates exceeded those of the LGP by 35 % across the equatorial Pacific for the area 80° - 110° W and 5° N - 5° S, and therefore did not support the SALH [*Bradtmiller et al.*, 2006]. However, other studies have shown that 'El-Niño-like' conditions persisted in the eastern equatorial Pacific (EEP) during the LGP [*Beaufort et al.*, 2001; *Koutavas et al.*, 2002; *Kulongoski et al.*, 2009]. Bradtmiller *et al*. [2006] suggested that this may have led to decreased productivity in the EEP due to deepening of the thermocline, and hence negated the impact of any enhanced silica leakage in SAMW/AAIW on diatom productivity in the EEP during the LGM.

Two studies of the EEP show decreased opal burial in the EEP in MIS 4 and MIS 2 (~11-24ka), relative to MIS 3 (~59-24ka) which contains a prominent opal accumulation peak [*Kienast et al.*, 2006; *Richaud et al.*, 2007]. Although pCO_2 during MIS 3 was lower than during the Holocene, it was greater than during the LGP or MIS 4 [*Petit et al.*, 1999; *Ahn and Brook*, 2008]; and it was therefore suggested that the SALH could only have a very small impact on pCO_2 [*Kienast et al.*, 2006]. However, this MIS 3 opal peak was later suggested to have resulted from enhanced opal preservation rather than increased opal productivity, as the record of the diatom biomarker brassicasterol showed no clear increase during MIS 3 [*Dubois et al.*, 2010].

Another study of the SALH in the EEP invoked it as a cause of deglacial CO_2 rise, and found that a rise in the ratio of C_{38} and C_{37} alkenone (coccolithophorid biomarkers) to brassicasterol and β-sitosterol (diatom biomarkers) increased at ~15.5 ka, approximately coeval with the rise in pCO_2 [*Higginson and Altabet*, 2004]. Although the timing of the changes in the biomarker ratio and the change in pCO_2 support the SALH, the authors note that the productivity of coccolithophorids appears to decline after 15.5 ka, and therefore that other mechanisms must contribute to the deglacial pCO_2 rise.

The 2006 study of the Pacific sector of the SO by Bradtmiller *et al*., determined that glacial opal fluxes were greater than those of the Holocene at core sites south of the APF, but showed the reverse result at core sites north of the APF. The offset of

the increased diatom productivity north of the APF was determined to be insufficient to offset the Holocene decreases to the south, suggesting that silicic acid leakage from the Pacific sector of the SO was possible [*Bradtmiller et al.*, 2009]. Records of δ^{30}Si from the EEP support this proposal, in that they suggest that the uptake of silicic acid by diatoms in the EEP was possibly lowered due to the enhanced glacial input of Fe into the EEP during the Last Glacial Maximum (LGM, ~19-24 ka), leading to the creation of a silicic acid excess [*Pichevin et al.*, 2009]. A more recent study has since advocated that the communication of excess silicic acid from the EEP to the eastern tropical North Pacific (ETNP) contributed to the enhancement of diatom productivity over coccolithophorids, in agreement with the SALH [*Arellano-Torres et al.*, 2011].

The study of the SALH in the equatorial Atlantic during the LGP produced a different result to that of the EEP, finding that glacial opal fluxes exceeded those of the Holocene for the area 0° - 40° W and 5° N - 5° S, in accordance with the SALH [*Bradtmiller et al.*, 2007]. This result, in combination with the findings of other studies of the SALH suggest that a fundamental difference in low latitude productivity exists between the Atlantic and Pacific basins in response to silicic acid leakage, and that the potential still exists for a glacial SALH scenario to have occurred.

To date, no study has examined the SALH as a cause of pCO_2 drawdown during Marine Isotope Stage (MIS) 4 [*Martinson et al.*, 1987] (~70-59 ka, on the Hulu-Sanbao speleothem-tuned Greenland ice core δ^{18}O GICC05 age scale, see 3.5). The beginning of MIS 4 was coincident with a large and rapid (~47 ppm in ~4 ka) decrease in pCO_2 which began around 71 ka [*Petit et al.*, 1999; *Ahn and Brook*, 2008] (Figure 3.2). Data suggests that MIS 4 (along with MIS 6, 5d, 5b and 2) was a period of high productivity in the equatorial Atlantic, with a shallow nutricline and thermocline due to an intensification in equatorial divergence and upwelling [*Jansen et al.*, 1996; *Abrantes*, 2000; *Flores et al.*, 2000]. These conditions coincided with periods of aridity on the African continent [*deMenocal et al.*, 1993; *Zhao et al.*, 2003; *Scholz et al.*, 2007], and periods of increased NE Trade Wind strength [*Flores et al.*, 2000; *Abrantes*, 2003]. Taken together, the data from the tropical Atlantic suggests that any enhancement of Si in intermediate waters during MIS 4 may have been able to influence productivity in the surface ocean.

Previous results suggest that the equatorial Atlantic is a suitable location to measure changes in low latitude productivity in response to silicic acid leakage [*Bradtmiller et al.*, 2007]. Additionally, a number of studies have shown elevated sedimentary opal during MIS 4 in eastern equatorial Atlantic sediments [*Gardner and Burckle*, 1975; *Stabell*, 1986; *deMenocal et al.*, 1993; *Verardo and McIntyre*, 1994; *Abrantes*, 2001], which may be indicative of enhanced opal productivity during this period. Of these studies, several noted the abundant occurrence of the large centric

diatom *Ethmodiscus rex* (*E. rex*) which appeared to dominate export productivity in some glacial periods, including MIS 4 [*Gardner and Burckle*, 1975; *Stabell*, 1986; *Abrantes*, 2001] (see Figures 3.3 and 3.4).

E. rex has the largest cells of any known diatom, with cell diameters up to 1.9 mm and volumes of 10^9 µm^3 [*Villareal et al.*, 1999] (Figure 3.3). In plankton samples, *E. rex* is not found in large numbers relative to the total diatom flora. Where they are found, planktic *E. rex* cells appear to be restricted to tropical and subtropical waters and live in the upper 200m of the water column [*Gardner and Burckle*, 1975, *and references therein*]. Estimates of the abundance of *E. rex* in tropical waters are around 1-5 cells m^{-3} [*Belyayeva*, 1970; *Villareal*, 1993]. *E. rex* is capable of regulating its buoyancy in order to partition its nutrient acquisition (with N acquired at depth, and C and Si acquired at the surface), as an adaptation to an open-ocean oligotrophic environment [*Villareal*, 1993; *Villareal et al.*, 1999].

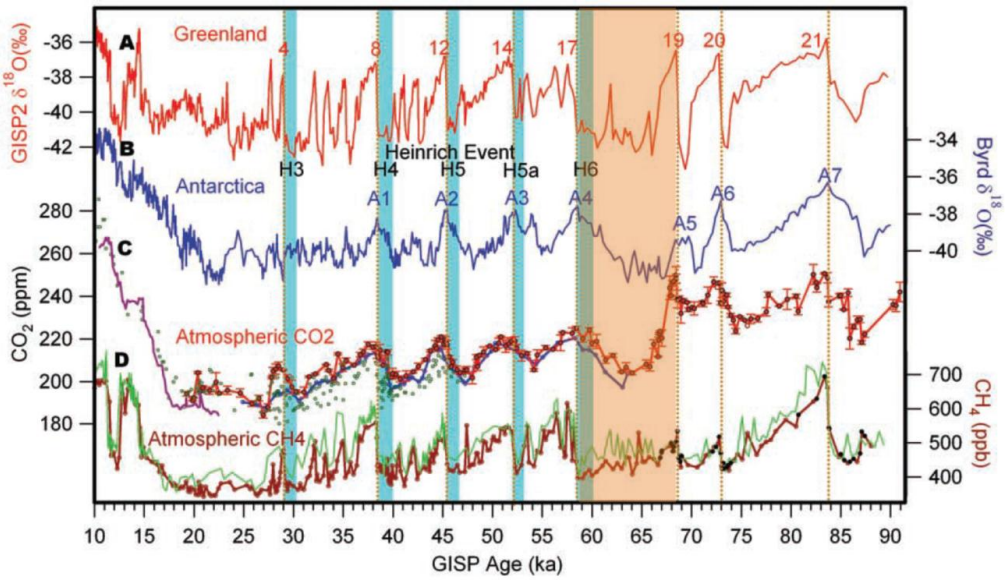

Figure 3.2 – A plot of $\delta^{18}O$ (temperature proxy) for Greenland (red curve A) and Antarctica (blue curve B), with a composite record of Antarctic ice-core CO_2 (curve C). Marine Isotope Stage 4 is highlighted by a shaded orange box. Reproduced from Ahn and Brook [2008].

Despite its size, data indicate that *E. rex* does not contribute greatly to overall opal production in the modern ocean, although this is based on a conservative estimate of abundance data [*Villareal et al.*, 1999].

The occurrence of thick layers of monospecific *E. rex* ooze in the equatorial Atlantic has been documented by a number of studies, [*Gardner and Burckle*, 1975; *Stabell*, 1986; *Abrantes*, 2001]. The oozes occur as beds ranging from a few centimetres in thickness to several meters, and are composed almost entirely of layers of broken frustules of *E. rex,* interspersed with pelagic and hemipelagic facies which contain few or no *E. rex* (see Figure 3.3) [*Gardner and Burckle*, 1975].

A current view of the occurrence of thickly-laminated diatomaceous ooze is that it is the result of selective physical segregation of large, buoyant diatoms at oceanic frontal zones, where they come to dominate opal export [*Kemp et al.*, 2006]. Despite the fact that, ordinarily, *E. rex* does not contribute greatly to opal export, individual cells have an Si:N ratio of 0.95, and an Si:C ratio of 7.24 [*Villareal et al.*, 1999], or about 6-7 times higher than the average values of 0.13 and 1.12, respectively [*Brzezinski*, 1985].

Figure 3.3 – (left panel) Valve view of *Ethmodiscus rex*, x 150 magnification (field view ~2mm), reproduced from Wiseman and Ingram Hendey [1953]; (right panel) Scanning Electron Micrograph (SEM) image of broken *Ethmodiscus rex* frustule fragments, in Miocene age sediments from DSDP Site 520, reproduced from Kemp *et al.* [2006].

If the abundances of *E. rex* were higher in glacial periods, they may have represented a very large uptake of silicic acid, possibly supplied by thermocline waters, as suggested to explain the occurrence of *E. rex* ooze in the tropical Indian Ocean during the LGP [*Broecker et al.*, 2000].

The extent of *E. rex* ooze in the eastern equatorial Atlantic suggests the possibility of a widespread change in the dominant phytoplankton type from coccolithophorids to diatoms during MIS 4 (Figures 3.4 and 3.5) [*Gardner and Burckle*, 1975; *Stabell*, 1986; *Abrantes*, 2001], and additionally demonstrates that the occurrence of *E. rex* ooze was not just restricted to frontal zones.

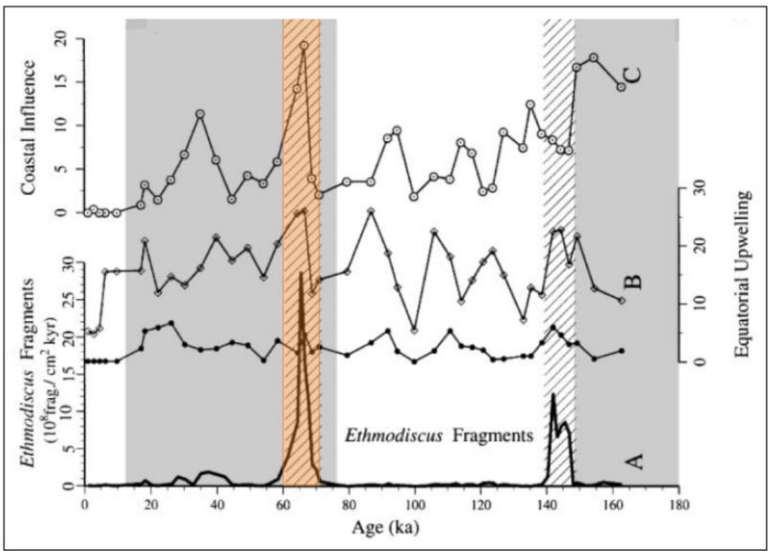

Figure 3.4 - A plot of the number of *E. rex* fragments (bottom left axis) recorded in core M16772 (Gulf of Guinea, eastern equatorial Atlantic). The orange hatched area represents MIS 4, grey bands represent glacial periods. Reproduced from Abrantes [2001].

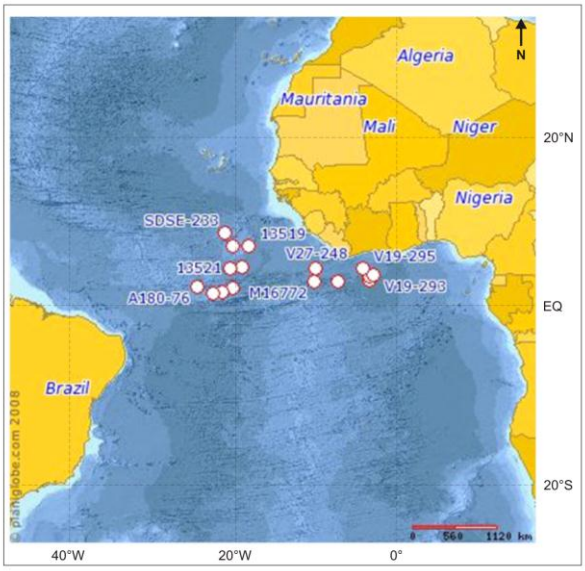

Figure 3.5 – The extent of *E. rex* ooze in the equatorial Atlantic, based on data from Gardner and Burckle [1975], Stabell [1986] and Abrantes [2001].

3.3 Sampling rationale, core locations and oceanographic setting

The equatorial Atlantic Ocean was chosen as a suitable location to test the SALH as a cause of MIS 4 pCO_2 drawdown due to the suggestion that iron (Fe) limitation of phytoplankton growth does not appear to have significantly affected the low latitude Atlantic over glacial-interglacial timescales [*deMenocal et al*., 1993]. This may be contrasted with the equatorial Pacific, where Fe limitation may have been a more important factor [*Moore et al*., 2004]. Fe is an essential micronutrient for oceanic phytoplankton [*Martin*, 1990; *Ridgwell and Watson*, 2002], and additionally may

strongly limit the growth of diatoms [*Timmermans et al*., 2004; *Brzezinski et al*., 2011]. The largest global source of Fe comes from the deserts of North Africa, and subsequently the largest global deposition of Fe on the oceans occurs on the Mediterranean and North Atlantic/equatorial Atlantic regions, downwind of the North African coast [*Prospero*, 1996; *Guerzoni* et al., 1997; *Maher et al*., 2010]. During glacial periods, north-east trade wind strength probably increased, delivering more Fe onto the North and equatorial Atlantic region [*Flores et al*., 2000; *Abrantes* 2003]. The suggestion, therefore, that the Atlantic region has effectively never been Fe-limited removes glacial-interglacial variation in aeolian Fe delivery as a complicating factor on glacial-interglacial changes in opal flux rates.

Additionally, primary productivity in the equatorial Atlantic region may potentially have been strongly influenced by the flux and preformed chemistry of southern-sourced intermediate water [*Sarmiento et al*., 2004] (see Chapter 5). The possibility that a pool of unutilised silicic acid was created in the Atlantic sector of the Southern Ocean during MIS 4 is suggested by silicon isotope data [*Brzezinski et al*., 2002]. This may then have 'leaked' to the low latitude Atlantic through AAIW/SAMW [*Sarmiento et al*., 2004].

Some assumptions are made regarding the testing of the SALH in the equatorial Atlantic region, principally that the dominant control on diatom productivity is Si availability. Testing the SALH using changes in opal accumulation assumes that other factors which may influence productivity, such as the effect of wind strength on upwelling, remain the same over glacial-interglacial timescales. An important control on the strength of Atlantic winds and upwelling patterns is the position of the Inter-Tropical Convergence Zone (ITCZ), which can strongly affect primary productivity [*Flores et al.*, 2000]. Furthermore, this approach assumes that concentrations of nitrate and phosphate are also not limiting phytoplankton growth in the equatorial Atlantic.

This investigation uses a similar approach to that of [*Bradtmiller et al.*, 2007] to investigate the SALH as a cause of CO_2 drawdown during MIS 4. A suite of five cores were selected, covering an area 0° - 40° W and 5° N - 5° S. The three easterly cores ODP 663A (1°11.87'S, 11°52.71'W, 3708 m water depth), VM19-296 (1°25.12'N, 9°4.59'W, 5017 m water depth) and RC24-01 (0°33.0'N, 13°39.0'W, 3837 m water depth) lie in the divergence created by the boundaries of the broad, westward-flowing South Equatorial Current and the weaker, more variable eastward-flowing Northern Equatorial Counter Current [*Bourles et al.*, 1999; *Stramma and Schott*, 1999]. Core descriptions from Lamont-Doherty Earth Observatory Core Repository and Ruddiman *et al.* [1986] suggest weak to moderate bioturbation in cores used in this study throughout all intervals, but do not suggest a particular enhancement in bioturbation in any of the studied intervals.

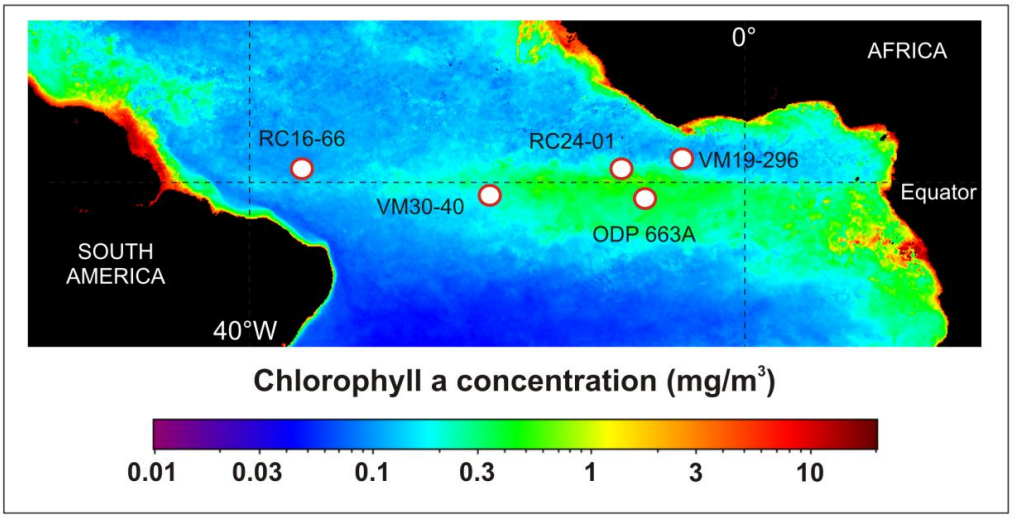

Figure 3.6 – Plot of core locations used in this study over Aqua MODIS chlorophyll a concentration (mg/m^3). Chlorophyll data is the annual composite SeaWiFS data for the year 2007 from http://oceancolor.gsfc.nasa.gov.

All cores, except RC16-66, also lie in (or close to) a filament of high-chlorophyll surface water (chlorophyll a concentration 0.03-1 mg/m^3), indicating high productivity and should therefore respond to any changes in nutrient supply through upwelling (Figure 3.6). In addition VM19-296 had previously been identified as containing intervals of monospecific *E. rex* ooze [*Gardner and Burckle*, 1975].

The cores cover a range of depths (~3.7 - ~5 km). The South Equatorial Current is fed by the Benguela Current, the sources of which include Indian and South Atlantic subtropical thermocline water; saline, low-oxygen tropical Atlantic water; and cooler, fresher subantarctic water [*Peterson and Stramma*, 1991; *Garzoli and Gordon*, 1996]. Cores VM30-40 (0°12.0'N, 23°9.0'W, 3706 m water depth) and RC16-66 (0°45.0'N, 36°37.01'W, 4424 m water depth) underlie the Equatorial Undercurrent. The Equatorial Undercurrent is fed by the North Brazil Current and the North Equatorial Counter Current. RC16-66 also directly underlies the North Brazil Current, which is in the region where the southern-sourced water masses AAIW and South Atlantic Central Water enter the subthermocline North Brazil Current between the equator and 9°N, and west of 44°W [*Bub and Brown*, 1996]. The modern primary productivity in the equatorial Atlantic decreases from east to west, although the coast of South America supports upwelling (Figure 3.6). VM30-40 is on the eastern edge of the upwelling filament from the West African margin, but does not currently experience as high a nutrient supply as the more easterly cores. RC16-66 is situated in the region between the eastern equatorial Atlantic upwelling region, and the filament of higher-productivity water in the western Atlantic offshore of French

Guyana/Suriname (top left Figure 3.6) and records generally lower primary productivity (chlorophyll a concentration ~0.1 mg/m^3).

The method used in this investigation was to measure sedimentary opal using the alkaline extraction of [*Mortlock and Froelich*, 1989], and to measure the $^{18}O/^{16}O$ ratio ($\delta^{18}O$) of planktic foraminifera to provide core age control (see Chapter 2.5). The radionuclides ^{231}Pa, ^{230}Th, ^{232}Th, ^{234}U and ^{238}U were measured (see Chapter 2.3) in order to provide a ^{230}Th-normalised flux estimate in order to account for variations in core sedimentation rate due to sediment focusing/winnowing [*Bacon*, 1984; *Suman and Bacon*, 1989; *Francois et al.*, 2004]. Additionally, the excess Pa/Th ratio ($_{xs}^{231}Pa/^{230}Th_0$) was used as a measure of diatom palaeoproductivity [*Chase et al.*, 2002; *Bradtmiller et al.*, 2006; 2007]. The ultimate aim of these measurements was the production of quantitative estimates of the amount of opal burial in MIS 5a (~83-71ka) and MIS 4 (~71-60 ka).

To ascertain that the opal fluxes represent past export productivity and not opal preservation, additional proxies of authigenic uranium (providing qualitative measurements of organic carbon flux), organic carbon accumulation rates and sedimentary concentrations of diatom sterol biomarkers were measured. A qualitative count of *E. rex* fragments on specially-prepared microscope slides was also made to determine what contribution *E. rex* may have made to MIS 4 opal flux (see Chapter 2.9).

3.4 Thorium and protactinium proxy background

The radionuclides thorium (^{230}Th) and protactinium (^{231}Pa) have important applications in palaeoceanography. Thorium-230 (^{230}Th) (half-life, $t_{1/2}$ = 75.7 ka) is produced at a rate of 2.52 x 10^{-2} dpm m^{-3} yr^{-1} from the decay of ^{234}U (uranium-234). Protactinium-231 (^{231}Pa) (half-life, $t_{1/2}$ = 32.5 ka) is produced at a rate of 2.33 x 10^{-3} dpm m^{-3} yr^{-1} from the decay of ^{235}U (uranium-235) [*Yu et al.*, 1996; *Henderson and Anderson*, 2003]. Because the U parent isotopes have a relatively homogeneous concentration of ~3 µg/l due to its oceanic residence time of ~400,000 years [*Ku et al.*, 1977; *Mangini et al.*, 1979], ^{230}Th and ^{231}Pa are produced at a constant initial activity ratio (β^{Pa}/β^{Th}) of 0.093 [*Henderson and Anderson*, 2003]. The relevant sections of the decay series of ^{235}U, ^{238}U and ^{232}Th are shown in Equation 3.1:

1. $^{235}U(7 \times 10^8 \text{ yr}) \rightarrow {}^{231}Th(26 \text{ hr}) \rightarrow {}^{231}Pa(3.25 \times 10^4 \text{ yr}) \rightarrow \ldots..$

2. $^{238}U(4.47 \times 10^9 \text{ yr}) \rightarrow {}^{234}Th(24 \text{ d}) \rightarrow {}^{234}Pa(6.8 \text{ hr}) \rightarrow {}^{234}U(2.45 \times 10^5 \text{ yr}) \rightarrow {}^{230}Th(7.57 \times 10^4 \text{ yr}) \rightarrow \ldots.$

3. $^{232}Th(1.4 \times 10^{10}\ yr) \rightarrow {}^{228}Ra(5.8\ yr) \rightarrow \ldots..$

Equation 3.1 – Decay series of (1)^{235}U, (2)^{238}U, and (3) ^{232}Th. Half-lives (in parentheses) for ^{230}Th and ^{234}U are from Cheng *et al.* [2000] and ^{231}Pa from Henderson and Anderson [2003]. All other half-lives are from Plant *et al*. [1999].

The thorium isotope ^{230}Th exists as a neutral oxide species in seawater, and is removed from the water column readily by sinking particles, in a process known as 'particle scavenging' [*Bacon and Anderson*, 1982]. The water column profile of ^{230}Th shows increasing activity, from <0.1 dpm m^{-3} in the upper water column, to ≈ 1 dpm m^{-3} near the ocean bottom [*Nozaki et al.*, 1981; *Bacon and Anderson*, 1982]. This distribution is most readily explained by a 'reversible particle scavenging' model, where ^{230}Th adsorbed to sinking particles continues to exchange with the dissolved ^{230}Th pool as the particles fall vertically through the water column [*Bacon and Anderson*, 1982; *Nozaki et al.*, 1987]. The affinity of ^{230}Th for particles over the dissolved phase may be understood by the calculation of a distribution co-efficient (K_d) for ^{230}Th, which is defined as ^{230}Th concentration per mass of particles divided by the ^{230}Th concentration per mass of water. The open ocean value for the K_d of ^{230}Th is ~10^7, indicating that ^{230}Th is highly insoluble in seawater [*Henderson and Anderson*, 2003].

The high insolubility of ^{230}Th means that it has a very short oceanic residence time ($^{SW}\tau_{scav}$) from ~16-40 years [*Anderson et al.*, 1983a], with an average residence time of 26 years [*Yu et al.*, 1996]. This short residence time limits the degree to which ^{230}Th is redistributed laterally by ocean currents, leading to the expectation that it is removed to sediments in the area of the ocean in which it formed [*Bacon and Anderson*, 1982; *Bacon and Rosholt*, 1982]. In actuality, a small degree of lateral advection of ^{230}Th occurs, but this is assumed to be small and for palaeoceanographic applications the flux of ^{230}Th (F_{230}) is considered equal to the rate of production of ^{230}Th (P_{230}) from ^{234}U decay (Equation 3.2). This has been shown to be a valid assumption by modelling [*Henderson et al.*, 1999] and sediment trap studies [*Scholten et al.*, 2001; *Yu et al.*, 2001a]. However, the interpretation of ^{230}Th data from areas underlying sea-ice [*Henderson et al.*, 1999] or close to hydrothermal vents [*Shimmield and Price*, 1988] must be interpreted with caution, due to the enhanced scavenging of ^{230}Th that occurs in these settings.

$$P_{TH} = Z \,.\, (^{234}U) \,.\, \lambda^{230}$$

Equation 3.2 – The flux of ^{230}Th (P_{TH}) is assumed to be approximately equal to its rate of production in the water column, where (^{234}U) is the production rate of ^{234}U (2750 dpm m^{-3}), λ_{230} is the decay constant of ^{230}Th from ^{234}U; and Z is the depth of the water column in metres. Reproduced from Henderson and Anderson [2003].

When ^{230}Th is measured in sediments it will belong to one of three groups:

1) Detrital ^{230}Th ($^{230}Th^{det}$) is locked into the mineral structure of eroded continental debris, and falls through the water column rapidly, without undergoing any interaction with seawater.
2) Scavenged ^{230}Th ($^{230}Th^{scav}$) is removed from seawater by sinking particles. Because $^{230}Th^{scav}$ is not added to (supported) by the decay of in-situ ^{234}U, it decays away over time. Its activity ($A_{Th\text{-}230}{}^{scav}$) is therefore dependent on its initial activity ($^{0}A_{Th\text{-}230}{}^{scav}$) when it is deposited, and the time (t, in ka) since deposition:

$$A_{Th\text{-}230}{}^{scav} = {}^{0}A_{Th\text{-}230}{}^{scav}\, e^{-(0.693t/75.7)}$$

Equation 3.3 – Activity of scavenged ^{230}Th, where 75.7 ka is the half-life of ^{230}Th [*Francois et al.*, 2004].

3) Additionally, ^{230}Th may derive from authigenic uranium (U_{auth}) in sediment. Authigenic U forms under suboxic conditions, when uranium (VI) in sedimentary pore water is reduced to the insoluble (IV) species, leading to a decrease in pore water U concentration; and subsequent diffusion of U from the overlying bottom waters into the sediment.

$$^{238}U_{auth}\ (ppm) = {}^{238}U_{T} - (^{238}U/^{232}Th)_{D}\ (^{232}Th_{T})$$

Equation 3.4 – Calculation of authigenic uranium in sediment. Subscript T denotes total radionuclide concentration, and $(^{238}U/^{232}Th)_D$ is the average detrital ratio of ^{238}U to ^{232}Th (=0.6 ± 0.1). Reproduced from Chase *et al.* [2001].

This causes an enrichment in sedimentary uranium which is termed U_{auth} [*Barnes and Cochran*, 1990; *Klinkhammer and Palmer*, 1991], and particulate non-lithogenic U may also be created in surface ocean waters [*Anderson*, 1982a]. U_{auth} is the difference between total and detrital uranium (Equation 3.4).

Because the thorium flux-normalisation technique relies on measuring only the scavenged fraction, the influences of the detrital and authigenic phases must be accounted for. To make this correction, it is assumed that the U decay series are in secular equilibrium within lithogenic phases, and that any authigenic uranium created is coeval with sedimentary deposition (see Chapter 2.3 for details).

$$^{230}Th_{xs} = {}^{230}Th_{meas} - \{(0.6 \pm 0.1)^{232}Th_{meas})\} - \left\{[^{238}U_{meas}\text{-}(0.6\pm0.1) \,.\, {}^{232}Th_{meas}] \,.\, \left[1\text{-}e^{-\lambda 230t}) + \frac{\lambda_{230}}{\lambda_{230}\text{-}\,\lambda_{234}} \,.\, (e^{-\lambda 234t} - e^{-\lambda 230t}) \,.\, \left(\left(\frac{^{234}U}{^{238}U}\right)_{init}\text{-}1\right)\right]\right\}$$

Equation 3.5 – Calculation of unsupported (scavenged) ^{230}Th in sediment. All nuclide measurements are expressed in activities (A). The first term in curly brackets corrects for the influence of detrital ^{230}Th, and the second term in curly brackets corrects for the influence of authigenic uranium. Reproduced from Henderson and Anderson [2003].

Once $^{230}Th_{xs}{}^{0}$ is known, it can be used to calculate the thorium-normalised flux of a component (i) into the sediment [*Bacon*, 1984; *Suman and Bacon*, 1989]:

$$F_i = Z(^{234}U)\lambda^{230}\frac{f_i}{^{230}Th_{xs}{}^{0}}$$

Equation 3.6 – Flux normalisation, where F_i is the normalised flux of component i (e.g. opal) to the sediment in g m^{-2} yr^{-1}; Z is the depth of the water column in metres, f_i is the weight fraction of component i in the sediment, (^{234}U) is the seawater activity of ^{234}U in dpm m^{-3}, λ^{230} is the decay constant of ^{230}Th (2.3 x 10^{-5} dpm/cm^3/ka), and $^{230}Th_{xs}{}^{0}$ is the activity of unsupported ^{230}Th. Reproduced from Henderson and Anderson [2003].

Radionuclides may also be used to determine changes in past opal export productivity (palaeoproductivity). A degree of correlation exists between excess Pa/Th (termed $^{231}Pa_{xs}/^{230}Th_{xs}$) in sediment and particle flux, as recorded in sediment trap studies [*Kumar et al.*, 1993; *Kumar et al.*, 1995]. In the open ocean, the majority of sinking particles are biogenic in origin [*Honjo*, 1980], leading to the expectation that the sedimentary ($^{231}Pa_{xs}/^{230}Th_{xs}$) in open ocean regions can reveal information about past productivity changes. Calculation of excess (unsupported) Pa, to allow the calculation of $^{231}Pa_{xs}/^{230}Th_{xs}$, uses the following algorithm:

$$^{231}Pa_{xs} = {}^{231}Pa_{meas} - \{0.046(0.6 \pm 0.1)^{232}Th_{meas}\} - \{[0.046^{238}U_{meas}\text{-}(0.6\pm0.1)^{232}Th_{meas}][1\text{-}e^{-\lambda 231t}]\}$$

Equation 3.7 – Calculation of unsupported ^{231}Pa, see Chapter 2.3 for details. Reproduced from Henderson and Anderson [2003].

The principles behind the use of $^{231}Pa_{xs}/^{230}Th_{xs}$ as an export productivity proxy rely on the differences in oceanic residence time between ^{230}Th and ^{231}Pa. Whereas ^{230}Th is scavenged intensely in all areas of the ocean due its high particle affinity, and has a short $^{SW}T_{scav}$, ^{231}Pa has a sufficiently long average $^{SW}T_{scav}$ (~130 years) [*Yu et al.*,

1996] to allow a degree of lateral advection, from regions of low particle flux (e.g. the North Atlantic) to regions of high particle flux (e.g. the SO) (Figure 3.7).

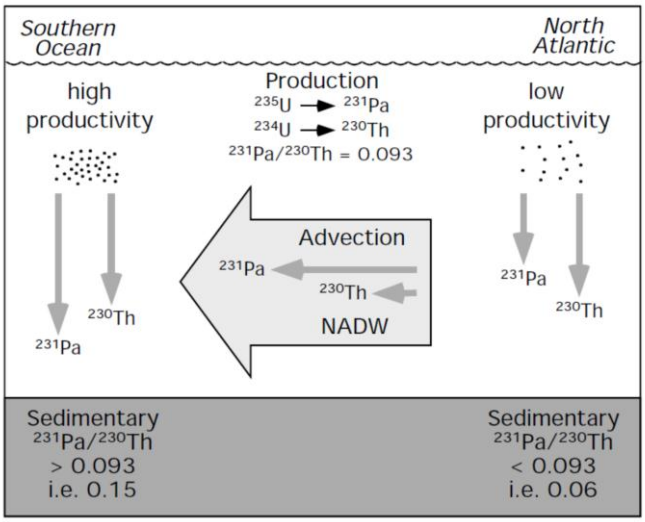

Figure 3.7 – Schematic representation of ^{231}Pa and ^{230}Th fractionation in the oceans. The length of the grey arrows symbolises the size of fluxes. ^{230}Th is scavenged rapidly at all locations in the oceans, whereas ^{231}Pa may be transported by diffusion from low-productivity to high-productivity areas. Sedimentary $^{231}Pa_{xs}/^{230}Th_{xs}$ is a function of lateral diffusive transport and export productivity. Reproduced from Henderson and Anderson [2003].

Where more ^{231}Pa is scavenged extensively by high particle export, values of $^{231}Pa_{xs}/^{230}Th_{xs}$ will be higher than the $^{231}Pa/^{230}Th$ production ratio of 0.093. Where productivity is lower, the $^{231}Pa_{xs}/^{230}Th_{xs}$ will be lower than 0.093 due to less scavenging of ^{231}Pa (Figure 3.7). Studies have shown that ^{231}Pa sorbs preferentially onto opal [*Chase et al.*, 2002; *Gueguen and Guo*, 2002]. In the SO, where export productivity is dominated by opal, $^{231}Pa_{xs}/^{230}Th_{xs}$ has been interpreted as an indicator of past changes in export productivity [*Kumar et al.*, 1993; *Francois et al.*, 1997; *Anderson et al.*, 1998]. Where the $^{231}Pa_{xs}/^{230}Th_{xs}$ is closely correlated to the $^{230}Th_{xs}$-normalised preserved opal flux rate, this observation has been interpreted as a reliable indicator of past diatom export productivity [*Bradtmiller et al.*, 2006; 2007; *Bradtmiller et al.*, 2009]. Hence, this approach was applied to the reconstruction of equatorial opal export productivity during MIS 4 in this investigation.

A potential complication to the use of $^{231}Pa_{xs}/^{230}Th_{xs}$ as a palaeoproductivity proxy is the tendency for insoluble nuclides such as ^{230}Th and ^{231}Pa to be removed from the water column at the margins of ocean basins, a process known as 'boundary scavenging' [*Spencer et al.*, 1981]. Generally, the effect of boundary scavenging on sedimentary $^{231}Pa_{xs}/^{230}Th_{xs}$ in open ocean regions is considered small [*Henderson and Anderson*, 2003]. The causes of enhanced boundary scavenging include the enhanced supply of eroded continental particles, the enhanced production of biogenic particles due to upwelling, and increased redox cycling of Fe and Mn [*Cochran*, 1992]. A recent study of the effect of boundary scavenging on the Lüderitz upwelling cell in the south-east Atlantic (off Namibia), which supports high primary productivity, suggests that the boundary scavenging does affect sedimentary $^{231}Pa_{xs}/^{230}Th_{xs}$, but

that the dominant control on $^{231}Pa_{xs}/^{230}Th_{xs}$ in this region is the mode of the Atlantic Meriodional Overturning Circulation (AMOC) [*Lippold et al*., 2012]. Given that the core sites in this investigation are situated at least several hundred kilometres from the areas of greatest coastal upwelling (red and yellow colours in Figure 3.6), it was considered that boundary scavenging would have had (at most) a small effect on the $^{231}Pa_{xs}/^{230}Th_{xs}$ data gathered in this investigation. Nonetheless, the potential effect of an east-west Atlantic gradient in ^{230}Th (which is more easily scavenged then ^{231}Pa) is explored further in Section 3.7.2.

The advantage of the use of $^{231}Pa_{xs}/^{230}Th_{xs}$ as an export productivity proxy (over biogenic phases) is that it is insensitive to dissolution of biogenic phases during the first stages of diagenesis [*Henderson and Anderson*, 2003]. However, records of $^{231}Pa_{xs}/^{230}Th_{xs}$ as export productivity indicators must be interpreted cautiously, as oceanic circulation may strongly impact $^{231}Pa_{xs}/^{230}Th_{xs}$ in areas of high net deep water flux, such the North Atlantic. Again, using $^{231}Pa_{xs}/^{230}Th_{xs}$ as a 'palaeocirculation' proxy relies on the solubility (and therefore $^{SW}\tau_{scav}$) differences between ^{231}Pa and ^{230}Th. Whilst ^{230}Th is scavenged rapidly, ^{231}Pa may be advected away from its area of formation by deep currents, leading to a value of $^{231}Pa_{xs}/^{230}Th_{xs}$ lower than that of the $^{231}Pa/^{230}Th$ production ratio of 0.093. Conversely, the site to which the ^{231}Pa is transported will see an increase in sedimentary $^{231}Pa_{xs}/^{230}Th_{xs}$. A number of studies have used $^{231}Pa_{xs}/^{230}Th_{xs}$ as a tracer of the strength of North Atlantic Deep Water export, which has been linked to the climate of high northern latitudes in the Late Quaternary [*Yu et al.*, 2001a; *McManus et al.*, 2004; *Guihou et al.*, 2010].

Authigenic uranium (U_{auth}) is correlated to organic carbon flux in a variety of well-oxygenated open ocean settings [*Anderson*, 1982a; *Kumar et al.*, 1995; *Zheng et al.*, 2002], hence in this investigation it was also used as a proxy for organic carbon flux, which is insensitive to remineralisation (see Equation 3.4 for U_{auth} calculation). Additionally, I measured the ratio between diatom sterol biomarkers [*Volkman*, 1986; *Rampen et al.*, 2010] and coccolithophorid alkenone biomarkers [*Marlowe et al.*, 1990; *Sawada and Shiraiwa*, 2004] as a supplementary constraint on whether opal accumulation is preservation or productivity-dominated.

3.5 Core age model development

3.5.1 ODP 663A

The North Greenland Ice Core Project (NGRIP) $\delta^{18}O$ record was used as a tuning target for all marine core age models developed in this study. The NGRIP $\delta^{18}O$ is on the Greenland Ice Core Chronology 2005 (GICC05) age model back to 60 ka [*Andersen et al.*, 2007]. Between 60 and 100 ka the NGRIP $\delta^{18}O$ record has been tuned to the $\delta^{18}O$ record from Chinese speleothems [*Barker et al.*, 2011], based on

the observed in-phase relationship between the speleothem records and Greenland temperature during MIS 3 [*Wang et al.*, 2001; *Wang et al.*, 2008].

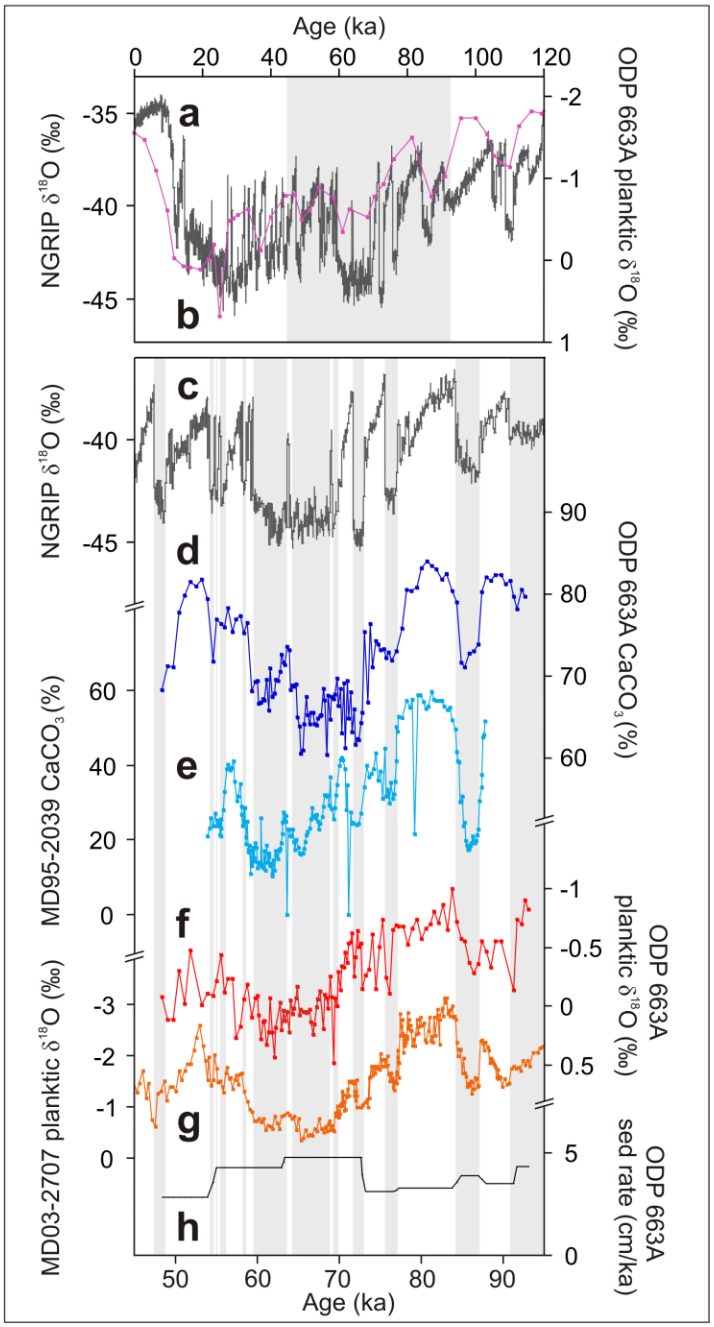

Figure 3.8 – ODP 663A age model development. a) Grey curve (top panel) - NGRIP $\delta^{18}O$ (0-120 ka) [*Andersen et al.*, 2007]; b) Pink curve - low-resolution planktic $\delta^{18}O$ record of ODP 663A for the last 120 ka [*deMenocal et al.*, 1993]. The shaded grey area in the top panel represents the expanded 45-95 ka window shown in the lower panel. Expanded window (lower box): c) NGRIP $\delta^{18}O$ (45-95 ka) (grey); d) high resolution % $CaCO_3$ record of ODP 663A (dark blue - this study); e) % $CaCO_3$ of MD95-2039 (light blue - Iberian margin) [*Thomson et al.*, 1999]; f) high-resolution planktic (*G. ruber, white*) $\delta^{18}O$ record of ODP 663A (red - this study); g) planktic (*G. ruber*) $\delta^{18}O$ record of core MD03-2707 from the Guinea Basin (orange) [*Weldeab et al.*, 2007]; h) linear sedimentation rate changes (black) as calculated from the tuning of ODP 663A %$CaCO_3$ record to the $\delta^{18}O$ record of NGRIP. All curves are plotted in a 45-95 ka window with other oxygen isotope records used in tuning plotted for comparison. The grey shaded area in the top panel highlights the 45-95 ka interval is shown in the lower panel. The grey shaded lines in the lower panel correspond to northern hemisphere cold periods from the NGRIP oxygen isotope record.

The approximate location of MIS 4 was identified from the low-resolution planktic $\delta^{18}O$ record (*Globigerinoides ruber*) of ODP 663A (Figure 3.8 - top panel), and millennial-scale age control for ODP 663A was then derived by tuning its high-resolution record of sedimentary calcium carbonate ($CaCO_3$) (see Chapter 2.1) to the NGRIP $\delta^{18}O$ record. Comparison of the ODP 663A $CaCO_3$ record to NGRIP $\delta^{18}O$ reveals clear similarities, even when a linear sedimentation rate is assumed (Figure 3.8, curves c and d). The $CaCO_3$ record in ODP 663A is thought to relate to millennial-scale oscillations in northern hemisphere climate and changes in deepwater chemistry [*Sarnthein et al.*, 1994; *Sarnthein et al.*, 2000]. This is demonstrated by the comparison of the age-controlled $CaCO_3$ record from ODP 663A to that of Iberian Margin core MD95-2039 [*Thomson et al.*, 1999] which shows an in-phase relationship (Figure 3.8, curves d and e).

The high-resolution planktic $\delta^{18}O$ record (*Globigerinoides ruber,* white) of ODP 663A (01°11.87'S, 11°52.71'W, 3708 m water depth) was also plotted on this age model, and compared to that of MD03-2707 (02°30.11'N, 09°23.68'E, 1295 m water depth) (Figure 3.8, curves f and g), which records a close link between West African monsoon hydrology and high northern hemisphere climate [*Weldeab et al.*, 2007]. The close correspondence of both $\delta^{18}O$ records provides additional support for the NGRIP-tuned age model of ODP 663A.

3.5.2 VM19-296

Age control for VM19-296 (01°25.12'N, 09°4.59'W, 5017 m water depth) was derived by tuning the high-resolution record of sedimentary $\%CaCO_3$ (see Chapter 2.1) from VM19-296 to the record of $\%CaCO_3$ record of ODP 663A, and was considered reasonable given the proximity of both cores (see Figure 3.8).

The $\%CaCO_3$ record of VM19-296 was tuned to the NGRIP $\delta^{18}O$ record, and the $\%CaCO_3$ record of ODP 663A. One implication of the low VM19-296 $CaCO_3$ content during MIS 4 was that insufficient foraminiferal calcite existed to allow the reconstruction of a coherent planktic $\delta^{18}O$ record. However, the coherence of the %opal records in VM19-296 and ODP 663A (Figure 3.9) gives additional confidence in the age control of VM19-926.

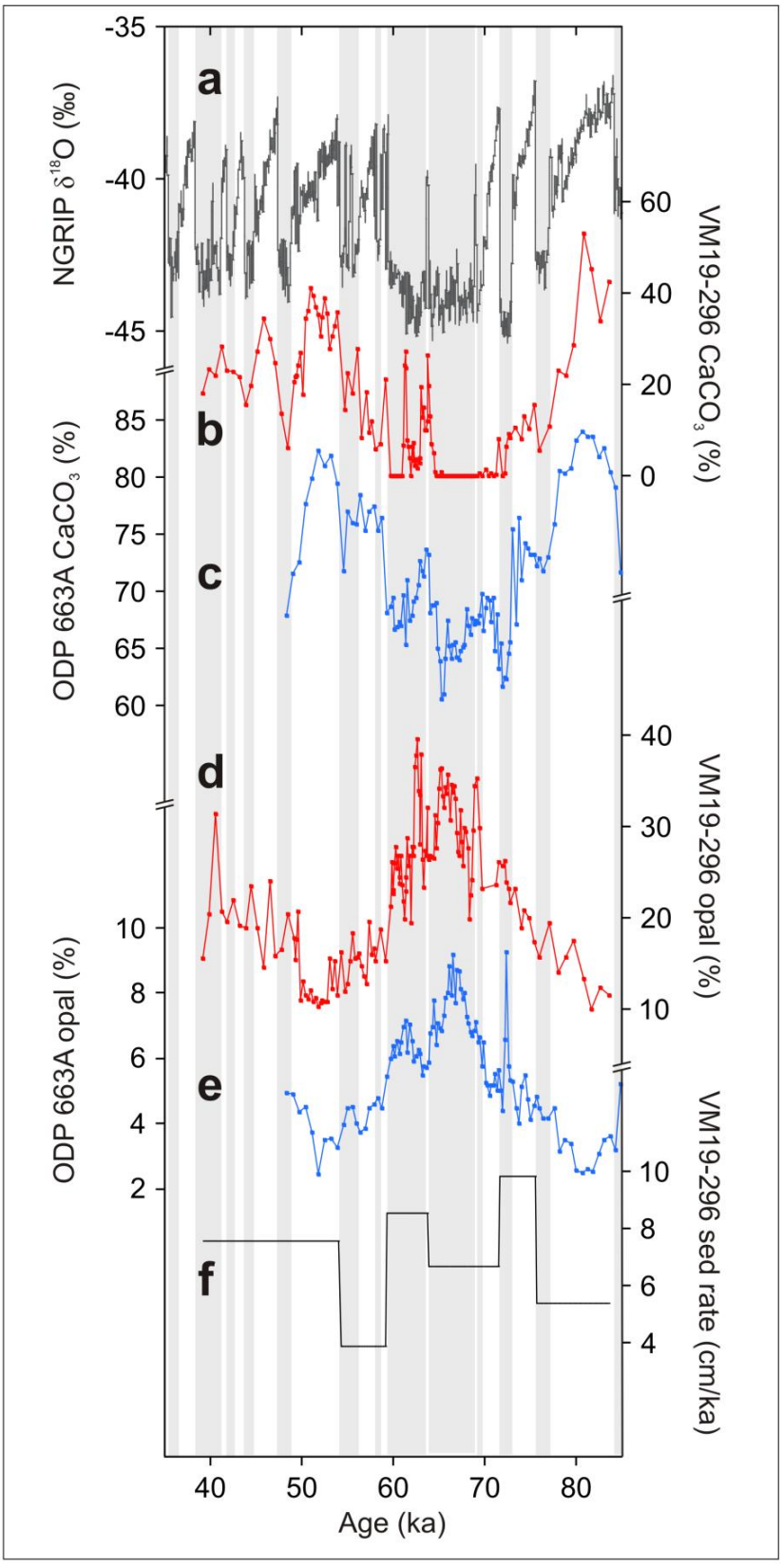

Figure 3.9 – VM19-296 age model development a) NGRIP $\delta^{18}O$ record (grey); b) VM19-296 %$CaCO_3$ record (red); c) ODP 663A % $CaCO_3$ record (blue); d) VM19-296 %opal record (red); e) ODP 663A %opal record (blue); f) VM19-296 linear sedimentation rates (black) calculated from tuning the VM19-296 %$CaCO_3$ record to NGRIP $\delta^{18}O$. The age model for VM19-296 was created by tuning the opal record to that of ODP 663A, as insufficient foraminiferal $CaCO_3$ existed to create a $\delta^{18}O$ record for the core. Grey bands represent northern hemisphere cold periods from the NGRIP $\delta^{18}O$ record.

3.5.3 RC24-01

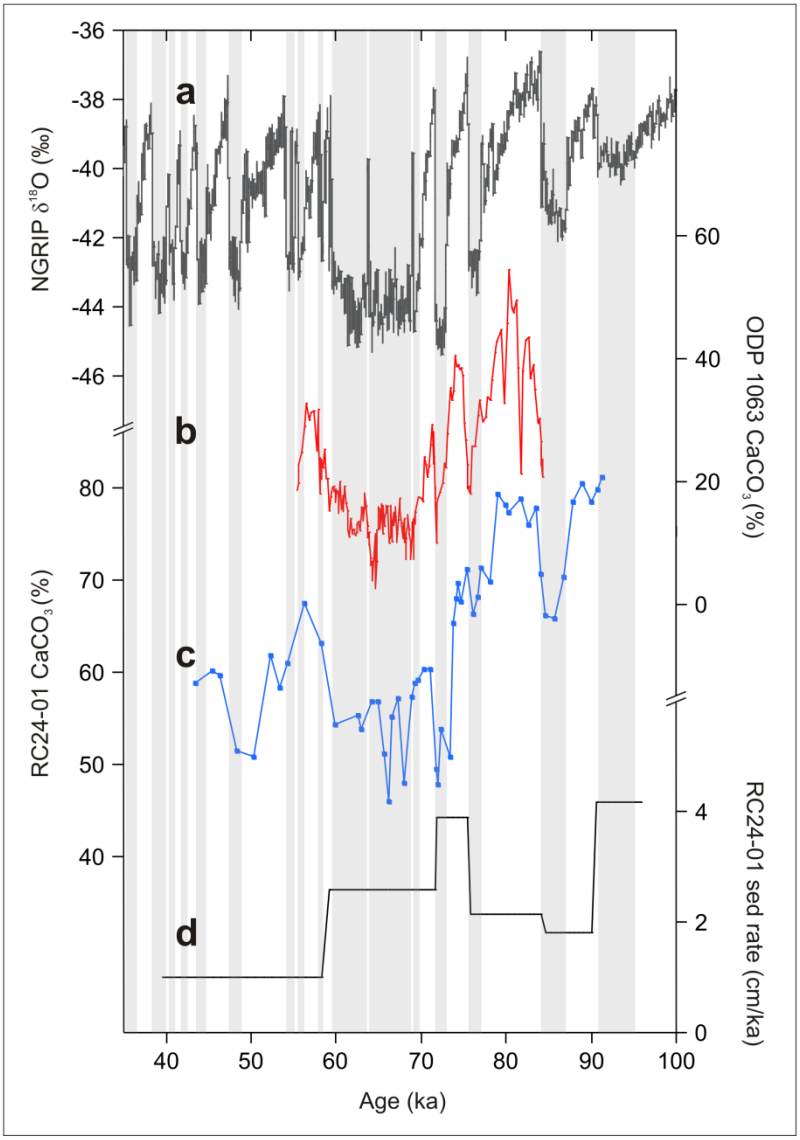

Figure 3.10 – RC24-01 age model development. a) NGRIP $\delta^{18}O$ (grey); b) ODP 1063 % $CaCO_3$ record (red) [*Thornalley et al.*, submitted ms]; c) RC24-01 %$CaCO_3$ record (blue); d) RC24-01 linear sedimentation rates (black) calculated by tuning the RC24-01 %$CaCO_3$ record to the % $CaCO_3$ record of ODP 1063 [*Thornalley et al.*, submitted ms]. Grey bands represent northern hemisphere cold periods from the NGRIP $\delta^{18}O$ record.

Age control for RC24-01 (00°33.0'N, 13°39.0'W, 3837 m water depth) (Figure 3.10) was derived by tuning its record of %$CaCO_3$ to that of ODP 1063 (33°41'N, 57°36'W, 4584 m water depth). ODP 1063 age control was obtained by tuning core reflectance (a proxy for $CaCO_3$ content) and magnetic susceptibility to records of orbital precession and obliquity [*Grützner et al.*, 2002], and further refined by tuning its planktic $\delta^{18}O$ record (*Globorotalia inflata*) to NGRIP $\delta^{18}O$ (see Chapter 5.1.4) [*Thornalley et al.*, submitted ms].

3.5.4 VM30-40

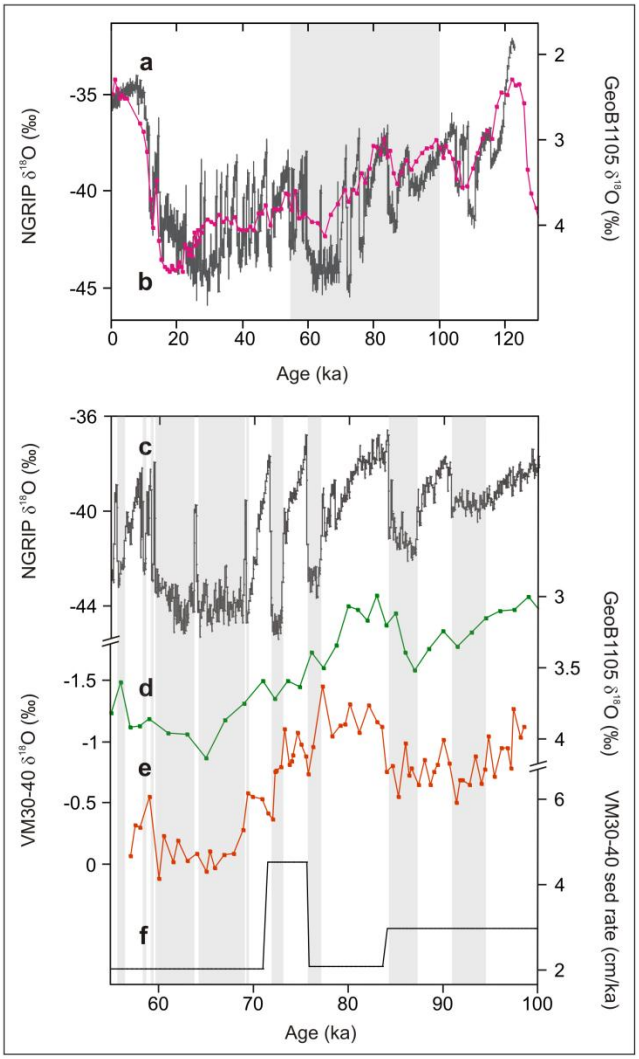

Figure 3.11 – VM30-40 age model development. (Top panel, 0-130ka) a) NGRIP $\delta^{18}O$ (grey); b) Planktic $\delta^{18}O$ record from core GeoB1105 (pink) [*Wefer et al.*, 1996]. The grey shaded area in the top panel represents the 55-100 ka in the NGRIP $\delta^{18}O$ record. (Bottom panel): c) NGRIP $\delta^{18}O$ 55-100 ka (grey); d) Planktic $\delta^{18}O$ record from core GeoB1105 (green) [*Wefer et al.*, 1996]; e) VM30-40 planktic $\delta^{18}O$ (*G.ruber*) (this study - red); f) VM30-40 sedimentation rates (black), generated by tuning the planktic $\delta^{18}O$ record to NGRIP. Grey bands in the bottom panel represent northern hemisphere cold periods from the NGRIP $\delta^{18}O$ record.

Age control for VM30-40 (00°12.0'N, 23°9.0'W, 3706 m water depth) was derived by tuning the high resolution planktic $\delta^{18}O$ record (*Globigerinoides ruber, white*) to the $\delta^{18}O$ record from NGRIP [*Andersen et al.*, 2007] (Figure 3.11). The VM30-40 $\delta^{18}O$ record was also compared to the low-resolution planktic $\delta^{18}O$ record from mid-EEA core GeoB1105 [*Wefer et al.*, 1996] (Figure 3.11, curves b and c). The $\delta^{18}O$ record of GeoB1105 has been linked to the climate of high northern latitude through surface water heat transport, modulated by the strength of southeast trade winds [*Wefer et al.*, 1996].

3.5.5 RC16-66

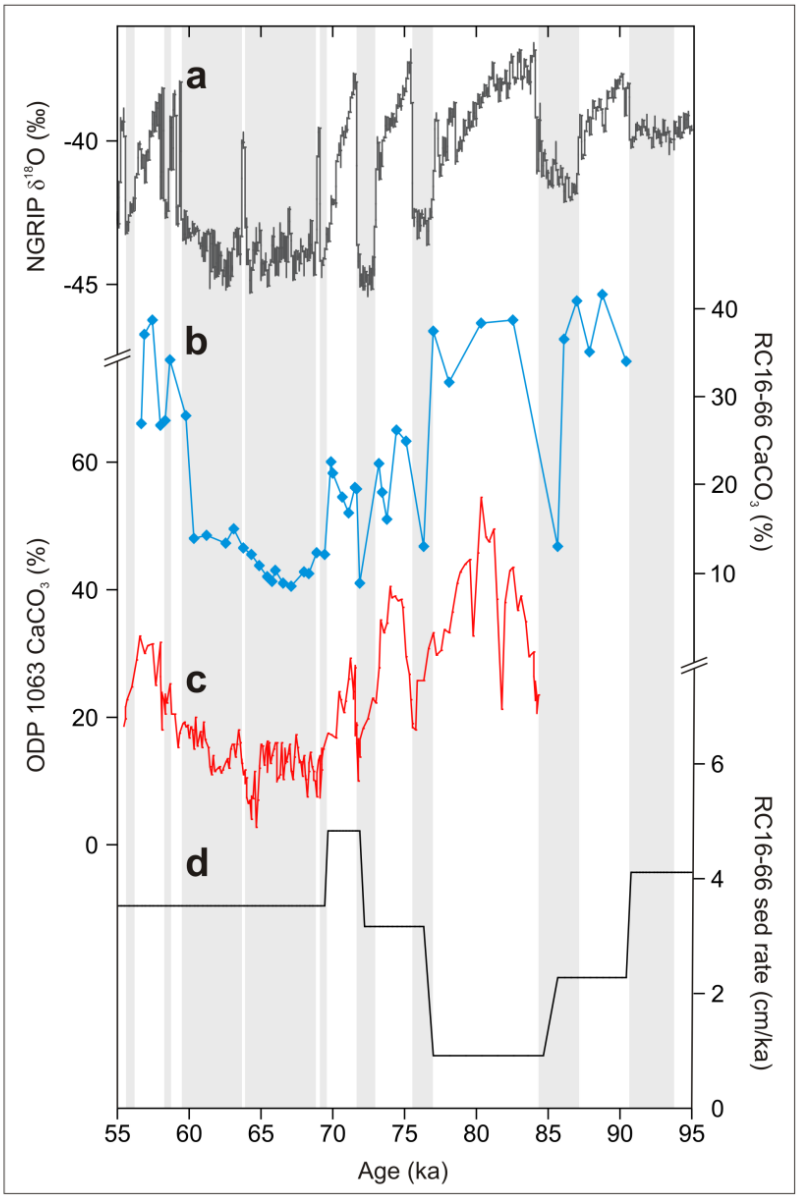

Figure 3.12 – RC16-66 age model development. a) NGRIP $\delta^{18}O$ (grey); b) RC16-66 %$CaCO_3$ (blue); c) ODP 1063 %$CaCO_3$ (red) [*Thornalley et al.,* submitted ms]; d) RC16-66 sedimentation rate. The grey bands represent northern hemisphere cold periods in the NGRIP $\delta^{18}O$ record.

Age control for RC16-66 (00°45.0'N, 36°37.01'W, 4424 m water depth) was derived by tuning its %$CaCO_3$ record to the NGRIP $\delta^{18}O$ record [*Andersen et al.*, 2007]. The coherence between the RC16-66 %$CaCO_3$ record and that of ODP 1063 (33°41'N, 57°36'W, 4584 m water depth) in a subsequent comparison gives confidence in the age model (Figure 3.12). Age model uncertainty on all cores is ~1-2 ka.

3.6 Results

3.6.1 Comparison of ^{230}Th-normalised opal flux rates and sedimentary $^{231}Pa_{xs}/^{230}Th_{xs}$

The opal flux results from ODP 663A (Figure 3.13) show a sustained increase in opal flux over ~12 kyr, beginning at around 81 ka (~0.04 g/cm^2/ka), and peaking in the early part of MIS 4 (~0.08 g/cm^2/ka). The large transient increase in opal flux ~72 ka is notable because it is nearly coincident with the beginning of the large and rapid pCO_2 drawdown ~71 ka [*Ahn and Brook*, 2008], although opal flux begins to decrease rapidly at the same time that pCO_2 rapidly decreases.

However, the possibility remains that this transient increase in opal accumulation may be due to enhanced opal preservation rather than a productivity signal (see Section 3.4). The opal flux in ODP 663A also increases from ~0.05 to 0.075 g/cm^2/ka in MIS 5b (~87-84 ka), which is consistent with a small increase in $_{xs}(^{231}Pa/^{230}Th)_0$, suggesting a period of enhanced diatom productivity. However, the $_{xs}(^{231}Pa/^{230}Th)_0$ record of ODP 663A for most of the studied interval does not visibly correlate with the opal flux record, which appears to question the use of $_{xs}(^{231}Pa/^{230}Th)_0$ as a measure of past opal productivity in these core sections. Nonetheless, this does not preclude the opal flux record from giving information on past changes in opal export productivity, provided that opal flux correlates with other palaeoproductivity proxies (see 3.4.4).

The highest $_{xs}(^{231}Pa/^{230}Th)_0$ (~0.075) in ODP 663A probably occurs either during warm D-O 20, or cold D-O 20 (~75-77 ka). Neither cold D-O 20 nor warm D-O 20 experienced a particularly high opal accumulation rate, and another positive excursion in $_{xs}(^{231}Pa/^{230}Th)_0$ ~79-80 ka is approximately coincident with the lowest opal flux rate (~0.04 g/cm^2/ka). The peak MIS 4 opal accumulation rate of ~0.08 g/cm^2/ka corresponds to $_{xs}(^{231}Pa/^{230}Th)_0$ of ~0.07, when the expectation from previous work [*Bradtmiller et al.*, 2006; 2007; *Bradtmiller et al.*, 2009] would be that the $_{xs}(^{231}Pa/^{230}Th)_0$ should probably have been higher in this interval. Despite this finding, a modest increase in $_{xs}(^{231}Pa/^{230}Th)_0$ of ~0.02 accompanies an opal flux increase of ~0.02 g/cm^2/ka at the beginning of MIS 4 at ~70 ka, suggesting that opal flux may have still influenced the $_{xs}(^{231}Pa/^{230}Th)_0$ record in ODP 663A, at least during early MIS 4.

The results from VM19-296 (Figure 3.14) also show a maximum opal accumulation flux in the early part of MIS 4, in agreement with data from ODP 663A. Again, $_{xs}(^{231}Pa/^{230}Th)_0$ shows no visible correlation with opal flux, suggesting that factors other than opal export are more important influences on $_{xs}(^{231}Pa/^{230}Th)_0$ in this core. The peak MIS 4 opal flux in VM19-296 is much higher (~0.4 g/cm^2/ka) than in

ODP 663A and RC24-01, possibly due to the accumulation of large numbers of giant *E. rex* frustules. This core has previously been identified as containing monospecific intervals of *E. rex* during glacial periods [*Gardner and Burckle*, 1975], which may be due to its position, close to an equatorial frontal zone [*Kemp et al.*, 2006].

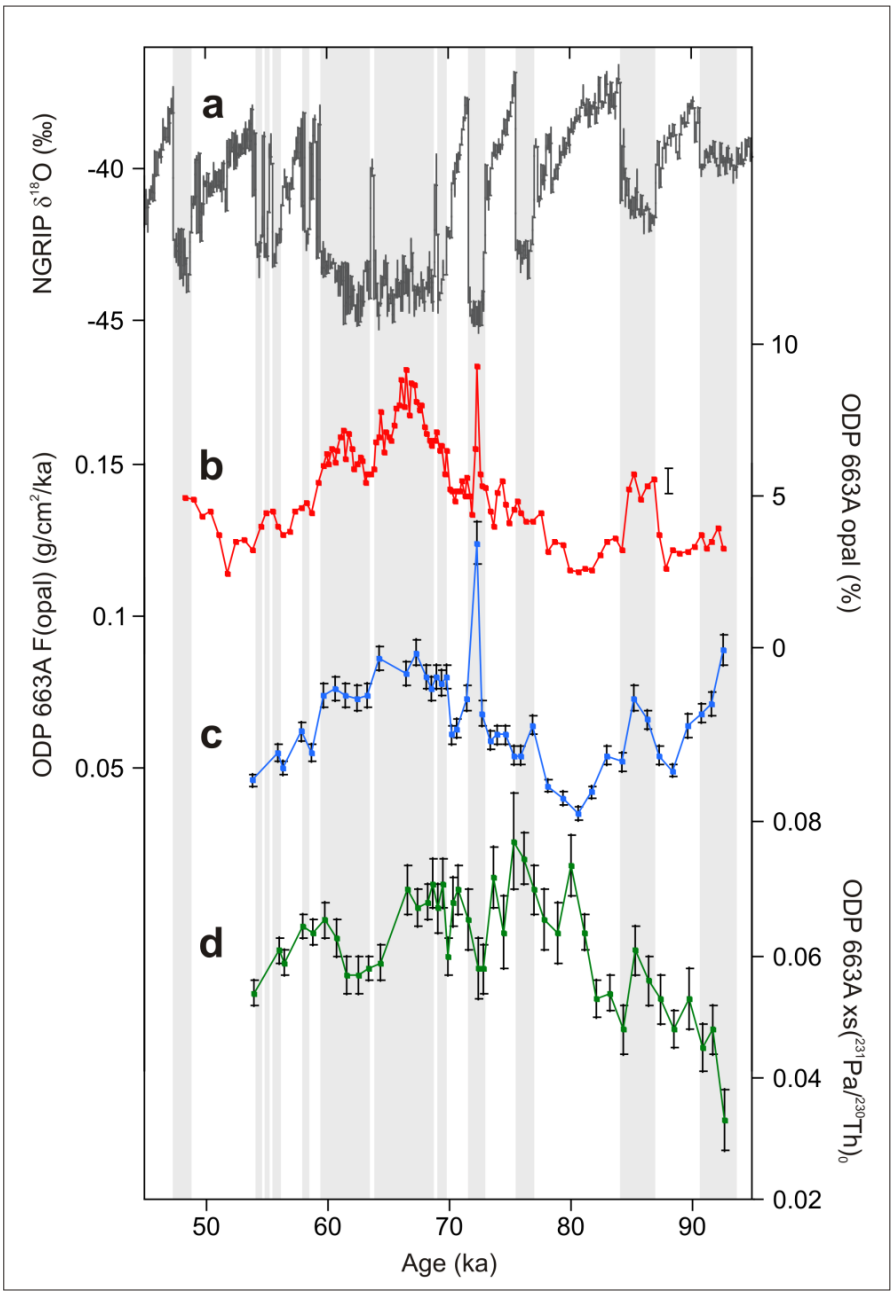

Figure 3.13 – ODP 663A opal flux comparison plot. a) NGRIP $\delta^{18}O$ (grey); b) ODP 663A %opal (red) with long-term precision shown by error bar; c) ODP 663A thorium-normalised preserved opal flux rate [F(opal)] (blue), with error bars in black; d) ODP 663A $_{xs}(^{231}Pa/^{230}Th)_0$ (green), with error bars in black. Average long-term precision on % opal measurements is ~ 4.5 % of measured value. Grey bands represent northern hemisphere cold periods from the NGRIP $\delta^{18}O$ record.

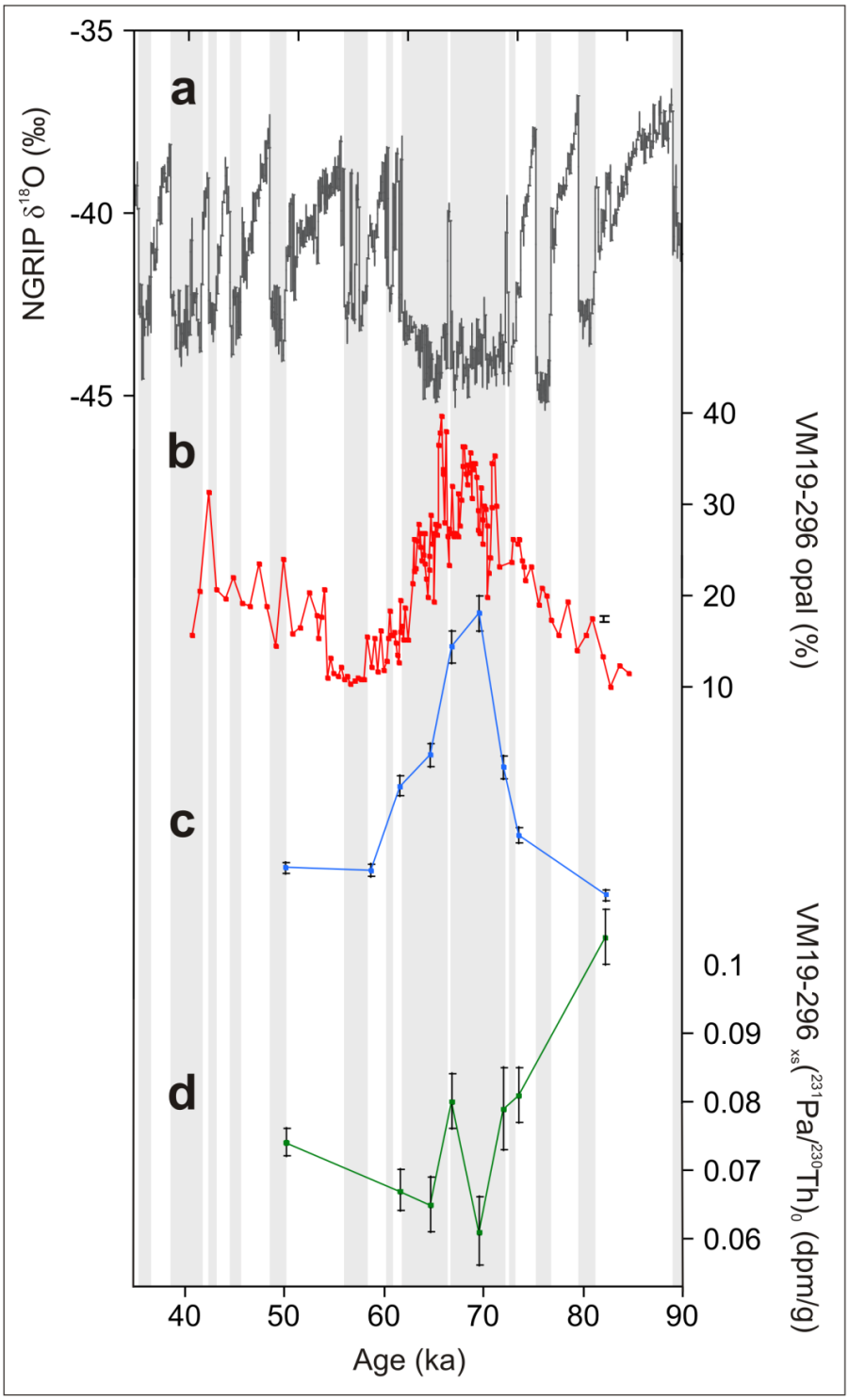

Figure 3.14 – VM19-296 opal flux comparison plot. a) NGRIP $\delta^{18}O$ (grey); b) VM19-296 %opal (red) with long-term precision shown by error bar; c) VM19-296 thorium-normalised preserved opal flux rate [F(opal)] (blue) with error bars in black; d) VM19-296 $_{xs}(^{231}Pa/^{230}Th)_0$ (green), with error bars in black. Average long-term precision on % opal measurements is ~ 4.5 % of measured value. Grey bands represent northern hemisphere cold periods from the NGRIP $\delta^{18}O$ record.

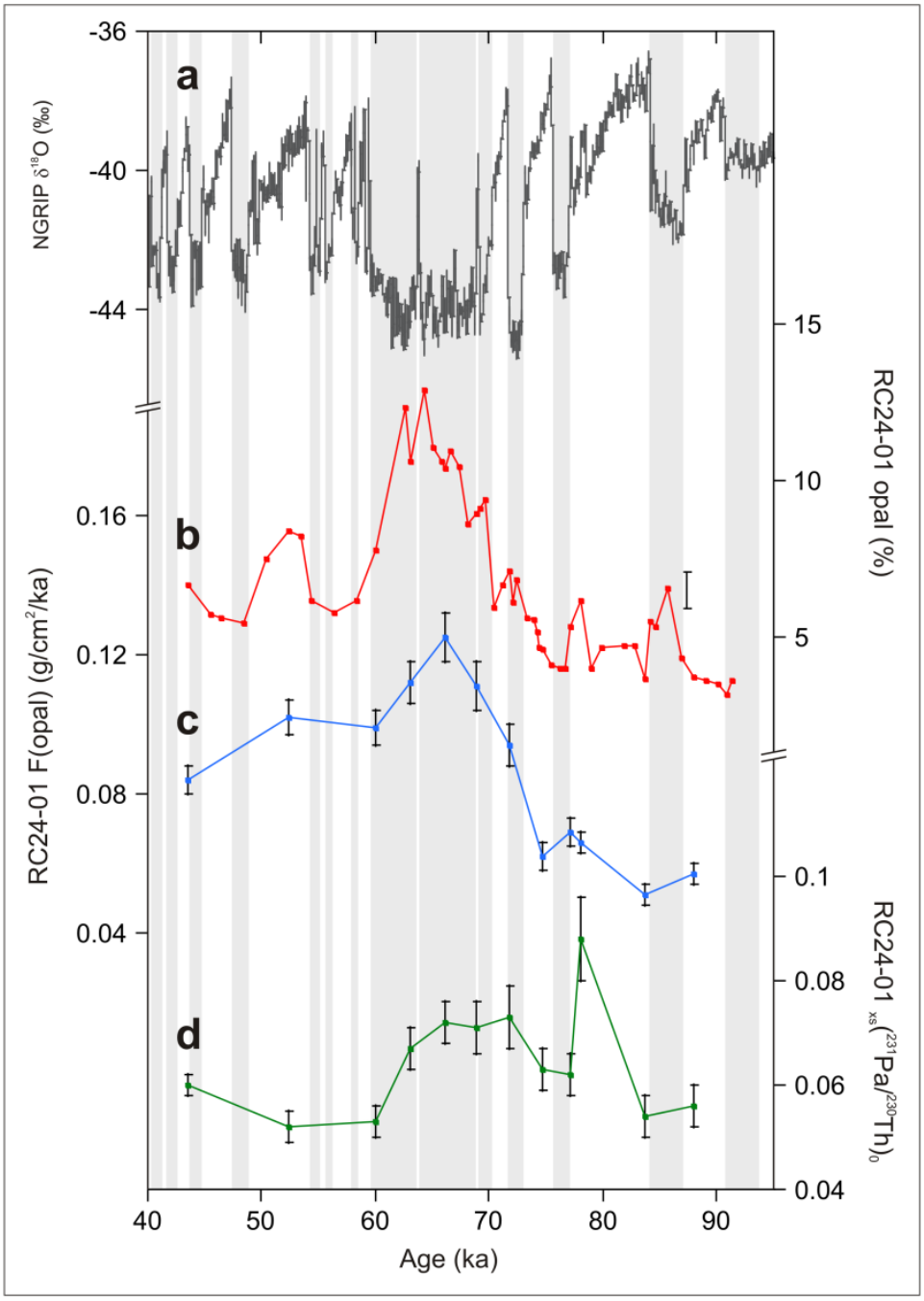

Figure 3.15 – RC24-01 opal flux comparison plot. a) NGRIP $\delta^{18}O$ (grey); b) RC24-01 %opal (red) with long-term precision shown by error bar; c) RC24-01 thorium-normalised preserved opal flux rate [F(opal)] (blue) with error bars in black; d) RC24-01 $_{xs}(^{231}Pa/^{230}Th)_0$ (green), with error bars in black. Average long-term precision on % opal measurements is ~ 4.5 % of measured value. Grey bands represent northern hemisphere cold periods from the NGRIP $\delta^{18}O$ record.

The fact that $_{xs}(^{231}Pa/^{230}Th)_0$ does not generally correlate with F(opal) in VM19-296 suggests that a bottom water control on $_{xs}(^{231}Pa/^{230}Th)_0$ may operate in VM19-296 during MIS 4 that is absent in the other cores [*Thomas et al.*, 2006] (see Section 3.4.2). In common with ODP 663A, however, VM19-296 does show a modest (~ 0.02) increase in $_{xs}(^{231}Pa/^{230}Th)_0$ which is coincident with increasing opal flux (~69 ka),

suggesting that opal flux may still exert some control on $_{xs}(^{231}Pa/^{230}Th)_0$ in this core during MIS 4 (Figure 3.14).

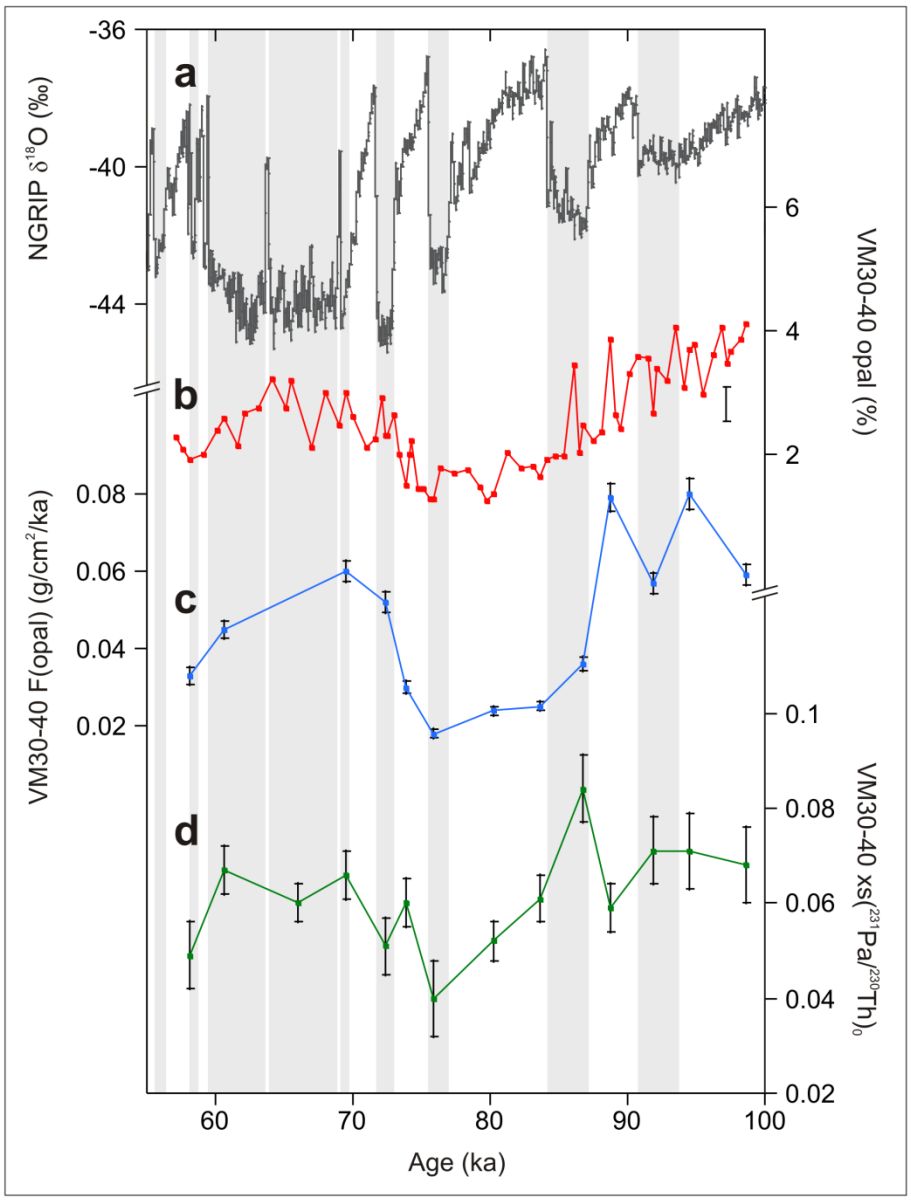

Figure 3.16 – VM30-30 opal flux comparison plot. a) NGRIP $\delta^{18}O$ (grey); b) VM30-40 %opal (red) with long-term precision shown by error bar; c) VM30-30 thorium-normalised preserved opal flux rate [F(opal)] (blue) with error bars in black; d) VM30-40 $_{xs}(^{231}Pa/^{230}Th)_0$ (green), with error bars in black. Average long-term precision on % opal measurements is ~ 4.5 % of measured value. Grey bands represent northern hemisphere cold periods from the NGRIP $\delta^{18}O$ record.

The increase in $_{xs}(^{231}Pa/^{230}Th)_0$ between ~62 and ~50 ka (warm D-O 14) in Figure 3.14 is difficult to explain, but may be due an increased influence of northern component water, which has a generally higher ^{231}Pa content [*Thomas et al.*, 2006], on the VM19-296 core site.

The results from RC24-01 (Figure 3.15) show a maximum (~0.13 g/cm^2/ka) in opal flux during MIS 4. The maximum opal flux in RC24-01 is approximately temporally coincident with the opal flux maxima in ODP 663A and VM19-296. As with ODP 663A, the increase in opal flux is not as large as in VM19-296, which may be because VM19-296 accumulated more *E. rex* – related opal during MIS 4 than the other cores.

The sustained increase in opal flux in RC24-01 (Figure 3.15) from values of ~ 0.06 g/cm^2/ka at ~ 74 ka, to a maximum of ~ 0.13 g/cm^2/ka during MIS 4 at ~ 67 ka, is greater than that recorded in ODP 663A. The position of RC24-01, just north of the equator and on a similar latitude to VM19-296 suggests that opal fluxes were generally higher north of the equator than south of it.

The $_{xs}(^{231}Pa/^{230}Th)_0$ data from RC24-01 shows a slight correlation with opal flux, although the minimum value of ~0.085 in $_{xs}(^{231}Pa/^{230}Th)_0$ probably occurs in MIS 5b (~87ka), around ~8 ka prior to the maximum in opal flux (~ 0.08 g/cm^2/ka) during MIS 5c, although age model uncertainty could put it into MIS 5c. Again, this suggests that factors other than opal flux were important in the control of sedimentary $_{xs}(^{231}Pa/^{230}Th)_0$ (see 3.4.2).

The pattern of opal flux changes in VM30-40 (Figure 3.16) is broadly co-incident with that in RC24-01. VM30-40 records an increase of ~0.04 g/cm^2/ka, beginning ~ 76 ka and reaching a maximum during MIS 4 ~ 69 ka, although higher values of opal may have been reached during MIS 4 but are not shown in this record. The highest opal flux values in VM30-40 are recorded between 94 and 89 ka, during northern hemisphere interstadials, and are unlike VM19-296, RC24-01 and ODP 663A in this respect. These maxima in opal flux are not coincident with maximum values in the $_{xs}(^{231}Pa/^{230}Th)_0$, demonstrating that factors other than opal flux are important in controlling $_{xs}(^{231}Pa/^{230}Th)_0$ in VM30-40. Nonetheless, the increase in opal flux that begins at ~ 76 ka is coincident with an increase in $_{xs}(^{231}Pa/^{230}Th)_0$ of ~0.02, which is consistent with the $_{xs}(^{231}Pa/^{230}Th)_0$ records of ODP 663A, RC24-01 and VM19-296.

The record of opal flux in RC16-66 varies very little throughout the studied interval (Figure 3.17). Maximum values of opal flux occurred ~74 ka and 67 ka, but show no coherent glacial-interglacial pattern. The record of $_{xs}(^{231}Pa/^{230}Th)_0$ in RC16-66 shows no correlation to opal flux. The error bars on the record of $_{xs}(^{231}Pa/^{230}Th)_0$ are large, probably due to the influence of detrital input from the Amazon plume [*Vital and Stattegger*, 2000]. The pattern of opal accumulation in RC16-66 is consistent with the study of Rühlemann *et al*. [1996], and additionally suggests that rates of productivity were lower in the western equatorial Atlantic [*Gregg et al.*, 2003].

Overall, across all cores studied, the thorium-normalised opal flux rates decrease from east to west, as might be expected if modern patterns of upwelling

reflect conditions that prevailed in the past (Figure 3.6). This is illustrated in Figure 3.18.

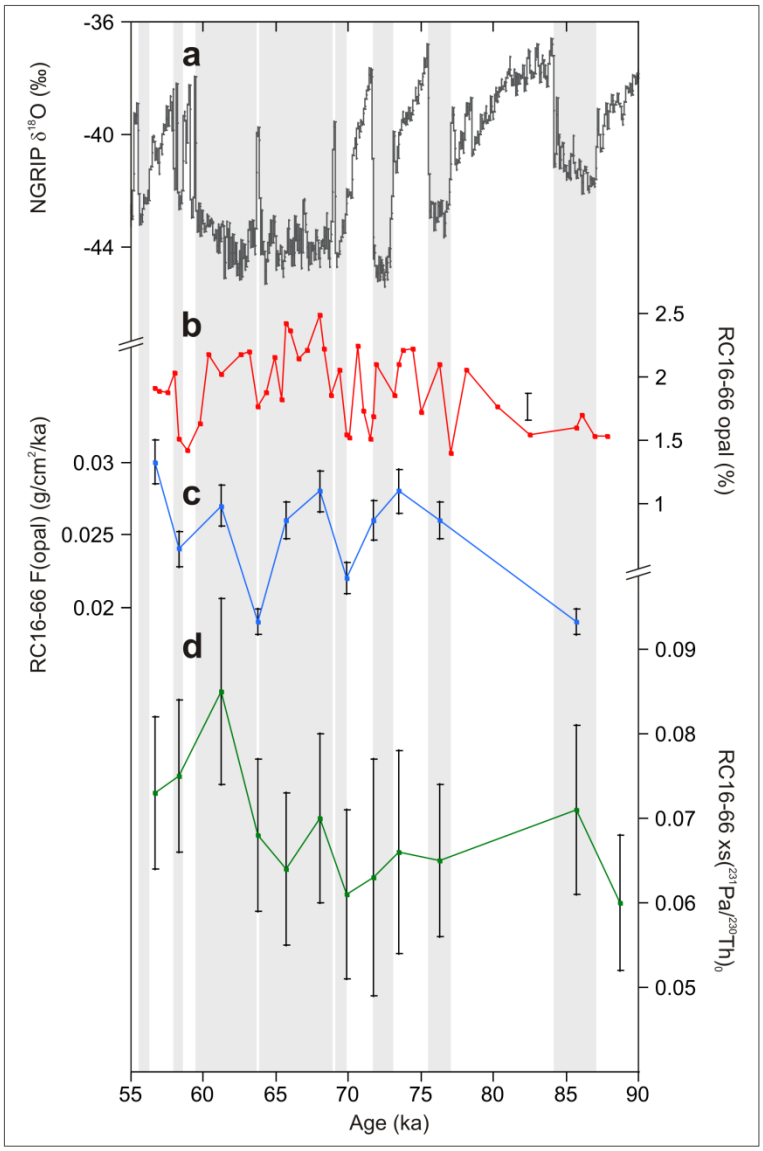

Figure 3.17 – RC16-66 opal flux comparison plot. a) NGRIP $\delta^{18}O$ (grey); b) RC16-66 %opal (red) with long-term precision shown by error bar; c) RC16-66 thorium-normalised preserved opal flux rate [F(opal)] (blue) with error bars in black; d) RC16-66 $_{xs}(^{231}Pa/^{230}Th)_0$ (green), with error bars in black. Average long-term precision on % opal measurements is ~ 4.5 % of measured value. Grey bands represent northern hemisphere cold periods from the NGRIP $\delta^{18}O$ record.

Figure 3.18 illustrates the percentage in opal flux rates, relative to the long-term mean, plotted on the same axes of time and percentage change in opal flux rate (+100 % to -100 %), and with each core chromatically from west (red) to east (violet). The maxima in MIS 4 opal flux appears to be nearly co-incident (within age model error) in ODP 663A and RC24-01, but the maxima appears to occur earlier in VM19-296 and VM30-40, much closer to the initiation of glacial conditions ~69 ka, but probably still too late to be coincident with the major pCO_2 decrease ~71 ka [*Ahn and Brook*, 2008].

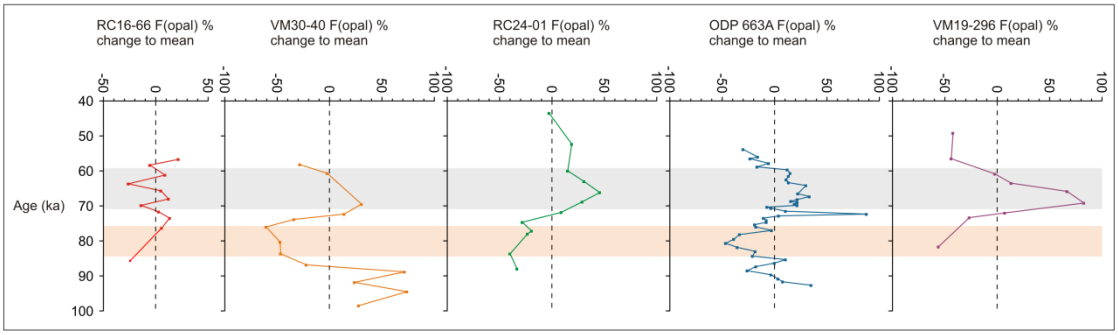

Figure 3.18 – Plot of percentage changes in opal flux rates, in all cores arranged from the western equatorial Atlantic (left) to the eastern equatorial Atlantic (right) on the same axes of time and percentage change in F(opal) relative to the long-term mean (represented by the dashed line in each plot, see Table 3.1). The grey band represents MIS 4 and the orange band MIS 5a, as used to calculate the average opal flux values in Table 3.2.

Table 3.1 shows the long-term mean opal flux rate in each core, which record a general increase from the western to the eastern tropical Atlantic. The mean opal flux rate increases ~35-70 % in VM30-40, RC24-01 and ODP 663A relative to RC16-66. In VM19-296 the increase is ~790 % relative to RC16-66, probably reflecting greater upwelling in the EEA.

Table 3.1 – Long-term mean values of opal flux (g/cm^2/ka) for each of the core in this study, from west (left) to east (right).

Core	RC16-66	VM30-40	RC24-01	ODP 663A	VM19-296
Long-term mean F(opal) (g/cm^2/ka)	0.025	0.046	0.086	0.066	0.222

3.6.2 Comparison of glacial (MIS 4) and interglacial (MIS 5a) opal burial

Total amounts of opal burial were calculated for the equatorial Atlantic in MIS 4 (70-59 ka), and MIS 5a (84-77 ka), using the averaged opal accumulation rates for all cores across the defined time periods (Table 3.2).

Table 3.2 – Average values for opal flux (in g/cm^2/ka) in all cores during MIS 4 (70-59 ka) and MIS 5a (84-77 ka). The average percentage change in the fluxes of all cores was then used to estimate total opal burial for MIS 4 and MIS 5a (see Figure 3.18).

CORE	RC16-66	VM30-40	RC24-01	ODP 663A	VM19-296
F(opal) MIS 4	0.024	0.053	0.112	0.078	0.311
F(opal) MIS 5a	0.019	0.025	0.062	0.047	0.098
% increase into MIS 4	26.3	112	80.6	66.0	217.3
Mean uncertainty	0.001	0.002	0.005	0.003	0.01
Uncertainty (%)	23.9	50.2	45.6	34.1	86.1

The equatorial Atlantic region was defined as the area 0° - 40° W and 5° N - 5° S (equivalent to 4.95 x 10^6 km^2). The average opal flux rates for each core are shown in Table 3.2. The average percentage increase in opal accumulation was calculated as 100.4 % ± 48, based on the average percentage difference between opal fluxes in all cores from MIS 5a to MIS 4.

The total opal burial rate across the equatorial Atlantic during MIS 5a is ~2.5 Gt/ka, based on the average opal accumulation rate across all cores. The extra opal buried during MIS 4 would therefore be ~5 Gt/ka, based on an average proportional increase in opal flux of 100 %, across the whole equatorial Atlantic region. If this production of opal represents a similar increase in surface productivity, and that production remained constant it is a first-order confirmation of the SALH. This conclusion is supported by other studies in the equatorial Atlantic [*Stabell*, 1986; *deMenocal et al.*, 1993; *Verardo and McIntyre*, 1994; *Abrantes*, 2001].

3.6.3 Ethmodiscus rex valve counts

The occurrence of the diatom *E. rex* was tested by counting the number of fragments of *E. rex* frustule in sediment slides under a light microscope (see Section 2.9 for all methods). Identification of the species as *Ethmodiscus rex* [*Rattray*, 1890] came from observation of a whole valve by Dr. J. Pike (personal communication). Observations of broken perforate frustules (Figure 3.21) were then interpreted as being those of *E. rex*, in agreement with [*Gardner and Burckle*, 1975; *Stabell*, 1986; *Abrantes*, 2001].

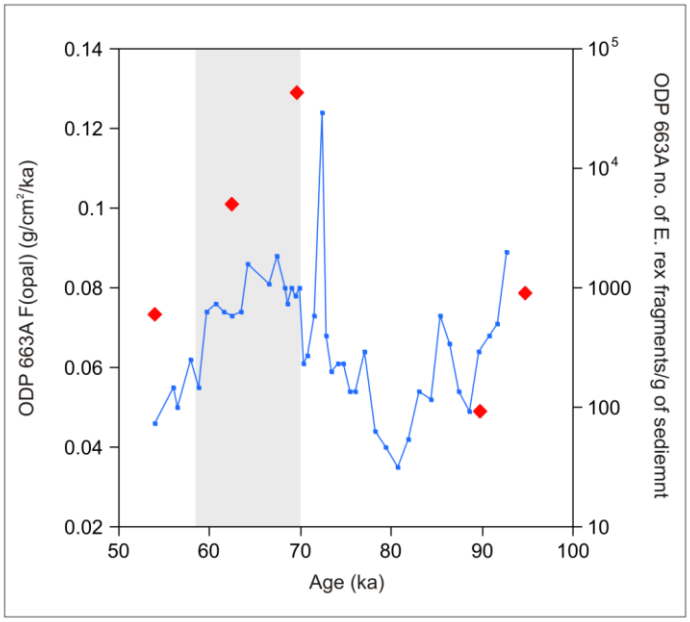

Figure 3.19 – Comparison of opal flux in ODP 663A (blue curve) (g/cm^2/ka), with qualitative counts of *E. rex* fragments (red markers) for selected intervals in the same core (note log scale). Counts are normalised to 1 gram of sediment, and the grey shaded bar represents MIS 4.

Unfortunately, none of the samples contained sufficient densities of whole *E. rex* frustules to perform a quantitative valve count, after the method of *Schrader and Schuette* [1968]; but counting the number of fragments still yielded a qualitative estimate of *E. rex* abundance, and were normalised to 1 gram of sediment (Figure 3.19). Other whole diatom valves were counted in the same random field of view, and were also normalised to 1 gram of sediment to compare counts between samples (Figure 3.20).

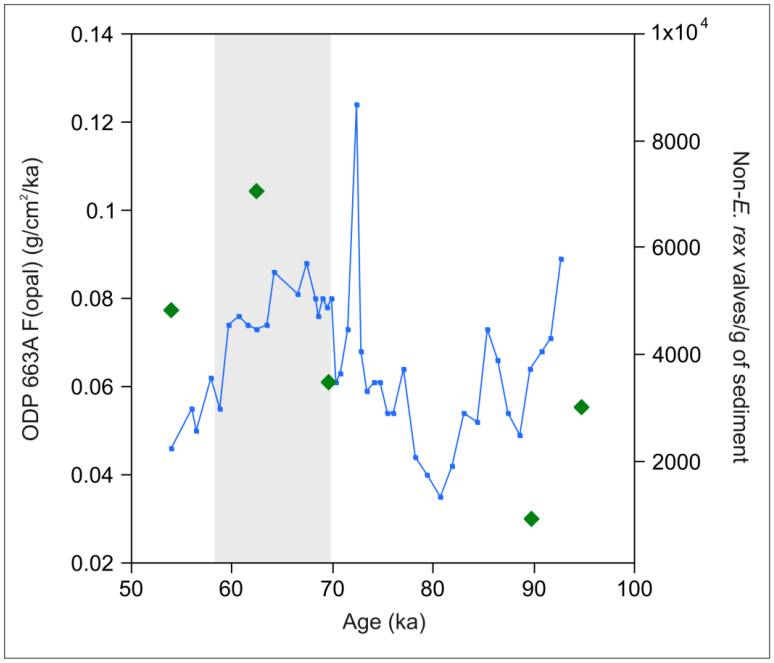

Figure 3.20 - Comparison of opal flux in ODP 663A (blue curve) (g/cm^2/ka), with qualitative counts of non-*E. rex* diatom valves, (green markers) normalised to 1 gram of sediment for comparison between samples. Note that this is a qualitative index of diatom abundance as our samples did not contain a sufficient density of diatom valves for more quantitative methods to apply. The grey shaded bar represents MIS 4.

Fragments of *E. rex* increased greatly in abundance during MIS 4 (Figure 3.19), which may have had implications for the organic carbon pump in the EEA during this period. *E. rex* is one of the largest living diatoms known, with cell volumes in the order 10^9 µm^3, and a Si:C ratio of 7.24, ~6-7 times that of average diatoms [*Brzezinski*, 1985; *Villareal et al.*, 1999]. Despite their high Si:C ratio, the extreme size and internal volume of *E. rex* may have allowed them to contribute significantly to the export flux of C_{org} as well as the export flux of opal in the EEA.

The abundance of other diatom types also increased significantly during MIS 4 (Figure 3.20), broadly coincident with the increase in *E. rex* (Figure 3.19), with minimum values recorded ~90 ka and increasing across the MIS 5/4 transition, although the maximum count of other diatoms occurs later in MIS 4 than the maximum in *E. rex* fragments.

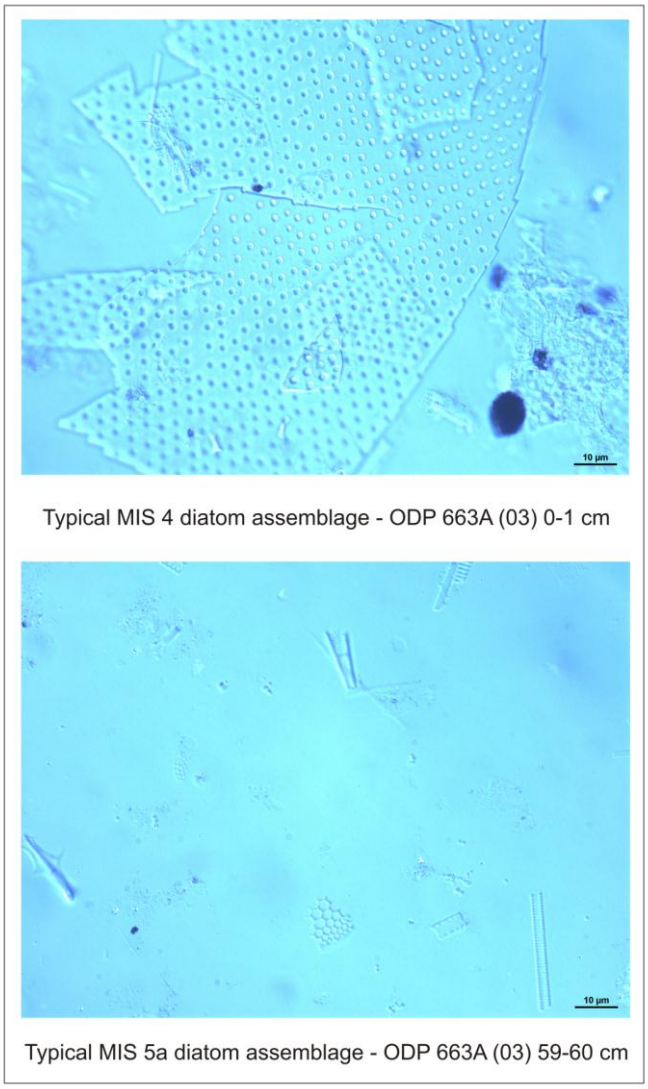

Figure 3.21 – Light microscope images of typical MIS 4 diatom assemblage (top panel), and typical MIS 5a diatom assemblage (bottom panel). Note the occurrence of significant amounts of large fragments of perforate *E. rex* frustules in the top panel image (identified by J. Pike, personal communication), and their absence in the bottom panel image. See Chapter 2 for details of diatom slide preparation and counting method.

3.6.4 Biomarker study

Biomarkers in marine sediments have been used in numerous palaeoceanographic investigations as proxies to indicate the level of palaeoproductivity for total and specific phytoplankton groups, for example [*Prahl et al.*, 1993; *Villanueva et al.*, 1997; *Sicre et al.*, 2000; *Schefuß et al.*, 2004], and also in palaeotemperature reconstruction [*Rostek et al.*, 1997; *Pelejero et al.*, 1999; *Zhou et al.*, 2007].

Diatom palaeoproductivity may be inferred from studies of the sedimentary content of the sterol group of biomarkers. Sterols are important membrane lipids that are found in all eukaryotic cells, and can be used as biomarkers for certain classes of phytoplankton. However, few sterols can be used as unambiguous biomarkers for

specific algal groups [*Volkman*, 1986]. This is also true for the diatoms, and none of the major sterols appear to be unambiguous diatom biomarkers [*Rampen et al.*, 2010]. Despite this finding, high concentrations of sterols are present in most groups of diatoms, with 24-methylcholesta-5,24(28)-dien-3β-ol being the most common, followed by the Δ^5 groups of sterols [*Rampen et al.*, 2010]. Hence, concentrations of sterols have been used in a number of studies to infer the contribution of diatoms to a variety of marine and freshwater sediments [*Sicre et al.*, 2001; *Seki et al.*, 2004; *Castañeda et al.*, 2011].

The biomarker 24-methylcholesta-5,22E-dien-3β-ol, more commonly known as brassicasterol, is found in some major diatom groups [*Volkman*, 1986]. Brassicasterol has been used in several studies to aid the reconstruction of diatom palaeoproductivity [*Ikehara et al.*, 2000; *Sachs and Anderson*, 2005; *Dubois et al.*, 2010]. Here we use the raw abundance ratio of total alkenone against brassicasterol abundance in sediment as a measure of the relative dominance of export productivity by $CaCO_3$-producers and diatoms.

In order to measure the abundance of diatoms to coccolithophorids, we calculated a simple ratio of the raw abundance of sterol (diatom biomarker) to total alkenone (Figure 3.22). Core ODP 663A was chosen to measure biomarker ratios as this core had the highest resolution opal flux record, which would allow determination of whether changes in the biomarker abundance ratio had any effect on pCO_2. Living species of the Haptophyte algae, including the coccolithophorids, produce alkenones, which are long-chain (C_{37} -C_{39}) unsaturated ketones [*Volkman et al.*, 1980; *Marlowe et al.*, 1990; *Volkman et al.*, 1995]. The presence of long-chain alkenones in oceanic sediment has been used in a number of studies to infer changes in past and present coccolithophorid productivity [*Prahl et al.*, 1993; *Villanueva et al.*, 1997; *Schefuß et al.*, 2004].

The plot of the raw abundance ratio of total alkenones to brassicasterol demonstrates that the abundance of diatoms significantly increased relative to coccolithophorids at the MIS 5/4 transition, at ~ 72 ka (Figure 3.22). The record does not show an increase in sterol to alkenone ratio in MIS 4 relative to MIS 5a, as might be expected based on the greater opal accumulation rate recorded in ODP 663A during MIS 4. However, the large maximum in the brassicasterol:alkenone ratio record ~ 72 ka is coeval with a large, transient increase in opal flux (and %opal) in ODP 663A. It also corresponds to the interval in which the maximum opal:$CaCO_3$ ratio occurs (Figure 3.22). This apparent sudden increase in diatoms relative to coccolithophorids appears to precede the decrease in pCO_2 at the beginning of MIS 4 by 1-2 ka, although this is the same order of the uncertainty in the core age model [*Ahn and Brook*, 2008].

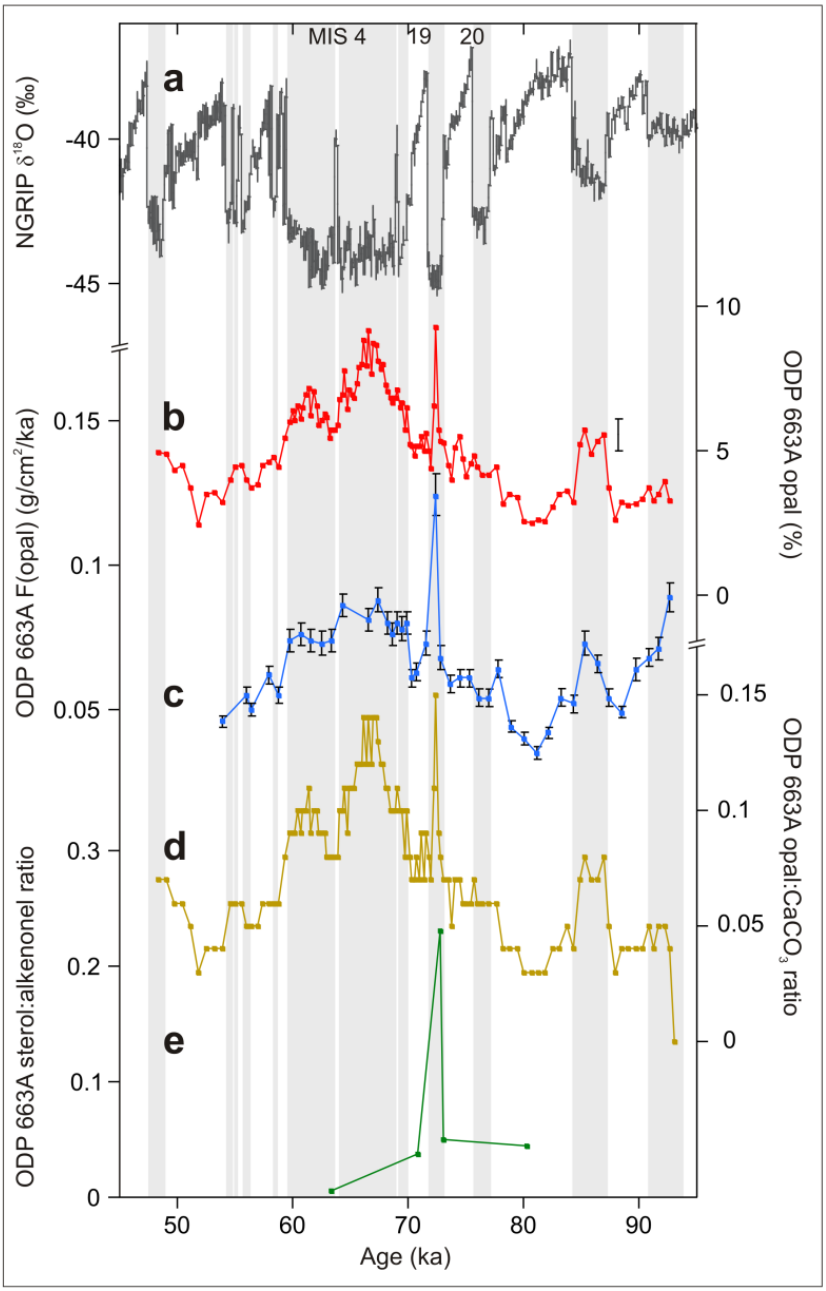

Figure 3.22 - ODP 663A opal flux biomarker comparison plot. a) NGRIP $\delta^{18}O$ (grey); b) ODP 663A %opal (red); c) ODP 663A thorium-normalised preserved opal flux rate [F(opal)] (blue); d) opal:$CaCO_3$ ratio; e) Raw abundance ratio of sterol to alkenone biomarkers (green) (see Chapter 2.10 for methods), note that this is a qualitative measure. Grey bands represent northern hemisphere cold periods from the NGRIP $\delta^{18}O$ record; MIS 4, D-O 19 and 20 are labelled.

Aside from the coeval maxima in opal flux and brassicasterol: alkenone ratio ~ 72 ka, the abundance ratio of sterol to alkenone does not correlate with opal flux, but this cannot necessarily be expected, given the range of different controls on opal [*Ragueneau et al.*, 2000] and sedimentary biomarkers [*Zonneveld et al.*, 2010]. Therefore, the lower brassicasterol:alkenone ratios in MIS 4 does not preclude high diatom export productivity in this interval.

3.7 Discussion

Using records of percent biogenic opal or preserved opal fluxes as an indicator of palaeoproductivity can be problematic, as several studies have indicated that large degrees of spatial and temporal variation in opal preservation exist [*Johnson*, 1976; *Archer et al.*, 1993; *Dubois et al.*, 2010]. Additionally, decoupling of the Si and C cycles can occur in some instances [*Berger and Herguera*, 1992; *Kumar et al.*, 1995]. Of key importance is the need to distinguish whether the increase in the accumulation of opal in MIS 4 (relative to MIS 5a) in sediments of the eastern equatorial Atlantic (EEA) is due to an enhancement of opal productivity, or an enhancement in opal preservation. This is a critical distinction, as increased glacial opal productivity would support the SALH whereas increased glacial opal preservation would not. Here we address issues of preservation and productivity separately to distinguish between the two scenarios.

3.7.1 Opal preservation in the EEA during the MIS 5a/4 transition

In the modern EEA, studies have recorded strong opal dissolution in the water column, and at the sediment-water interface, with only ~ 1% of opal produced in surface waters buried in sediment [*Treppke et al.*, 1996; *Abrantes*, 2000]. Despite this observation (and the presumption that it was also true in the past), the spatial pattern of opal burial in sediment is still found to be consistent with rates of opal productivity in the overlying water [*Treppke et al.*, 1996].

Assessing the rate of opal dissolution through time is not straightforward, but it appears that the past preservation of biogenic opal in the EEA may have been a function of the export flux [*Pokras*, 1986]. Higher opal flux rates may initially increase the absolute rate of opal dissolution in sedimentary pore waters but this increases pore water silica saturation and provides a protective 'buffer' to further opal dissolution [*Pokras*, 1986]. Sediments are therefore only likely to suffer strong opal dissolution in situations where the export productivity of opal is low, and protective 'buffering' of opal is minimal. In our dataset it was thought that the dissolution of opal was more likely to affect the western tropical Atlantic (core RC16-66) where opal export flux is the lowest of all cores used in this study, and appears to be relatively invariant on G-IG timescales. It is possible, then, that greater rates of opal dissolution occurred in RC16-66 than in the other cores used in this study, which may also have had an effect on the $_{xs}(^{231}Pa/^{230}Th)_0$ record of the core (see Chapter 3.7.2).

Another important factor to consider when assessing opal preservation potential is the overall core sedimentation rate. To gauge changes in overall sedimentation throughout time, a sedimentary 'focusing factor' was calculated for each of the cores.

The focusing factor is calculated by dividing the sedimentation rate (the result of interpolation between age-depth tie-points between the NGRIP $\delta^{18}O$ record and that of the core), by the ^{230}Th-normalised overall flux rate, which is termed F(total).

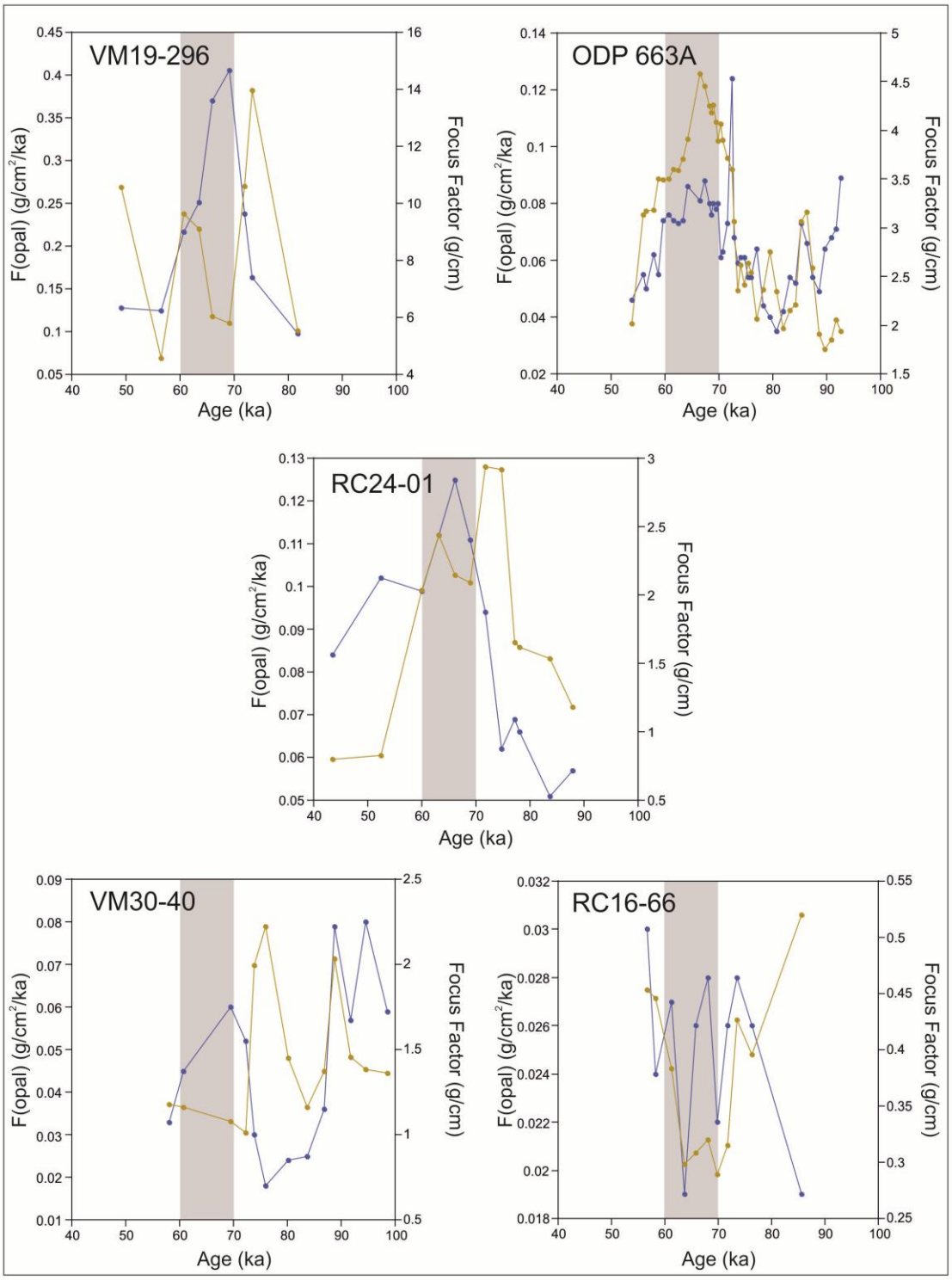

Figure 3.23 – Comparison of F(opal) (blue curve) with Focusing Factor (FF), a proxy for changes in core sedimentation rate which accounts for sediment focusing and winnowing. Grey bands represent MIS 4 from the NGRIP $\delta^{18}O$ record.

The focusing factor (FF) therefore accounts for change in the overall sedimentation rate, whilst also accounting for sedimentary distribution by bottom-water currents [*Francois et al*., 2004]. The plots of FF versus opal accumulation (Figure 3.23) show that in all cores except ODP 663A, maximum values of FF did not occur during MIS 4. Therefore it is likely that sedimentary focusing was not an important control on sedimentary opal preservation in the cores, except in ODP 663A, where the closer association of FF and F(opal) suggest that it may have been more important.

Furthermore, the high mean FF in ODP 663A (Table 3.3) and the association of FF and F(opal) (Figure 3.23) may suggest that opal formed a greater proportion of the sedimentary flux at this core site. A possible reason for this could be the selective concentration and sedimentation of larger diatoms such as *E. Rex* at oceanic frontal zones, as proposed by Kemp *et al*., [2006]. VM19-296 also contains a large proportion of sedimentary opal, and has a high FF value (Table 3.3). The FF value is much greater in VM19-296 than all the other cores due to its extremely low sedimentation rate during MIS 4, which may be explained by enhanced $CaCO_3$ loss, partly due to its greater water depth. Notably, FF is higher in RC16-66 than in either of VM30-40 or RC24-01, which probably reflects greater terrigenous input to the RC16-66 core site (see Figure 3.23 and 3.24).

Table 3.3 – Long-term mean values of focusing factor (sedimentation rate/^{230}Th-normalised total sedimentary flux rate), units g/cm. The cores are arranged from east to west (top to bottom).

Core	Depth (m)	Mean Focusing Factor (FF)
VM19-296	5017	8.429
ODP 663A	3708	3.061
RC24-01	3837	1.848
VM30-40	3706	1.496
RC16-66	4424	2.678

To add further information on opal preservation, diatom valve abundance counts were undertaken using prepared microscope slides from selected intervals from ODP 663A, according to the method of Scherer [1994] (see Section 2.9 and appendix for details of full methodology). A method exists to assess the degree of opal preservation using a four-stage preservation index of the vellum of the tropical diatom *Azpeitia nodulifer* [*Warnock et al.*, 2007], but unfortunately the diatom slides contained an insufficient density of diatoms to make use of this method. Although quantification of the amount of opal dissolution was not possible, I suggest that it is

reasonable, knowing that all areas of the ocean are undersaturated with respect to silicic acid [*Stumm and Morgan*, 1981], to assume that an increase in opal accumulation represents an increase in diatom export productivity.

In order to address the relative effects of opal productivity and preservation in the equatorial Atlantic during MIS 4, I compared our opal flux records with other palaeoproductivity proxies (see Section 3.7.3).

3.7.2 Controls of $_{xs}(^{231}Pa/^{230}Th)_0$ and its use as a palaeoproductivity proxy

Previous investigations of this kind have used the $_{xs}(^{231}Pa/^{230}Th)_0$ of bulk sediment as a record of the rate of past productivity by opal-producing phytoplankton, based on the observation that biogenic opal is an effective scavenger of ^{231}Pa from the water column [*Anderson et al.*, 1983b], and may therefore control $_{xs}(^{231}Pa/^{230}Th)_0$ in high-productivity areas of the ocean [*Chase et al.*, 2002]. At sites where downcore $_{xs}(^{231}Pa/^{230}Th)_0$ is positively correlated with the thorium-normalised opal flux rate, the opal flux records are interpreted as being productivity-dominated, based on calibrations between $_{xs}(^{231}Pa/^{230}Th)_0$, thorium-normalised opal flux and primary productivity data [*Bradtmiller et al.*, 2006; 2007; *Bradtmiller et al.*, 2009].

However, in this investigation, the records of $_{xs}(^{231}Pa/^{230}Th)_0$ and opal flux in all cores generally show a low degree of correlation ($r = 0.055 – 0.439$ at $p < 0.05$), see Figures 3.13 - 3.17), demonstrating that opal flux was not the dominant control on $_{xs}(^{231}Pa/^{230}Th)_0$ in the equatorial Atlantic during MIS 4. There are a number of reasons why records of $_{xs}(^{231}Pa/^{230}Th)_0$ and opal flux may become decoupled; these are (1) temporal variability in opal preservation [*Johnson*, 1976; *Archer et al.*, 1993; *Dubois et al.*, 2010], (2) past variations in the flux of $CaCO_3$ or detrital material; both of which may influence $_{xs}(^{231}Pa/^{230}Th)_0$ [*Chase et al.*, 2002; *Geibert and Usbeck*, 2004], (3) changes in the radionuclide content of deep water masses bathing the site [*Thomas et al.*, 2006], or (4) past variations in oceanic deepwater flow speed [*Yu et al.*, 1996; *Marchal et al.*, 2000].

The lower opal flux rates recorded in RC16-66 relative to ODP 663A, RC24-01, VM19-296 and VM30-40 possibly meant that opal preservation was poorer in RC16-66 than in the other cores, based on the findings of [*Pokras*, 1986]. Therefore, poor opal preservation in RC16-66 may have contributed to the decoupling of the opal flux and $_{xs}(^{231}Pa/^{230}Th)_0$ records in RC16-66, but it is unlikely to have affected $_{xs}(^{231}Pa/^{230}Th)_0$ in the other cores. On the other hand, it is likely that AABW with a high silicic acid content [*Schlitzer*, 2000] was bathing deep Atlantic sites during MIS 4 [*Govin et al.*, 2009]; and whilst this would have increased the preservation potential of opal in deep water, it would also have led to a more uniform pattern in opal flux changes across the MIS 5/4 transition. Because the recorded pattern of opal flux

increases in MIS 4 approximate modern productivity patterns (Table 3.2 and Figure 3.6), it is reasonable to relate changes in opal flux to changes in diatom export productivity.

Variations in the flux of detrital (terrigenous) material (non-$CaCO_3$, non-opal), and $CaCO_3$ may also have affected the sedimentary $_{xs}(^{231}Pa/^{230}Th)_0$ in our cores. To account for the input of terrigenous material, I use the ^{230}Th-normalised flux of ^{232}Th, which has been used in previous studies as a proxy for terrigenous input [*Brewer et al*., 1980; *Luo et al*., 2001; *Pourmand et al*., 2004]. The ^{230}Th-normalised flux of ^{232}Th is calculated according to Equation 3.8:

$$F(^{232}Th) = (^{232}Th) \times {}^{230}Th\text{-norm } F$$

Equation 3.8 – Calculation of ^{230}Th-normalised flux of ^{232}Th; where F(^{232}Th) is the ^{230}Th-normalised flux of ^{232}Th (in dpm/cm^2/ka, ^{232}Th is the activity of ^{232}Th in sediment (in dpm g^{-1}), and ^{230}Th-norm F is the ^{230}Th-normalised sediment accumulation rate (in g/cm^2/ka).

The ^{230}Th-normalised flux of ^{232}Th [F(^{232}Th)], of all cores is plotted on the same scale below (Figure 3.24) to illustrate differences in terrigenous accumulation rate. RC16-66 (red curve) shows the highest terrigenous input, which is consistent with a high detrital input from the Amazon plume [*Vital and Stattegger*, 2000], and is also in agreement with the findings of Bradtmiller et al. [2007].

ODP 663A (blue curve), VM30-40 (orange curve) and RC24-01 (green curve) all show little change in terrigenous flux between MIS 5a and MIS 4, compared to their long-term average values (see Table 3.4), whilst VM19-296 (violet curve) shows a maximum in terrigenous input during MIS 4 (~70 ka). Terrigenous input in RC16-66 peaks ~ 71 ka, just prior to the beginning of MIS 4, before declining to around average values at ~ 63 ka.

If terrigenous (detrital) input significantly affected $_{xs}(^{231}Pa/^{230}Th)_0$ in our cores, it would preferentially scavenge the more particle-reactive ^{230}Th over ^{231}Pa [*Henderson and Anderson*, 2003; *Geibert and Usbeck*, 2004], leading to the expectation that $_{xs}(^{231}Pa/^{230}Th)_0$ would be lowest in the core with the highest terrigenous input (RC16-66). Because the long-term mean $_{xs}(^{231}Pa/^{230}Th)_0$ of RC16-66 is slightly higher than all the other cores (except VM19-296, see Table 3.2), it seems that terrigenous input can be discounted as an influence on $_{xs}(^{231}Pa/^{230}Th)_0$ in RC16-66. Furthermore, the terrigenous input during MIS 4 is relatively invariant between MIS 5a and MIS 4 in VM30-40, RC24-01 and ODP 663A. Additionally, the large maximum in $_{xs}(^{231}Pa/^{230}Th)_0$ recorded ~54 ka in VM19-296 (Figure 3.14) cannot be explained by increasing terrigenous flux.

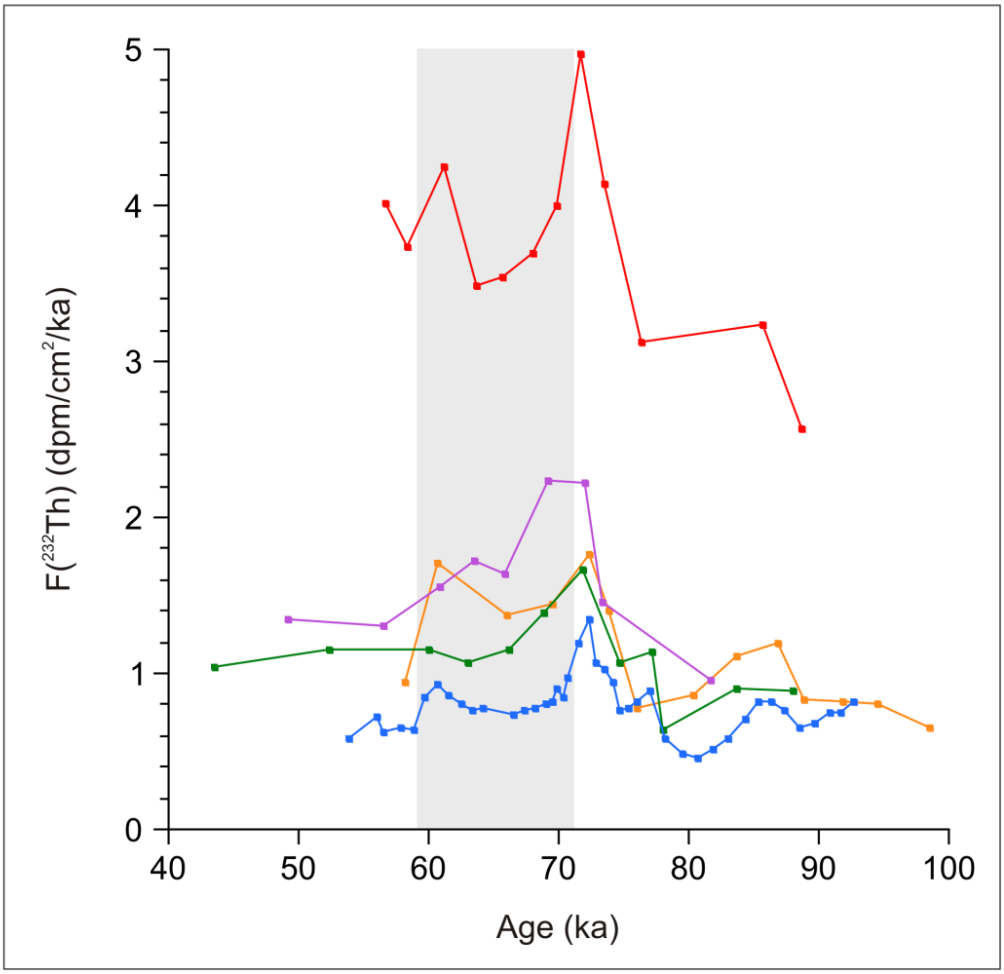

Figure 3.24 – A plot of ^{230}Th-normalised flux of ^{232}Th [F(^{232}Th)], on the same axes for comparison. The cores are assigned the same colours as in Figures 3.18 and 3.19; RC16-66 (red), VM30-40 (orange), RC24-01 (green), ODP 663A (blue) and VM19-296 (violet). The grey shaded bar represents MIS 4, from the NGRIP δ^{18}O record.

A plausible explanation for the $_{xs}(^{231}Pa/^{230}Th)_0$ variability ~74-69 ka are changes in oceanic circulation or chemistry, which may affect the sedimentary $_{xs}(^{231}Pa/^{230}Th)_0$ ratio through changes in deep water flow speed [*Yu et al.*, 1996; *Marchal et al.*, 2000], or by altering the ^{231}Pa content of deep water [*Thomas et al.*, 2006]. The $_{xs}(^{231}Pa/^{230}Th)_0$ has been suggested to record changes in the strength of Atlantic Meridional Overturning Circulation (AMOC) in oligotrophic areas of the North Atlantic [*McManus et al.*, 2004; *Gherardi et al.*, 2005; *Guihou et al.*, 2010; *Negre et al.*, 2010]. The interpretation of the $_{xs}(^{231}Pa/^{230}Th)_0$ ratio from two cores from the western and eastern basins of the North Atlantic suggest that AMOC shoaled or weakened during MIS 4 [*Guihou et al.*, 2010].

Table 3.4 – Long-term mean values of ^{230}Th-normalised flux of ^{232}Th for all cores. Cores are arranged from west (left) to east (right).

CORE	RC16-66	VM30-40	RC24-01	ODP 663A	VM19-296
Mean F(^{232}Th)	3.837	1.102	1.107	0.788	1.644

The hypothesised cause of the weakening in AMOC was iceberg discharge disrupting the formation of deepwater in the North Atlantic, and the $_{xs}(^{231}Pa/^{230}Th)_0$ record of [*Guihou et al.*, 2010] shows high-frequency variability across the MIS 5/4 transition, in a period where the climate of high northern latitudes oscillated rapidly between cold and warm throughout D-O events 19 and 20 [*Andersen et al.*, 2007; *Ahn and Brook*, 2008]. In the modern ocean, EEA water at ~3600 m is composed of approximately 80% NADW and 20% AABW [*Broecker et al.*, 1991], so presumably any previous shoaling or weakening of AMOC, and related decline in NADW production might be seen in the $_{xs}(^{231}Pa/^{230}Th)_0$ record of ODP 663A (3708 m water depth).

The values of $_{xs}(^{231}Pa/^{230}Th)_0$ in VM19-296 (5017 m water depth) are lower than expected during MIS 4 given the high opal flux recorded in the core. A possible explanation for this could be the northward incursion of Antarctic Bottom Water (AABW), which may have influenced the deep EEA and the VM19-296 core site during MIS 4 [*Verardo and McIntyre*, 1994; *Broecker and Clark*, 2001; *Broecker and Clark*, 2003; *Govin et al.*, 2009]. The pattern of $CaCO_3$ dissolution in VM19-296 is consistent with the influence of low [CO_3^{2-}] AABW during MIS 4 (see Chapter 4.3). AABW has a low ^{231}Pa content, probably due to scavenging onto opal particles as the AABW transits the Southern Ocean [*Thomas et al.*, 2006], which may have counteracted any increased $_{xs}(^{231}Pa/^{230}Th)_0$ in VM19-296 due to increased opal flux during MIS 4. The very high ratio of $_{xs}(^{231}Pa/^{230}Th)_0$ recorded at ~54 ka (warm D-O 14) is difficult to explain, but may possibly be due to an increased influence of northern component water, which has a generally higher ^{231}Pa content [*Thomas et al.*, 2006], on the VM19-296 core site.

To summarise the controls on the $_{xs}(^{231}Pa/^{230}Th)_0$ record of the cores studied (see Figures 3.24, 3.25 and 3.26): The $_{xs}(^{231}Pa/^{230}Th)_0$ of RC16-66 does not correlate with changes in opal or $CaCO_3$ flux, or terrigenous input, but may be influenced by high detrital influence from the Amazon Plume [*Vital and Stattegger*, 2000]; the $_{xs}(^{231}Pa/^{230}Th)_0$ record of VM30-40 seems to be influenced by both F($CaCO_3$) and terrigenous input; the $_{xs}(^{231}Pa/^{230}Th)_0$ record of RC24-01 correlates with opal flux through most of the studied interval, but decouples ~78 ka, possibly associated with oceanic circulation changes; the $_{xs}(^{231}Pa/^{230}Th)_0$ record of ODP 663A and the $_{xs}(^{231}Pa/^{230}Th)_0$ record of VM19-296 may be related to changes in deep water

chemistry associated with enhanced AABW advection to lower latitudes during MIS 4 [*Verardo and McIntyre*, 1994; *Govin et al.*, 2009].

To shed further light on the relationship between opal accumulation and diatom productivity, a ratio of the abundance of sedimentary Pa ($^{231}Pa_{xs}$) against the ^{230}Th-normalised opal flux was calculated for all cores (Figure 3.25).

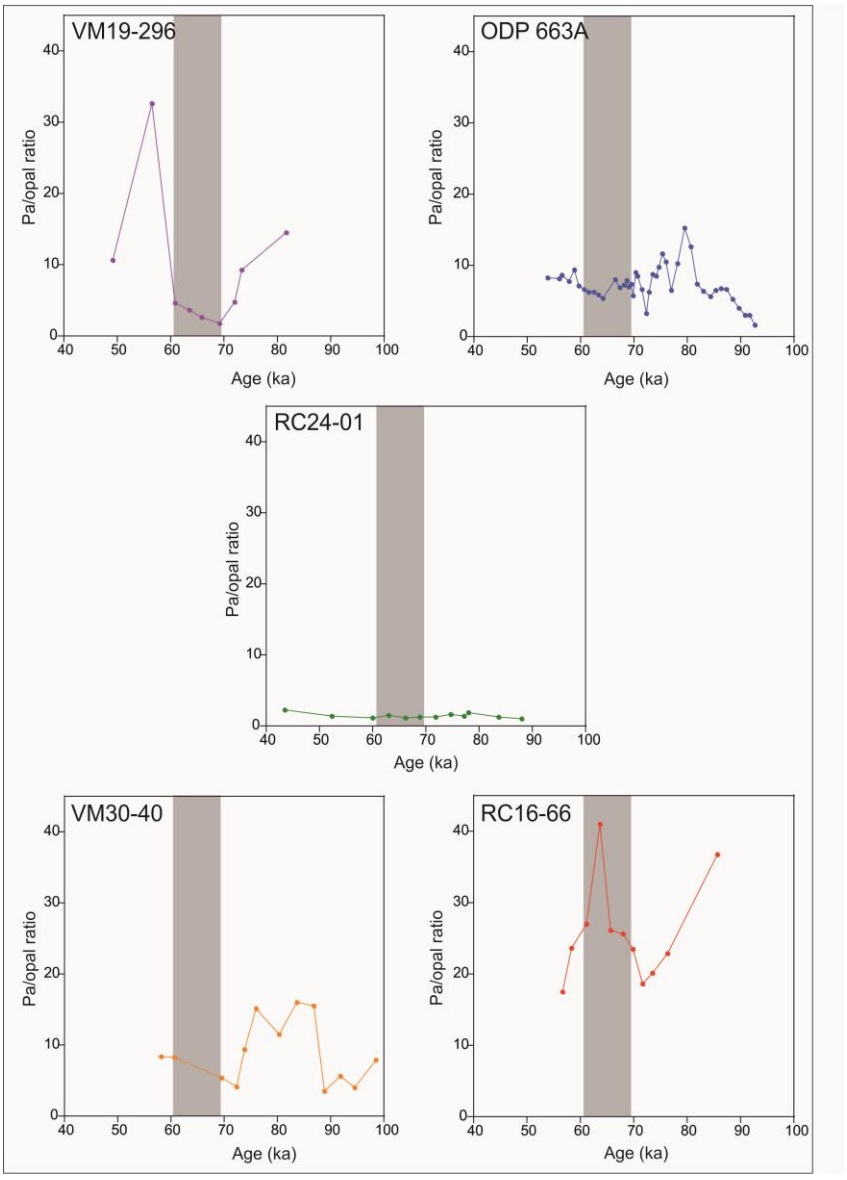

Figure 3.25 – A plot of $(^{230}Pa)_{xs}$/opal flux [F(opal)], on the same axes for comparison. The cores are assigned the same colours as in Figures 3.18 and 3.19; RC16-66 (red), VM30-40 (orange), RC24-01 (green), ODP 663A (blue) and VM19-296 (violet). The grey shaded bar represents MIS 4, from the NGRIP $\delta^{18}O$ record.

In all cores apart from RC16-66, Pa/opal is low during MIS 4, which further supports the idea that the $_{xs}(^{231}Pa/^{230}Th)_0$ records in the equatorial Atlantic are primarily controlled by changes in ocean chemistry and circulation. The Pa/opal record in RC16-66 is interesting in that it shows large changes, in the absence of

significant changes in opal accumulation. The Pa/opal record of RC16-66 probably reflects the increased influence of AABW during MIS 4 [*Guihou et al*; 2010], and/or increased boundary scavenging of radionuclides [*Spencer et al.*, 1981].

3.7.3 Comparison with other palaeoproductivity proxies

These data reveal a decrease in the amount of opal accumulation from the east to west in the equatorial Atlantic during MIS 4 (see Figure 3.18 and Table 3.1).

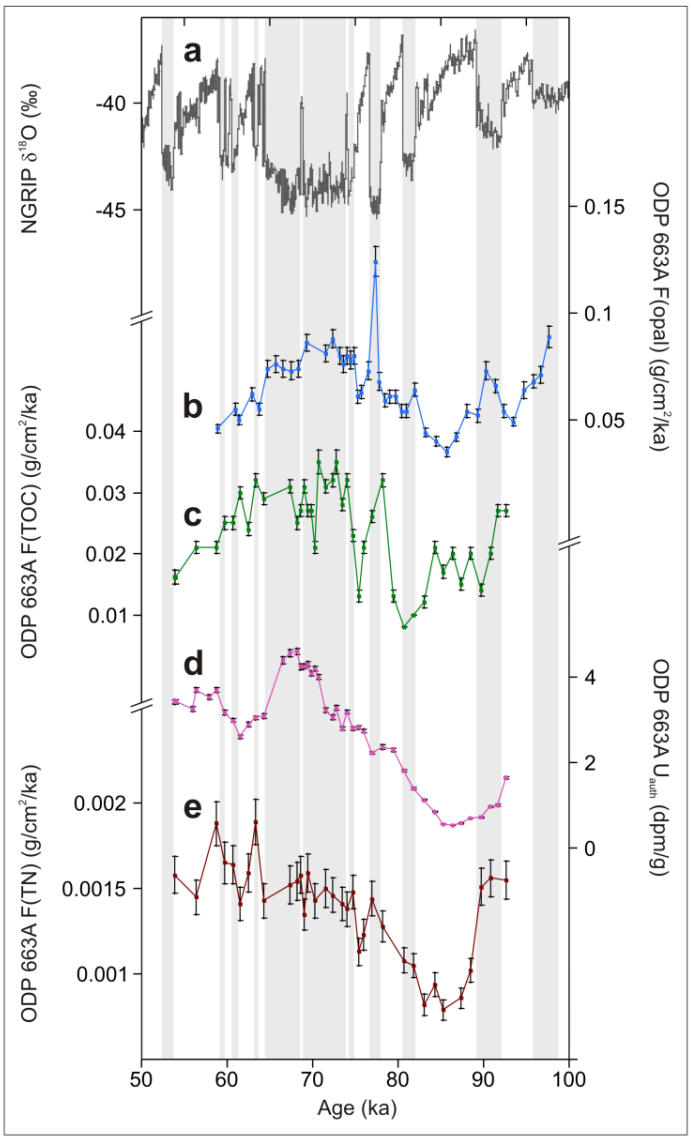

Figure 3.26 - ODP 663A opal flux and palaeoproductivity proxy comparison plot. a) NGRIP $\delta^{18}O$ (grey); b) ODP 663A thorium-normalised opal flux rate [F(opal)] (blue), with error bars in black; c) ODP 663A thorium normalised total organic carbon flux [F(TOC)] (green), with error bars in black; d) ODP 663A authigenic uranium accumulation rate (U_{auth}) (pink), with error bars in black; e) ODP 663A thorium normalised total nitrogen flux [F(TN)] (brown), with error bars in black. Grey bands represent northern hemisphere cold periods from the NGRIP $\delta^{18}O$ record.

Despite the non-linear relationship between opal and organic carbon (C_{org}) fluxes, diatoms are major exporters of C_{org} in the ocean [*Ragueneau et al.*, 2000], therefore if increases in opal accumulation represent episodes of enhanced diatom productivity, the records of U_{auth} and possibly C_{org} should correlate with changes in opal flux. It is generally agreed that ocean-wide, the relative abundance of diatoms increases as primary productivity increases [*Raymont*, 1980].

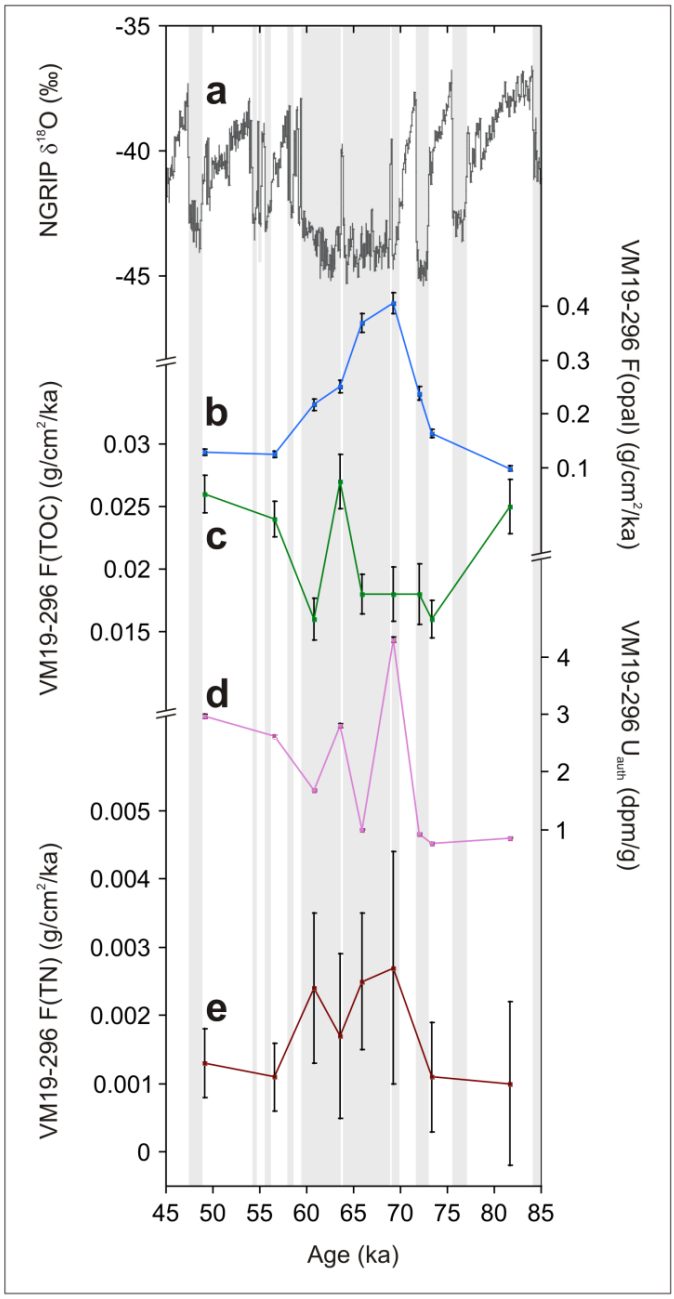

Figure 3.27 - VM19-296 opal flux and palaeoproductivity proxy comparison plot. a) NGRIP $\delta^{18}O$ (grey); b) VM19-296 thorium-normalised opal flux rate [F(opal)] (blue), with error bars in black; c) VM19-296 thorium normalised total organic carbon flux [F(TOC)] (green), with error bars in black; d) VM19-296 authigenic uranium accumulation rate (U_{auth}) (pink), with error bars in black; e) VM19-296 thorium normalised total nitrogen flux [F(TN)] (brown), with error bars in black. Grey bands represent northern hemisphere cold periods from the NGRIP $\delta^{18}O$ record.

In order to distinguish whether or not the increased opal fluxes recorded in equatorial Atlantic cores reflect enhanced diatom export productivity and not preservation, parallel downcore records of other palaeoproductivity proxies, authigenic uranium (U_{auth}), and sedimentary concentrations of total organic carbon (TOC) and total nitrogen (TN) were measured in all cores (see Figures 3.26 – 3.30).

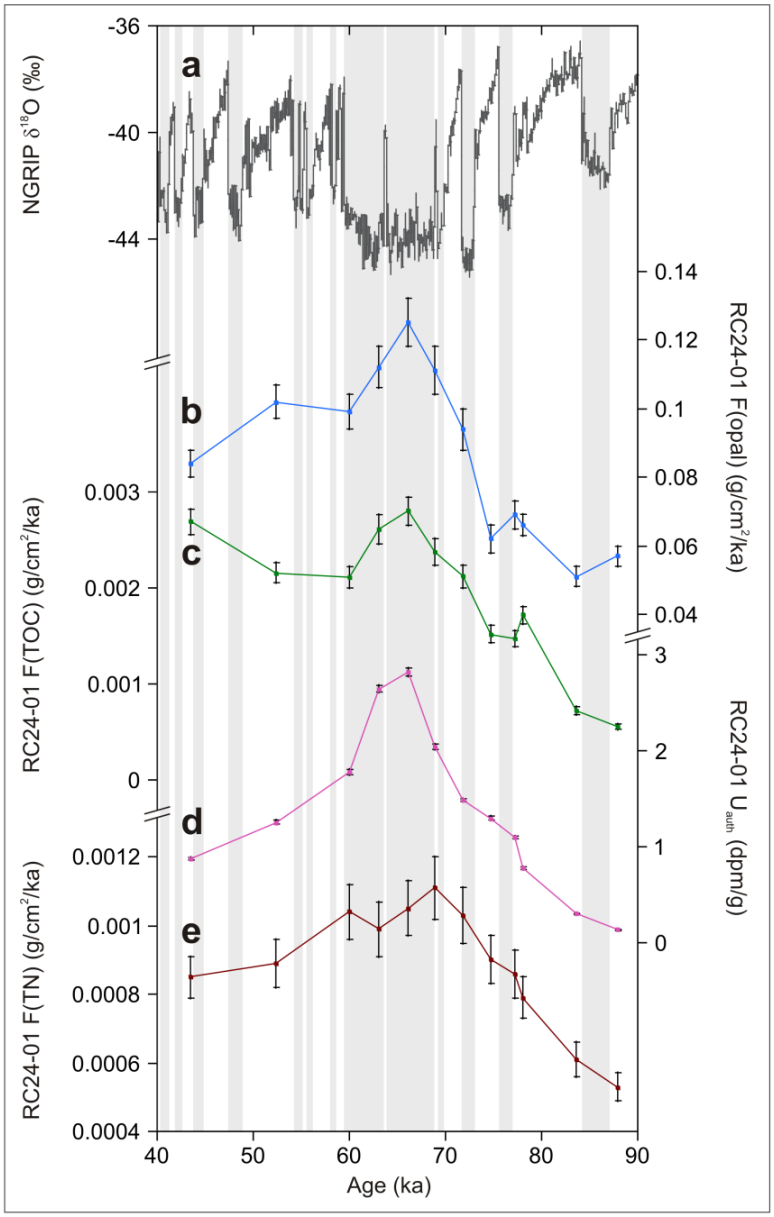

Figure 3.28 - RC24-01 opal flux and palaeoproductivity proxy comparison plot. a) NGRIP $\delta^{18}O$ (grey); b) RC24-01 thorium-normalised opal flux rate [F(opal)] (blue), with error bars in black; c) RC24-01 thorium normalised total organic carbon flux [F(TOC)] (green), with error bars in black; d) RC24-01 authigenic uranium accumulation rate (U_{auth}) (pink), with error bars in black; e) RC24-01 thorium normalised total nitrogen flux [F(TN)] (brown), with error bars in black. Grey bands represent northern hemisphere cold periods from the NGRIP $\delta^{18}O$ record.

U_{auth} is used in this investigation as a proxy for organic carbon export [*Kumar et al.*, 1995; *Anderson et al.*, 1998; *Chase et al.*, 2001]. Uranium in well-oxygenated seawater is present mainly as the conservative form of uranyl (UO_2) ions that bind to carbonate ions to form $UO_2(CO_3)_3^{4-}$ [*Tribovillard et al.*, 2006]. Under anoxic conditions it is precipitated as an amorphous tetravalent phase, U_{auth} [*Anderson*, 1987]. When the flux of organic carbon to the sediment exceeds the threshold supply of oxygen diffused from bottom water, U_{auth} begins to precipitate, and exhibits a positive, but

non-linear correlation to the organic carbon flux [*Klinkhammer and Palmer*, 1991; *Rosenthal et al.*, 1995]. See Equation 3.4 for calculation of U_{auth}.

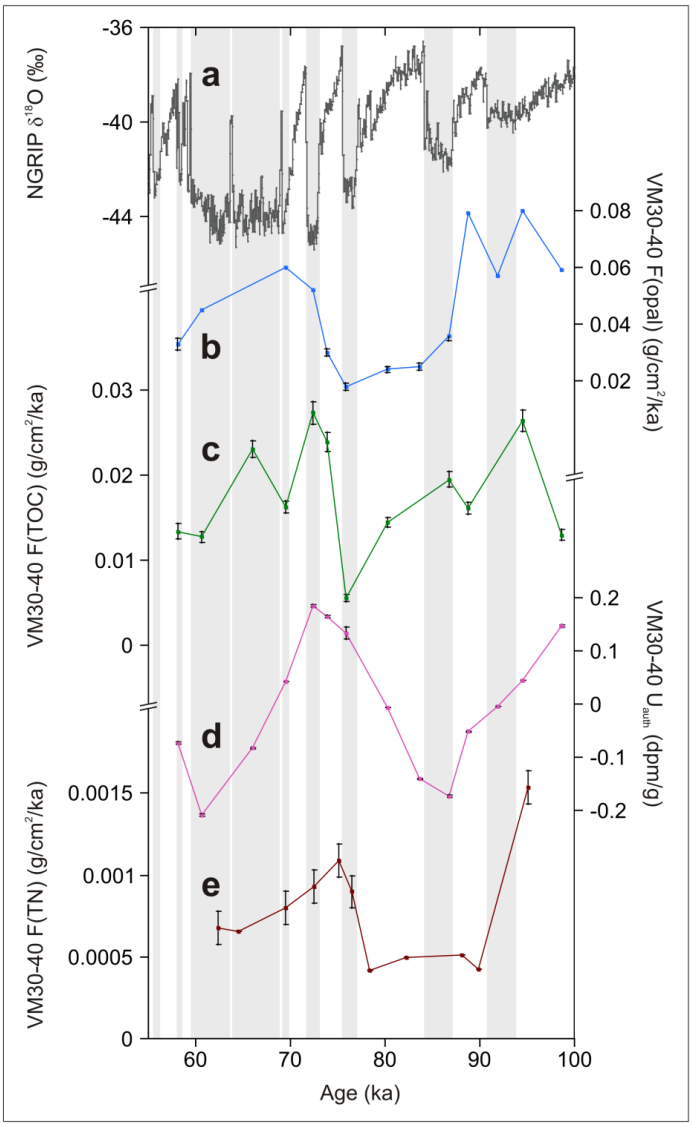

Figure 3.29 – VM30-40 opal flux and palaeoproductivity proxy comparison plot. a) NGRIP $\delta^{18}O$ (grey); b) VM30-40 thorium-normalised opal flux rate [F(opal)] (blue), with error bars in black; c) VM30-40 thorium normalised total organic carbon flux [F(TOC)] (green), with error bars in black; d) VM30-40 authigenic uranium accumulation rate (U_{auth}) (pink), with error bars in black; e) VM30-40 thorium normalised total nitrogen flux [F(TN)] (brown), with error bars in black. Grey bands represent northern hemisphere cold periods from the NGRIP $\delta^{18}O$ record.

However, the use of U_{auth} as a palaeoproductivity proxy may be complicated by the local sedimentation rate. Where sedimentation rates (see focusing factor, FF; in Figure 3.23) are lower, uranyl ions have more time to diffuse from the water column into the sediment, making U_{auth} higher than it would be otherwise [*Crusius and Thomson*, 2000]. In the case of cores ODP 663A and RC24-01, FF either increased or remained high during MIS 4, which means that sedimentation rate probably had little effect on U_{auth} in these cores (Figure 3.23). Conversely, FF in VM19-296, VM30-

40 and RC16-66 decreased or remained low during MIS 4, meaning that sedimentation rate may have had a greater effect on U_{auth} in these cores (Figure 3.23).

Furthermore, additional complications with the use of U_{auth} as a palaeoproductivity proxy can arise from changes in redox conditions (after initial U_{auth} formation). U_{auth} in sediment may be remobilised if oxygen penetrates sediment to a depth where U_{auth} has accumulated [*Morford et al*., 2001; *McManus et al*., 2005]. This can occur when the oxygen content of bottom water increases, or the organic matter flux to sediment decreases, or both. Changes in conditions such as these at the sediment-water interface can lead to the loss of a primary U_{auth} signal, or vertical migration of the U_{auth} signal to a depth where favourable conditions for reprecipitation of U_{auth} are found [*McManus et al*., 2005]. In the context of the eastern equatorial Atlantic cores (VM19-296, ODP 663A and RC24-01), the likely increase in organic matter flux in the equatorial Atlantic during MIS 4 [*Sarnthein et al*., 1992] probably led to good overall preservation of the original U_{auth} signal in this period, with potentially poorer U_{auth} preservation in MIS 5 and 3. It is more difficult to assess changes in redox chemistry at the VM30-40 and RC16-66 core sites with the data currently available.

In the modern EEA, the export flux of opal contributes 3-20 % to the total export flux at 853 m, and 10-19 % at 3921 m [*Treppke et al.*, 1996], with $CaCO_3$ (in the form of coccolithophorids, planktic foraminifera and pteropods) making up the majority of the rest of the export flux [*Wefer and Fischer*, 1993]. Around 87 % of organic carbon is recycled in the upper 400 m of the water column in the EEA [*Bishop et al.*, 1977]. On longer timescales, however, data suggests that G-IG variations in opal accumulation in tropical Atlantic cores are positively correlated with TOC accumulation, and increases of both are taken to indicate increased surface productivity [*Verardo and McIntyre*, 1994; *Wagner*, 2000].

Increases during MIS 4 in the preserved export flux of TOC [F(TOC)], preserved export flux of TN [F(TN)], and U_{auth} in ODP 663A (Figure 3.26), VM19-296 (Figure 3.27) and RC24-01 (Figure 3.28) point to enhanced export productivity in the EEA during MIS 4. The coherence to which F(TOC) and, to a lesser degree F(TN), visibly correlate with F(opal) in ODP 663A and RC24-01 suggests that diatoms were dominating TOC export. The prominent opal maximum in ODP 663A (Figure 3.26) at ~ 77-78 ka coincides with a period of enhanced TOC flux, but is not reflected in the U_{auth} record. Nonetheless, the possibility remains that this represents a large and rapid diatom productivity increase, which is approximately coeval with the period in which pCO_2 was decreasing most rapidly [*Ahn and Brook*, 2008].

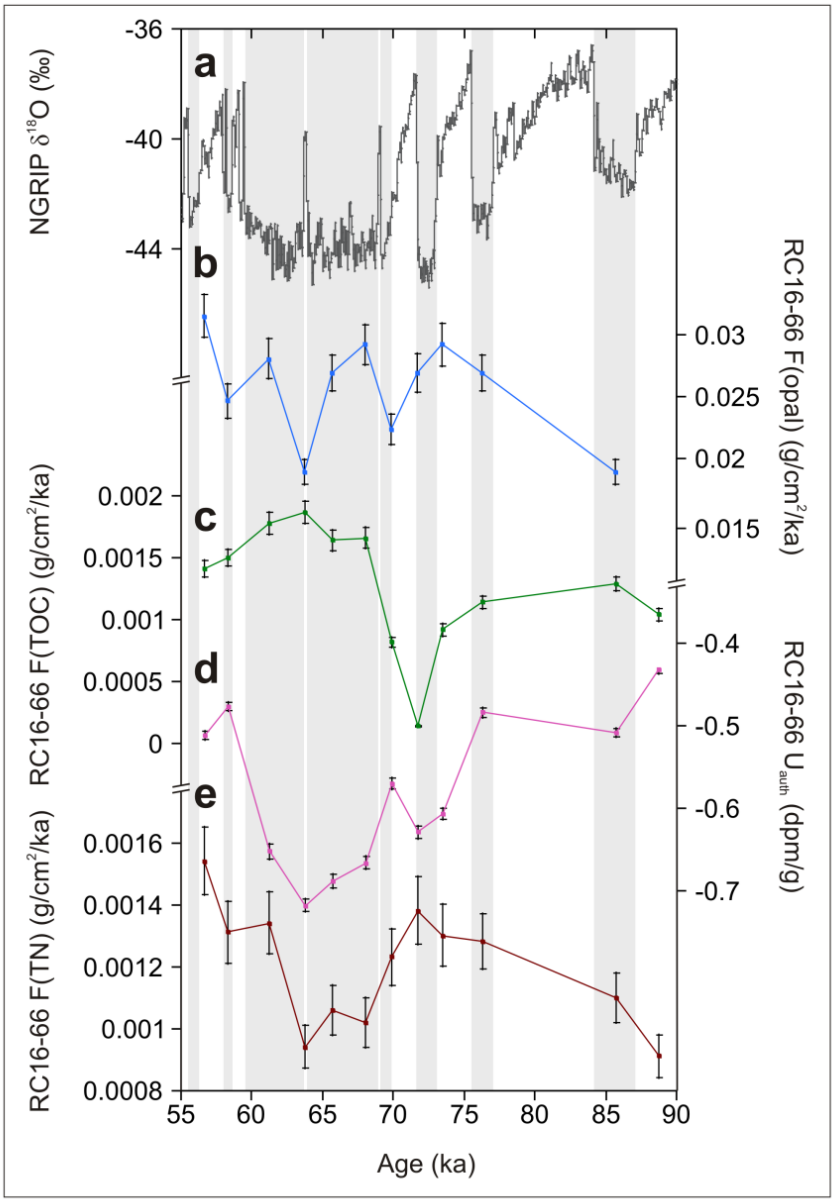

Figure 3.30 – RC16-66 opal flux and palaeoproductivity proxy comparison plot. a) NGRIP $\delta^{18}O$ (grey); b) RC16-66 thorium-normalised opal flux rate [F(opal)] (blue), with error bars in black; c) RC16-66 thorium normalised total organic carbon flux [F(TOC)] (green), with error bars in black; d) RC16-66 authigenic uranium accumulation rate (U_{auth}) (pink), with error bars in black; e) RC16-66 thorium normalised total nitrogen flux [F(TN)] (brown), with error bars in black. Grey bands represent northern hemisphere cold periods from the NGRIP $\delta^{18}O$ record.

In VM19-296 the flux of TOC is unrelated to opal flux, but a maximum in U_{auth} ~ 69 ka corresponds to maximum in opal flux (Figure 3.27), which suggests that production of opal was associated with high levels of TOC.

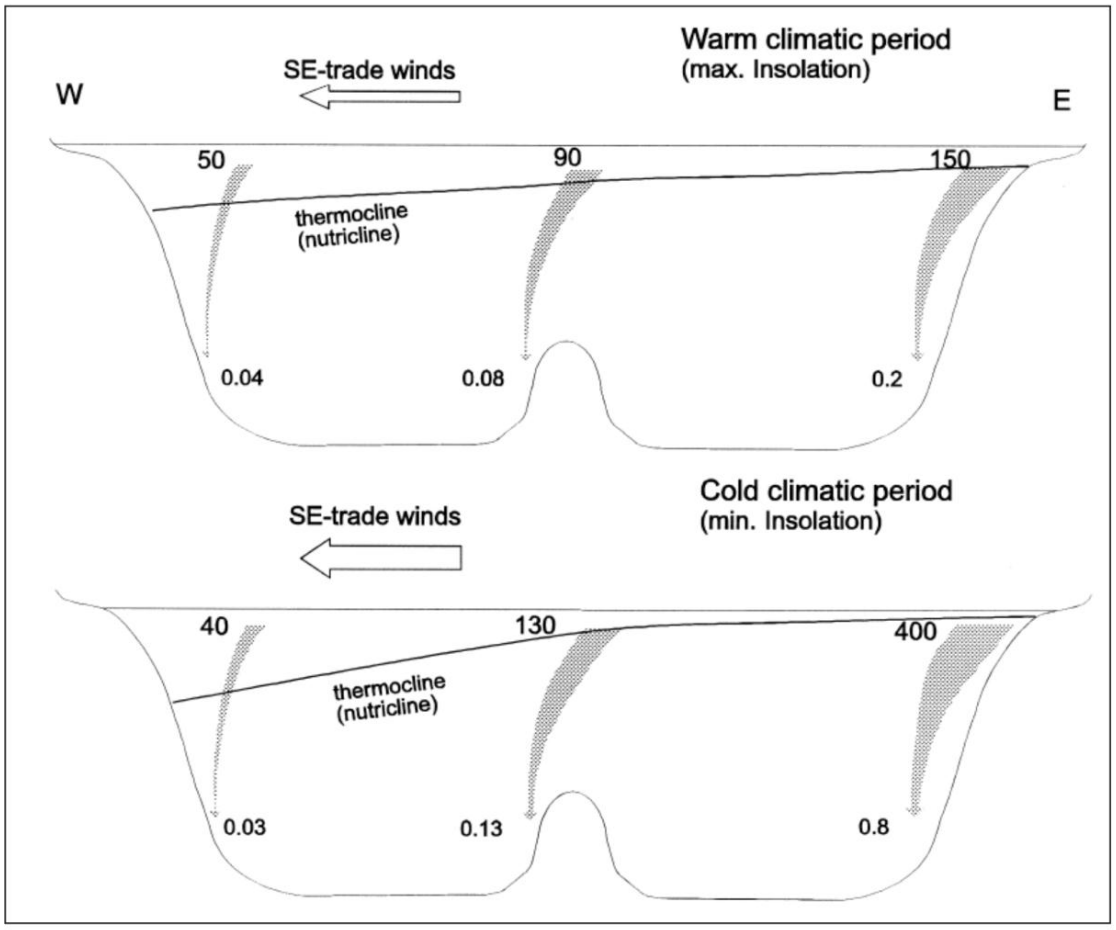

Figure 3.31 – Schematic illustration of the mechanism which may account for productivity differences between the eastern and western equatorial Atlantic. The series of numbers at the top of each figure are palaeoproductivity estimates, and the bottom set of number represent the accumulation of TOC (g/cm^2/ka) [*Rühlemann et al.*, 1996]. The figure was reproduced from Höll *et al*. [1999].

Palaeoproductivity maxima in VM30-40 (Figure 3.29) correlate less well with opal flux and suggest that maximum levels of productivity occurred prior to MIS 4 in the central equatorial Atlantic, probably during cold D-O 19 (~72-73 ka). Palaeoproductivity proxy records in RC16-66 (Figure 3.30) show generally decreasing productivity during MIS 5a, but do not support enhanced productivity during MIS 4. Similarly, the lack of opal increase in RC16-66 during MIS 4 was possibly due to differences in the depth of the thermocline between the east and west equatorial Atlantic regions [*Rühlemann et al.*, 1996; *Höll et al.*, 1999], with a deeper thermocline (nutricline) in the west compared to the east (Figure 3.31).

These findings from palaeoproductivity proxy records support one of the central requirements of the SALH, namely that an increase in the diatom-associated organic carbon pump would have affected the $CaCO_3$:C_{org} export ratio in the EEA [*Matsumoto et al.*, 2002]. Based on these records, and a palaeoproductivity reconstruction of EEA

core M16772 (1°21'S, 11°58'W, 3912 m water depth) from organic carbon and planktic foraminiferal transfer functions, organic carbon export productivity increased ~50 % in MIS 4 relative to MIS 5a [*Sarnthein et al.*, 1992]. Further support for enhanced MIS 4 productivity comes from the benthic $\delta^{13}C$ record the Guinea Basin core GeoB1105-3/4 (1°39.9'S, 12°25.7'W, 3225 m water depth) [*Bickert et al.*, 1999], which shows ~-3 ‰ values during MIS 4.

3.7.4 Influence of Ethmodiscus rex on opal and organic carbon export

The large mass and high sinking rate (510m day^{-1}) of *E. rex* [*Smayda*, 1971] may have helped to preserve the organic carbon within the diatom's cells, and may help to explain the maximum in U_{auth} in ODP 663A ~70-67 ka (Figure 3.26), coeval with the greatest abundance of *E. rex*, based on our qualitative fragment count (Figure 3.19).

The occurrence of *E. rex* oozes has been the topic of much debate between palaeoceanographers [*Gardner and Burckle*, 1975; *Mikkelsen*, 1977; *Abrantes*, 2001; *Kemp et al.*, 2006]. While it has previously been suggested that *E. rex* oozes were a product of episodic productivity 'blooms' [*Gardner and Burckle*, 1975], later work showed that *E. rex* is not an opportunistic feeder which capitalises on high nutrient levels. Rather it is adapted to an oligotrophic water column, using a strategy of vertical migration to acquire nutrients [*Villareal et al.*, 1999]. It had previously been suggested that *E. rex* oozes were a result of differential dissolution of opal, with *E. rex* frustules proposed as being more resistant to dissolution [*Mikkelsen*, 1977]. A subsequent study cast doubt on this hypothesis by showing that *E. rex* is in fact not a dissolution resistant species [*Lange et al.*, 1994].

Most recently, the occurrence of *E. rex* oozes in the Late Pleistocene glacial periods in the EEA has been attributed to the selective concentration of *E. rex* frustules at oceanic frontal zones by tropical instability waves (TIW), after enrichment of silicic acid in the EEA thermocline by runoff of silica-rich water from the African continent, associated with strong episodes of the African monsoon [*Abrantes*, 2001; *Kemp et al.*, 2006]. A number of lines of evidence are inconsistent with this scenario of riverine silica supply (see Chapter 3.7.7). The occurrence of intervals of monospecific *E. rex* ooze across a large area encompassing the eastern and central equatorial Atlantic (Figure 3.5) during MIS 4 is also difficult to explain using only the riverine silica/frontal zone concentration mechanism. Alternatively, I suggest that the enrichment of thermocline silicic acid (see Chapter 5), possibly combined with eolian Fe input, is better able to explain the pattern of low-latitude opal export observed during MIS 4.

Moreover, the occurrence of large numbers of *E. rex* fragments during MIS 4 is approximately coincident with increases in the abundance of other types of diatom (Figure 3.20), which suggests an overall increase in siliceous phytoplankton, rather than physical concentration and deposition of *E. rex* cells at oceanic fronts, which affects mainly larger, buoyancy-regulating species such as *E. rex* alone [*Kemp et al.*, 2006]. It is likely that *E. rex* cells made a greater contribution to organic carbon accumulation than other diatom species during the early part of MIS 4, due to its large cell size [*Villareal et al.*, 1999].

Studies of diatoms in the equatorial Pacific have shown that the addition of Fe to seawater may have promoted the growth of large diatoms, provided that sufficient Si is available [*Timmermans et al.*, 2004; *Brzezinski et al.*, 2011]. MIS 4 was a period of increased African aridity [*deMenocal et al.*, 1993; *Zhao et al.*, 2003; *Scholz et al.*, 2007], NE Trade Wind strength [*Flores et al.*, 2000; *Abrantes*, 2003], eolian deposition [*Zabel et al.*, 2002] and increased upwelling due to greater equatorial divergence [*Flores et al.*, 2000]; all of which could have favoured the growth of a large diatom species such as *E. rex*, as well as other diatom species.

3.7.5 Changes in brassicasterol to alkenone ratio through the MIS 5/4 transition

ODP 663A records a large, transient increase in sterol to alkenone abundance ratio ~72 ka (Figure 3.22), which is coeval with an increase in opal flux, and a maximum opal:$CaCO_3$ ratio. Taken as evidence of enhanced diatom productivity at the expense of coccolithophorids, this event could signify a SALH-type scenario occurring in the EEA. However, the timing of the change appears to precede the major pCO_2 drawdown during MIS 4 by 1-2 ka (Figure 3.33), which suggests that it may be a local rather than a basin-wide change. A possible contributory factor to this apparent increase in diatom productivity could be terrestrial input containing abundant Fe (Figure 3.32), as studies have shown that co-limitation of diatom growth (particularly large diatoms such as *E. rex*) by Si and Fe can occur [*Timmermans et al.*, 2004; *Brzezinski et al.*, 2011]. Interestingly, terrestrial input appears to have had less of an effect on opal export during MIS 4 in all cores (Figure 3.32).

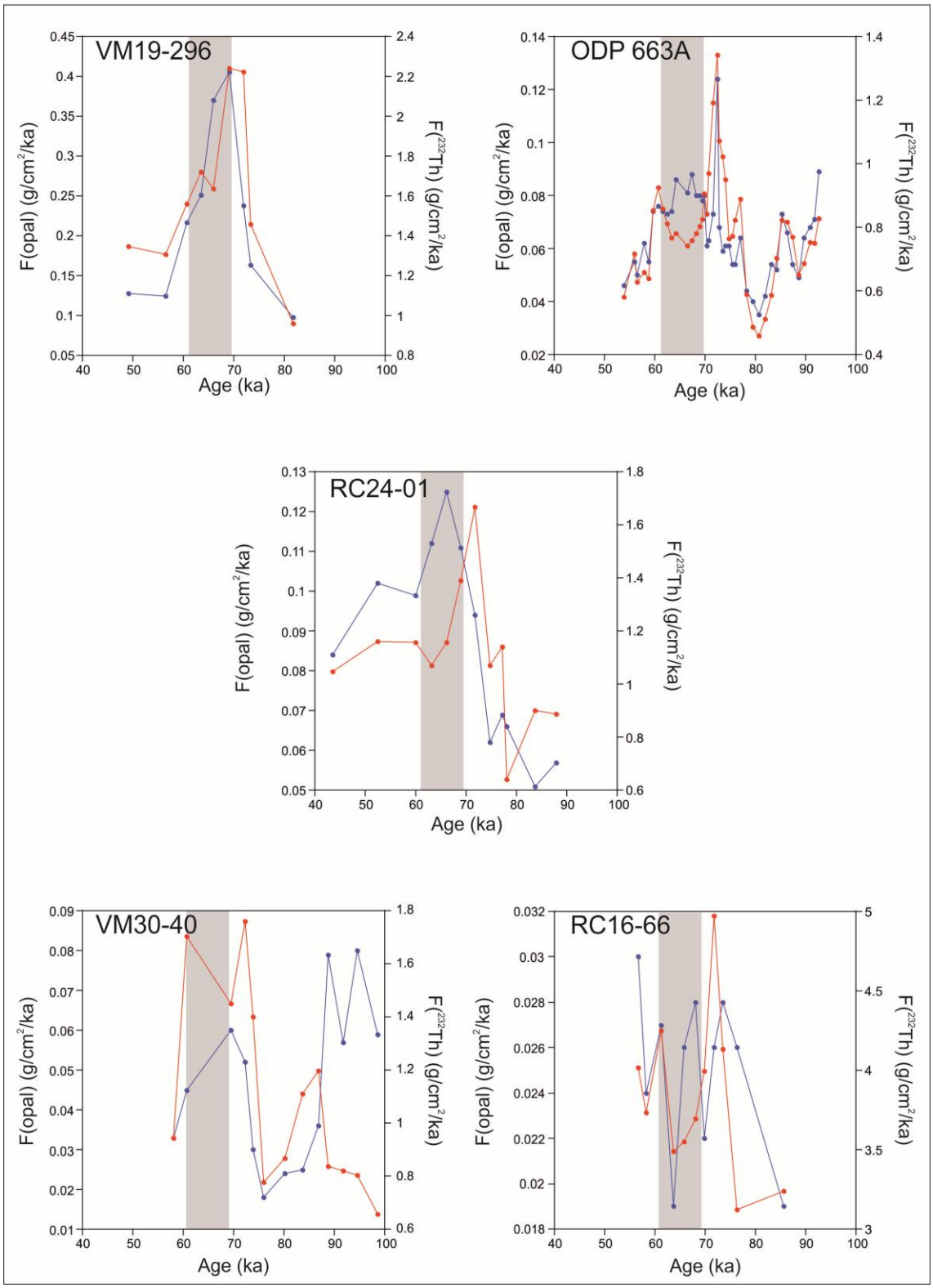

Figure 3.32 – A comparison of the thorium-normalised opal flux plot [F(opal)] (blue curve) to the thorium-normalised flux of ^{232}Th (red curve) , a proxy for terrigenous input [*Brewer et al.*, 1980; *Luo et al.*, 2001; *Pourmand et al.*, 2004]. The data are for all cores used in this study. Cores are arranged E-W (from left to right and top to bottom).

Unfortunately, I was unable to quantify the sedimentary abundance of biomarkers against a known standard, thereby preventing the quantification of absolute changes in brassicasterol or alkenone concentrations. Additionally, both brassicasterol and alkenones may be diagenetically altered [*Zonneveld et al.*, 2010], leading to misinterpretation of the biomarker record. Under conditions of lowered redox potential (for example during episodes of high primary productivity), the preservation of some specific types of lipid is favoured relative to the total organic carbon content of sediment [*Rodger Harvey et al.*, 1995; *Schulte et al.*, 2000], meaning that changes in biomarker ratios must be interpreted cautiously. Therefore, only the peak in brassicasterol:alkenone at ~72 ka is considered robust as it is supported by a range of other proxies.

3.7.6 Comparison to other EEA opal productivity records

The interpretation of the MIS 4 peak in opal accumulation agrees with the interpretation of increases in marine diatom valves in EEA core CAMEL-1 (5°6'25 N, 21°2'36 W, 2658 m water depth) as representing enhanced opal export productivity [*Flores et al.*, 2000]. Similarly, a large increase in the number of *E. rex* fragments in the MIS 4 section of EEA core M16772 (1°21' S, 11°58' W, 3912 m water depth) are attributed to enhanced opal productivity due to an increase in equatorial divergence and upwelling, rather than representing an opal preservation artefact [*Abrantes*, 2001]. The interpretation is also supported by increased levels of sedimentary opal found in sections of other EEA cores corresponding to MIS 4 [*Gardner and Burckle*, 1975; *Stabell*, 1986; *Verardo and McIntyre*, 1994].

3.7.7 Possible sources of dissolved silica to the EEA during MIS 4

Possible sources of silicic acid to the surface waters of the EEA include riverine input [*Abrantes*, 2001], eolian transport of particulate lithogenic silica from continental Africa [*Bowles*, 1975; *Adegbie*, 2001], and upwelled thermocline water of a high-latitude southern origin [*Brzezinski et al.*, 2002]. The aridity of the African continent increased during MIS 4 [*deMenocal et al.*, 1993; *Zhao et al.*, 2003; *Scholz et al.*, 2007], which presumably caused a decrease in riverine discharge to the ocean. This supposition is supported by the measurement of low barium/calcium (Ba/Ca) ratios (a proxy for sea surface salinity/river run-off) in a sediment core adjacent to the mouth of the Niger River [*Weldeab et al.*, 2007]. Additionally, the K/Al ratio (a chemical weathering proxy) in the sediment of a core adjacent to the mouth of the Congo (Zaire) River recorded low chemical weathering rates throughout MIS 4 [*Schneider et al.*, 1997]; also suggesting that input of riverine silica to the ocean was unlikely to have been higher during MIS 4. Furthermore, the occurrence of some opal-rich MIS 4

sediments ~4000 km from West African riverine influence seems to preclude riverine silicic acid supply as a cause of increased opal export throughout the whole of the eastern equatorial Atlantic during MIS 4 (see Figure 3.5) [*Gardner and Burckle*, 1975; *Stabell*, 1986].

Eolian input to the EEA during MIS 4 was higher than in MIS 5a or MIS 3 [*Bowles*, 1975; *Adegbie*, 2001; *Zabel et al.*, 2002; *Abouchami and Zabel*, 2003]. Estimates of silicic acid input to the surface ocean through the dissolution of particulate lithogenic silica range from 0.0 – 6.7 mmol Si m^{-2} yr^{-1} [*Tréguer et al.*, 1995], which is more than sufficient to relieve Si-limitation of diatom productivity in surface waters, when it has been demonstrated that diatoms are able to outcompete a common coccolithophorid (*E. huxleyi*) where silicic acid concentrations are >2 µM [*Egge and Aksnes*, 1992]. In the modern ocean, dust from the Sahara may be deposited over a vast area of the Atlantic, from as far west as the Bahamas [*Ott et al.*, 1991] and French Guyana in northern South America [*Prospero et al.*, 1981].

The path of the northeast trade winds and the Saharan Air Layer (SAL) varies seasonally between 0 - 25°N [*deMenocal et al.*, 1993; *Sultan and Janicot*, 2000], depending on the position of the Intertropical Convergence Zone (ITCZ). The largest amounts of dust transported from Africa by northeast trade winds occur during boreal winter. Winter eolian dust is sourced mainly from the south Saharan and Sahel regions, with the greatest proportion of deposition taking place over the EEA [*Kalu*, 1979; *Prospero et al.*, 1981; *deMenocal et al.*, 1993]. In boreal summer, the ITCZ moves southwards and supplies the Sahel region with monsoon rains, causing a switch in the main African dust sources to the western and central Saharan regions. Under this atmospheric circulation regime, dust is transported by the SAL, also known as the mid-tropospheric African easterly jet stream [*Jaenicke and Schütz*, 1978; *Sarnthein et al.*, 1981]. Alternation of the sources of African dust deposited on the EEA also takes place over G-IG and millennial timescales, and are linked to ice volume and climate of high northern latitudes [*Gasse*, 2000; *Moreno et al.*, 2002; *Abouchami and Zabel*, 2003].

Despite greater eolian deposition onto the EEA during MIS 4, the occurrence of known MIS 4 opal-rich deposits (including *E. rex* oozes) seems to be restricted to an area 5°S - 5°N and 5°E to 25°W (Figure 3.5), which implies that eolian delivery of silica to the surface ocean was not a dominant control on patterns of diatom export productivity, and that upwelling at the equatorial divergence was a more important control. If low-latitude diatom productivity was controlled solely by eolian deposition patterns, then the occurrence of opal-rich MIS 4 sediment would presumably be widespread between the limits of the northeast trade winds and the SAL (0-25°N) [*deMenocal et al.*, 1993; *Sultan and Janicot*, 2000]. However, a record from core

M12392-1 (25°16'N, 16°05'W, 2575 m water depth) shows relatively low opal levels throughout MIS 4 [*Abrantes*, 2000], when compared to the EEA cores from 5°S - 5°N [*Gardner and Burckle*, 1975; *Stabell*, 1986; *Abrantes*, 2001]. Additionally, greater terrigenous input to the EEA during MIS 4 should be recorded in our cores, but does not appear to have been significantly enhanced relative to MIS 5a (Figure 3.24).

Conversely, episodes of enhanced diatom growth recorded on the Bermuda Rise (~33°N) [*Keigwin and Boyle*, 2008; *Gil et al*., 2009; *Lippold et al.*, 2009] may possibly be linked to episodes of enhanced glacial input of Saharan dust to the Bermuda Rise region [*Herwitz et al.*, 1996]. In any case, delivery of eolian Fe may have had an important effect on diatom growth rates in some parts of the EEA during MIS 4, as studies have demonstrated that co-limitation of diatom growth rates by Si and Fe can occur, particularly in the case of large diatoms [*Timmermans et al.*, 2004; *Brzezinski et al.*, 2011], and that contribution of aeolian Fe may have contributed to opal flux increases in the EEA (see Figure 3.30).

Variations in the amount of silicic acid supplied within SAMW/AAIW could potentially have removed Si-limitation on diatoms in the EEA. Silicate and salinity profiles demonstrate that AAIW is present as a layer in the EEA at depths of 800-1000 m [*Schlitzer*, 2000]. In the modern ocean AAIW influences the EEA after flowing eastward from the NBC at 3 - 4°S of the equator and also more weakly at 1 - 2°N [*Suga and Talley*, 1995]. During MIS 4, the silicic acid content and/or the rate of volumetric production of AAIW was possibly increased (see Chapter 5), possibly allowing enhanced upwelling in the EEA [*Jansen et al.*, 1996; *Abrantes*, 2000] to increase the silicic acid concentration in the euphotic zone, and enable diatoms to outcompete coccolithophorids [*Egge and Aksnes*, 1992]. Despite the coincidence of enhancements in upwelling and thermocline silica in the western tropical Atlantic, and enhanced opal flux rates in the EEA, the mechanism for bringing AAIW from depths of 800-1300 metres into the euphotic zone is as yet unknown (see Chapter 5).

3.7.8 Opal ballasting

A variety of modelling and geochemical studies have shown that the export of organic carbon to the deep ocean is dependent on the flux of $CaCO_3$ in the water column, for example [*Klaas and Archer*, 2002; *Barker et al.*, 2003; *Hofmann and Schellnhuber*, 2009], in the effect known as 'ballasting'. Opal is thought to be less important in ballasting than $CaCO_3$ due to its lower density [*Klaas and Archer*, 2002]. In terms of the SALH, the expectation of reduced $CaCO_3$ export and increased opal export in a glacial period would lead to a reduction in $CaCO_3$ ballasting of organic carbon and a subsequent reduction in organic carbon burial in sediment.

These data in fact exhibit the opposite trend in the organic carbon and U_{auth} records (see Section 3.7.3) in the EEA during MIS 4. This suggests that the transfer of particulate organic carbon (POC) to the sediment by diatoms is quite efficient, which may be due to the influence of large diatoms such as *Ethmodiscus rex*, which have a large size [*Villareal et al.*, 1999] and high sinking rate on death [*Smayda*, 1971].

3.7.9 Comparison of opal flux rate changes to the pCO_2 record

The mode and timing of changes in MIS 4 opal accumulation in the EEA suggest a sustained (but probably small) contribution of the SALH to pCO_2 drawdown (Figure 3.31). If the changes in upwelling that occurred in the Atlantic also occurred in the Pacific and Indian basins, then a change in the dominant phytoplankton type from coccolithophorids to diatoms could have occurred. Although opal data spanning the MIS 5/4 transition is sparse, it suggests that this may have been a possibility in the Pacific [*Rea et al.*, 1991], but not in the Indian Ocean [*Borole*, 1993].

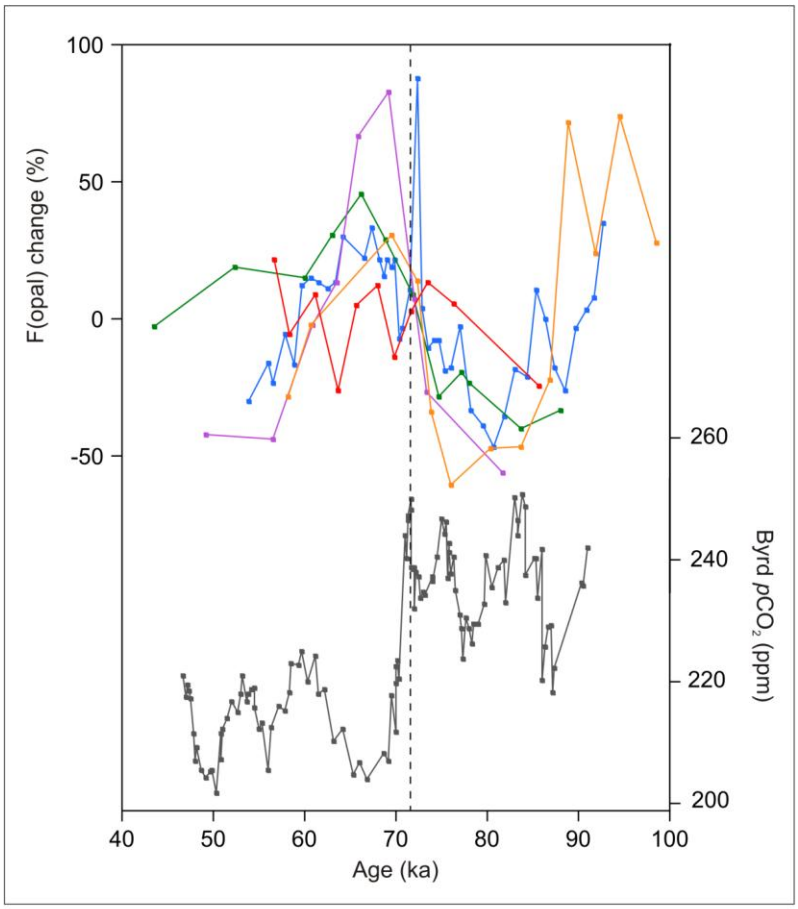

Figure 3.33 – A plot of relative changes in opal flux in all cores, arranged chromatically from west (red) to east (violet). RC16-66 (red), VM30-40 (orange), RC24-01 (green), ODP 663A (blue) and VM19-296 (violet) are plotted relative to their long-term mean opal accumulation (Table 3.1), and are shown on the same axis for comparison. Byrd pCO_2 is plotted beneath using the age control of Ahn and Brook [2008]. The dashed line marks the initiation of the ~ 47 ppm decrease in pCO_2 that occurred ~ 71 ka, at the beginning of MIS 4.

The transient increase in opal flux recorded in ODP 663A ~72ka (but not in other cores) suggests the possibility that changes in local conditions may have allowed brief periods of diatom dominance relative to coccolithophorids, but that these were probably not on a basin-wide scale, and consequently did not impact pCO_2.

Although opal accumulation increased as pCO_2 fell after D-O 19 (in accordance with the SALH), I suggest that changes in opal flux rate occurred in response to glacial conditions, rather than playing a driving role in initiating them (Figure 3.33). Tropical opal accumulation was probably dependent on changes in oceanic circulation and upwelling, which changed in response to cooling at high northern latitudes [*deMenocal et al.*, 1993; *Verardo and McIntyre*, 1994; *Flores et al.*, 2000].

Despite these findings, a SALH scenario could nonetheless have provided an additional feedback that contributed to pCO_2 drawdown during MIS 4. It is more likely that some as-yet undefined combination of other biogeochemical and physical mechanisms, as reviewed by [*Hain et al.*, 2010; *Sigman et al.*, 2010], contributed more greatly to the ~47 ppmv pCO_2 drop observed across the MIS 5/4 transition [*Ahn and Brook*, 2008].

3.8 Conclusions

Increases in biogenic opal recorded in eastern equatorial Atlantic cores during MIS 4 appear to be the result of enhanced diatom productivity, rather than enhanced diatom preservation, based on correlation of thorium-normalised opal accumulation rates with a range of other palaeoproductivity proxies. This study suggests that the SALH is a plausible mechanism to explain at least part of the 47 ppmv pCO_2 drawdown that occurred during MIS 4 ~71-56 ka, probably through feedback processes that came into operation after the initial pCO_2 decrease at ~71 ka [*Ahn and Brook*, 2008]. Despite this finding, it does not necessarily follow that diatoms were able to outcompete $CaCO_3$-producers in the equatorial Atlantic throughout MIS 4, as predicted by the SALH (see Chapter 4).

It is important to bear in mind when analysing palaeoproductivity changes across large areas of ocean that proxy records may reflect local rather than basin-wide changes. In the case of this investigation, broad increases in opal flux are a common feature of three cores from the eastern equatorial Atlantic: VM19-296, ODP 663A and RC24-01. At the outset of this investigation, it was hoped that by comparing changes in the $_{xs}(^{231}Pa/^{230}Th)_0$ ratio to the opal flux record, it could confirm the opal flux changes as being productivity based [*Bradtmiller et al*., 2006, 2007]. A combination of changes in overall sedimentation rate, decreases in $CaCO_3$ export and a probable reorganisation of oceanic circulation in the Atlantic at the MIS 5a/4

boundary [*Piotrowski et al*., 2005; *Guihou et al*., 2010], complicates the use of $_{xs}(^{231}Pa/^{230}Th)_0$ as a palaeoproductivity proxy in this instance.

In order to confirm that the opal flux increases seen in all cores (except RC16-66) reflected increased opal productivity (over increased opal preservation), measurements of authigenic uranium (U_{auth}), total organic carbon (TOC) and total nitrogen (TN) were made. In all the eastern cores (VM19-296, ODP 663A and RC24-01), maximum levels of U_{auth} broadly correspond to maximum opal fluxes. In general, TOC and TN profiles in the cores did not correlate to U_{auth}, but as TOC and TN are subject to different controls this was not unexpected. The TOC and TN records in ODP 663A and RC24-01 support enhanced productivity during MIS 4. In VM19-296 increased productivity during MIS 4 is supported by the TN record but not the TOC record.

As discussed in Section 3.7.3, U_{auth} signals in sediment may be influenced by both sedimentation rate and bottom water oxygenation/organic matter flux. In ODP 663A, both of these factors may have influenced U_{auth}, but the broad agreement in U_{auth} trends across the eastern equatorial Atlantic (VM19-296, ODP 663A and RC24-01) suggest that changes in opal accumulation were productivity-driven, at least in the eastern part of the Atlantic basin.

A key point of the SALH is that diatom productivity was limited predominantly by the availability of silicic acid, and assumes that other limiting nutrients (N, P, Fe) were all present in non-limiting concentrations. It is suggested that the glacial inventory of N was increased by around 25% during glacial periods [*Altabet et al*., 1995; *Ganeshram et al*., 1995], which implies that N was not limiting on low-latitude productivity. Similarly, aeolian deposition of iron was likely higher during glacial periods, leading to the expectation that Fe was also not limiting [*Bowles*, 1975; *Adegbie*, 2001; *Zabel et al*., 2002; *Abouchami and Zabel*, 2003]. It is possible that low latitude productivity was not limited by Fe, Si or N; but may instead have been limited by P availability [*Pichevin et al*., 2009].

The SALH also assumes that a mechanism existed that would bring silicic acid from the depths at which AAIW dominates (~800-1000 m), into the euphotic zone (<200 m), which is unknown at present. Furthermore, the mean position of the ITCZ in the Atlantic is linked to high northern latitude climate changes on glacial-interglacial timescales [*Chiang et al*., 2003]. During MIS 4, it is likely that the mean position of the ITCZ was further south than during MIS 5a, which may have had an important bearing on productivity changes through its effect on wind strength and direction (and therefore upwelling), and regional sea-surface temperatures (SSTs). All of these factors complicate the characterisation of regional productivity changes in the equatorial Atlantic during MIS 4.

In general, the data support an enhancement of low latitude productivity during MIS 4, which may have had a significant effect on pCO_2 (see Chapter 6) without necessarily meeting all the conditions imposed by the SALH.

Chapter 4 - Decreased $CaCO_3$ burial in the eastern equatorial Atlantic during Marine Isotope Stage 4: productivity decrease or dissolution increase?

4.1 Introduction

4.1.1 Background

This Chapter examines the effect that a SALH scenario may have had on low latitude coccolithophorid export productivity of calcium carbonate ($CaCO_3$). Coccolithophorids tend to dominate $CaCO_3$ productivity in the modern low latitude ocean [*Thurman and Trujillo*, 2002] (Figure 4.1). A central theme of the SALH is its prediction that coccolithophorids would be replaced by diatoms if sufficient silicic acid became available in the surface waters of the low latitude oceans, which are silica-poor in the modern ocean [*Nelson et al.*, 1995].

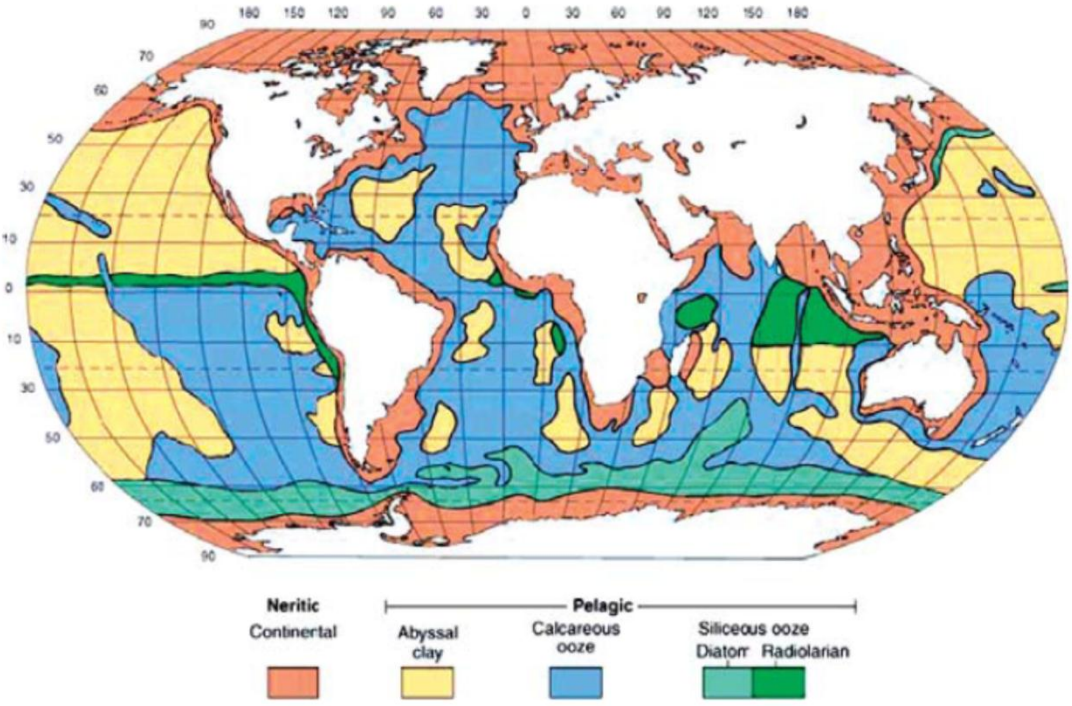

Figure 4.1 – Map of the major types of sediment across the modern ocean floor. The low latitude Atlantic is dominated by calcareous ($CaCO_3$) ooze, produced mainly by coccolithophorids [*Jin et al.*, 2006]. Reproduced from Thurman and Trujillo [2002].

In the open ocean, $CaCO_3$ production is almost exclusively biogenic [*Sarmiento and Gruber*, 2006]. Globally, coccolithophores are the major calcifiers (producers of $CaCO_3$) in the world ocean [*Jin et al.*, 2006] (see equation 4.1), and as such their rate of productivity has an important bearing on the global export ratio of $CaCO_3$ to organic carbon (C_{org}), which is estimated at ~0.1 [*Sarmiento et al.*, 2002]. Because the production of $CaCO_3$ removes alkalinity from the surface ocean, a decrease in coccolithophorid productivity would lead to less $CaCO_3$ being exported from the surface to the deep ocean, and an increase in surface ocean alkalinity. This would then result

in CO_2 being drawn down out of the atmosphere into the ocean to compensate for changes in surface- and whole- ocean alkalinity [*Sigman and Boyle*, 2000] (see Chapter 1.4).

Equation 4.1

$$Ca^{2+} + 2HCO_3^- \leftrightarrow CaCO_3 + H_2O + CO_2$$

If a SALH scenario occurred during MIS 4 where coccolithophorids were partly or completely replaced as the dominant phytoplankton in the low latitude Atlantic, it should be manifest as a decrease in the record of accumulated sedimentary $CaCO_3$ record during MIS 4. Therefore the thorium-normalised accumulation rate of sedimentary $CaCO_3$ was measured in a suite of cores from the low latitude Atlantic (see Section 3.5 for information on core location and age control), to test this prediction of the SALH.

4.1.2 Approach to reconstructing changes in $CaCO_3$ accumulation in the EEA during the MIS 5a-4 transition

The previous chapter (Chapter 3) concluded that opal accumulation rates in three cores (VM19-296, ODP 663A and RC24-01) from the eastern equatorial Atlantic (EEA) were higher in MIS 4 than in MIS 5a, and that this was a result of enhanced diatom productivity in the surface ocean, in agreement with the SALH. However, this finding alone does not constitute an adequate confirmation of a SALH scenario occurring during MIS 4, as the importance of the mechanism is its ability to have an impact on global $CaCO_3$:C_{org} (and hence pCO_2), rather than any change in the absolute abundance of diatoms [*Matsumoto and Sarmiento*, 2008].

Within deep marine sediments the mineral calcite (the most stable polymorph of $CaCO_3$) is almost exclusively of biogenic origin [*Sarmiento and Gruber*, 2006], and contributes significantly to most open-ocean sediments, with about 13% of the $CaCO_3$ produced in the surface ocean exported to the deep ocean and buried each year [*Milliman and Droxler*, 1996; *Lee*, 2001; *Iglesias-Rodriguez et al.*, 2002]. This is contrasted with the relatively low efficiency with which organic matter is exported, with only ~ 0.3 % of an estimated 53 ± 8 Pg C yr^{-1} of organic matter produced in surface waters being buried in sediment [*Behrenfeld and Falkowski*, 1997; *Carr*, 2001; *Marra et al.*, 2003; *Dunne et al.*, 2007]. The relatively high burial rate of $CaCO_3$ represents an important sink of carbonate alkalinity from the surface ocean, and imbalances between the rate of $CaCO_3$ burial and the input of alkalinity by rivers can, over timescales of hundreds to thousands of years, affect pCO_2 [*Broecker and Peng*, 1987; *Sigman and Boyle*, 2000; *Sarmiento and Gruber*, 2006] (see Chapter 1.4).

The aim of this chapter is to measure the accumulation of sedimentary $CaCO_3$ in the same suite of cores examined in Chapter 3 (see Figure 4.2). The accumulation of $CaCO_3$ in oceanic sediment is a function of (1) the production rate of $CaCO_3$ by calcareous microfossils in the euphotic zone, and (2) the rate of $CaCO_3$ dissolution in the deep ocean [*Sarmiento and Gruber*, 2006]. The rate of $CaCO_3$ dissolution is itself a function, firstly, of the saturation state of deep sea water with respect to carbonate (ΔCO_3^{2-}) [*Keir*, 1980; *Archer*, 1991; *Hales and Emerson*, 1997]. Secondly, the rate of $CaCO_3$ dissolution depends on the flux of organic matter to the sediment, as bacterial remineralisation of organic matter (OM) within sedimentary pores produces CO_2 that can dissolve some $CaCO_3$ (up to ~20-40 %) above the lysocline. Where this occurs it is termed supralysoclinal dissolution [*Emerson and Bender*, 1981; *Archer*, 1991; *Hales*, 2003; *Barker*, 2006].

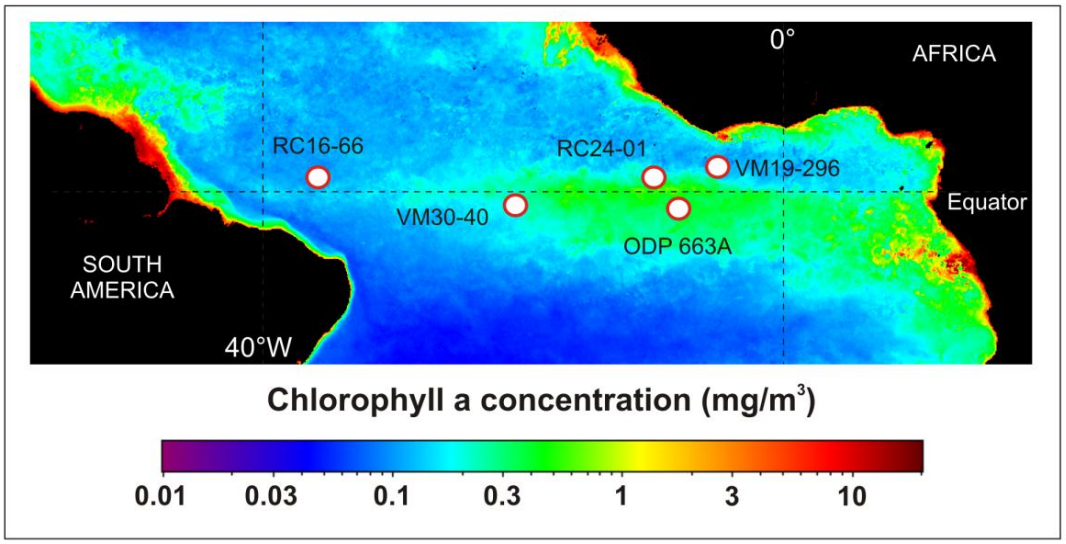

Figure 4.2 - Plot of core locations used in this study over Aqua MODIS chlorophyll a concentration (mg/m^3). Chlorophyll data is the annual composite SeaWiFS data for the year 2007, sourced from http://oceancolor.gsfc.nasa.gov

The effect of sediment focusing/winnowing on $CaCO_3$ accumulation is accounted for in this study by normalising the sedimentary $CaCO_3$ content in samples to the measured ^{230}Th particle flux rate [*Bacon*, 1984; *Francois et al.*, 1990; *Francois et al.*, 2004]. Using the same approach as that used to examine changes in opal flux (see Chapter 3), each measured $CaCO_3$ accumulation rate [$F(CaCO_3)$] will be normalised to the long-term mean in that core and presented as a percentage deviation from the mean in order to examine relative changes. Uncertainty in thorium-normalised flux estimates was calculated by using Equation 4.2:

Equation 4.2

$$\Delta z = Z \times [(\Delta x/X)^2+(\Delta y/Y)^2]^{1/2}$$

The relative change in $CaCO_3$ accumulation/burial between MIS 5a to MIS 4 will then be estimated for the whole equatorial Atlantic (EEA) region (0° - 40° W and 5° N - 5° S, area 4.95 x 10^6 km^2) after [*Bradtmiller et al.*, 2007]. I also examine $CaCO_3$ accumulation changes in the eastern equatorial Atlantic, where opal flux records indicate that major changes in phytoplankton composition occurred (see Chapter 3).

The eastern equatorial Atlantic region was defined as the area (0° - 15° W and 5° N - 5° S, area 1.855 x 10^6 km^2). Sedimentary $CaCO_3$ content was measured using coulometry (see Chapter 2.1), and the level of $CaCO_3$ dissolution was examined qualitatively using a foraminiferal fragmentation index, after Curry and Lohmann [1986] and Le and Shackleton [1992].

4.1.3 Changes in sedimentary $CaCO_3$ in the equatorial Atlantic during MIS 4

When attempting to identify G-IG changes in $CaCO_3$ productivity it is important to carefully consider other causes of G-IG $CaCO_3$ variation. A number of palaeoceanographic studies record a widespread $CaCO_3$ minimum in the EEA [*Curry and Lohmann*, 1986; *Verardo and McIntyre*, 1994] (see Figure 4.3), the west Atlantic [*Broecker and Clark*, 2001], and the North Atlantic [*Crowley*, 1983] during MIS 4 (~70-59 ka) [*Martinson et al.*, 1987], which has been attributed to the northward expansion of glacial Antarctic Bottom Water (AABW) with a low carbonate ion [CO_3^{2-}] concentration [*Verardo and McIntyre*, 1994; *Broecker and Clark*, 2001; *Broecker and Clark*, 2003; *Govin et al.*, 2009]. AABW has been defined in the modern ocean as all volumes of water formed to the south of the Antarctic Circumpolar Current (ACC), with neutral densities greater than 27.28 kg m^{-3}, which are not detected at the Drake Passage Sill [*Orsi et al.*, 1999].

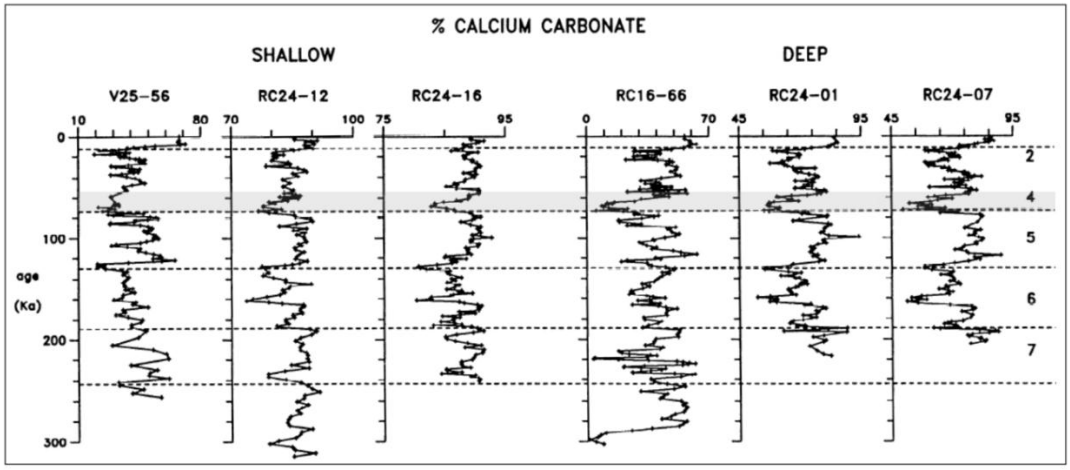

Figure 4.3 – Plot of % $CaCO_3$ from a suite of cores spanning the equatorial Atlantic for the past 300 ka. MIS 4 (highlighted by a grey band) shows minima in $CaCO_3$ during MIS 4 across the whole equatorial Atlantic. The cores are taken from depths between 3486 – 4424 m water depth. Plot reproduced from Verardo and McIntyre [1994].

On average, the AABW formed in the south western Weddell Sea that influences the Atlantic sector of the SO is colder and less saline than its counterparts in the other basins with θ < -1°C and S <34.64 psu [*Orsi et al.*, 1999]. Due to its low temperature, AABW is dense compared to other water masses, and sinks beneath them to occupy some of the deepest parts of the Atlantic [*Broecker*, 1991; *Schlitzer*, 2000].

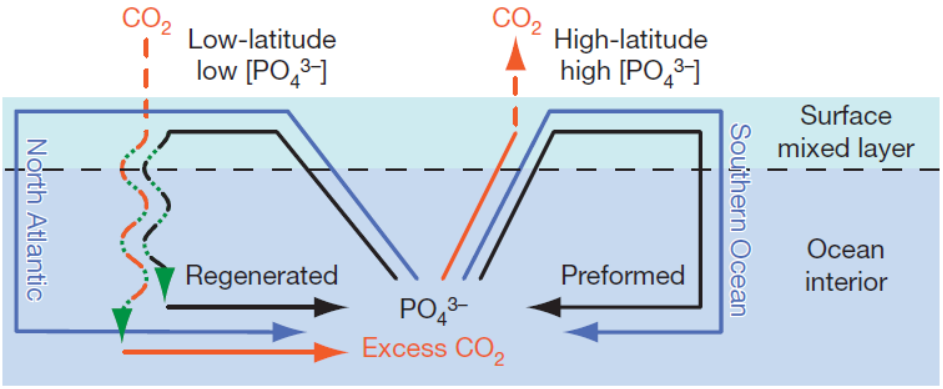

Figure 4.4 – Schematic representation of the oceans biological pump, illustrating the production and regeneration of nutrients and ΣCO_2. Reproduced from Sigman et al. [2010].

The water that sinks in the subantarctic zone to form AABW is nutrient-rich, and also initially CO_2-rich through regeneration of sinking biogenic particles in the oceans interior, although it releases some of its sequestered CO_2 to the atmosphere at high southern latitudes [*Sigman et al.*, 2010]. Because the biological pump in the subantarctic zone is inefficient (possibly due to Fe-limitation), the preformed nutrient content of the sinking water remains high, while the ΣCO_2 content is lowered through CO_2 loss to the atmosphere. This leads to the formation of AABW with low [CO_3^{2-}], which is undersaturated with respect to $CaCO_3$ [*Sigman et al.*, 2010] (Figure 4.4).

4.2 Results

4.2.1 ODP 663A

The %$CaCO_3$ record of ODP 663A (red curve b in Figure 4.5) reveals maxima over 80% in sedimentary $CaCO_3$ levels during MIS 5c (~91-87 ka), MIS 5a (~83-80 ka) and MIS 3 (warm D-O 14 ~53-51 ka). Minimum values of 60-65% are recorded during cold D-O 19 (~72 ka) and during MIS 4 (~65 ka).

The thorium-normalised $CaCO_3$ accumulation rate [F($CaCO_3$)] record of ODP 663A (blue curve c in Figure 4.5) show the highest $CaCO_3$ accumulation rate (~ 1.75 g/cm^2/ka) during MIS 5c, ~ 90 ka, and a prominent decrease of ~ 1 g/cm^2/ka from MIS 5c to MIS 5b (~87-85 ka).

Values of $CaCO_3$ accumulation during MIS 5a (~ 83-77 ka) are variable but average ~ 1.25 g/cm^2/ka. $CaCO_3$ accumulation decreases to a minimum during MIS 4 (~ 67 ka), but the trend is a gradual decrease beginning ~ 78 ka, probably during cold D-O 20. Decreasing $CaCO_3$ accumulation across the MIS 5/4 transition is in general agreement with the SALH, but no rapid changes are recorded ~71-69 ka, as might be expected if changes in $CaCO_3$ production in the surface ocean were influencing the pCO_2 record [*Ahn and Brook*, 2008].

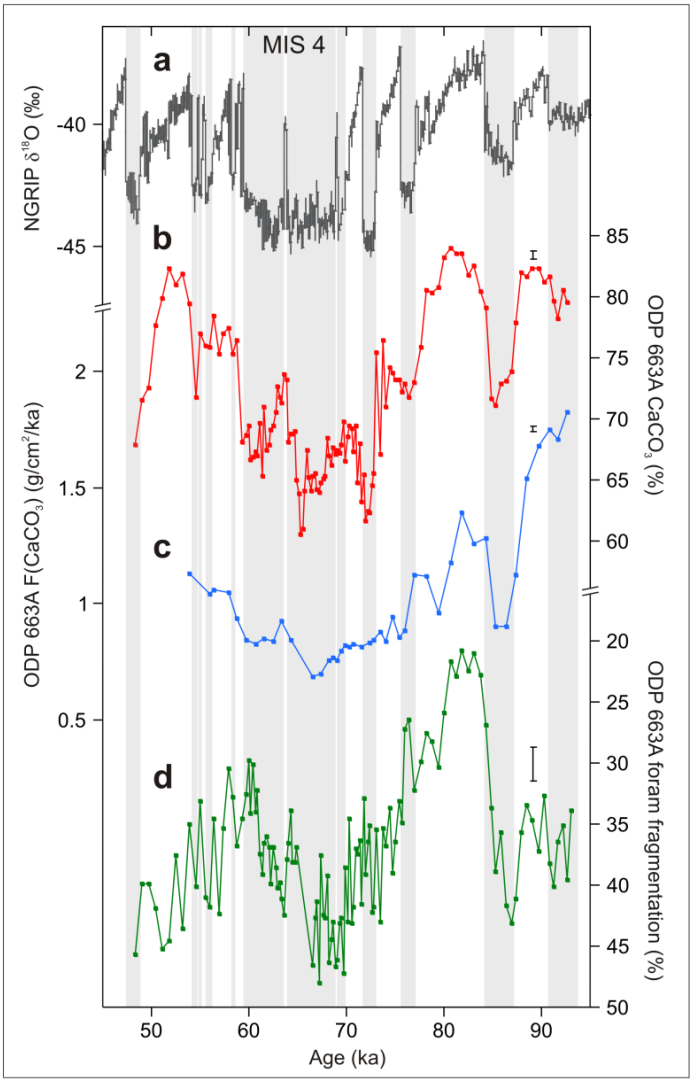

Figure 4.5 – a) NGRIP $\delta^{18}O$ (‰), grey; b) ODP 663A %$CaCO_3$, red; c) ODP 663A F($CaCO_3$) (g/cm^2/ka), blue; d) Foraminiferal fragmentation index (%), green. Accuracy on $CaCO_3$ measurements is -1.32 %, and precision is 0.39 (1σ) (see Section 2.1). Absolute errors in F($CaCO_3$) are 0.003-0.009 g/cm^2/ka in ODP 663A. Precision on foraminiferal fragmentation repeat counts is 6.35% (see Chapter 2.4). All error bars shown represent maximum error estimate. Cold periods in the NGRIP $\delta^{18}O$ record are marked by grey bands, and MIS 4 is labelled. See Section 3.5 for details of core age models.

The record of foraminiferal fragmentation in ODP 663A (green curve d in Figure 4.5) shows a minimum of ~20 % fragmentation during MIS 5a (~ 83-80 ka), indicating that $CaCO_3$ was best preserved at the ODP 663A core site (1°11.87'S, 11°52.71'W,

3708 m water depth) during this interval. From ~80 ka the degree of foraminiferal fragmentation increased to ~48 % ($CaCO_3$ preservation decreased) between ~70-67 ka, during MIS 4. Values of fragmentation decrease again to ~30 % at the beginning of MIS 3 (~ 60 ka).

4.2.2 VM19-296

The %$CaCO_3$ record of VM19-296 (red curve b in Figure 4.6) shows maximum values of ~55 % during MIS 5a (~ 80 ka), decreasing to 0 % during cold D-O 19 (~ 71 ka) and remaining there until ~64 ka and an increase in %$CaCO_3$, probably associated with D-O 18 at ~63 ka. Values of %$CaCO_3$ begin to increase and reach a maximum of ~40 % during warm D-O 14 (~51 ka) (MIS 3).

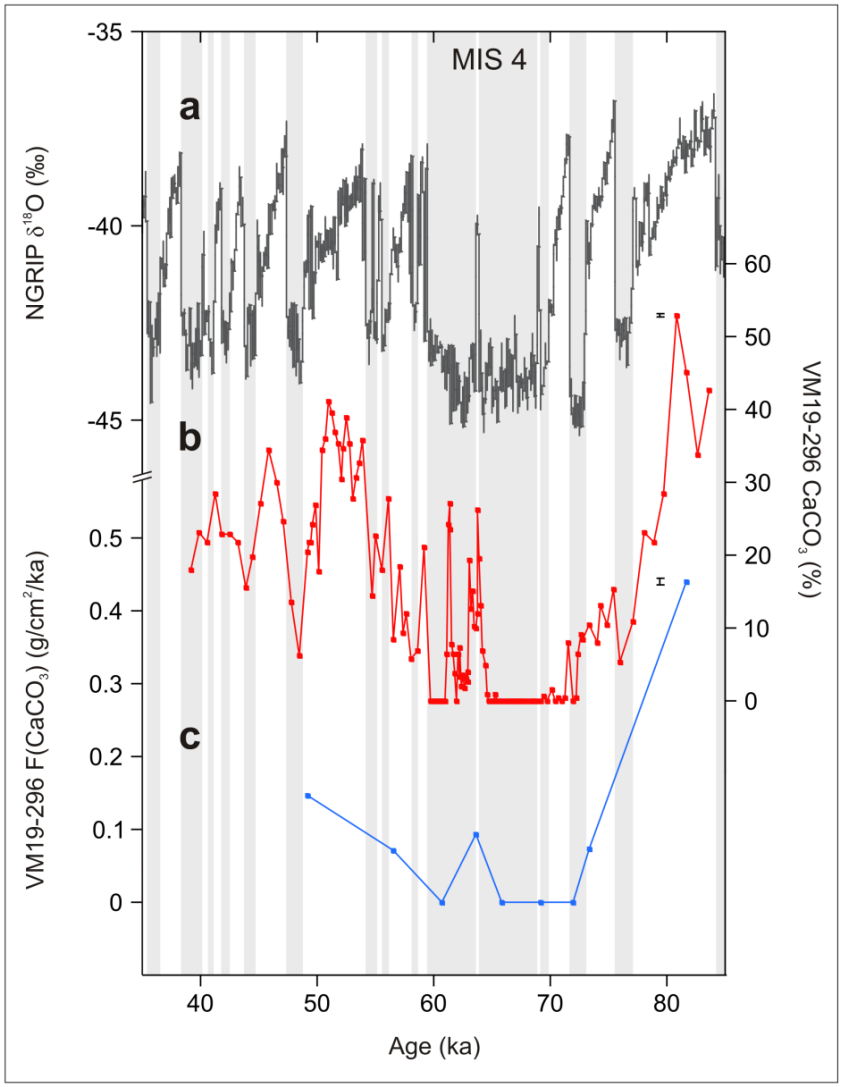

Figure 4.6 - a) NGRIP $\delta^{18}O$ (‰) (grey); b) VM19-296 %$CaCO_3$ (red); c) VM19-296 F($CaCO_3$) (g/cm^2/ka) (blue). Accuracy on $CaCO_3$ measurements is -1.32 %, and precision is 0.39 (1σ) (see Chapter 2.1). Absolute errors in F($CaCO_3$) are 0.0007-0.0028 g/cm^2/ka in VM19-296 (see Chapter 2.1). All error bars shown represent maximum error estimate. Cold periods in the NGRIP $\delta^{18}O$ record are marked by grey bands, and MIS 4 is labelled. See Chapter 3.5 for details of core age models.

The record of $CaCO_3$ accumulation rate (blue curve c in Figure 4.6) follows that of the $\%CaCO_3$ record, with maximum values of ~0.45 g/cm^2/ka MIS 5a (~ 80 ka), decreasing to 0 g/cm^2/ka between ~71 and 67 ka, with a modest increase of 0.1 g/cm^2/ka recorded during D-O 18 (~63 ka) and an MIS 3 maximum in $CaCO_3$ accumulation occurring ~ 49 ka.

4.2.3 RC24-01

The $\%CaCO_3$ record of RC24-01 (red curve b Figure 4.7) follows the general pattern of those from ODP 663A and VM19-296. The highest $\%CaCO_3$ values (~80 %, similar to ODP 663A) are recorded during MIS 5a between ~83 and 79 ka; with a 15 % decrease occurring ~79 ka, and another decrease of 20 % occurring ~73 ka to reach near-minimum values during cold D-O 19. Values of $\%CaCO_3$ remain between 50 and 60 % during MIS 4, before increasing at the onset of MIS 3 (~60 ka) to reach maximum MIS 3 values of ~67 % at ~57 ka.

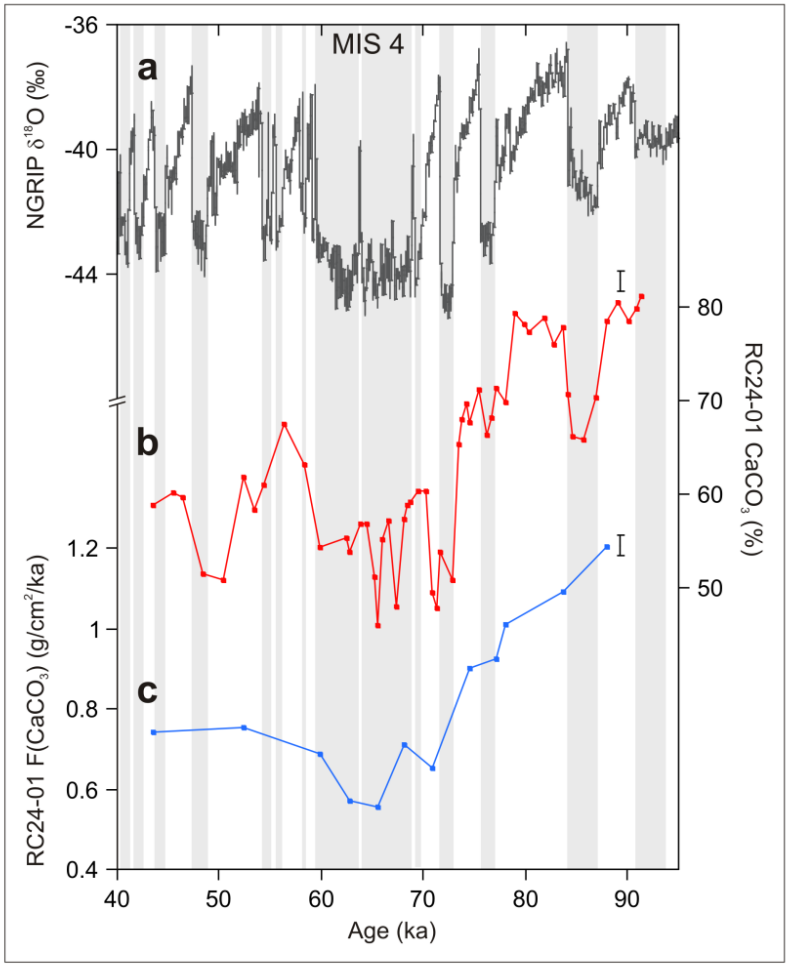

Figure 4.7 - a) NGRIP $\delta^{18}O$ (‰) (grey); b) RC24-01 $\%CaCO_3$ (red); c) RC24-01 $F(CaCO_3)$ (g/cm^2/ka) (blue). Accuracy on $CaCO_3$ measurements is -1.32 %, and precision is 0.39 (1σ) (see Chapter 2.1). Absolute errors in $F(CaCO_3)$ are 0.017-0.038 g/cm^2/ka in RC24-01 (see Chapter 2). All error bars shown represent maximum error estimate. Cold periods in the NGRIP $\delta^{18}O$ record are marked by grey bands, and MIS 4 is labelled. See Chapter 3.5 for details of core age models.

The $CaCO_3$ accumulation rate of RC24-01 (blue curve c in Figure 4.7) exhibits steadily decreasing values from a maximum of 1.2 g/cm^2/ka during MIS 5c (~88 ka) to a minimum of 0.6 g/cm^2/ka during MIS 4 (~65 ka). From this point, values increase to 0.7-0.8 g/cm^2/ka during MIS 3.

4.2.4 VM30-40

The %$CaCO_3$ record of VM30-40 (red curve b in Figure 4.8) shows maximum values of ~80-90% from the beginning of the record at ~99 ka through MIS 5c, 5b and 5a (~99-88 ka). The %$CaCO_3$ of the sediment declines sharply to minimum values of ~65 % during MIS 5b (~87-84 ka) and cold D-O 19 (~ 72 ka). Values of %$CaCO_3$ remain between 65 and 75 % throughout MIS 4.

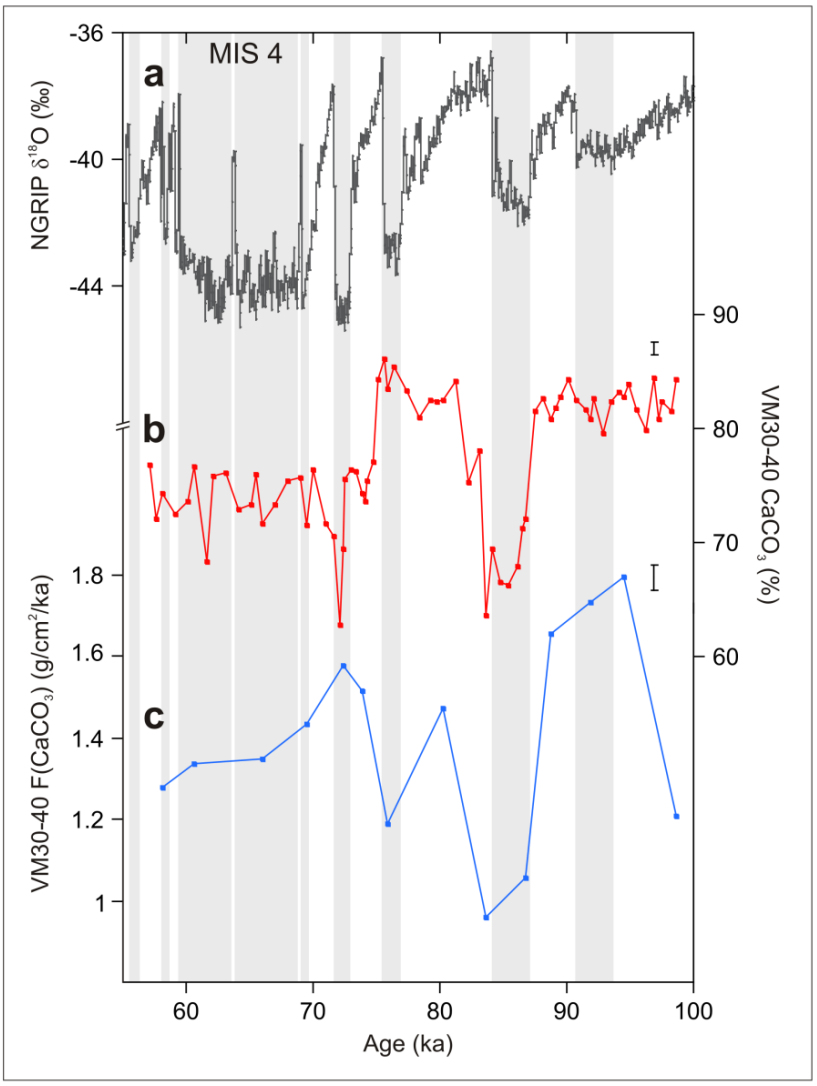

Figure 4.8 - a) NGRIP $\delta^{18}O$ (‰)(grey); b) VM30-40 %$CaCO_3$ (red); c) VM30-40 F($CaCO_3$) (g/cm^2/ka) (blue). Accuracy on $CaCO_3$ measurements is -1.32 %, and precision is 0.39 (1σ) (see Chapter 2.1). Absolute errors in F($CaCO_3$) are 0.02-0.05 g/cm^2/ka in VM30-40 (see Chapter 2). All error bars shown represent maximum error estimate. Cold periods in the NGRIP $\delta^{18}O$ record are marked by grey bands, and MIS 4 is labelled. See Chapter 3.5 for details of core age models.

The $CaCO_3$ accumulation rate of VM30-40 (blue curve c in Figure 4.8) reveals maximum values of ~1.8 g/cm^2/ka near the beginning of the record (~ 95 ka), decreasing to a minimum value of ~1 g/cm^2/ka at ~ 83 ka, probably during MIS 5b. Values of $CaCO_3$ accumulation decrease from ~1.6 g/cm^2/ka during cold D-O 19 (~72 ka) to ~1.3 g/cm^2/ka during MIS 4 (~60 ka).

4.2.5 RC16-66

The %$CaCO_3$ record of RC16-66 (Figure 4.9) shows maximum values (35-40 %) during MIS 5c (~91-87 ka), MIS 5a (~83-77 ka) and MIS 3 (~57 ka, warm D-O 17). Warm D-O 19 and 20 record lower %$CaCO_3$ (15-30 %). MIS 4 records a minimum of ~10 % $CaCO_3$ at ~67 ka, similar to that recorded in cold D-O 19 (~72 ka).

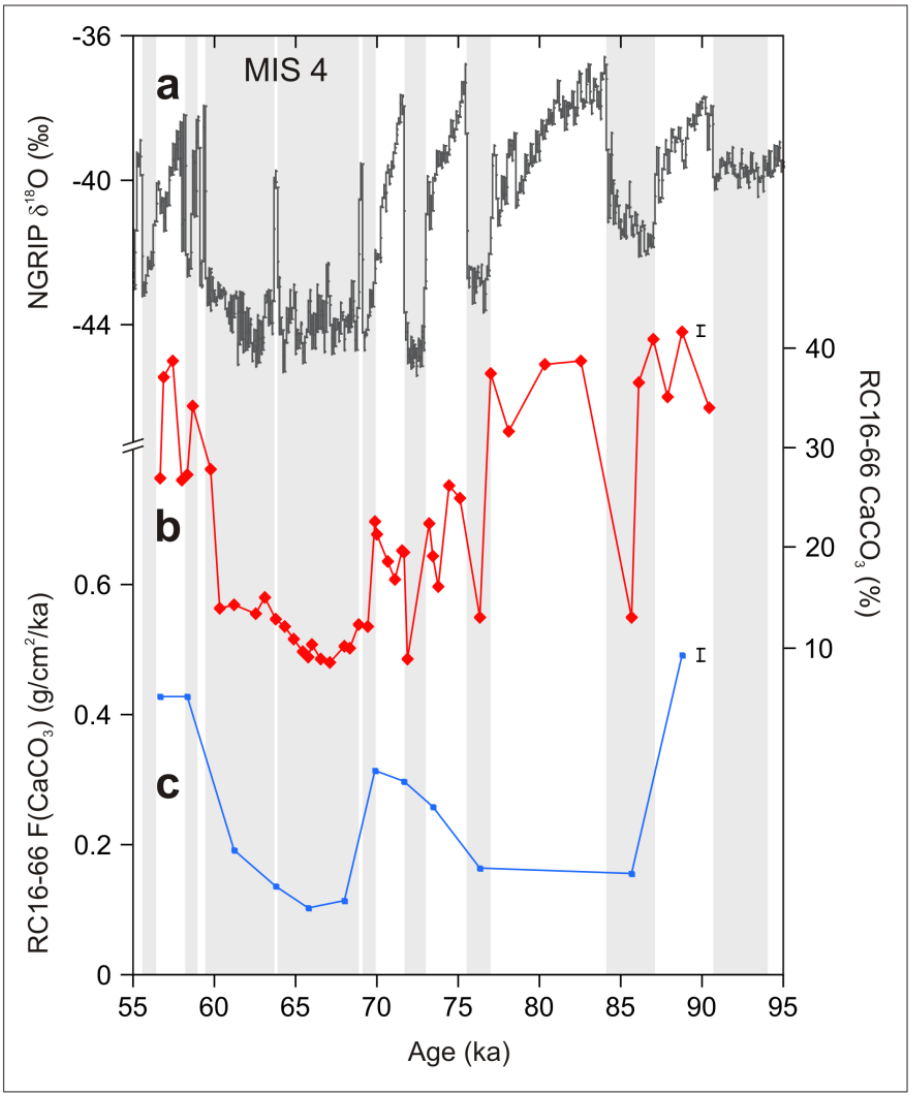

Figure 4.9 - a) NGRIP $\delta^{18}O$ (‰) (grey); b) RC16-66 %$CaCO_3$ (red); c) RC16-66 F($CaCO_3$) (g/cm^2/ka) (blue). Accuracy on $CaCO_3$ measurements is -1.32 %, and precision is 0.39 (1σ) (see Chapter 2.1). Absolute errors in F($CaCO_3$) are 0.001-0.008 g/cm^2/ka in RC16-66. All error bars shown represent maximum error estimate. Cold periods in the NGRIP $\delta^{18}O$ record are marked by grey bands, and MIS 4 is labelled. See Chapter 3.5 for details of core age models.

The $CaCO_3$ accumulation rate of RC16-66 (blue curve c in Figure 4.9) records a maximum 0.5 g/cm^2/ka during MIS 5c (~89 ka), with ~0.4 g/cm^2/ka recorded during early MIS 3. Values of $CaCO_3$ accumulation decrease from 0.3 g/cm^2/ka during warm D-O 19 (~70 ka) to a minimum of ~0.1 g/cm^2/ka during MIS 4 (~66 ka).

4.2.6 General patterns of $CaCO_3$ accumulation in the equatorial Atlantic during the MIS 5/4 transition

Results from cores across the equatorial Atlantic show a clear minimum in $CaCO_3$ accumulation during MIS 4. In all cores apart from VM30-40 the maximum $CaCO_3$ accumulation occurs within MIS 5, and slowly decreases to reach minimum values during MIS 4 (Figure 4.10). Absolute values of $CaCO_3$ accumulation rate depend strongly on the water column depth overlying the cores, with higher rates recorded in shallower cores (ODP 663A, RC24-01 and VM30-40), and lower values recorded in deeper cores (RC16-66 and VM19-296). ODP 663A and RC24-01 share a similar pattern of F($CaCO_3$) decrease throughout the MIS 5a/4 transition; with F($CaCO_3$) decreasing from ~1.4 g/cm^2/ka to ~0.7 g/cm^2/ka in ODP 663A; and from ~1.1 g/cm^2/ka to ~0.6 g/cm^2/ka in RC24-01.

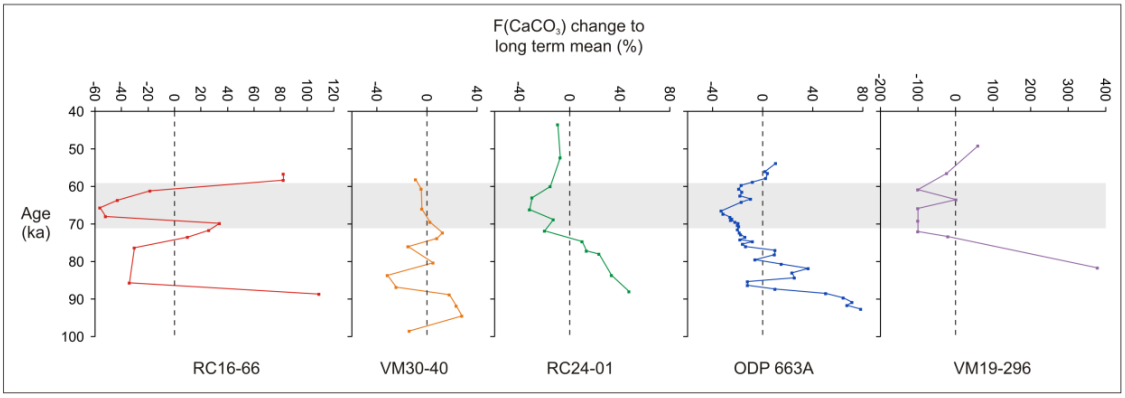

Figure 4.10 – A comparison of F($CaCO_3$) in all cores, normalised to the long term mean value of F($CaCO_3$) in each core (see Table 4.1). RC16-66, VM30-40, RC24-01 and ODP 663A are plotted on the same y-axis. VM19-296 is plotted on a separate y-axis, as percent changes in F($CaCO_3$) were disproportionately large in VM19-296 when values of F($CaCO_3$) fell to 0 during MIS 4. The cores are arranged chromatically from west (red) to east (violet). The dashed line represents the long-term average (see Table 4.1). The shaded grey bar represents MIS 4, from the NGRIP $\delta^{18}O$ record.

The third core from the EEA, VM19-296, shows a F($CaCO_3$) decrease from ~0.4 g/cm^2/ka in MIS 5a to 0 g/cm^2/ka in MIS 4. Unlike the increase in F(opal) (see Chapter 3), the MIS 4 $CaCO_3$ minima are not restricted to the EEA. In VM30-40, an F($CaCO_3$) minimum of ~1 g/cm^2/ka occurs during MIS 5b (~85 ka), which is greater than that which occurs in MIS 4 (~ 1.3 g/cm^2/ka). The F($CaCO_3$) in VM30-40 shows

greater variability in MIS 5c to 5a than in the other cores. Nonetheless, VM30-40 still records an F($CaCO_3$) decrease of ~0.3 g/cm^2/ka across the MIS 5/4 transition.

The foraminiferal fragmentation index (Figure 4.5) shows minimal levels of fragmentation (~20 %) in ODP 663A during MIS 5a, and maximum levels of fragmentation (~45 %) in MIS 4. The fragmentation record indicates that the greatest extent of $CaCO_3$ dissolution occurred during MIS 4, which is consistent with other research on $CaCO_3$ dissolution in the EEA during MIS 4 [*Curry and Lohmann*, 1986; *Verardo and McIntyre*, 1994], and the North Atlantic [*Crowley*, 1983].

Table 4.1 – Long term mean $CaCO_3$ accumulation rates for all EEA cores, arranged from west (left) to east (right).

CORE	RC16-66	VM30-40	RC24-01	ODP 663A	VM19-296
Water depth (m)	4424	3706	3837	3708	5017
Mean F($CaCO_3$) (g/cm^2/ka)	0.235	1.401	0.818	1.022	0.092
Mean uncertainty	0.005	0.012	0.028	0.005	0.00094

A comparison of the relative changes in $CaCO_3$ accumulation across the equatorial Atlantic (normalised to the long-term mean value) is shown in Figure 4.10 with long-term mean $CaCO_3$ accumulation rates shown in Table 4.1.

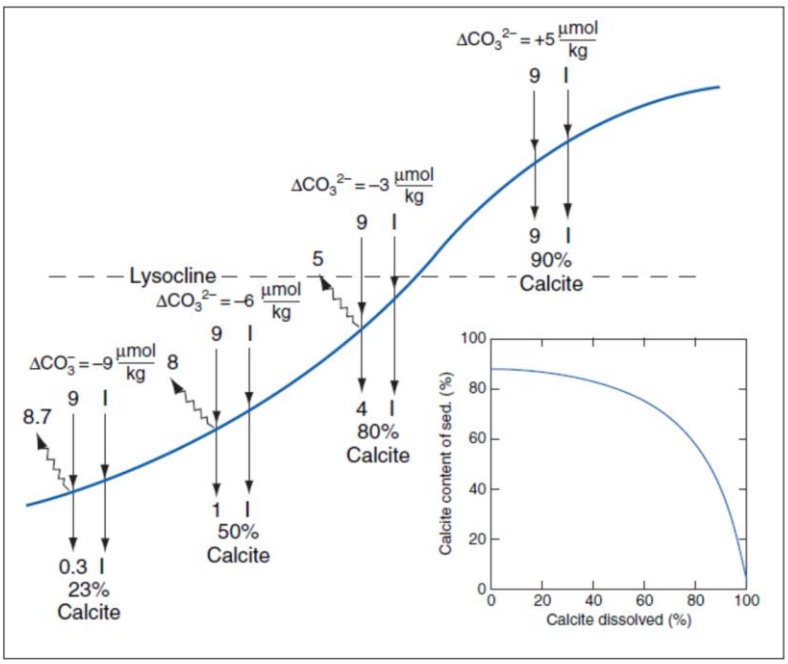

Figure 4.11 – A diagram showing the sensitivity of %$CaCO_3$ in sediment to dissolution. This example assumes an initial sedimentary $CaCO_3$ content of 90 % (the other 10 % being refractory/lithogenic material). If the initial content is lower, the dissolution sensitivity is increased (see Table 4.4). The straight arrows represent burial of $CaCO_3$ and non-$CaCO_3$ material, and the wavy arrow represent dissolution. Reproduced from Broecker and Peng [1982].

The greatest percent change occurs in VM19-296, but this is largely due to the core having the lowest long-term mean $CaCO_3$ accumulation rate due to its water depth (5017 m), beneath the depth of the calcite lysocline, which is currently ~4.4 km in the Atlantic [*Thunell*, 1982] (see Figure 4.12).

Similarly, RC16-66 displays large percent changes in its $CaCO_3$ accumulation rate throughout the record, relative to VM30-40, RC24-01 and ODP 663A; but it also has a low long-term mean $CaCO_3$ accumulation, due to its water depth (4424 m), resulting in larger percentage changes relative to VM30-40, RC24-01 and ODP 663A. From the minimum $\%CaCO_3$ values in RC16-66 and VM19-296 (0-10 %) during MIS 4 it can estimate that near-complete dissolution of calcite has taken place during this interval. If the amount of initial $CaCO_3$ content in sediment above the lysocline at the RC16-66 core site is less than 90 %, it would make the core more sensitive to $CaCO_3$ dissolution (Figure 4.11).

The remaining cores (VM30-40, RC24-01 and ODP 663A) have comparable long-term mean $CaCO_3$ accumulation rates (0.8-1.4 $g/cm^2/ka$). VM30-40, from the central equatorial Atlantic, shows a slight increase in $CaCO_3$ accumulation rate during MIS 4 (~13 %) (Table 4.2). RC24-01 and ODP 663A show a consistent reduction of ~-32 to 37 % during MIS 4, which suggests that a reduction in $CaCO_3$ accumulation was more pronounced in the eastern equatorial Atlantic during MIS 4. VM30-40, RC24-01 and ODP 663A all have similar water depths (3700-3900 m).

Mean $CaCO_3$ accumulation rates for all cores were then used to calculate total $CaCO_3$ burial across the Atlantic during MIS 5a (84-77 ka) and MIS 4 (70-59 ka). The equatorial Atlantic region was defined as the area 0° - 40° W and 5° N - 5° S (equivalent to 4.95×10^6 km^2), the same as that used to calculate relative changes in opal burial during MIS 4 and MIS 5a (see Chapter 3).

Table 4.2 – Comparison of $CaCO_3$ accumulation rates across MIS 4 (70-59 ka) and MIS 5a (84-77 ka). Note that $CaCO_3$ accumulation in 'MIS 5a' in RC16-66 is the average of data points from warm D-O 19 and 20, and MIS 5c.

CORE	RC16-66	VM30-40	RC24-01	ODP 663A	VM19-296
F($CaCO_3$) MIS 4	0.136	1.373	0.632	0.805	0.024
F($CaCO_3$) MIS 5a	0.340	1.216	1.009	1.189	0.440
% change (MIS 5a-4)	-60.00	+12.91	-37.36	-32.29	-94.55
Uncertainty (%)	12.9	4.2	9.1	1.9	0.5

Overall, $CaCO_3$ burial rates were lower during MIS 4 than during MIS 5a, although the trend is opposite in VM30-40 (Table 4.2). The comparison of a $CaCO_3$ accumulation rate of 0.340 $g/cm^2/ka$ in RC16-66 during MIS 5a is not strictly

comparable to the other cores as it is a mean value of $CaCO_3$ accumulation between warm D-O 19 and 20, and MIS 5c (Figure 4.9). Hence, the average is based on relative changes in VM30-40, RC24-01, ODP 663A and VM19-296. The average $CaCO_3$ accumulation change in all cores is ~-38 %. The average percentage reduction in $CaCO_3$ accumulation in the EEA (excluding VM30-40) is ~-55 %.

Assuming a mean $CaCO_3$ accumulation rate across the equatorial Atlantic of 0.782 g/cm^2/ka during MIS 5a (the mean of all cores – see Table 4.2), a ~38 % reduction across the equatorial Atlantic (area 4.95 x 10^6 km^2) equates to a reduction in the $CaCO_3$ burial rate of 3.42 Gt/ka during MIS 4, from a burial rate of 5.52 Gt/ka during MIS 5a.

We also consider the EEA alone, as it appears from changes in opal flux (see Chapter 3) that the largest impact on coccolithophore export productivity would occur during this region during MIS 4. Assuming a mean long-term $CaCO_3$ accumulation rate across the EEA (0° - 15° W and 5° N - 5° S, area 1.855 x 10^6 km^2) of 0.644 g/cm^2/ka during MIS 5a (the mean of RC24-01, ODP 663A and VM19-926 – see Table 4.2), a reduction of 55 % from MIS 5a to MIS 4 equates to a reduction in $CaCO_3$ burial of 0.94 Gt/ka during MIS 4.

The fact that the most pronounced decrease in F($CaCO_3$) during MIS 4 occurs in the EEA agrees with the SALH, in that coccolithophore productivity would be most reduced in areas where diatoms appear to dominate surface productivity in cores RC24-01, ODP 663A and VM19-296 (see Chapter 3). A core such as VM30-40, which does not record maximum opal fluxes during MIS 4 records a slight $CaCO_3$ accumulation increase in MIS 4 relative to MIS 5a (Table 4.2). Although the relative decrease in $CaCO_3$ accumulation in RC16-66 during MIS 4 is large, this does not represent a significant change in $CaCO_3$ burial because of the low long term mean $CaCO_3$ accumulation in RC16-66 (Table 4.1).

4.3 Discussion

In order to validate the SALH as a mechanism of pCO_2 drawdown during MIS 4, it has to be shown to have had an impact on the inorganic to organic carbon export ratio ($CaCO_3$:C_{org}) of the low-latitude ocean, through a decline in $CaCO_3$ relative to opal production and export from the surface ocean [*Matsumoto and Sarmiento*, 2008]. Although the data initially support the SALH in that average MIS 4 $CaCO_3$ accumulation is lower than MIS 5a across the equatorial Atlantic, the effects of dissolution must be distinguished from those of productivity on the $CaCO_3$ record.

In order to do this, the modern-day bottom-water [CO_3^{2-}] was calculated for each core site using the 'CO2calc' application [*Robbins et al.*, 2010]. The input data is described in Table 4.3. The values of [CO_3^{2-}] calculated for the modern (in situ) bottom

waters bathing each core, and the core-top %$CaCO_3$ values are shown in Table 4.4. The values of $\Delta[CO_3^{2-}]$ are calculated by subtracting the in situ $[CO_3^{2-}]$ from the carbonate ion concentration which is required for saturation with respect to calcite ($[CO_3^{2-}]_{sat}$). Values of $[CO_3^{2-}]_{sat}$ are calculated using the relationship in Equation 4.3, where Z is water depth in km [*Broecker and Peng*, 1982]:

Equation 4.3

$$[CO_3^{2-}]_{sat} = 90\exp[0.16(Z-4)]$$

Table 4.3 – Input data used to calculate $[CO_3^{2-}]$ using the 'CO2calc' application [*Robbins et al.*, 2010]. In this application K_1 and K_2 values (see Chapter 1.4) are from [*Mehrbach et al.*, 1973], refit by [*Dickson and Millero*, 1987]. Salinity, potential temperature, phosphate and silicate concentrations are from the eWOCE database [*Schlitzer*, 2000] and Total Alkalinity and TCO_2 data are from the Global Ocean Data Analysis Project (GLODAP) database, available at http://cdiac.ornl.gov.

CORE	RC16-66	VM30-40	RC24-01	ODP 663A	VM19-296
Water depth (m)	4424	3706	3837	3708	5017
Pressure (dbar)	4457	3735	3867	3737	5053
Salinity (pss)	34.6	35.25	34.75	34.75	34.75
Potential Temp (°C)	1.0	2.0	2.1	2.1	2.0
Total Alk (µmol/kg)	2340	2335	2350	2348	2345
TCO_2 (µmol/kg)	2180	2190	2190	2190	2200
$[PO_4^{3-}]$ (µmol/kg)	2.0	1.5	1.5	1.5	1.5
$[Si(OH)_4]$ (µmol/kg)	75	40	55	55	55

The negative values of %dissolution in VM30-40, RC24-01 and ODP 663A (Table 4.4) indicate that the %$CaCO_3^{init}$ of modern sediments above the calcite saturation horizon is probably 85 or 90 %, meaning that core-top dissolution is approximately ~40-60 %. The %$CaCO_3^{init}$ of VM19-296 is likely to be similar as it is located in the same general equatorial upwelling area as the other cores (Figure 4.2), which suggests that its modern core-top calcite dissolution is 75-85 %. The terrigenous flux to the sediment at the RC16-66 core site is likely to be higher due to the influence of the Amazon river plume [*Dobson et al.*, 1997], and therefore we assume a %$CaCO_3^{init}$ of 80 % for RC16-66 [*Archer*, 1991].

The calculated in situ $[CO_3^{2-}]$ values have been marked on a plot of the $[CO_3^{2-}]$ profile in the eastern equatorial Atlantic [*Broecker*, 2008] (Figure 4.12). This plot shows that all cores except VM19-926 lie above the modern calcite saturation horizon. The highly dissolved nature of VM19-296 can be explained by its position below the saturation horizon. Similar levels of calcite dissolution (assuming the same initial $CaCO_3$ composition) in RC16-66 indicate that supralysoclinal dissolution (calcite dissolution in cores above the calcite saturation horizon) may be occurring at this site,

which is in agreement with estimates from in situ techniques [*Martin and Sayles*, 1996] and benthic flux chambers from the Ceara Rise [*Jahnke and Jahnke*, 2004].

Table 4.4 – Calculated values of in-situ [CO_3^{2-}] using CO2calc are shown in the first row. The Δ[CO_3^{2-}] values shown in the second row were calculated by subtracting values of [$CO_3^{2-}]_{sat}$, as calculated using the relationship in Equation 4.3 [*Broecker and Peng*, 1982]; from the calculated in situ [CO_3^{2-}]. Core-top % $CaCO_3$ values for ODP 663A are taken from ODP Initial Reports vol. 108 part A [*Ruddiman et al.*, 1986], and for VM19-296 from [*Broecker*, 2008]. Core-top %$CaCO_3$ values for RC24-01, VM30-40 and RC16-66 were taken from [*Bradtmiller et al.*, 2007]. Core- top dissolution values are calculated for ODP 663A, RC24-01, VM30-40 and RC16-66, with initial $CaCO_3$ contents of sediments above the calcite saturation horizon (%$CaCO_3^{init}$) of 75-90 %.

CORE	RC16-66	VM30-40	RC24-01	ODP 663A	VM19-296
In situ [CO_3^{2-}] (µmol/kg)	105.9	100.1	108.4	107.6	97.9
In situ Δ[CO_3^{2-}] (µmol/kg)	+9.6	+14.2	+20.7	+21.7	-8.0
Core-top $CaCO_3$ (%)	57	78	81	75	57
Core-top Diss. (%) initial 90%	85	61	53	67	85
Core-top Diss. (%) initial 85%	77	37	25	47	77
Core-top Diss. (%) initial 80%	67	11	-7	25	67
Core-top Diss. (%) initial 75%	56	-18	-42	0	56
Core-top Diss. (%) initial 70%	43	-52	-83	-29	43

The pattern of core-top dissolution in ODP 663A, RC24-01 and VM30-40 suggests that, in the modern ocean, more intense supralysoclinal dissolution occurs slightly to the south of the equator (ODP 663A is ~1.2°S) than on the equator (RC24-01 is ~0.3°N and VM30-40 is ~0.1°N), which is supported by sediment trap data [*Wefer and Fischer*, 1993]. This situation may have been different in past interglacials, as during MIS 5a (~84-77 ka) ODP 663A has the highest average %$CaCO_3$ and therefore appears to be the less affected by dissolution (Table 4.5).

During MIS 4, the flux of $CaCO_3$ decreased by ~-38 % relative to MIS 5a across the equatorial Atlantic (Table 4.2). If it is assumed that the export flux of $CaCO_3$ (and C_{org}) remained constant across the MIS 5/4 transition (no SALH scenario), then we can calculate the degree of undersaturation in [CO_3^{2-}] required to account for the change in sedimentary %$CaCO_3$ by dissolution alone. If this were the case then it cannot be confirmed that a reduction in $CaCO_3$ production actually occurred. The average %$CaCO_3$ in MIS 5a sediment from VM30-40, RC24-01 and ODP 663A is 75 % (Table 4.5), similar to the modern core-top average of 78 % for the same cores. This suggests that the %$CaCO_3^{init}$ during MIS 5a was also 85-90 % in these cores, suggesting that the approximate extent of calcite dissolution in the same cores during MIS 5a was probably ~40-60 %.

A similar value of %$CaCO_3^{init}$ is assumed for VM19-296 during MIS 5a, and a %$CaCO_3^{init}$ value of 80% for RC16-66 for the same interval, to reflect greater

terrigenous input from the Amazon river [*Archer*, 1991]. In VM30-40, RC24-01 and ODP 663A $\%CaCO_3$ decreases by ~10 % in MIS 4 relative to MIS 5a (Table 4.5), and assuming that $\%CaCO_3^{init}$ remained the same in these cores, then dissolution may have increased by ~15-20 % during MIS 4.

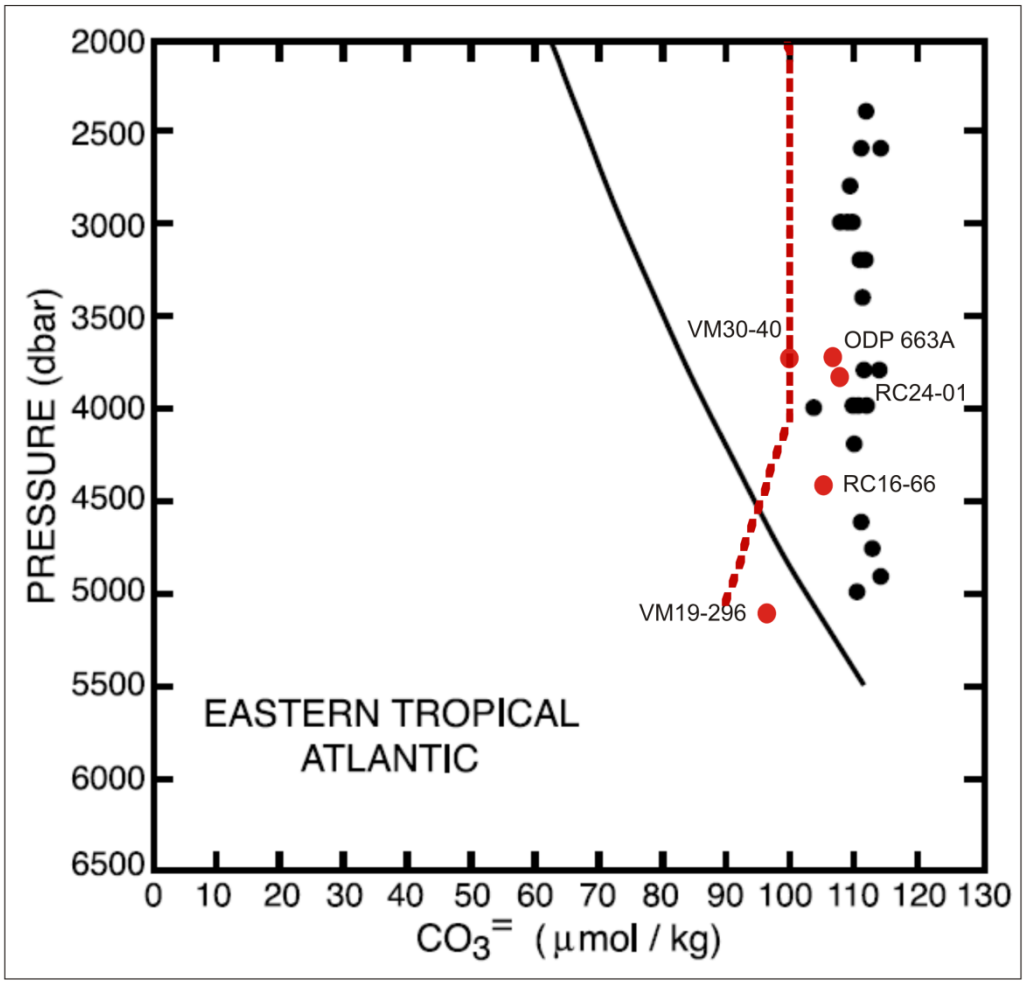

Figure 4.12 -A plot of core locations used in this study (red markers) superimposed on a plot of $[CO_3^{2-}]$ as a function of pressure (in dbar) in the eastern equatorial Atlantic, reproduced from [*Broecker*, 2008]. Also superimposed is a red dashed line showing the approximate $[CO_3^{2-}]$ profile for a transect through the western Atlantic [*Chung et al.*, 2003], for comparison to RC16-66. The solid black line represents the $[CO_3^{2-}]$ saturation concentration based on a ΔV (partial molar volume; see Chapter 1.4) of 36.4 cc/mol [*Ingle*, 1975]. Combined uncertainties for measured thermodynamic constraints used to calculate the calcite saturation horizon [*Ingle*, 1975; *Mucci*, 1983; *Millero*, 1995] have been equated to an error of ±470 metres in the calcite saturation depth in the Atlantic [*Chung et al.*, 2003].

The relationship between carbonate accumulation and sedimentary $\%CaCO_3$ has been modelled by Archer (1991), and plotted as contours on axes of $\Delta[CO_3^{2-}]$ and initial calcite rain rate (Figure 4.13). In order to reconstruct what change in $\Delta[CO_3^{2-}]$ may have occurred during MIS 4, I converted calcite accumulation rate, or $F(CaCO_3)$ from units of $g/cm^2/ka$ to $\mu mol/cm^2/yr$. I then traced this accumulation contour to meet

the measured average $\%CaCO_3$ for the MIS 4 interval in each core, assuming a $\%CaCO_3^{init}$ of 80 % for RC16-66 and 90 % for all other cores.

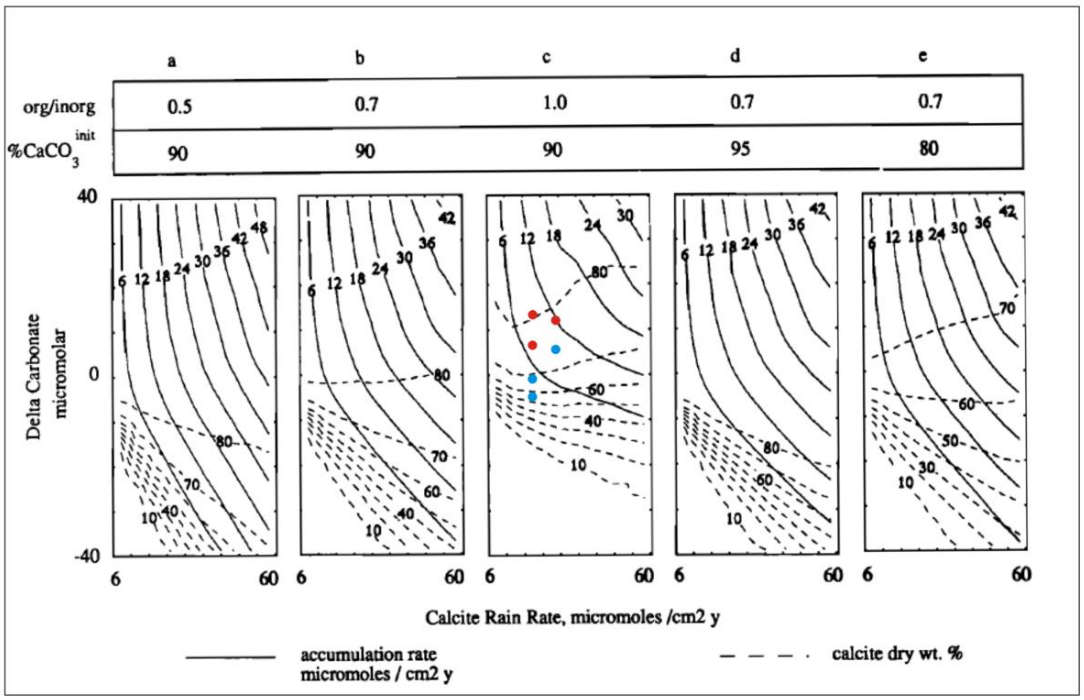

Figure 4.13 – Contours of calcite accumulation rate (solid lines, in units of µmol/cm^2/yr) and dry weight %calcite in sediment (dashed lines), on axes of $\Delta[CO_3^{2-}]$ and initial calcite rain rate (µmol/cm^2/yr). Data from this study are shown by red markers. Contour plot reproduced from [*Archer*, 1991]. Red markers show the position of the three cores VM30-40, RC24-01 and ODP 663A which have been plotted according to their mean calcite accumulation rate [$F(CaCO_3)$] and mean $\%CaCO_3$ for MIS 5a (84-77 ka). Initial calcite rain rates were then assumed constant in MIS 4, to see if reasonable change in $\Delta[CO_3^{2-}]$ could account for changes in mean $\%CaCO_3$ in MIS 4 (70-59 ka) (blue markers). The calcite accumulation rates during MIS 5a and MIS 4 in both VM19-296 and RC16-66 were too low to register a meaningful value of initial calcite rain or $\Delta[CO_3^{2-}]$.

The organic carbon/inorganic carbon (org/inorg) export ratio of was assumed to be 1.0, after values >1.0 for the modern eastern equatorial Atlantic were reported by [*Archer*, 1996]. The results (Table 4.5) demonstrate that reasonable decreases in $[CO_3^{2-}]$ of ~7-16 µmol/kg occurred in MIS 4 relative to MIS 5a when initial calcite rain rates were assumed constant across this interval. This result can be compared to other studies which suggest that decreases in $[CO_3^{2-}]$ of ~14-20 µmol/kg may have occurred in the glacial Atlantic [*Anderson and Archer*, 2002; *Broecker and Clark*, 2002; *Yu et al.*, 2008], and is supported qualitatively by the foraminiferal fragmentation index in ODP 663A (Figure 4.5). It is likely that bottom-water decreases in $[CO_3^{2-}]$ caused near-complete dissolution of $CaCO_3$ in the deeper cores VM19-296 and RC16-66 during MIS 4, possibly as a result of the enhanced incursion of AABW into the Atlantic [*Verardo and McIntyre*, 1994; *Govin et al.*, 2009] due to reduced NADW export [*Duplessy et al.*, 1988; *Rutberg et al.*, 2000].

Table 4.5 – Results from comparison of $CaCO_3$ accumulation and $\%CaCO_3$ data to the data model output of [*Archer*, 1991]. Data are plotted on the contour plots shown in Figure 4.13 [*Archer*, 1991]. The values labelled 'n/a' plotted outside the contour space limits.

CORE	RC16-66	VM30-40	RC24-01	ODP 663A	VM19-296
Initial $CaCO_3$ rain rate ($\mu mol/cm^2/yr$)	n/a	24	20	20	n/a
Mean $\%CaCO_3$ (MIS 5a)	36.48	71.8	74.55	80.05	32.38
$\Delta[CO_3^{2-}]$ (MIS 5a)	n/a	12	13	13	n/a
Mean $\%CaCO_3$ (MIS 4)	13.38	73.80	55.01	67.54	3.97
$\Delta[CO_3^{2-}]$ (MIS 4)	n/a	7	-4	0	n/a

The results from ODP 663A, RC24-01 and VM30-40 suggest that calcite dissolution alone could have produced the changes in $CaCO_3$ accumulation recorded in the eastern equatorial Atlantic during MIS 4. Increased dissolution could have resulted from either a shoaling of the calcite lysocline, or increased supralysoclinal dissolution due to organic carbon remineralisation, or a combination of both. A study of foraminiferal fragmentation in a suite of cores from the Sierra Leone Rise (eastern equatorial Atlantic) indicated that the glacial lysocline may have been ~1000 metres shallower relative to its interglacial position [*Curry and Lohmann*, 1986], a sufficient change to place all the cores studied beneath the calcite saturation horizon. In either case, dissolution may account for changes in $CaCO_3$ accumulation without invoking decreased export productivity of $CaCO_3$ by coccolithophorids.

Both ODP 663A and RC24-01 currently lie in more productive waters than VM30-40 (Figure 4.15), and both appear to record larger changes in $\Delta[CO_3^{2-}]$ than VM30-40. A palaeoproductivity reconstruction using foraminiferal transfer functions in the EEA supports a ~50% increase in primary productivity in MIS 4 [*Sarnthein et al.*, 1992], and if patterns of equatorial upwelling and primary productivity were similar to the modern ocean (Figure 4.15), RC24-01 and ODP 663A could have experienced greater supralysoclinal dissolution than VM30-40. Additionally, despite the suggestion that VM30-40 could have been more dissolved during MIS 4, its rate of calcite accumulation was greater during this interval, implying higher $CaCO_3$ productivity, and argues against a SALH scenario having occurred in the central equatorial Atlantic.

These records were compared with the record of ^{230}Th-normalised $CaCO_3$ flux from core V28-82 (49°27'N, 22°16'W, 3935 m water depth) from the North Atlantic during MIS 4 [*McManus et al.*, 1998], to try to distinguish the effect of equatorial upwelling on $CaCO_3$ flux rate. The relative changes in $CaCO_3$ fluxes are of the same order as those recorded for a deeper core from the equatorial Atlantic such as VM19-296 (Figure 4.14). V28-82 is situated outside the equatorial upwelling/high productivity

region, and it is suggested by McManus *et al*., [2008] that the $CaCO_3$ flux record in North Atlantic sediments reflects smaller changes in biogenic $CaCO_3$ burial, and larger changes in terrigenous input, which vary by a factor of 2-5; mainly due to large input of ice-rafted debris (IRD) during Heinrich Events. However, the IRD input throughout MIS 4 is relatively low (Figure 4.14), allowing the possibility that changes in ocean chemistry and circulation had a much larger influence on $CaCO_3$ accumulation in the North Atlantic [*Yu et al*., 1998]. Other studies support large changes in Atlantic circulation and CO_3^{2-} content during glacial periods [*Anderson and Archer, 2002*; *Broecker and Clark*, 2002]. This comparison supports the revised hypothesis that $CaCO_3$ accumulation in the equatorial Atlantic during MIS 5a/4 was controlled by changes in ocean circulation and CO_3^{2-} content.

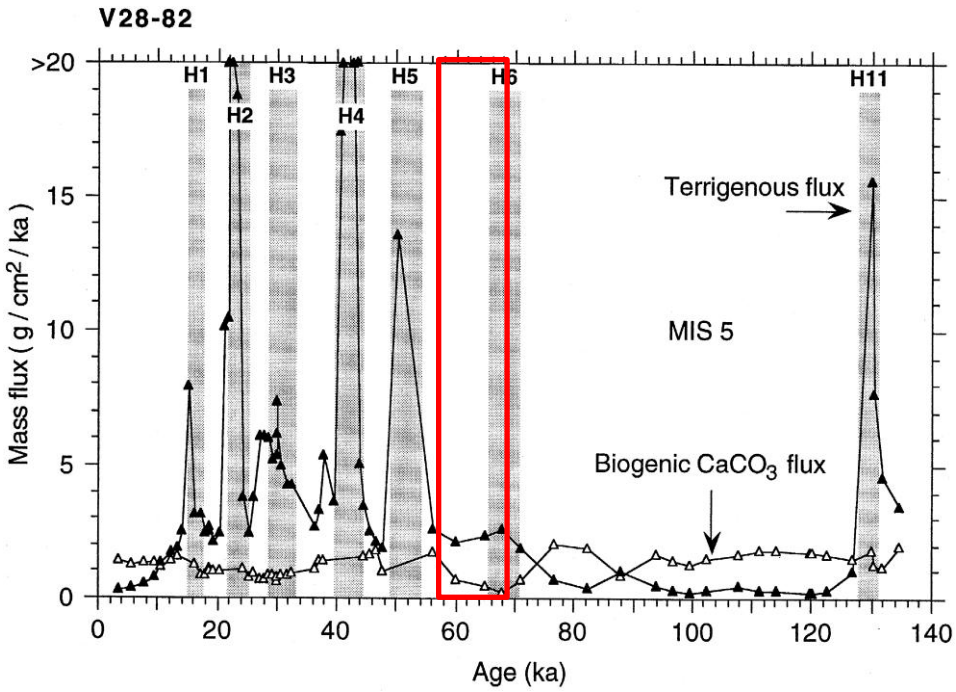

Figure 4.14 – Major component bulk mass fluxes from V28-82 (49°27'N, 22°16'W, 3935 m water depth) [*McManus et al*., 1998]. The interval of interest is highlighted by a red box.

The results of this study suggest that reasonable changes in $CaCO_3$ dissolution during MIS 4 may have been able to account for the total changes in $CaCO_3$ accumulation in MIS 4 relative to MIS 5a, due to either a shoaling of the glacial calcite lysocline [*Curry and Lohmann*, 1986], or an increase in supralysoclinal dissolution, or both. However, this does not preclude changes in the calcite rain ratio due to decreased productivity from having occurred, rather that these changes are more modest than previously thought. Additional work in the equatorial Atlantic measuring changes in the abundance of coccoliths tests, thorium-normalised $CaCO_3$ profiles and foraminiferal fragmentation indices would shed further light on the matter and this remains an interesting topic for future research.

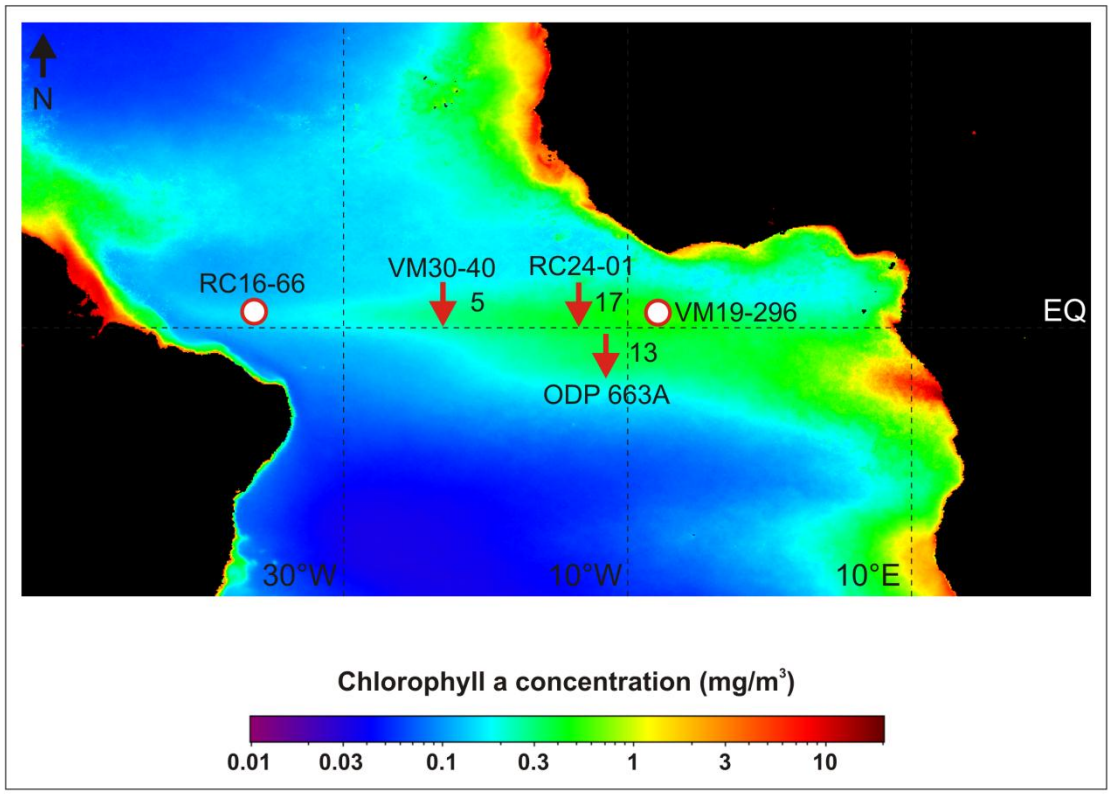

Figure 4.15 – Plot of estimated decreases in $\Delta[CO_3^{2-}]$ in MIS 4 (70-59 ka) relative to MIS 5a (84-77 ka) assuming no change in initial $CaCO_3$ and C_{org} fluxes, indicated by the figures next to the red arrows. Changes in bottom water chemistry are the most likely explanation for the extreme $CaCO_3$ dissolution seen in RC16-66 and VM19-296 (indicated by white markers). Chlorophyll data is a 13-year composite SeaWiFS data, sourced from http://oceancolor.gsfc.nasa.gov.

Lastly, relative changes in $CaCO_3$ accumulation in all cores were compared with the pCO_2 record [*Ahn and Brook*, 2008] (Figure 4.16). The timing of decreases in the $CaCO_3$ flux, coincident with increases in the C_{org} flux associated with enhanced diatom productivity (see Chapter 3), suggests that a SALH scenario probably did not cause, but may have contributed to the ~47 ppm pCO_2 drawdown that occurred ~71 ka at the initiation of MIS 4 [*Ahn and Brook*, 2008] (see Figure 4.16).

As can be seen in Figure 4.16, $CaCO_3$ is decreasing in all cores except RC16-66 at the initiation of the pCO_2 drawdown. It has been suggested that more efficient transport of particulate organic carbon (POC) to the deep ocean than POC originating from pico- and nannoplankton, could have had a similar effect on pCO_2 to that of reduced $CaCO_3$ export; although in the former case it would be an increase in the dissolved inorganic carbon (DIC) gradient that would bring about a change in pCO_2 [*Ridgwell*, 2003]. A box modelling study further explores the potential pCO_2 drawdown associated with this scenario (see Chapter 6).

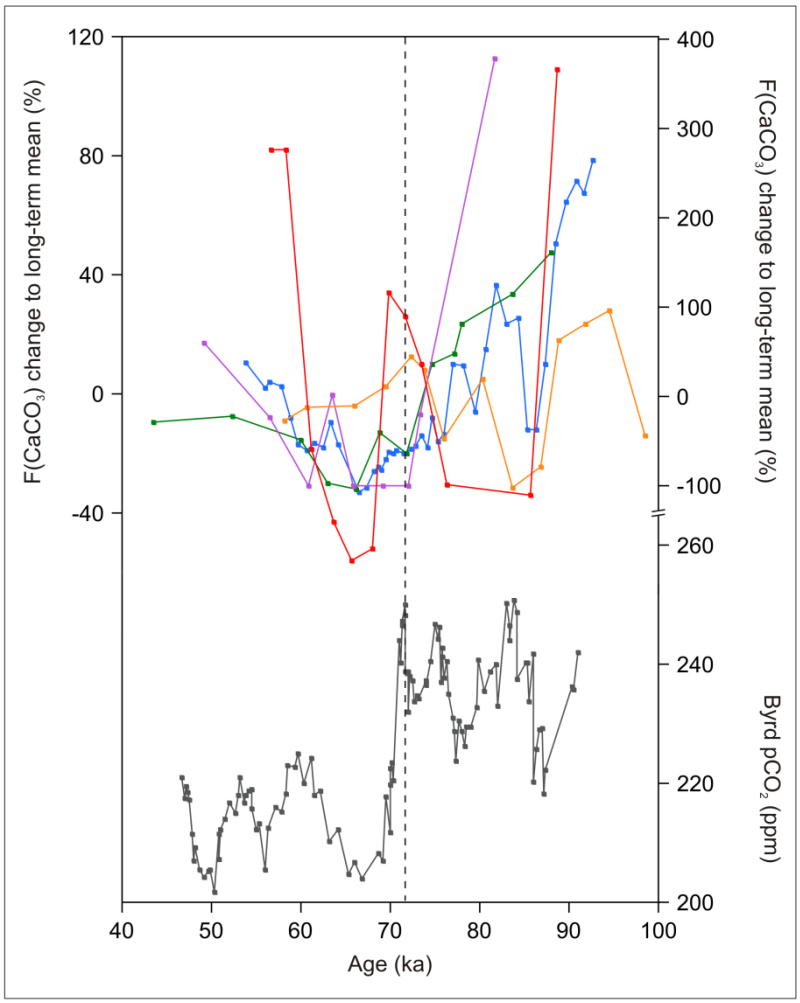

Figure 4.16 – A plot of relative changes in $CaCO_3$ accumulation rate in all cores, arranged chromatically from west (red) to east (violet). RC16-66 (red), VM30-40 (orange), RC24-01 (green), ODP 663A (blue) and VM19-296 (violet) are plotted relative to their long-term mean $CaCO_3$ accumulation (Table 4.1), and are shown on the same axis for comparison, except VM19-296 (note different scale on the left). Byrd pCO_2 is plotted beneath using the age control of [*Ahn and Brook*, 2008]. The dashed line marks the initiation of the ~ 47 ppm decrease in pCO_2 that occurred ~ 71 ka, at the beginning of MIS 4.

4.4 Conclusions

The results of this investigation suggest that there was a mean reduction of ~38 % in $CaCO_3$ accumulation in sediment in the EEA during MIS 4. This corresponds to an approximate reduction of ~3.42 Gt/ka in the $CaCO_3$ burial rate across the equatorial Atlantic during MIS 4. Some of the $CaCO_3$ loss recorded during MIS 4 is undoubtedly due to increased dissolution (particularly in deeper cores such as VM19-296 (5017 m) and RC16-66 (4424 m)), probably because of increased incursion of $CaCO_3$-corrosive AABW into the EEA [*Verardo and McIntyre*, 1994; *Govin et al.*, 2009]. Studies of foraminiferal fragmentation, and spectral analysis of biogenic records from the eastern equatorial Atlantic suggest that the boundary between $CaCO_3$-corrosive AABW and

NADW was 3700-3750 metres [*Curry and Lohmann*, 1986; *Verardo and McIntyre*, 1994].

Some dissolution is also evident in one of the shallower cores (ODP 663A – 3708 m) (see Figure 4.5). Calcite dissolution affected a number of cores over the depth range 2500-5000 metres in the eastern equatorial Atlantic, and suggests that the glacial calcite lysocline may have shoaled by 1000 metres [*Curry and Lohmann*, 1986].

The current position of ODP 663A, RC24-01 and VM30-40 above the modern calcite lysocline (Figure 4.12) suggests this evidence of increased dissolution during MIS 4 was probably a result of shoaling of the lysocline [*Curry and Lohmann*, 1986], in combination with enhanced supralysoclinal dissolution of $CaCO_3$ due to increasing organic carbon export in the equatorial upwelling zone [*Sarnthein et al.*, 1992].

Although these results do not preclude a reduction in the rain ratio of $CaCO_3$:C_{org} to the sea floor from occurring during MIS 4, the change in $CaCO_3$ accumulation recorded in our cores may be explained by reasonable changes in $CaCO_3$ dissolution [*Archer*, 1991]. Taken together with the results of Chapter 3, these findings likely suggest that the SALH may not have had as significant an effect on low latitude $CaCO_3$ export during MIS 4 as previously thought [*Matsumoto and Sarmiento*, 2008]. However, it may potentially allow changes in $CaCO_3$:C_{org} (and pCO_2) by the efficiency with which diatoms transfer POC through the water column [*Ridgwell*, 2003]. The pCO_2 drawdown that could have been associated with a SALH scenario occurring in the EEA during MIS 4 is examined quantitatively in Chapter 6.

Chapter 5: Evidence for increased silica leakage in Antarctic Intermediate Water (AAIW) to the tropical Atlantic during MIS 4

5.1 Introduction

5.1.1 Background

In the modern equatorial Atlantic, diatom growth is primarily limited by the availability of silicic acid [$Si(OH)_4$] [*Sarmiento et al.*, 2004], which they use to build their protective frustule [*Armstrong and Brasier*, 2005]. However, under conditions of plentiful silica, diatoms are able to dominate primary productivity [*Egge and Aksnes*, 1992; *Dugdale and Wilkerson*, 1998]. Mesocosm experiments conducted with semi-continuous nutrient addition show that diatoms are able to outcompete a common coccolithophore (*Emiliana huxleyi*) and other picoplankton when $Si(OH)_4$ is greater than ~2 µM and PO_4^{3-} (phosphate) and NO_3^- (nitrate) are present in non-limiting concentrations [*Egge and Aksnes*, 1992]. Changes in the supply of $Si(OH)_4$ to the surface waters of the equatorial Atlantic might then be expected to influence the ratio of silica to carbonate producers in this region.

The supply of nutrients to the low latitude Atlantic thermocline is determined by the flux and chemistry of Antarctic Intermediate Water (AAIW) and Subantarctic Mode Water (SAMW) spreading north from their formation regions around the Subantarctic Front (SAF) within the Southern Ocean (SO) [*Sarmiento et al.*, 2004]. In the modern ocean, Upper Circumpolar Deep Water (UCDW) upwells south of the Antarctic Polar Front (APF), and has an Si:N ratio between 2 and 3 which sustains high diatom productivity in Antarctic Surface Water (AASW) [*Brzezinski et al.*, 2001; *Pondaven et al.*, 2000]. As a result, primary productivity in AASW is dominated by diatoms [*Nelson et al.*, 1995]. The high diatom production in the surface waters and subsequent dissolution of biogenic silica at depth maintains a high $Si(OH)_4$ content in deep waters of the SO, in which around 80 % of the biogenic opal export is recycled in the water column [*Tréguer et al.*, 1995]. Furthermore, diatoms in this region take up 4-5 times as much silica per unit of organic matter than those from other regions of the world ocean [*Pondaven et al.*, 2000; *Brzezinski et al.*, 2001], due partly to the fact that the SO is Fe limited (which increases the uptake of silica relative to nitrate in diatoms in a ~4:1 ratio) [*Takeda*, 1998; *Franck et al.*, 2000]. This leaves AASW depleted in $Si(OH)_4$ but high in preformed nitrate and phosphate concentrations, with an Si:N of ≤0.5 [*Schlitzer*, 2000; *Sarmiento et al.*, 2004]. The extent of silica depletion relative to nitrate can be defined by the pseudo-tracer Si*, where $Si^* = [Si(OH)_4] - [NO_3^-]$ (Figures 5.1 and 5.2) [*Sarmiento et al.*, 2004]. AASW is defined as water with a temperature of -1.0 °C to -1.8

°C, and salinity of 34.00 [*Hofmann et al.*, 1996]. During austral summer, increased insolation warms the circumpolar surface waters and isolates a core of colder AASW at ~100 m depth, which is referred to as Winter Water (WW) [*Sievers and Nowlin*, 1984]. WW is the only type of AASW that retains the same temperature and salinity properties regardless of season [*Hofmann et al.*, 1996].

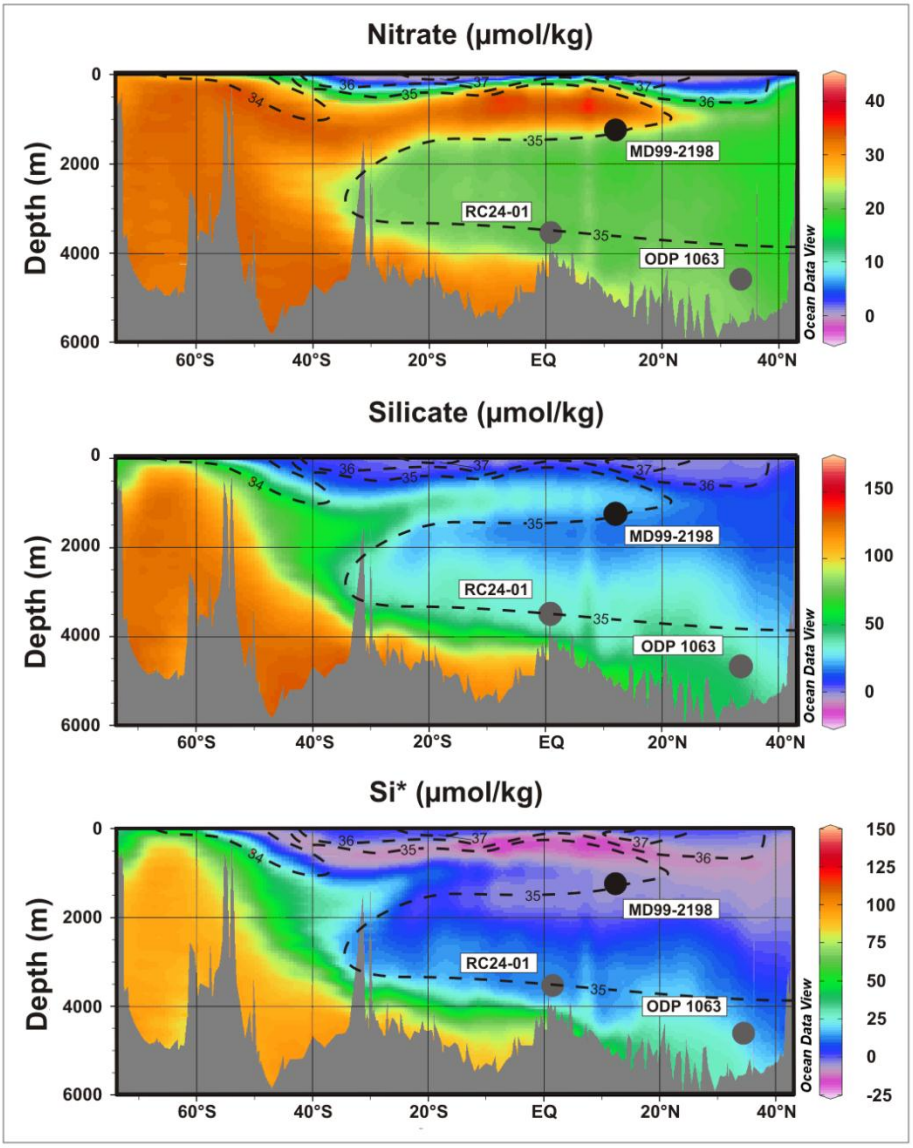

Figure 5.1 - Concentrations of nitrate (top panel), silicate/silicic acid (middle panel) and the pseudo-tracer Si* (bottom panel) from a transect through the western Atlantic from ~75°S to 40°N, with core locations plotted by latitude and depth. AAIW is identifiable as a tongue of low salinity, high-nitrate, low-silicate, low Si* water extended from high southern latitude to low latitude. Contours in black are salinity, units are practical salinity scale (pss-78) (Schlitzer, 2000). Tracer data is from the World Ocean Circulation Experiment (WOCE) online database (Schlitzer, 2000).

AAIW is created by subduction of WW from the Bellingshausen Sea, west of the Antarctic Peninsula, and just to the south of the Polar Front (PF) [*Sievers and Nowlin*, 1984; *Meredith et al.*, 1999]. SAMW, a related water mass, forms through the seasonal

convective overturning of surface waters in the south Indian and southeast Pacific oceans [*Aoki et al.*, 2007], and it is proposed that the densest varieties of SAMW formed here transit the Drake Passage and contribute to AAIW [*McCartney*, 1977; *Hanawa and Talley*, 2001]. SAMW is a pycnostad (layer of near-uniform density), which forms a circumpolar belt that encompasses the Subantarctic Zone (SAZ), between the Subtropical Front (40-45°S) and the Subantarctic Front (45-55°S), as well as the PF. SAMW has a low Si*, due to depletion of silicic acid by diatoms (Figure 5.2) [*Sarmiento et al.*, 2004].

AAIW and SAMW mix with other subtropical waters at the Brazil-Malvinas Confluence (35°S-40°S), with the relative influence of each water mass varying from year to year, and in some years the presence of AAIW has been recorded directly beneath the subtropical thermocline [*Piola and Gordon*, 1989]. As AAIW spreads northwards it mixes into the waters of the Atlantic thermocline [*You*, 1999].

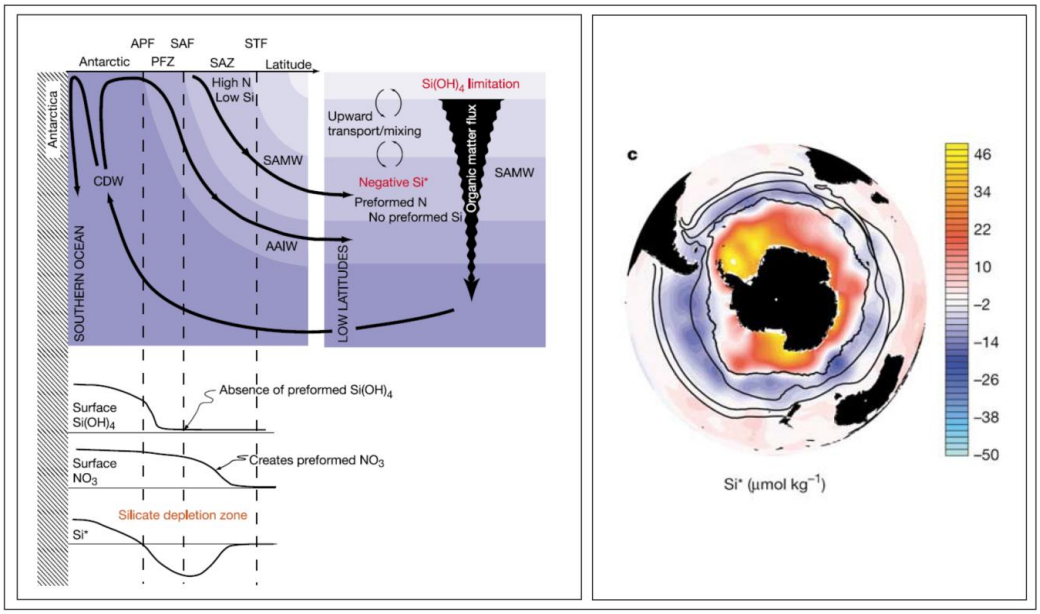

Figure 5.2 – Schematic diagram illustrating the formation of low Si* water (left panel), and illustration of Si* concentration in circumpolar waters (right panel). APF = Antarctic Polar Front, PFZ = Polar Frontal Zone, SAF = Subantarctic Front, SAZ = Subantarctic Zone, STF = Subtropical Front, CDW = Circumpolar Deep Water. Low Si* waters in the SAZ are coloured blue, in particular in the southeast Pacific where SAMW forms. Reproduced from Sarmiento *et al*. [2004].

The influence of AAIW at lower latitudes has been recorded through its presence as a salinity minimum along an isopycnal (σ_0 ~27.3 kg m^{-3}); extending from ~50°S to the Straits of Florida, via the north coast of South America, the Caribbean Sea and the Yucatan Channel. AAIW may be traced further north, to the west of deeper, higher-salinity Mediterranean Overflow Water (MOW). The influence of AAIW

extends northward to Cape Hatteras, and as far northeast as 60°N, 20°W; just south of Iceland [*Tsuchiya*, 1989].

If the $Si(OH)_4$ uptake of diatoms in the SO were to be decreased, for example by the addition of aeolian Fe, then any 'unused' silicic acid would 'leak' from the SO to low latitudes via AAIW (and possibly SAMW) [*Brzezinski et al.*, 2002; *Matsumoto et al.*, 2002]. Furthermore, glacial periods were marked by greater dust deposition at high southern latitudes [*Petit et al.*, 1999], which suggests that a glacial decrease in the $Si(OH)_4$ uptake of SO diatoms was a possibility. An additional effect would be the glacial depletion of NO_3^-, which data suggests occurred in the Southern Ocean in each of the last three glaciations [*Brzezinski et al.*, 2002], which would result in a lowering of the Si:N export ratio of SAMW/AAIW exported to low latitudes.

Higher glacial rates of $Si(OH)_4$ supply within AAIW may then have alleviated Si-limitation in the low latitudes and promoted an ecosystem shift away from carbonate producers toward silica producers [*Brzezinski et al.*, 2002; *Matsumoto et al.*, 2002]. In the modern ocean, low-latitude primary productivity is dominated by carbonate ($CaCO_3$)-producing phytoplankton (most commonly coccolithophores) [*Honjo*, 1976; *Thurman and Trujillo*, 2002]. The low-latitude ocean, defined as 50°S - 60°N in relevant geochemical box models; [*Toggweiler and Sarmiento*, 1985; *Matsumoto et al.*, 2002], accounts for ~85 % of the area of the world ocean and hence has an important impact on the global export ratio of inorganic to organic carbon ($CaCO_3$:C_{org}), estimated most recently as ~0.1 [*Sarmiento et al.*, 2002]. The net result of a shift from carbonate to Si-producing phytoplankton in the low latitude ocean and consequent reduction in the rain ratio of $CaCO_3$:C_{org} in sinking particulate matter, is higher seawater alkalinity and thus lowering of atmospheric CO_2 [*Sigman and Boyle*, 2000; *Matsumoto and Sarmiento*, 2002; *Matsumoto et al.*, 2008]. This mechanism is referred to as the Silicic Acid Leakage Hypothesis (SALH).

5.1.2 Previous investigations of the SALH

Previous investigations into the SALH during the last glacial and deglacial periods have focused either on silica accumulation changes in the tropical Atlantic, [*Bradtmiller et al.*, 2007] or $Si(OH)_4$ concentrations in AAIW reconstructed using the silicon isotopic composition of sponge spicules [*Hendry and Robinson*, 2012]. In this investigation these approaches were combined with sedimentary Nd isotope analyses to investigate changes in the supply rate and chemistry of AAIW and contemporary changes in opal accumulation within the Atlantic Ocean during the last transition to glacial conditions during Marine Isotope Stage (MIS) 5 to 4, which occurred around 71 ka [*Martinson et al.*, 1987]. This was an interval of large and rapid pCO_2 change (~47

ppmv in 2-3 ka) that occurred around 71 ka, around the initiation of MIS 4 [*Ahn and Brook*, 2008], and also a period in which opal flux rates and opal burial are known to have increased in the equatorial Atlantic (see Chapter 3).

I measured sedimentary neodymium isotope and sponge spicule silicon isotope ratios on samples from sediment core MD99-2198 which lies within modern AAIW (see Figure 5.1), in order to reconstruct past changes in the silicic acid content of AAIW, and test one of the central predictions of the SALH. I also reconstructed opal accumulation rates in Bermuda Rise core ODP 1063 (33°41'N; 57°37'W; 4595 m water depth), and RC24-01 (0˚33'N; 13˚39'W; 3837 m water depth) from the eastern equatorial Atlantic; in order to gauge any effect on surface diatom productivity during this interval, with the goal of testing the viability of model studies that have simulated the effect that a SALH scenario may have had on pCO_2 drawdown during MIS 4 [*Matsumoto and Sarmiento*, 2002; *Matsumoto et al.*, 2008].

5.1.3 Nd and Si proxy background

Neodymium (Nd) isotopes have been shown in many studies to be a responsive tracer of water mass mixing, given the short oceanic residence time of Nd of ~500-1000 years [*Tachikawa et al.*, 2003] and the fact that distinct isotopic variations exists between different water masses, for example [*Piepgras and Wasserburg*, 1980; 1982; *Piepgras and Jacobsen*, 1988; *Jeandel*, 1993; *Jeandel et al.*, 1998; *Tachikawa et al.*, 2003]. Due to the oceanic residence time being of the same order as the global oceanic mixing time (~1500 years) [*Broecker and Peng*, 1982], Nd can be considered a quasi-conservative tracer. Unlike stable isotope and nutrient proxies, quasi-conservative tracers are insensitive to bias by temperature changes or biological processes [*Frank*, 2002; *Goldstein and Hemming*, 2003; *Vance et al.*, 2004]. These potential sources of inaccuracy are accounted for by mass-fractionation correction during isotope analysis, by normalising the measured $^{143}Nd/^{144}Nd$ ratio to that of a standard (see Chapter 2.7).

Consequently, the change in the neodymium isotope composition (given the notation ε_{Nd}) of a water mass can only occur by addition of Nd released from the Earth's crust by hydrothermal processes and weathering, and therefore depends on the ε_{Nd} of the continental source [*Frank*, 2002]. The ε_{Nd} signatures of different water masses depend primarily on the age of the continental crust surrounding the source basin, with the oldest crustal rocks having the most negative values of ε_{Nd}, and mantle-derived rocks such as mid-ocean ridge basalts showing more positive values of ε_{Nd} due to ^{147}Sm (the parent isotope of ^{143}Nd) preferentially remaining in the mantle during

continental crust formation [*Frank*, 2002]. Nd isotope ratios are expressed in the Equation 5.1:

$$\varepsilon_{Nd} = \left[\frac{\left(\frac{^{143}Nd}{^{144}Nd}SAMPLE\right) - \left(\frac{^{143}Nd}{^{144}Nd}CHUR\right)}{\frac{^{143}Nd}{^{144}Nd}CHUR} \right] 10{,}000$$

Equation 5.1 – Calculation of eNd; where CHUR is the Chondritic Uniform Reservoir and currently has the value 0.512638 [*Jacobsen and Wasserburg*, 1980]. Reproduced from Frank [2002].

It has been shown that the ε_{Nd} of deep and intermediate water masses exhibit less variability, in comparison with the ε_{Nd} of surface waters [*Piepgras and Wasserburg*, 1982; *Piepgras and Wasserburg*, 1983; 1987; *Piepgras and Jacobsen*, 1988; *Spivack and Wasserburg*, 1988; *Shimizu et al.*, 1994]. Therefore the sedimentary ε_{Nd} record is able to document past changes in deep and intermediate water masses at Atlantic intermediate depth core sites. The modern day ε_{Nd} value of -13.5 ± 0.5 of North Atlantic Deep Water (NADW) is determined by efficient mixing of Labrador Sea Water (LSW), and water from the Norwegian and Greenland Seas [*Piepgras and Wasserburg*, 1987; *Lacan and Jeandel*, 2005a].

Studies indicate that the Nd isotopic composition of NADW, and another northern-sourced water mass termed Glacial North Atlantic Intermediate Water (GNAIW) have remained nearly constant at ε_{Nd} = -13.5 ± 0.5 for the last ~ 150 ka, despite GNAIW probably forming in different locations to NADW [*van de Flierdt et al.*, 2006; *Foster et al.*, 2007].

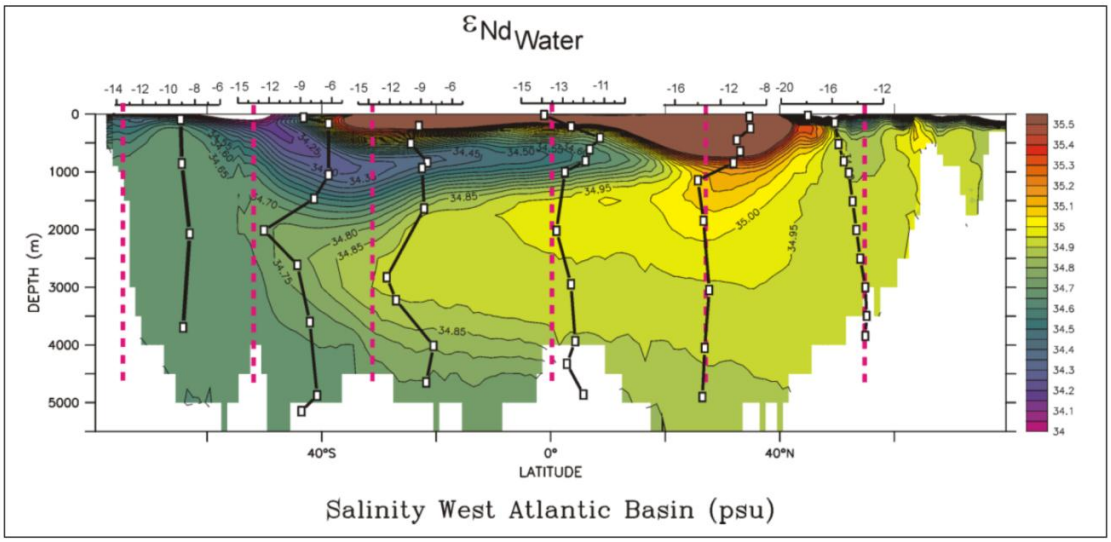

Figure 5.3 – Water mass distribution characterised by salinity [*Levitus et al.*, 1982], for an N-S transect through the modern Atlantic. High-salinity NADW forming at high northern latitudes is represented by yellow, lower-salinity AABW by green and AAIW by blue. Profiles of measured seawater ε_{Nd} values are superimposed and illustrate the differences between the various water masses [*Piepgras and Wasserburg*, 1987; *Jeandel*, 1993; *von Blanckenburg*, 1999]. Figure reproduced from von Blanckenburg [1999].

It has been proposed that exchange of seawater with sediments to the south of Iceland (more positive ε_{Nd}) and sediments of the Greenland shelf (more negative ε_{Nd}) altered the Nd isotopic composition of GNAIW that had caused it to reflect the modern ε_{Nd} signature of NADW [*van de Flierdt et al.*, 2006].

Fortunately, the Nd isotopic composition of NADW remains distinguishable from AAIW (ε_{Nd} -7 to -9) [*Piepgras and Wasserburg*, 1982; *Bertram and Elderfield*, 1993; *Jeandel*, 1993; *Jeandel et al.*, 1998; *Stichel et al.*, 2012], which allows the characterisation of northern- and southern-sourced Atlantic water masses, which is of great benefit to palaeoceanographic research. More positive ε_{Nd} values reflect the input of Pacific deep and intermediate waters, which mainly have a more positive ε_{Nd} value (i.e. more radiogenic) of ≈ -2.7 to -3.4 [*Amakawa et al.*, 2009], which probably reflects input of Nd from radiogenic island-arc sources with an ε_{Nd} of up to +20 [*Frank*, 2002]. The more positive Nd isotopic composition value of AAIW may reflect the contribution of SAMW to AAIW [*McCartney*, 1977; *Piola and Gordon*, 1989]. Data from a central Pacific Fe-Mn crust appears to support the notion that the Nd isotopic composition of Pacific water appear to have remained stable over at least the last 150 ka [*Abouchami et al.*, 1997], although data from a deep-sea coral skeleton suggests that the Nd isotopic composition of the SO became more radiogenic during Heinrich Stadial (HS) 1 (~16.7 ka), which questions the stability of the Nd isotopic composition of the Southern Ocean member [*Robinson and van de Flierdt*, 2009] (see Section 5.3).

Core-top ε_{Nd} measurements from MD99-2198 [*Pahnke et al.*, 2008] matched closely with nearby measurements of seawater ε_{Nd} [*Piepgras and Wasserburg*, 1987], suggesting that ε_{Nd} within the sediment reflected that of overlying seawater. Changes in the ε_{Nd} over the past 25 ka at the MD99-2198 core site have therefore been interpreted as reflecting changes in the relative influences of AAIW and NADW/GNAIW on the Tobago Basin [*Pahnke et al.*, 2008].

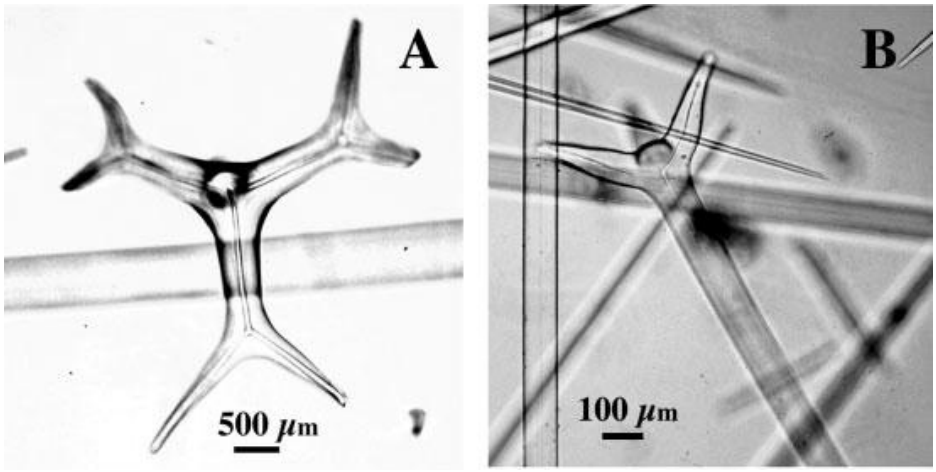

Figure 5.4 – Typical megascleres (spicules visible to the naked eye) of demosponges. Reproduced from Uriz *et al.* [2003].

The silicon isotope ratio (δ^{30}Si) of benthic sponge spicules (the needle-like skeletal elements of sponges – see Figure 5.4) has been shown to be a robust recorder of the silicic acid concentration of the water in which the sponges grew [*Hendry et al.*, 2010; *Hendry and Robinson*, 2012]. Silicon is naturally present in three stable isotopes: ^{28}Si (92.22 %), ^{29}Si (4.68 %) and ^{30}Si (3.08 %), and is usually expressed in per mil (‰), relative to the NIST standard, NBS 28:

$$\delta^{x}\mathrm{Si} = \left\{ \frac{\frac{^{x}\mathrm{Si}}{^{28}\mathrm{Si}}\,\mathrm{SAMPLE}}{\frac{^{x}\mathrm{Si}}{^{28}\mathrm{Si}}\,\mathrm{NBS\ 28}} \right\} \mathrm{x}\ 1000$$

Equation 5.2 – Per mil notation, where x is either ^{29} Si or ^{30} Si. Sponge spicule silicon isotope ratios in this investigation will be reported as δ^{30}Si. Reproduced from Hendry and Robinson [2012].

The uptake of silicic acid in sponges leads to fractionation of Si isotopes, as the sponges preferentially take up the lighter ^{28}Si isotope, and consequently display very light δ^{30}Si values [*De La Rocha*, 2003]. The δ^{30}Si of living sponge spicules has been found to correlate well with silicic acid concentrations in a number of locations (see Figure 5.11 and Equation 5.3) [*Hendry and Robinson*, 2012].

5.1.4 Study area and methods

MD99-2198 (12.09˚N; 61.23˚W; 1330 m water depth) is situated in the Tobago Basin in the south eastern sector of the Caribbean Sea. Caribbean Sea surface waters are nutrient-depleted (0-80 m), and are underlain by high-salinity Subtropical Under Water (SUW) between ~80-100 m. Below this, a mixture of SUW and AAIW forms the main component of Caribbean thermocline waters present at depths ~500-900 m. The composition of intermediate waters at this site (termed Atlantic Intermediate Water - AIW, at depths ~900-1900 m) is a mixture of AAIW and Upper North Atlantic Deep Water (UNADW). UNADW dominates below 1900 m [*Wüst*, 1964; *Haddad and Droxler*, 1996] (see Figure 5.5).

AAIW enters the Tobago Basin via the subthermocline North Brazil Current (NBC), which contains approximately 60 ± 5% southern-sourced water [*Bub and Brown*, 1996]. Depending on the season, all or a part of these southern-sourced waters retroflect anticyclonically and flow eastwards, feeding into the North Equatorial Undercurrent (NEUC) [*Wilson et al.*, 1994; *Suga and Talley*, 1995]. North Atlantic Central Water (NACW) enters the region between the equator and 9°N and west of 44°W, and mixes with the southern-sourced water. This mixed water mass makes up approximately half of the region in volume and is predominantly of a southern origin [*Bub and Brown*, 1996].

The Tobago Basin is influenced by the Amazon and Orinoco river plumes [*Chérubin and Richardson*, 2007; *Molleri et al.*, 2010], and sediment from these sources may have contributed to the relatively high sedimentation rates observed in MD99-2198 (~10-30 cm/ka) in the past.

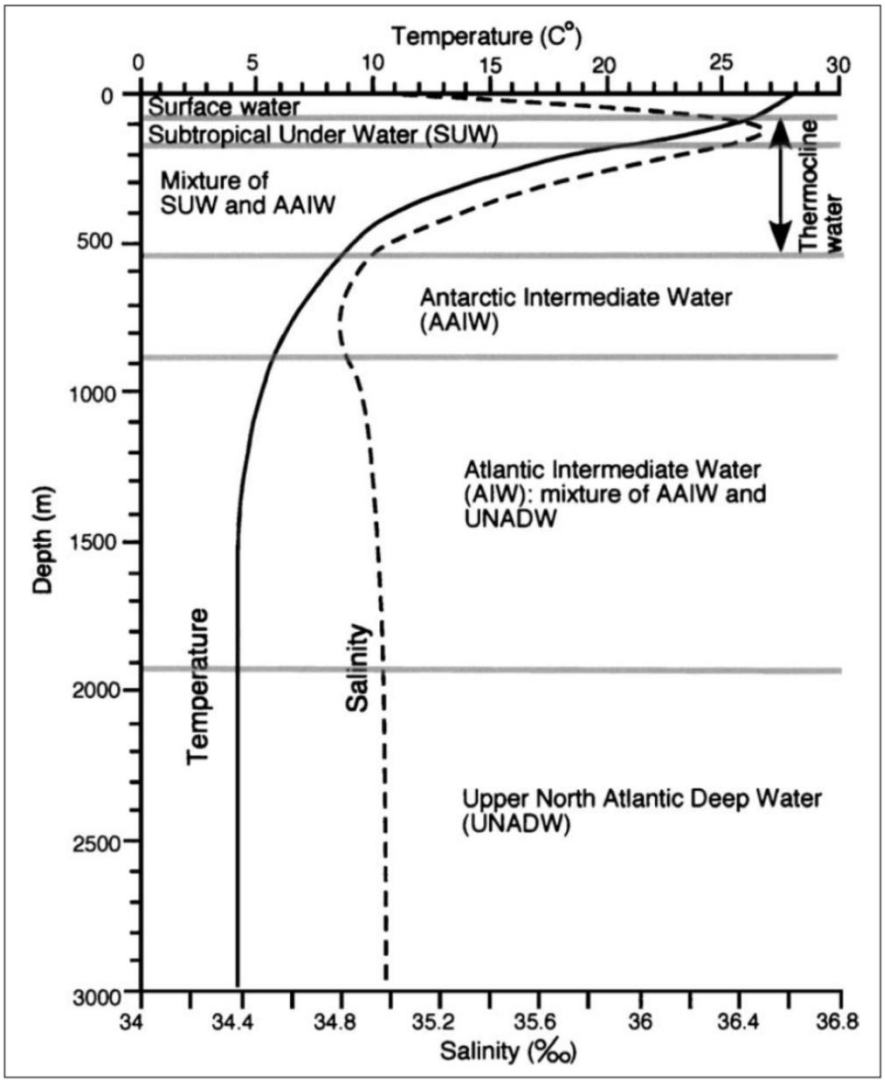

Figure 5.5 - Vertical profiles of temperature and salinity from the southern Caribbean Sea, after [*Wüst*, 1964]. The MD99-2198 core site (at 1330 m water depth) is bathed by a mixture of AAIW and UNADW, termed Atlantic Intermediate Water (AIW). Reproduced from Kameo *et al.* [2004].

The ODP core site 1063 (33°41'N; 57°37'W; 4595 m water depth) is situated on the Bermuda Rise, an area of very high sediment accumulation, mainly sourced from Canadian rivers [*Laine and Hollister*, 1981] (Figure 5.6). Sediments on the north side of the Bermuda Rise are resuspended by the Gulf Stream and deep recirculating gyres [*Laine and Hollister*, 1981]. Primary productivity is low due to the oligotrophic surface waters bounded by the North Atlantic Subtropical Gyre (NASG), and biogenic silica

production rates are amongst some of the lowest in the world ocean [*Brzezinski and Nelson*, 1995; *Nelson and Brzezinski*, 1997].

Despite its distance from the SO, the Bermuda Rise region is still influenced by AAIW, which is characterised by a high-silica signal and can be traced from the Straits of Florida to the northeast, as far north as 60°N [*Tsuchiya*, 1989].

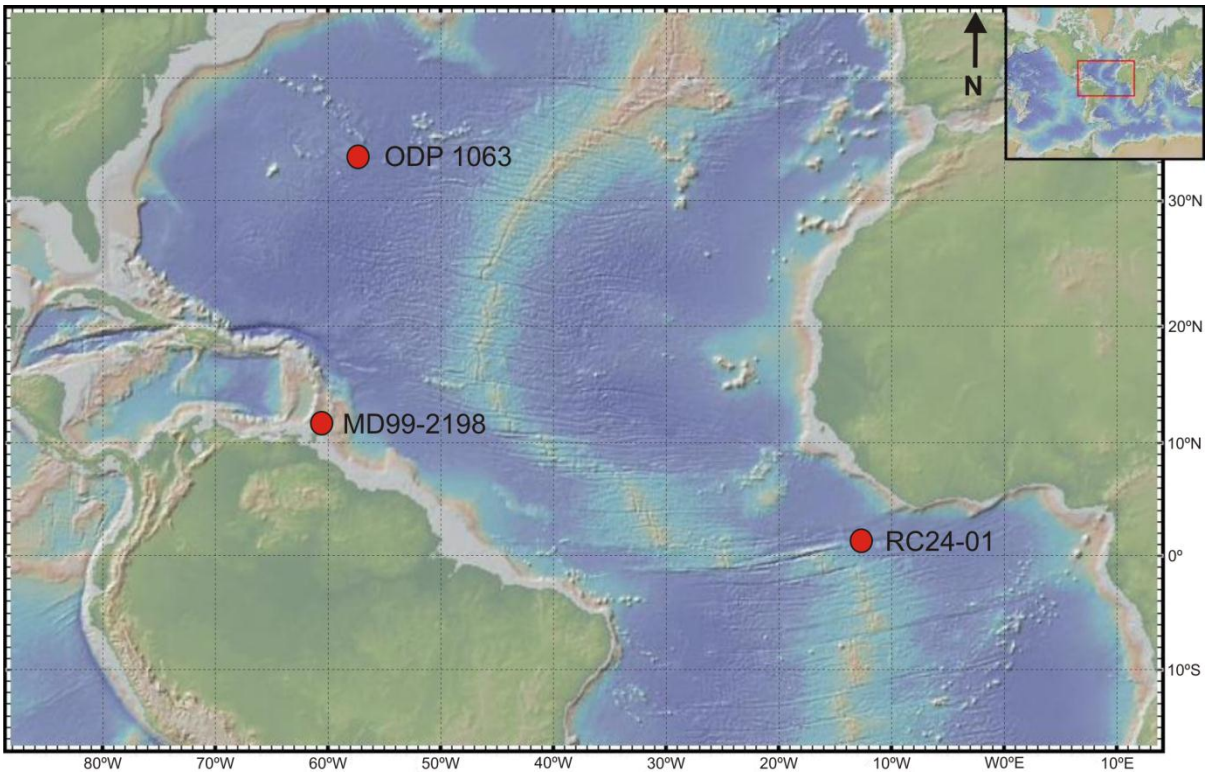

Figure 5.6 – Core locations of MD99-2198, ODP 1063 and RC24-01.

Opal flux records from the core RC24-01 (0˚33'N; 13˚39'W; 3837 m water depth) from the eastern equatorial Atlantic (EEA) were also compared to the Nd and Si isotopic records from MD99-2198 (see Chapter 3 for details of the age control on RC24-01). I measured sedimentary neodymium (Nd) isotopic ratios, expressed as ε_{Nd}; and sponge spicule silicon (Si) isotopic ratios, expressed as δ^{30}Si, were also measured on samples from MD99-2198 spanning the MIS 5/4 transition (~90-43 ka).

Nd isotope ratios were measured on the dispersed Fe-Mn oxyhydroxide phase extracted from fine (<63 μm) fraction of the bulk sediment. Porewater profiles of Rare Earth Elements (REEs) from marine pelagic sediments demonstrate that under oxic to suboxic conditions trace metals such as Nd are scavenged from seawater and incorporated into Fe-Mn oxyhydroxide coatings in the uppermost few centimetres of sediment [*Haley et al.*, 2004]. This observation has been exploited in a number of studies to reconstruct seawater Nd isotopic compositions using such dispersed Fe-Mn

hydroxide coatings, for example [*Rutberg et al.*, 2000; *Bayon et al.*, 2002; *Gutjahr et al.*, 2007; *Gutjahr et al.*, 2008; *Pahnke et al.*, 2008; *Piotrowski et al.*, 2008].

Using the same methodology, Pahnke *et al*. [2008] found that the core top value of MD99-2198 agreed within one epsilon unit with the seawater Nd isotopic compositions from stations near the Tobago Basin [*Piepgras and Wasserburg*, 1987], even though strontium (Sr) isotopes measured on the same leachates deviated significantly from seawater. This observation confirms the mass balance calculations by Gutjahr *et al*. [2007], implying that even in cases of significant detrital contamination of the Sr isotope signal, Nd isotopes can still preserve an authigenic signature. This investigation used exactly the same leaching protocol as Pahnke *et al*. [2008], with confidence that Fe-Mn leachates of bulk sediments at this site yield robust authigenic Nd isotopic compositions.

Core MD99-2198 (12.09˚N; 61.23˚W; 1330 m water depth) was sampled at 10 cm intervals between 1040 and 1110 cm, based on the approximate position of the MIS 5/4 transition from low-resolution benthic $\delta^{18}O$ data (*Globigerinoides sacculifer*) [*R. Zahn*, unpublished data]. Additional core samples were taken at ~100cm intervals either side of the MIS 5a/4 transition. The <63μm fraction of the sample (~4cm^3 bulk) was separated out by wet sieving. All carbonate was removed from the sample using buffered glacial acetic acid, until no signs of a reaction were detectable. Fe-Mn oxides were subsequently extracted using a 0.02 M solution of hydroxylamine hydrochloride (HH) for 2 hours, after [*Chester and Hughes*, 1967]. After drying down the solution at a high temperature to destroy the HH, the samples were redissolved in 3M HNO_3 for two-stage ion chromatography.

Separation of rare earth elements (REE) from the sample matrix was achieved using TRU-spec resin, and separation of Nd from the other REE was achieved using Ln-spec resin. Neodymium isotopes were measured in static mode on a Nu Plasma Multi-Collector Inductively-Coupled Plasma Mass Spectrometer (MC-ICP-MS) in the MAGIC laboratories at Imperial College London. Mass bias correction was accomplished using a $^{146}Nd/^{144}Nd$ ratio of 0.7219. During the course of the sample analyses (3 separate days) JNd_i standards yielded $^{143}Nd/^{144}Nd$ values of 0.512105 ± 0.000017 (2σSD, n=21), 0.512112 ± 0.000012 (2σ SD, n=14), and 0.512057 ± 0.000015 (2σ SD, n=19), respectively. All sample values were normalised to the recommended JNd_i $^{143}Nd/^{144}Nd$ ratio of 0.512115 [*Tanaka et al.*, 2000]. For full details of all methods used see Chapter 2.7, and full results are in Table A3 in printed appendix.

Sponge spicules were picked from the 63-215 μm fraction of the previously-separated coarse (<63 μm) fraction of MD99-2198. The species from which the spicules came were not identified as previous work had suggested that the species of

sponge does not affect the relationship between $[Si(OH)_4]$ and $\delta^{30}Si$ [*Hendry et al.*, 2010].

At Woods Hole Oceanographic Institution (WHOI) the sponge spicules were cleaned in H_2O_2, and dissolved in 0.4M NaOH at 100°C for three days. The solutions were then diluted and acidified to pH ~2-3. A cation exchange resin (BioRad AG50W-X12) was used to quantitatively separate Si from other major ions [*Georg et al.*, 2006]. Si isotopes were measured on a Thermo Neptune Multi-Collector Inductively Coupled Plasma Mass Spectrometer at WHOI. Full operating conditions are described in [*Hendry et al.*, 2010]. Solutions were run at least in duplicate. Samples and bracketing standards were spiked with Mg standard (Inorganic Ventures), and intensity-matched for ^{28}Si and ^{24}Mg signals within 10% (typically within 5%). The $^{29}Si/^{28}Si$ isotope ratios were corrected using a fractionation factor calculated using the measured $^{25}Mg/^{24}Mg$ ratios, see [*Cardinal et al.*, 2003] for details. External reproducibility from a diatomite standard (using all analyses) is 0.1‰ for $\delta^{29}Si$ and 0.23‰ for $\delta^{30}Si$, see Table A4 in printed appendix. For full method see Chapter 2.8 and electronic appendix.

5.1.5 Core Age Control

The North Greenland Ice Core Project (NGRIP) $\delta^{18}O$ record was used as a basis for all core age models used in this study. The NGRIP $\delta^{18}O$ is on the Greenland Ice Core Chronology 2005 (GICC05) age model back to 60 ka [*Andersen et al.*, 2007]. Between 60 and 100 ka the NGRIP $\delta^{18}O$ record has been tuned to the $\delta^{18}O$ record from Chinese speleothems [*Thornalley et al.*, submitted ms], based on the observed in-phase relationship between the strength of the East Asian Monsoon (EAM), as recorded by speleothems, and Greenland temperature during MIS 3 [*Wang et al.*, 2001; *Wang et al.*, 2008].

Age control for MD99-2198 (Figure 5.7) was derived by tuning its record of planktic foraminiferal $\delta^{18}O$ (*Globigerinoides ruber*, white, picked from 250-315 µm of the coarse fraction) to NGRIP $\delta^{18}O$. This approach assumes in-phase behaviour between millennial-scale oscillations in the tropics and the northern hemisphere temperature. We suggest that this is reasonable, because these regions are linked through meridional heat transport and the position of the Intertropical Convergence Zone (ITCZ) (which is sensitive to changes in North Atlantic temperature) [*Hüls and Zahn*, 2000; *Peterson et al.*, 2000; *Lea et al.*, 2003; *Cruz et al.*, 2005]. It has also been demonstrated that the primary control on the $\delta^{18}O$ of rainfall over tropical South America is the amount of precipitation, which is modulated by the position of the ITCZ [*Vuille et al.*, 2003; *Cruz et al.*, 2005].

The L* reflectance index (a measure of sediment brightness) may be used to distinguish sedimentological components such as free and bound Fe, $CaCO_3$, Fe-minerals (e.g. goethite), and clay [*Rogerson et al.*, 2006]. A high-resolution record of core reflectance (similar to L*) from the western tropical Atlantic was used to identify a link between sediment reflectance changes in the Cariaco Basin (northern coastal Venezuela) to Greenland ice core $\delta^{18}O$ changes, thereby demonstrating a clear linkage of the tropical hydrological cycle with high northern latitude climate [*Peterson et al.*, 2000]. In light of this finding, the L* index of MD99-2198 [*Hüls and Zahn*, 2000] can be used to provide additional support for the NGRIP-tuned age model of MD99-2198.

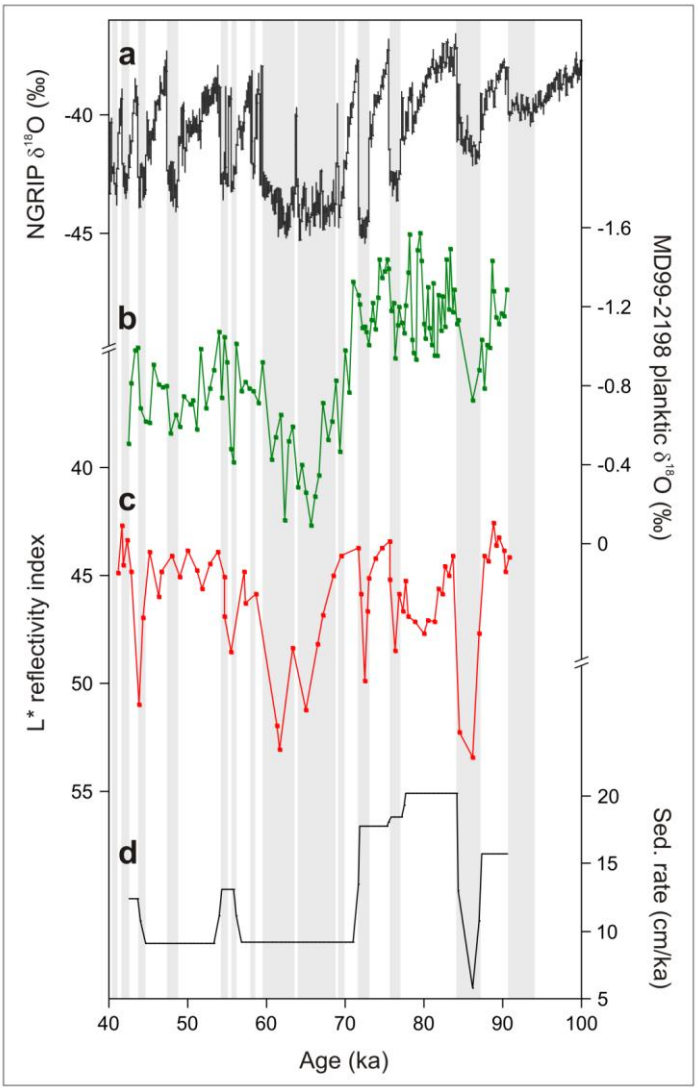

Figure 5.7 – Age model development for MD99-2198. (a) NGRIP $\delta^{18}O$ (grey); (b) planktic $\delta^{18}O$ record for MD99-2198 from white *G. ruber* (green); (c) MD99-2198 L* reflectivity [*Hüls and Zahn*, 2000] (red); (d) MD99-2198 sedimentation rate (cm/ka) (black). Cold periods are represented by grey bands.

Porosity data from MD99-2198 [*Labeyrie and Zahn*, 2005] was used to identify anomalous intervals in the core. On the basis of large increases in porosity (Figure 5.9), two intervals (995-1030 cm and 1375-1435 cm) were interpreted as representing

episodes of core slumping, and consequently were excised from the record, with the core depth modified accordingly. All records are based on the modified core depth.

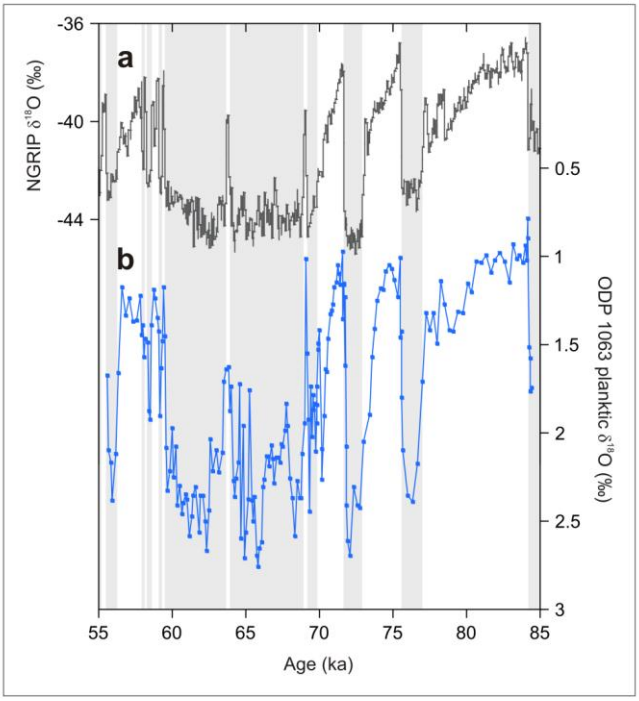

Figure 5.8 – (a) NGRIP $\delta^{18}O$; (b) ODP 1063 planktic $\delta^{18}O$ [*Thornalley et al.*, submitted ms]. Cold periods are represented by grey bands.

ODP 1063 age control was obtained by tuning core reflectance and magnetic susceptibility to records of orbital precession and obliquity [*Grützner et al.*, 2002], and further refined by tuning the planktic $\delta^{18}O$ record (*Globorotalia inflata*) to NGRIP $\delta^{18}O$ (see Figure 5.8) [*Thornalley et al.*, submitted ms].

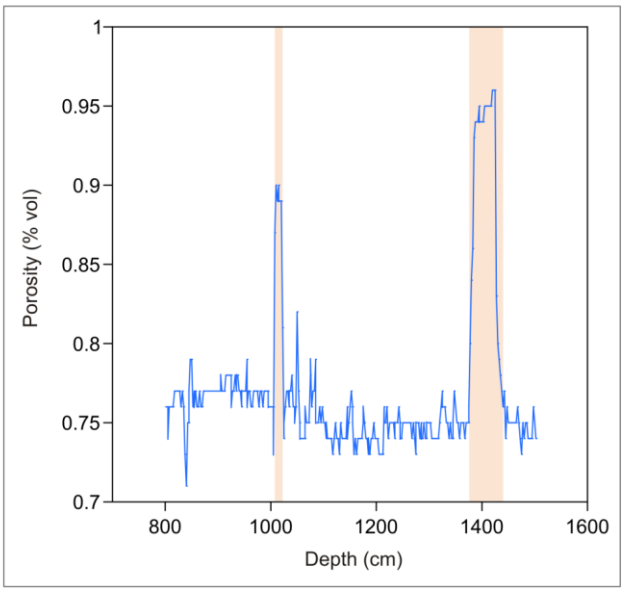

Figure 5.9 – Porosity data [*Labeyrie and Zahn*, 2005] for MD99-2198 plotted versus core depth. The intervals marked by orange bands were judged to be anomalous, and probably reflect slumping events. The marked intervals were excluded from the record and the core depth modified accordingly.

Age control for RC24-01 was derived by tuning its record of %$CaCO_3$ to that of ODP 1063, and the age scale for the Byrd pCO_2 record was derived by tuning the Byrd CH_4 record directly to that of NGRIP, following the approach of [*Ahn and Brook*, 2008].

5.2 Results

5.2.1 Low latitude silicic acid leakage during MIS 4

During the latter part of MIS 5 the Nd isotopic record from MD99-2198 (Figure 5.10, red curve) displays relatively unradiogenic values of ε_{Nd} = -10 to -11, which suggest a significant Northern Component Water (NCW) influence on the western tropical Atlantic during MIS 5a (see Table A3 in printed appendix).

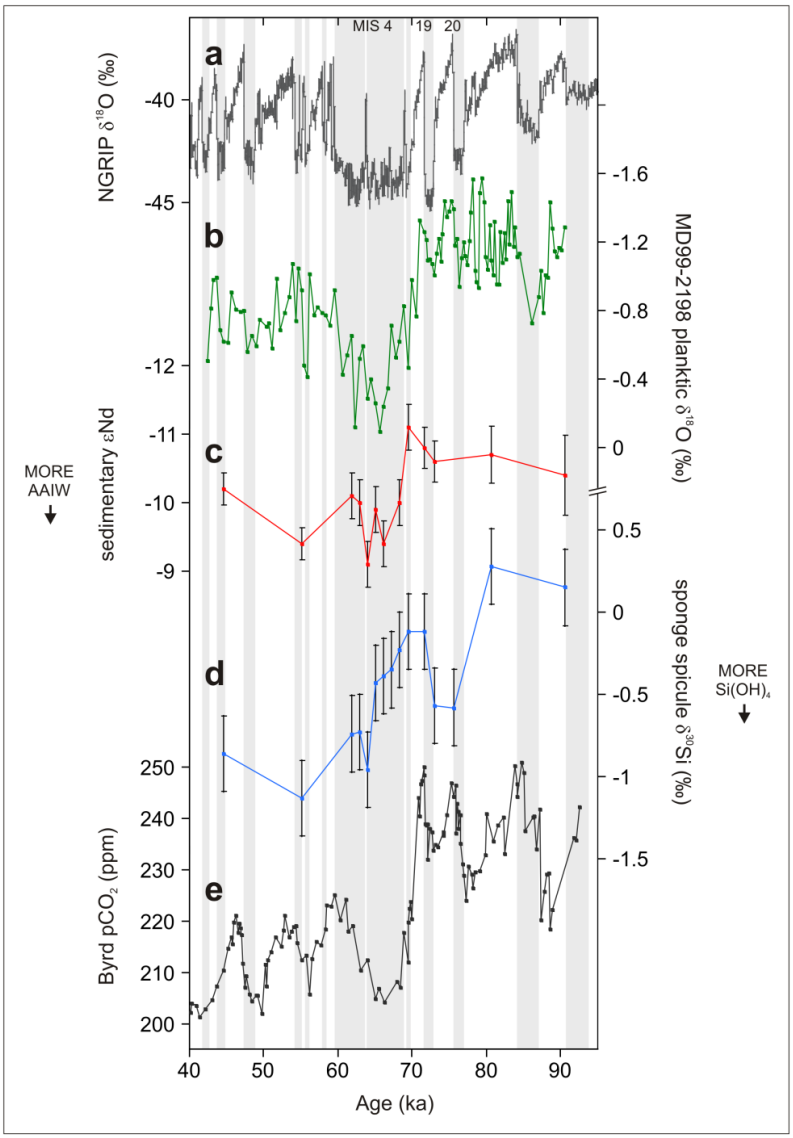

Figure 5.10 - (a) NGRIP $\delta^{18}O$ (‰), placed on an absolute age scale (see information on age model development) (grey); (b) MD99-2198 planktic $\delta^{18}O$ (green); (c) MD99-2198 sedimentary ε_{Nd} (red); (d) MD99-2198 sponge spicule $\delta^{30}Si$ (blue); (e) Byrd (Antarctica) ice core pCO_2 [*Ahn and Brook*, 2008] (black). Cold periods are marked by grey bands, and MIS 4, and cold D-O 19 and 20 are annotated. The results of the Nd and Si isotope analyses shown in this figure are presented in the appendix in Table A3 and A4 respectively.

These values are similar to the core top value of -11 and may correspond to mixing of NADW with a typical ε_{Nd} = -13 to -14 [*Piepgras and Wasserburg*, 1980; *Stordal and Wasserburg*, 1986; *Rutberg et al.*, 2000] with a smaller proportion of more

radiogenic AAIW, as in the modern ocean [*Piepgras and Wasserburg*, 1987; *Lacan and Jeandel*, 2005a].

During MIS 4, our record shows an abrupt change to a less negative (more radiogenic) ε_{Nd}, beginning at ~69 ka, and reaching a maximum at ~65 ka. Subsequently the ε_{Nd} values decrease to less radiogenic values of ε_{Nd} between 65 and 63 ka, with an intermediate NCW/AAIW ε_{Nd} signature of -10, suggesting a slight enhancement of NCW influence. The least negative value attained at ~65 ka is ε_{Nd} = -9.1, which is approaching the South Atlantic/AAIW ε_{Nd} value range of ~ -8 to -9.2 and probably reflects the greater influence of Pacific water with a more radiogenic ε_{Nd} [*Piepgras and Wasserburg*, 1980; 1982; *Jeandel*, 1993]. The rate of change in ε_{Nd} is also notable, with maximum and minimum values of ε_{Nd} separated by only ~7 ka.

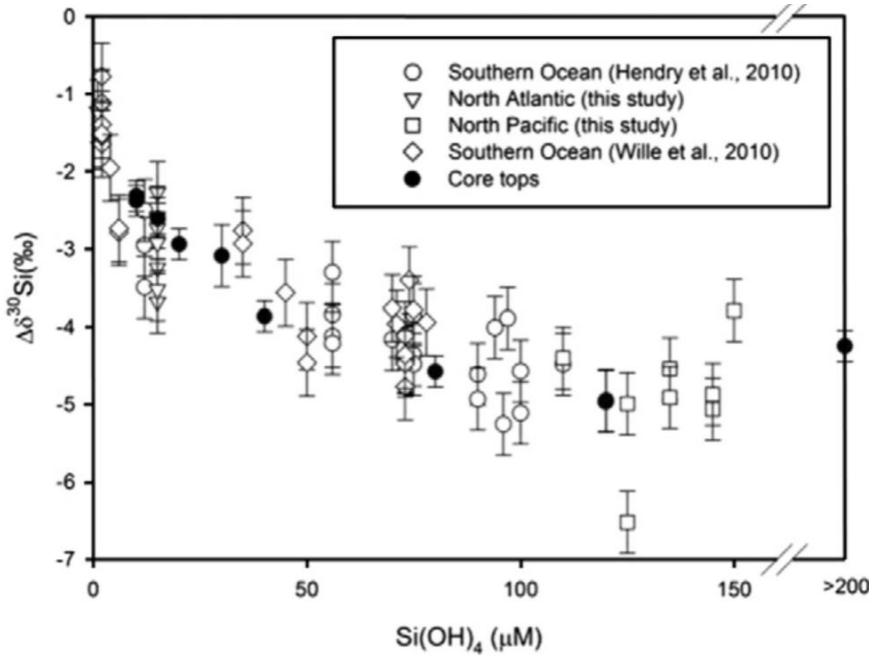

Figure 5.11 - Plot of $\Delta\delta^{30}$Si versus [$Si(OH)_4$] for sponges from a number of locations across the world ocean, with core top $\Delta\delta^{30}$Si values also plotted. Reproduced from Hendry and Robinson [2012]. See Equation 5.3 the for relationship between δ^{30}Si and [$Si(OH)_4$] used to calculate past changes in [$Si(OH)_4$].

The age model places the initiation of the change to more positive ε_{Nd} vales at ~68 ka, i.e. within MIS 4, but the potential error on the age model could also place it within warm D-O 19 (see green curve b in Figure 5.10), and does not preclude the change in ε_{Nd} from being more closely associated with the decline in pCO_2 (grey curve e, Figure 5.10). The ε_{Nd} record changes synchronously with the δ^{30}Si record during MIS 4, suggesting a common driver.

The δ^{30}Si data obtained in this study is interpreted to reflect changes in the ambient silicic acid concentration of AAIW using the relationship in Equation 5.3

[*Hendry and Robinson*, 2012], assuming a seawater $\delta^{30}Si$ value of +1.5 ± 0.07 ‰ for AAIW [*de Souza et al.*, 2012]. The systematic variation in the sponge spicule $\delta^{30}Si$ record of MD99-2198, from values of ~ -0.2 to 0.2 in MIS 5a to a peak MIS 4 value of ~ -0.9 is interpreted as an increase of ~15-20 µM in the silicic acid content of AAIW during MIS 4 relative to MIS 5a, calculated using Equation 5.3:

$$[Si(OH)_4] = (270/\Delta^{30}Si + 6.54)) - 53 \qquad (R^2 = 0.83)$$

Equation 5.3 – Calculation of silicic acid $[Si(OH)_4]$ concentration from sponge spicule $\delta^{30}Si$ data, based on the observed hyperbolic decay function observed when $[Si(OH)_4]$ is regressed against measured sponge spicule $\delta^{30}Si$ (see Figure 5.11) [*Hendry and Robinson*, 2012].

Where $\Delta\delta^{30}Si = \delta^{30}Si_{sponge} - \delta^{30}Si_{seawater}$. We assumed that $\delta^{30}Si_{seawater}$ remained within the range +1.5 to 2‰ within the interval of interest (compared to a modern value of +1.5‰ ± 0.07, 2 standard error) [*de Souza et al.*, 2012]. Whilst the possibility exists that the silicon isotope composition [$\delta^{30}Si(OH)_4$] of AAIW may not have been the same as in the modern ocean due to differences in silica input, this scenario was considered unlikely for two reasons. Firstly, the range in silicic acid concentration (and the silicon isotope composition) in modern AAIW is small, ~ 1.5-1.8 ‰ [*Cardinal et al.*, 2005; *Hendry et al.*, 2010; *de Souza et al.*, 2012] compared to that in sponges [*Hendry and Robinson*, 2012]. Given this variability, the possible range of silicic acid concentrations was plotted (dashed red curve b on Figure 5.12). Secondly, a major change is inferred in the silicic acid content of AAIW over a timescale <10 ka, which is of the same order as the oceanic residence time of dissolved silica, estimated at ~10-15 ka [*Tréguer et al.*, 1995; *Georg et al.,* 2009]. It is therefore suggested that even large changes in silica input to the oceanic reservoir could not alter its silicon isotope composition significantly over the timescale of our record. The results suggest an increase in ambient $[Si(OH)_4]$ of ~15 to 20 µM between MIS 5a and 4 (Figure 6). This increase would probably have been sufficient to alleviate Si limitation on low-latitude diatom production [*Egge and Aksnes*, 1992].

The changes in $\delta^{30}Si$ across MIS 5/4 in the MD99-2198 record are small compared to the range measured by Hendry and Robinson [2012] in different parts of the world ocean, and suffer from a large uncertainty. However, the pattern of variation in the $\delta^{30}Si$ record of MD99-2198 correlates ($r = -0.7$, $p < 0.05$) with that of the ε_{Nd} record, and therefore infers leakage of high-silica intermediate water of a southern origin during MIS 4, as the deep SO and Pacific are the only parts of the world ocean with sufficient silicic acid to affect changes in low latitude intermediate water [*Schlitzer*,

2000]. Also notable in the dataset is the large magnitude (~0.85 ‰) change in Si isotopic composition in the Tobago Basin between ~80 (MIS 5a) and 76 ka (cold D-O 20) which preceded the MIS 4 change (~69-64 ka). The Si isotopic composition remains depleted (indicating greater silicic acid content) into cold D-O 19 at ~73 ka (Figure 5.10). This change in Si isotopic composition is larger than that which occurred during MIS 4, and suggests a switch either in the proportion of AAIW present at intermediate depths in the Tobago Basin, or an increase in the silicic acid content of AAIW, or both.

The transitional depletion of δ^{30}Si values continues from cold D-O 19 (~73 ka), throughout MIS 4 (~69-59 ka) to a maximum value of -1.13 ‰ ~55 ka during MIS 3, before becoming less negative ~44 ka.

5.2.2 Low latitude opal accumulation during MIS 4

Silicic acid leakage during MIS 4 appears to have had no effect on the diatom export productivity at the MD99-2198 core site (green curve c, Figure 5.12). Conversely, the percent opal record from ODP 1063 (green curve (d) in Figure 5.13) demonstrates a sustained increase of ~200 % late in MIS 4 (beginning ~67 ka) from 3 % to 9 % opal.

Percent opal also increased by more than a factor of 3 (from 3 % to 10 %) in D-O stadial 19 (~72 ka); and from 3 % to 12 % in D-O stadial 20 (~77 ka). During both D-O stadials, silicic acid concentrations inferred from the MD99-2198 δ^{30}Si record may have been elevated relative to MIS 5a (Figure 5.10). The percent opal and thorium-normalised opal flux record from RC24-01 (green curve (f) in Figure 5.12) shows an increase in percent opal, and thorium-normalised opal flux [F(opal)]; throughout MIS 4. The increase in opal accumulation began ~ 75 ka, and reached a maximum ~65 ka, apparently within MIS 4. The timing of the increase in opal accumulation in RC24-01 can be constrained with reasonable precision (see RC24-01 age model in Section 3.5.3). The 50 % increase in opal accumulation recorded in RC24-01, from ~0.06 to 0.12 g/cm^2/ka, is approximately coeval with the increase in percent opal in the ODP 1063. The occurrence of increased sedimentary opal occurring within MIS 4 is supported by the robust age model of ODP 1063 (Figure 5.8).

The relationship between the silicic acid content of AAIW, as inferred from the δ^{30}Si record from the Tobago Basin and low latitude diatom productivity is not straightforward. The increases in δ^{30}Si at the Tobago Basin (during cold D-O 20 and 19, and during MIS 4) core site are approximately coeval with transient increases in sedimentary opal as recorded in ODP 1063 (Bermuda Rise).

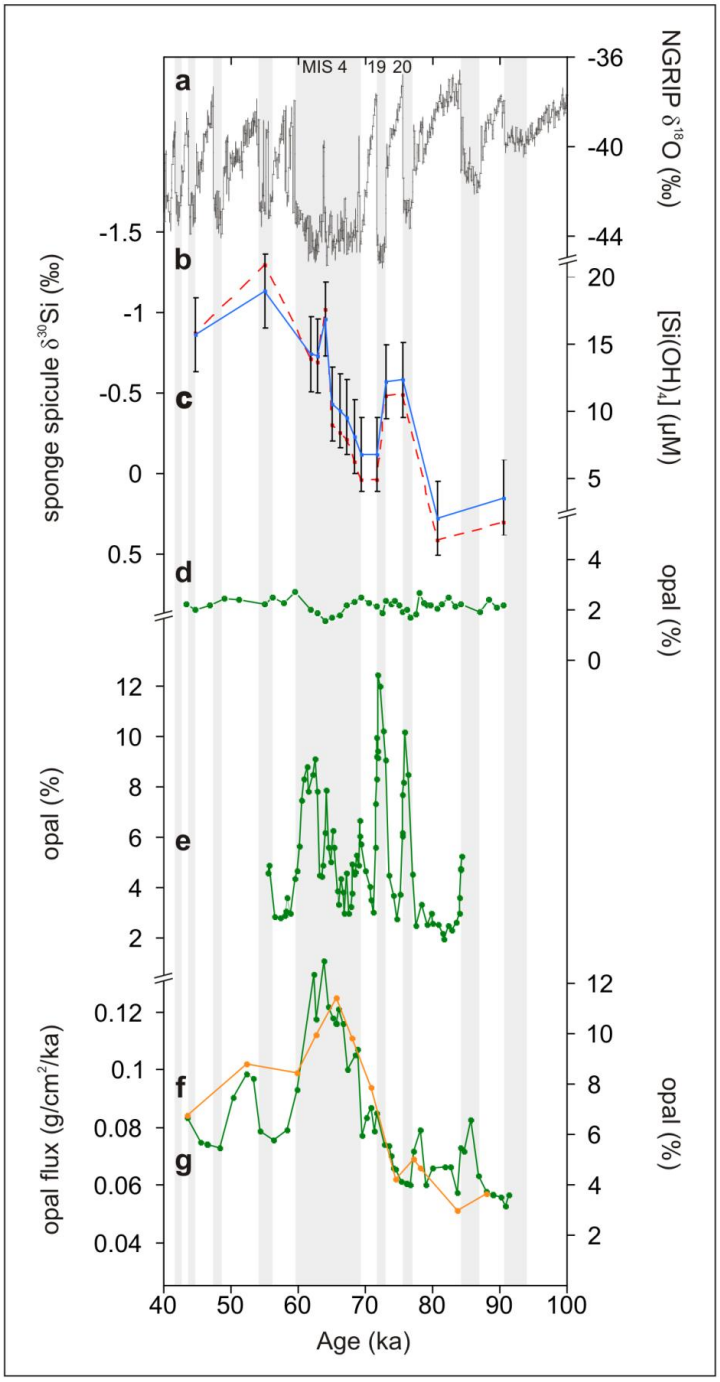

Figure 5.12 - (a) NGRIP $\delta^{18}O$ (‰), placed on an absolute age scale (see Figure 5.7); (b) Palaeo-silicic acid concentrations calculated from Equation 5.3; (c) MD99-2198 $\delta^{30}Si$, plotted with scale inverted relative to Figure 5.10; (d) MD99-2198 opal (%); (e) ODP 1063 opal (%), green curve; (f) RC24-01 thorium-normalised preserved opal flux rate (g/cm^2/ka), orange curve; (g) RC24-01 opal (%), green curve. All percent opal measurements are plotted on the same y-axis. Cold periods are marked by grey bands and MIS 4, and cold D-O 19 and 20 are annotated.

The equatorial Atlantic core RC24-01 records a sustained increase in sedimentary opal beginning ~69 ka at the MIS 5a/4 boundary, but does not show sharp increases during cold D-O 20 and 19. Contrasted with these records is the sedimentary opal record from MD99-2198 (Tobago Basin), which shows little variability throughout

MIS 5a, 4 and 3. These results suggest that diatom productivity is governed by a range of factors, including Si availability, strength and mode of upwelling, and Fe availability.

5.3 Discussion

The records of ε_{Nd} and $\delta^{30}Si$ from MD99-2198 (Figure 5.10) suggest a re-organisation of water masses in the low-latitude oceans during the transition in to MIS 4. The ε_{Nd} during MIS 5a is -10 to -11, similar to modern values, and is analogous to the modern scenario of Atlantic Intermediate Water (AIW), a combination of AAIW and Upper North Atlantic Deep Water (UNADW) [*Wüst*, 1964; *Haddad and Droxler*, 1996], bathing the MD99-2198 core site. The reconstruction of ε_{Nd} in MIS 5a further implies that some variety of northern component water (NCW), with a similar Nd isotopic signature to modern NADW, was influencing the mid depth western tropical Atlantic in this interval. This inference is in agreement with studies from several locations in the Atlantic, using sedimentary $_{xs}(^{231}Pa/^{230}Th)_0$ as an indicator of the strength of Atlantic Meridional Overturning Circulation (AMOC) changes as well as ε_{Nd} [*Rutberg et al.*, 2000; *Piotrowski et al.*, 2005; *Guihou et al.*, 2010].

In order to understand the ε_{Nd} record generated from MD99-2198, the effect that other water masses could have had on the Nd isotopic record in the Tobago Basin was considered. Southern and western Indian Ocean intermediate and deep waters have $\varepsilon_{Nd} \approx$ -7 to -9 (reflecting dominance of northward flowing circumpolar water), [*Piepgras and Wasserburg*, 1982; *Bertram and Elderfield*, 1993; *Jeandel*, 1993; *Jeandel et al.*, 1998], which are similar to the Nd isotopic composition of AAIW. Deep and intermediate waters from the Indian Ocean therefore have the potential to have influenced the intermediate depth Tobago Basin and contributed to the more radiogenic values of ε_{Nd} recorded during MIS 4.

A major mechanism for the exchange of heat and salt in surface and intermediate waters between the Indian Ocean and the South Atlantic is the intermittent shedding of large-scale rings, filaments and eddies of Indian Ocean water from the Agulhas current and retroflection off South Africa [*de Ruijter et al.*, 1999]. Studies have demonstrated that Agulhas Rings have sufficient density to potentially influence any depth in the Atlantic [*Schouten et al.*, 2000; *van Aken et al.*, 2003]. However, it is unlikely that variability in Agulhas Leakage had a significant influence on the Nd isotopic record of MD99-2198, as a study of the exchange of heat and salt between the Atlantic and Indian Oceans via the Agulhas retroflection suggests that the input of Indian Ocean water into the South Atlantic was relatively small during MIS 4 [*Peeters et al.*, 2004]. The inference of lower levels of Agulhas leakage in glacial periods is also consistent with models of Atlantic THC [*Knorr and Lohmann*, 2003; 2007]. However, newer results question the presumption of reduced Agulhas leakage during glacial

periods [*Martínez-Méndez et al.*, 2010], and so the influence of Indian Ocean water on the western tropical Atlantic remains difficult to constrain, and cannot be ruled out entirely as an influence on the MD99-2198 Nd isotopic record.

Another water mass that may have influenced the hydrography and hence the Nd isotopic composition in the Tobago Basin during MIS 5/4 is Mediterranean Overflow Water (MOW). Modern MOW at the outflow from the Strait of Gibraltar is characterised by an ε_{Nd} of -9.5 [*Tachikawa et al.*, 2004], a value within error of the minimum ε_{Nd} recorded during MIS 4 in MD99-2198. Records of benthic $\delta^{13}C$ from the Caribbean and Mediterranean Seas indicate that MOW may have extended to the Caribbean during the LGM, and that it was a more volumetrically important water mass during the last glacial period [*Oppo and Fairbanks*, 1987], therefore MOW cannot be fully excluded as a potential contributor to the Nd isotopic excursion recorded during MIS 4 in MD99-2198.

It is also possible for vertical changes in water mass boundaries to have influenced the Nd isotopic record from the Tobago Basin [*Xie et al.*, 2012]. MD99-2198 lies at the lower limit of modern AAIW (1330m, see Figure 5.1), and may therefore be sensitive to changes in the depth of the boundary between AAIW and Glacial North Atlantic Intermediate Water (GNAIW), a glacial analogue of NADW [*Oppo and Lehman*, 1993]. If AAIW shoaled to ~1000 metres during glacial periods, as predicted to have occurred in the Last Glacial Maximum (LGM) [*Curry and Oppo*, 2005], or was absent, the MD99-2198 core site would have been bathed by GNAIW [*Curry and Oppo*, 2005; *Marchitto and Broecker*, 2006]. GNAIW had a similar Nd isotopic signature to modern NADW [*van de Flierdt et al.*, 2006; *Foster et al.*, 2007], and therefore would have contributed to a less radiogenic ε_{Nd} during MIS 4, which is contrary to the trend in ε_{Nd} observed during MIS 4 in MD99-2198. Hence, shoaling of the AAIW-GNAIW boundary was discounted as an influence on the Nd isotopic record.

Additionally, a potential effect on the Nd isotopic record may result from "boundary exchange" processes at ocean-continental margins. Early diagenesis and scavenging processes are probably important controls on Nd sources and sinks [*Lacan and Jeandel*, 2005b]. However, little is known of the spatial and temporal variability of this process, hence I do not attempt to account for it in this investigation.

Finally, the above interpretations all assume an invariant Nd isotopic composition of the source region of southern water masses. This assumption may, however, be compromised by the fact that decreased export of NADW/GNAIW to the Southern Ocean will have an effect on the Nd isotopic composition of water masses formed in the Southern Ocean. Data extracted from a deep-sea coral skeleton from the Drake Passage indicate that intermediate waters during Heinrich Stadial (HS) 1 (~16.7 ka) became more radiogenic [*Robinson and van de Flierdt*, 2009], probably due to

reduced input of North Atlantic-sourced Nd to the Drake Passage, associated with decreased NADW export [*McManus et al.*, 2004]; resulting in more 'Pacific-like' values in the Southern Ocean. It remains to be seen whether a similar scenario could have made the Nd isotopic composition of SAMW and AAIW source regions more radiogenic during MIS 4. Heinrich Stadials are considered times of most pronounced changes in ocean circulation [*McManus et al.*, 2004; *Pahnke et al.*, 2008] and hence I considered similar magnitude changes in seawater Nd isotopes in the Southern Ocean during MIS 4 less likely. While the ε_{Nd} excursion recorded during MIS 4 may have been the result of decreased NADW export, my preferred interpretation is that elevated values reflect increased influence of AAIW in the Tobago Basin.

The results of this study take on more significance when they are examined alongside the Si isotope data. The correlation ($r = -0.7$ at $p < 0.05$) between the Nd isotopic record and the silicon isotopic record of silicic acid concentrations in MD99-2198 strongly imply that the water's origin was in the subantarctic zone (~100 µM of silicic acid) [*Schlitzer*, 2000]; as the mid- and northern Atlantic is depleted in silicic acid due to depletion by diatoms in subtropical anticyclonic gyre systems [*Levitus et al.*, 1993], with much lower values (see Figure 5.1). The only region of the ocean that contains sufficient silicic acid to affect a significant change in the silicic acid content of AAIW is the deep Southern Ocean and the deep Pacific [*Schlitzer*, 2000].

The most important sources of dissolved silica to the ocean are rivers [*Tréguer et al.*, 1995], which must also be considered as potential suppliers of silicic acid to the Tobago Basin during MIS 4. Although dissolved constituents carried by rivers cannot be mixed to the depths occupied by AAIW, the dissolved silica content of intermediate waters may potentially be influenced by the export production of diatoms and their subsequent remineralisation at depth. Amazon plume waters, for example, support high diatom productivity [*DeMaster et al.*, 1991; *DeMaster et al.*, 1996], and therefore have the potential to alter the silicic acid concentration of ocean water underlying areas where diatom export productivity has been enhanced through the influence of riverine silica.

Similarly, reversible scavenging of Nd by suspended riverine particles from major Indian rivers are able to mix a surface ε_{Nd} signature through the thermocline to intermediate depths in the eastern Indian Ocean [*Amakawa et al.*, 2000; *Nozaki and Alibo*, 2003]. If a similar situation existed in the Caribbean Sea during MIS 4, then the outflow of the Amazon and Orinoco Rivers may have been able to influence the Nd isotopic composition of AAIW.

The modern eastern Caribbean Sea is influenced by freshwater input from both the Orinoco River [*Chérubin and Richardson*, 2007] and the Amazon River [*Chérubin and Richardson*, 2007; *Molleri et al.*, 2010]. Input of sediment to the eastern Caribbean

during glacial periods is likely to have been lower from the Amazon River, due to decreased rainfall over South America because of a southward shift in the position of the ITCZ [*Peterson and Haug*, 2006].

However, sedimentary input from the Orinoco River may have been higher [*Bowles and Fleischer*, 1985] because despite Orinoco outflow also being modulated by the position of the ITCZ, the proximity of the Aves Ridge to the Orinoco plume may reflect volumetric increases in Orinoco River water during glacial lowstand [*Bowles and Fleischer*, 1985]. Despite this finding, other evidence suggests that Orinoco River water is not a significant contributor of dissolved silica to the Tobago Basin; firstly, Orinoco River water contains generally low concentrations of dissolved and suspended constituents due to a high runoff [*Lewis and Saunders*, 1989]. More importantly, sediments from the lower Orinoco River display a less radiogenic Nd isotopic composition (ε_{Nd} ~ -14) [*Goldstein et al.*, 1997], relative to Amazon River sediments (ε_{Nd} ~ -9.2) [*Goldstein et al.*, 1984]; which presumably would have made ε_{Nd} values during MIS 4 less radiogenic than those recorded in this study if Orinoco water was a significant contributor to the Tobago Basin during this interval.

A study of the $\delta^{13}C$ of benthic foraminifera from the southeast Pacific (east of New Zealand) has been interpreted as reflecting lower glacial formation rates of AAIW for the past three G-IG cycles [*Pahnke and Zahn*, 2005; *Crosta et al.*, 2007]. However, Pahnke and Zahn [2005] also acknowledge that similar glacial excursions in benthic $\delta^{13}C$ could have been produced by upward displacement of the boundary between AAIW, and Upper Circumpolar Deep Water (UCDW), which exhibits more depleted glacial $\delta^{13}C$ values [*Hodell et al.*, 2003].

Spatial displacement of the AAIW-UCDW boundary is consistent with the inferred movement of westerly wind belts equatorward during glacial periods [*Toggweiler et al.*, 2006]. Additionally, positive $\delta^{13}C$ excursions interpreted by Pahnke and Zahn [2005] as periods of enhanced AAIW formation, are correlated with periods of enhanced upwelling inferred from increased opal fluxes, recorded near the APF in the Atlantic sector of the SO [*Anderson et al.*, 2009]. A more southerly position of the westerly wind belt increases upwelling whilst simultaneously displacing the AAIW-UCDW boundary southward and downward near the core site used in the Pahnke and Zahn [2005] study. Furthermore, a number of benthic $\delta^{13}C$ records from various depths around New Zealand support the notion of displacement of the AAIW-UCDW boundary [*Elmore et al.*, 2011]. Whilst debate surrounding AAIW formation rates remains unresolved, it can be argued that there is no inconsistency between the inference of increased AAIW expression in the mid-depth western tropical Atlantic during MIS 4, and the benthic $\delta^{13}C$ record of Pahnke and Zahn [2005].

Elevated silicic acid in AAIW influencing the mid-depth western tropical Atlantic during MIS 4 appears to have been prevented from reaching the euphotic zone there, and therefore prevented from promoting greater diatom export productivity in the Tobago Basin, based on the opal record from MD99-2198. A lack of upwelling in this interval may have been related to the depth of the western Atlantic thermocline, which is thought to have deepened throughout MIS 4 [*Rühlemann et al.*, 1996; *Höll et al.*, 1999].

Conversely, in the EEA, the thermocline appears to have been shallower than it was in the western Atlantic during MIS 4 [*Abrantes*, 2000; *Flores et al.*, 2000], due to enhanced northeast trade wind strength [*Flores et al.*, 2000; *Abrantes*, 2003], and greater rates of upwelling [*Jansen et al.*, 1996; *Abrantes*, 2000]; which may explain why leaked silicic acid during MIS 4 may have been able to influence diatom export productivity in the EEA but not the western equatorial Atlantic. The increase in opal accumulation is coeval with more depleted δ^{30}Si values (i.e. greater silicic acid availability) during MIS 4, but the most depleted values of δ^{30}Si occur ~55 ka during MIS 3, which implies that some other control (possibly a change in the low latitude upwelling regime) prevented this excess silicic acid being fully utilised by diatoms during this period.

Furthermore, the opal increase in RC24-01 is correlated with a range of palaeoproductivity proxies (see Chapter 3.7.3), as well as glacial opal increases in other cores from across the EEA [*Gardner and Burckle*, 1975; *Stabell*, 1986; *Abrantes*, 2001], which strongly implies that the increase in opal accumulation during MIS 4 was a result of enhanced diatom export productivity rather than enhanced opal preservation. Authigenic uranium (U_{auth}) is used as a proxy for organic carbon flux [*Kumar et al.*, 1995; *Anderson et al.*, 1998; *Chase et al.*, 2001], and provides support for the interpretation of an enhanced organic carbon flux during MIS 4 from the F(TOC) record of RC24-01 (see Chapter 3). Additionally, the interpretation of an overall enhancement in export productivity during MIS 4 is consistent with a palaeoproductivity reconstruction using organic carbon and planktic foraminiferal transfer functions from an EEA core [*Sarnthein et al.*, 1992].

Despite the coincidence of the enrichment of the Atlantic thermocline with silica, and the enhancement of low latitude opal export; the mechanism required to raise AAIW from depths of 800-1000 metres into the euphotic zone (<200 metres) is as yet unidentified. If an increase in the silicic acid concentration of glacial AAIW meant that the silicic acid content of SAMW was similarly elevated, then SAMW could be more readily entrained into the euphotic zone than the deeper AAIW. The density of SAMW (σ_0 = 26.5-27.1) [*Hanawa and Talley*, 2001] is less than that of AAIW (σ_0 = 27.1-27.6) [*Piola and Georgi*, 1982; *Wong et al.*, 1999] when both water masses form, and it has

been demonstrated through the analysis of the $\Delta^{14}C$ of coral that surface water upwelled in the equatorial Pacific may trace its origin to the subantarctic zone of the Pacific [*Toggweiler et al.*, 1991], which has been identified as a SAMW formation region [*Aoki et al.*, 2007]. SAMW has also been identified as the main preformed nutrient conduit to the low latitudes, and has the potential to alleviate low latitude Si-limitation of diatom productivity [*Sarmiento et al.*, 2004]. If some unknown glacial process allowed silica-enriched SAMW to upwell in the equatorial Atlantic, it could explain the observed pattern of opal export (see below). A recent ocean circulation experiment using the HYbrid isopycnic-cartesian Coordinate Ocean general circulation Model (HYCOM) has demonstrated that SAMW-related tracer re-emergence in the Atlantic at tropical latitudes may be strongly dependent on shear-induced turbulent mixing, and furthermore that significant tracer re-emergence occurs in the North Atlantic [*Zuo et al.*, 2012]. This latter finding may offer a possible explanation for the patterns of sedimentary opal in ODP 1063 recorded in this study. The study of SAMW dynamics during glacial periods continues to be an interesting topic for future research.

The record of sedimentary opal from ODP 1063 (Bermuda Rise) is in line with results from a number of cores from the EEA, in that it shows an increase in late MIS 4. Interpreted as evidence of increased diatom productivity at the Bermuda Rise, and consistent with other studies [*Keigwin and Boyle*, 2008; *Gil et al.*, 2009; *Lippold et al.*, 2009], these findings imply that the northward penetration of AAIW was enhanced relative to its modern extent [*Schlitzer*, 2000] during northern hemisphere stadials, which is also in agreement with the findings of [*Pahnke et al.*, 2008]. The Bermuda Rise today is a stratified, oligotrophic environment with low diatom productivity [*Heath*, 1974], but the site has recorded significant past increases in diatom productivity [*Keigwin and Boyle*, 2008; *Gil et al.*, 2009; *Lippold et al.*, 2009]. Processes such as cold-core rings and mode-water eddies may have enabled silicic acid within AAIW/SAMW to be brought into the euphotic zone, and therefore to have enhanced diatom productivity [‘*The Ring Group’*, 1981; *Krause et al.*, 2009].

Melting icebergs are also thought to have the potential to affect diatom export productivity in waters overlying the Bermuda Rise, possibly due to their amplification of cold-core rings [*Gil et al.*, 2009]. Additionally, increased glacial eolian supply of Saharan dust to the Bermuda Rise [*Herwitz et al.*, 1996] and subsequent dissolution of particulate silica [*Tréguer et al.*, 1995], cannot be excluded as an influence on opal accumulation in ODP 1063, particularly as Fe appears to be important in co-limitation of diatom growth [*Timmermans et al.*, 2004; *Brzezinski et al.*, 2011].

More work is needed to attempt to constrain the amount of silicic acid leakage before accepting that a SALH-scenario was responsible for the enhanced sedimentary opal observed in ODP 1063 during MIS 4. Additional comparisons of thorium-

normalised opal flux rates with other proxies (for example, past eolian silica input), in order to better understand the controls on diatom export productivity at the Bermuda Rise. Although ODP 1063 shows an increased opal content during MIS 4, its highest values of percent opal occur during cold D-O 20 (~ 76 ka) and 19 (~ 72 ka) (Figure 5.12).

The most fundamental component of the SALH is its ability to decrease the low latitude export ratio of inorganic to organic carbon ($CaCO_3$:C_{org} rain ratio) from its present value of ~0.1 [*Sarmiento et al.*, 2002; *Matsumoto and Sarmiento*, 2008], through changes in surface- and whole-ocean alkalinity [*Matsumoto et al.*, 2002]. Hence, if the increase in diatom productivity over carbonate-producers caused a change in the $CaCO_3$:C_{org} rain ratio, it should be manifest in the record of pCO_2 [*Archer et al.*, 2000a; *Sigman and Boyle*, 2000]. The timing of the initiation of the changes in the MD99-2198 Nd and Si isotope records suggest that the SALH was probably not a primary driver of the ~ 47 ppmv pCO_2 drawdown that occurred across the MIS 5a/4 transition [*Ahn and Brook*, 2008], although age model error does potentially allow for much closer association (within ~1ka) of the change in pCO_2 recorded in the Byrd ice core, with the initiation of significant changes in the ε_{Nd} and δ^{30}Si records in MD99-2198 (Figure 5.10).

Nonetheless, the SALH is still likely to have provided an additional feedback that contributed to the low glacial values of pCO_2, possibly through diatoms enhancing the export of organic carbon to sediment and thereby increasing the water column gradient in dissolved inorganic carbon [*Ridgwell*, 2003]. A modelling study of the SALH scenario suggested that the potential pCO_2 drawdown associated with low-latitude changes in the carbonate pump alone is modest, at around 9 ppmv. However, this result is achieved using a highly simplified 8-box geochemical model configuration [*Matsumoto et al.*, 2002]. Matsumoto et al. [2002] note that a far greater pCO_2 drawdown (35-47 ppmv) may be achieved using General Circulation Models (GCMs), as GCMs have a greater sensitivity to low latitude pCO_2 forcing [*Matsumoto et al.*, 2002].

This finding leaves open the possibility that the SALH may have had a significant impact on pCO_2 drawdown during MIS 4, however, the data suggest that the SALH-associated pCO_2 drawdown must have occurred over longer timescales. The rapid pCO_2 decrease seen during MIS 4 is therefore probably mostly attributable to some combination of physical oceanographic mechanisms, with further significant contributions from marine biota [*Hain et al.*, 2010; *Sigman et al.*, 2010].

5.4 Conclusions

Used together, these new ε_{Nd} and δ^{30}Si records from the Tobago Basin are the first direct evidence of silica leakage in glacial AAIW. The silicic acid content of AASW may be more important in determining the silicic acid content of AAIW than its volumetric production rate, although this remains unconfirmed. A mechanism that is then able to transport sufficient quantities of AAIW from depths of 800-1000 m into the euphotic zone, such that it may affect diatom productivity, remains unknown.

Increases in opal accumulation in the eastern equatorial Atlantic during MIS 4, and increases in sedimentary opal in Bermuda Rise sediment during cold D-O 20, 19 and MIS 4 are consistent with the SALH; however they do not support overall enhanced diatom productivity in the low latitude ocean *per se*. The changes in the δ^{30}Si record are transitional, whilst the opal increases are transient, again suggesting that there is no simple relationship between low latitude diatom productivity with the silicic acid content of AAIW. It is probable therefore that co-limitation of diatom productivity by other factor(s) occurred.

The enhancement of diatom productivity is likely to strongly depend on the local rate of upwelling, and the delivery of Fe to surface waters. Where conditions suitable for diatom dominance are all met, enhancement of silica-based primary productivity over carbonate-based primary productivity may occur, consistent with the SALH. The silicon isotopic data additionally suggests that the greatest abundance of silicic acid was present in the Tobago Basin during MIS 3 (~55 ka), and that this was somehow from prevented from reaching the equatorial Atlantic euphotic zone, and/or that lower aeolian dust levels during MIS 3 prevented complete utilisation the excess silicic acid by low latitude diatoms.

Based on the age model used in this investigation, the SALH was probably not the primary driver of the ~47 ppmv pCO_2 decrease observed at the initiation of MIS 4 [*Ahn and Brook*, 2008], but could nonetheless have contributed to pCO_2 drawdown later during MIS 4 with the development of full glacial conditions.

Chapter 6 – Predictions of pCO_2 drawdown associated with the SALH during MIS 4: a simple 8-box geochemical model approach

6.1 Introduction

6.1.1 Background

A fundamental part of the SALH, and the main reason why it is of interest to palaeoclimatologists is its effect on atmospheric pCO_2 (see Chapter 1). In order to gauge the effect that the SALH may have had on pCO_2, data-constrained climate models must be used. A wide variety of climate models exist, which may be grouped into three general categories: box models, EMICs (Earth-system models of intermediate complexity) and GCMs (General Circulation Models or Global Climate Models).

Box models are highly simplified versions of complicated natural systems, which assume that chemical species or parameters of interest (e.g. nitrate in seawater) are mixed uniformly throughout discrete boxes (or reservoirs), which are linked by fluxes. The concentration of chemical species within a box may be modified as a function of time because of fluxes in and out of the box, due to production, consumption or decay of that species. The main advantage of box models is their simplicity, they usually do not require extensive computation and can give quick results. As such, they are useful for exploring new concepts and mechanisms of climate change. Their disadvantage is that they are of extremely coarse resolution, and are therefore usually limited to modelling large-scale processes, and must have highly parameterised constraints.

EMICs are intermediate between box models and GCMs in terms of size and complexity, and offer a trade-off between model resolution and computational cost. This is of great benefit to palaeoclimate research, which can only occasionally use GCMs to model the past climate, as it takes long periods of time (and amounts of computer power) to obtain results. The models Climber-3, MOM (Modular Ocean Model)-3, and the Grid ENabled Integrated Earth system model (GENIE) are examples of EMICs.

GCMs are highly complex 3D models that numerically solve the physical conservation equations for energy, mass, momentum and moisture as well as the equations of state associated with the general circulation of a planetary atmosphere and/or ocean. The main disadvantage of GCMs is that they are highly expensive in terms of computational cost. In one GCM, a horizontal resolution scale for atmospheric processes of 50 km, (with 32 vertical levels); and for oceanic processes a horizontal resolution of 8 km (low latitude) to 28 km (high latitude), with 50 vertical levels has

been achieved recently by researchers [*Delworth et al.*, 2011]. Coupled atmosphere-ocean GCMs (AOGCMs, such as HadCM3) are usually best suited to short-term meteorological and climatological predictions (10^1 – 10^2 years), rather than palaeoclimatological applications.

In this investigation, I use a simple biogeochemical box model to test the affect that the SALH may have had on pCO_2 and the past climate. Although the GENIE model offered a potential alternative, it is not yet able to realistically model the oceanic dissolved silica cycle (currently under development). The purpose of this modelling exercise was to assess what proportion of the ~47 ppmv drawdown recorded in Antarctic ice cores [*Ahn and Brook*, 2008] at the initiation of Marine Isotope Stage (MIS)-4 ~70 ka [*Martinson et al.*, 1987] may be reasonably attributed to the SALH mechanism.

6.1.2 A previous modelling test of the SALH

A SALH-scenario for the Last Glacial Maximum (LGM) was tested using a simple eight-box model [*Matsumoto et al.*, 2002], which used the following configuration (Figure 6.1). The eight boxes are 1) Continental Margin (cm), 2) Polar (po), 3) Subantarctic (sa), 4) Low Latitude (ll), 5) North (no), 6) Middle (md), 7) Atlantic (at), and 8) Deep (dp). Of these, the Continental Margin, Polar, Subantarctic, Low Latitude and North boxes represent the surface ocean, and the Middle, Atlantic and Deep boxes represent the subsurface. Most of the box dimensions are taken from an original seven-box model [*Toggweiler*, 1999], which was itself derived from an earlier three-box model [*Toggweiler and Sarmiento*, 1985] (Table 6.1). The model has eight state variables: silicic acid, nitrate, oxygen, potential temperature, alkalinity, ΣCO_2, $\delta^{13}C$, and $\Delta^{14}C$. All variables were normalised to a salinity of 35 psu. Gas exchange velocity, used in the determination of model atmospheric CO_2, was 3 m day^{-1}, after Toggweiler and Sarmiento [1985].

Table 6.1 – Model dimensions, derived from previous box models [*Toggweiler and Sarmiento*, 1985; *Toggweiler*, 1999]. Diatom fractions are derived from [*Nelson et al.*, 1995], Si:N ratios for high latitude waters are derived from [*Franck et al.*, 2000; *Pondaven et al.*, 2000], and low-latitude Si:N ratios are derived from [*Hutchins and Bruland*, 1998; *Takeda*, 1998]. Table data reproduced from Matsumoto *et al.* [2002].

Ocean box	Fractional Area % (10^{12} m^2)	Box depth (m)	Volume (10^{15} m^3)	Diatom fraction (%)	Si:N
Continental Margin	3.0 (10.5)	250	2.62	90.0	6.0
Polar	7.0 (24.4)	250	6.11	90.0	6.0
Subantarctic	7.0 (24.4)	250	6.11	70.0	6.0
North	3.0 (10.5)	250	2.62	60.0	3.0
Low-Latitude	80.0 (279.2)	100	27.92	50.0	1.5
Middle	-	500	117.79	-	-
Atlantic	-	900	144.14	-	-
Deep	-	3700	984.71	-	-
Total Ocean	100.0 (349.0)	-	1292.00	-	-

Interglacial model controls were determined by inverse modelling, rather than 'hand-tuning' variables. Inverse modelling solutions are shown in Table 6.3. For more detailed information see Matsumoto *et al*. [2002].

The interglacial state corresponded to observed nutrient distributions, see references within Matsumoto *et al*. [2002]. Preindustrial interglacial pCO_2 concentration was 280 ppmv, which agrees closely with ice core data [*Petit et al.*, 1999]. The value for the global $CaCO_3$:C_{org} export ratio, which is of key importance in controlling glacial-interglacial pCO_2 [*Archer et al.*, 2000a; *Sigman and Boyle*, 2000], used in the model was ~ 0.1 [*Sarmiento et al.*, 2002].

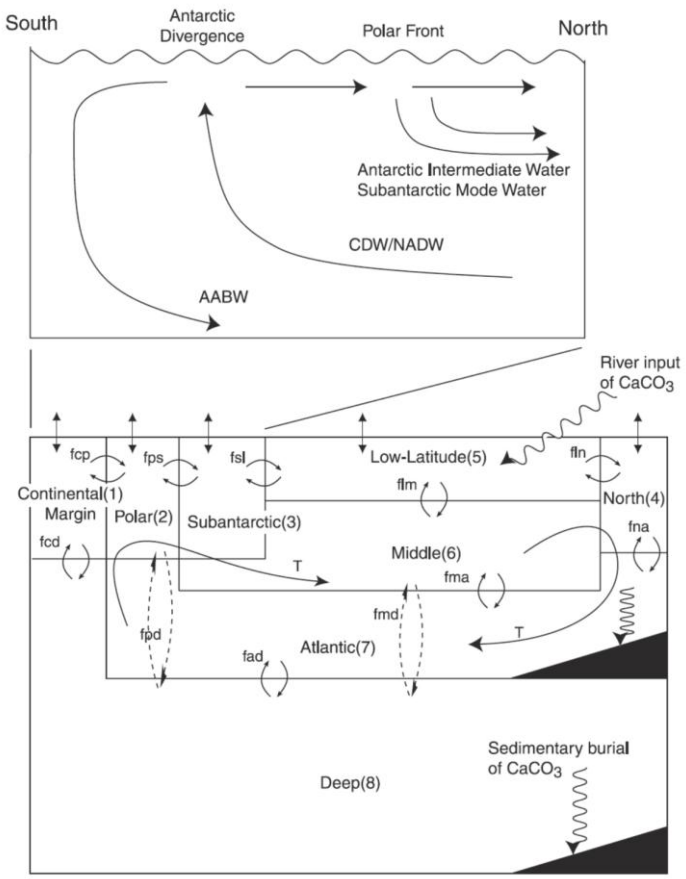

Figure 6.1 – Schematic representation of the simple 8-box model used in testing the SALH. Model dimensions and the interglacial control settings are shown in Table 1 (below). Figure and data table are reproduced from Matsumoto *et al*. [2002].

This value differs from previous estimates of 0.2-0.3 [*Toggweiler and Sarmiento*, 1985; *Broecker and Peng*, 1987; *Sigman et al.*, 1998; *Toggweiler*, 1999; *Archer et al.*, 2000a]. These estimates were derived from in-situ CO_2 measurements to calculate excess alkalinity and ΣCO_2 in Atlantic and Pacific deep water [*Li et al.*, 1969]. This method attributes the average difference between surface and deep alkalinity and

ΣCO_2 concentrations to simple remineralisation of particulates, and does not account for the contribution of nitrate to alkalinity.

Matsumoto *et al*. [2002] offer two reasons to explain why the use of a $CaCO_3$:C_{org} export ratio of 0.1 in their box model is more appropriate. Firstly, excess alkalinity and ΣCO_2 in deep waters are affected by the preferential remineralisation of organic matter over $CaCO_3$, which was not accounted for in the study of Li *et al*. [1969].

Table 6.2 – Model state for interglacial control [*Matsumoto et al.*, 2002]. Concentrations of the eight state variables are determined using water fluxes calculated by inverse modelling, see Table 6.3. Total inventories are given in moles, with $\delta^{13}C$ and $\Delta^{14}C$ in pseudo-moles. Pseudo-molar concentrations represent the fractional deviation of the isotopic ratios of the sample from the reference (i.e. $1+\delta^{13}C/1000$ and $1+\Delta^{14}C/1000$), weighted by the abundance of their 'carrier', which is pCO_2 in the atmosphere and ΣCO_2 in the ocean. All inventories are consistent with Toggweiler and Sarmiento [1985], and with estimates from the dataset of Levitus *et al.* [1993]. Reproduced from Matsumoto *et al*. [2002].

Box	θ, °C	NO_3^- (μmol kg^{-1})	H_4SiO_4 (μmol kg^{-1})	Si:N Ratio	O_2 (μmol kg^{-1})	Alkalinity (μmol eq kg^{-1})	ΣCO2 (μmol kg^{-1})	$\delta^{13}C$ (‰)	$\Delta^{14}C$ (‰)
cm	-1.0	24.5	59.8	2.4	295	2423	2259	1.4	-149
po	2.5	19.0	35.0	1.8	294	2405	2204	1.7	-115
sa	6.0	11.2	9.1	0.8	293	2309	2147	2.2	-85
no	3.3	8.4	4.9	0.6	313	2349	2115	1.8	-63
ll	22.1	4.1	3.7	0.9	208	2339	1987	2.0	-32
md	16.9	21.0	16.5	0.8	81	2346	2145	0.8	-62
dp	2.3	34.3	102.9	3.0	144	2428	2326	0.5	-180
Atmos	-	-	-		-	-	277 (ppm)	-6.6	9.9
Inventory		4.01×10^{16}	1.11×10^{17}			3.19×10^{18}	3.07×10^{18}	3.07×10^{18}	2.60×10^{18}

When the preferential remineralisation of organic matter is taken into account, a later study predicted a $CaCO_3$:C_{org} export ratio of 0.12 or less [*Yamanaka and Tajika*, 1997]. Furthermore, work on $CaCO_3$ cycling in a GCM by the same authors suggest that the modern ratio should be 0.08-0.1, which was supported by a subsequent study using an ocean biogeochemical box model [*Sarmiento et al.*, 2002].

The model of Matsumoto *et al*. [2002] simulated silicic acid leakage from the SO by reducing the Si:N uptake of diatoms in the Southern Ocean surface boxes, and allowing it to leak to the Low-Latitude box. When the model was run without consumption of leaked silicic acid by diatoms, in a 'non-SALH' scenario (i.e. no change in the status quo with regard to $CaCO_3$ export and pCO_2), the silicic acid concentration increased monotonically in the Low-Latitude box, as the high latitude Si:N (consumption) was progressively reduced from 6 to 1. To simulate silicic acid utilisation by diatoms in a 'SALH scenario', the silicic acid in the Low-Latitude was restored to its

original concentration, implying that diatoms contributed a larger share of primary productivity (whilst total organic carbon export was held constant). The result of this simulated silica leakage was a 9 ppmv decrease in atmospheric pCO_2.

Table 6.3 – Inverse model solutions for water exchange fluxes and organic carbon productivity. All water exchange fluxes (f) are in Sverdrups (Sv), 1 Sv = 1 x 10^6 m^3 sec^{-1}. Productivity is based on inversion results without prior estimates. Reproduced from Matsumoto *et al*. [2002].

	Priors	Solutions	A Priori	A Posteriori	Monte Carlo	Total
			Water Fluxes (Sv)			
T	20.0	11.2	100.0	73.5	10.4	74.2
fcd	20.0	28.9	100.0	59.1	7.4	59.6
fcp	20.0	14.3	100.0	84.4	7.1	84.7
fpd	20.0	18.0	100.0	47.8	8.6	48.6
fps	20.0	21.3	100.0	82.6	12.6	83.6
fsl	20.0	9.0	100.0	58.1	8.9	58.8
flm	60.0	54.9	100.0	58.0	10.2	58.9
fln	20.0	0.8	100.0	64.0	7.9	64.5
fna	20.0	10.0	100.0	71.4	6.7	71.7
fmd	20.0	5.6	100.0	37.0	2.8	37.1
fma	20.0	7.9	100.0	69.8	4.5	69.9
fad	20.0	2.0	100.0	39.2	3.9	39.4
			Production (Gt C yr^{-1})			
Continental Margin	0.70	0.47	10.00	1.26	0.17	1.27
Polar	0.70	0.53	10.00	1.48	0.14	1.49
Subantarctic	0.70	0.54	10.00	1.40	0.18	1.41
North	0.70	0.65	10.00	1.36	0.19	1.37
Low-Latitude	2.77	2.84	10.00	1.83	0.18	1.84

An alternative scenario involved complete consumption of excess silicic acid in AASW in the Subantarctic box, as suggested by some studies [*Kumar et al.*, 1995; *Francois et al.*, 1997; *Chase et al.*, 2001]. In this case, the subantarctic diatom fraction soon approached 100% when the Si:N export ratio was lowered from 6 to 5, because the organic carbon production in the Subantarctic box was much lower than that in the Low Latitude box. In this scenario any excess silicic acid leaked to lower latitudes, resulting in pCO_2 drawdown of 2 ppmv.

In an attempt to utilise more silicic acid in the Subantarctic box Matsumoto *et al*. [2002] lowered its initial diatom fraction from the prescribed 70%, but the atmospheric pCO_2 drawdown associated with this scenario was still only 2 ppmv, because the initial $CaCO_3$:C_{org} export ratio of non-diatoms was decreased in the interglacial control to compensate for the lowered Subantarctic diatom fraction, in order to maintain the global $CaCO_3$:C_{org} of 0.1 [*Sarmiento et al.*, 2002].

Under a slightly different glacial scenario, Matsumoto *et al*. [2002] were able to achieve greater atmospheric pCO_2 drawdown (24 ppmv) in their model when the overall export productivity is increased in the Subantarctic box, which may be expected to occur in glacial periods [*Petit et al.*, 1999] in response to enhanced Fe availability

[*Coale et al.*, 1996; *Hutchins et al.*, 2001; *Coale et al.*, 2004]. An increase in productivity is fuelled by available nitrate in the Subantarctic box, which is therefore mostly responsible for the increased pCO_2 drawdown. The partial effect on pCO_2 of weakening the carbonate pump under this model scenario is still a 2 ppmv drawdown, however [*Matsumoto et al.*, 2002].

Matsumoto *et al*. [2002] were able to achieve their most significant atmospheric pCO_2 drawdown in their 8-box model when the effect of carbonate compensation were included [*Broecker and Peng*, 1987]. A reduction of the global $CaCO_3$:C_{org} export ratio due to diatoms outcompeting carbonate-producing phytoplankton would reduce the export of $CaCO_3$ as calcite from the low-latitude surface ocean. In this scenario, the riverine input of alkalinity to the ocean exceeds the rate of calcite burial (which removes alkalinity from the surface ocean), and so the calcite lysocline deepens in order to preserve and bury more calcite to restore the oceanic alkalinity balance (see Chapter 1.4).

Model simulation of carbonate compensation can be achieved in two ways: "closed system" and "open system" [*Sigman et al.*, 1998]. In the former, the ocean-atmosphere system in the model is "closed" with respect to the input and output of alkalinity. In a closed system, sedimentary processes involving the burial of calcite are ignored, and hence such models do not simulate the calcite lysocline. Models utilising closed system carbonate compensation operate simply by restoring the deep ocean box carbonate ion concentration to its initial value by increasing or decreasing concentrations of alkalinity and DIC (ΣCO_2) equally in all the boxes in a 2:1 ratio [*Broecker and Peng*, 1987]. In the case of the Matsumoto *et al*. [2002] model, pCO_2 drawdown associated with closed system carbonate compensation is ~5 ppmv, achieved when the high-latitude Si:N export is reduced from 6 to 1, and the carbonate pump is most reduced [*Matsumoto et al.*, 2002].

Conversely, open systems model the major features of the oceanic carbonate system, including sedimentary calcite dissolution and burial, and the riverine input of alkalinity. Under their second scenario of silicic acid leakage (leakage to the Low-Latitude box), open system carbonate compensation in the model of Matsumoto *et al*. [2002] was able to draw down pCO_2 to ~ 230 ppmv when the high latitude Si:N export ratio is reduced from 6 to 3, which is an approximate decrease of 50 ppmv from the interglacial control value. This drawdown was accompanied by a ~ 1 km deepening of the model's calcite lysocline. The pCO_2 drawdown associated with a larger leakage of excess silicic (i.e. Si:N <3) acid did not reach steady state and therefore was not considered realistic [*Matsumoto et al.*, 2002]. In this Si:N range, surface $CaCO_3$ production is smaller than riverine input, and therefore $CaCO_3$ burial can never match riverine input, ensuring perpetual oceanic alkalinity increase and pCO_2 decrease. This

suggests that 3 is the upper limit of the high-latitude Si:N export ratios in models of this type.

While the SALH appears unable to account for peak glacial atmospheric pCO_2 using a simple box model, without invoking additional mechanisms such as SO stratification. GCMs show (as noted by Matsumoto *et al*. [2002]) much higher pCO_2 sensitivity to a reduced carbonate pump [*Archer et al.*, 2000b]. Therefore, if GCMs are more able to faithfully simulate the changes in the pCO_2 of the atmosphere than box modelling approaches, then the SALH may still be a viable mechanism to account for peak glacial atmospheric pCO_2. The finding that GCMs are more sensitive to changes in the low latitude carbonate pump comes from a comparison of the 'Harvardton Bear Equilibration Index' (HBEI), which is an expression of the ratio of the rate of gas exchange between the ocean and atmosphere to the rate of thermohaline circulation [*Broecker et al.*, 1999]. The findings concerning differences in HBEI between different model types, with GCM HBEIs being generally much greater than those of box models, suggest that exchange processes between warm and cold areas of the ocean is extremely important in determining the chemical properties of those regions [*Broecker et al.*, 1999].

In the conclusions to their study, Matsumoto *et al*. [2002] were unable to distinguish between the model scenarios of leakage to low latitude and enhancement of diatom productivity relative to carbonate producers (SALH scenario); or complete consumption in the subantarctic zone. Based on the finding of direct palaeoceanographic evidence of silicic acid leakage to the tropical western Atlantic in southern-sourced intermediate water (see Chapter 5), we propose that the second model scenario is a valid one, and assume it to be the case in our simulations.

In this investigation we return to the simplified box modelling approach to further test the SALH, but here utilising the additional constraints provided by our investigation of a suite of cores from the equatorial Atlantic during the Marine Isotope Stage (MIS) 5/4 transition ~ 71 ka [*Martinson et al.*, 1987], (see Chapters 3, 4 and 5). Explicitly, we compare the output of model runs with opal flux rate constraints from Chapter 3, and model a scenario of increased low latitude productivity, which is qualitatively supported by our Chapter 3 data. While a comprehensive GCM approach is beyond the scope of this study, the estimates of the SALH impact presented below provide as first order quantitative estimate of the sensitivity of atmospheric pCO_2 to SALH. Model equations were coded in MATLAB by Jamie Wilson (Cardiff University).

6.1.3 Model equations

Tracer concentrations (C_x) in surface boxes were calculated in the following way (Equation 6.1), where C_y is the tracer concentration in box *y*, $f_{y\rightarrow x}$ is the flux from

box *y* into box *x*, $f_{x\rightarrow y}$ is the flux from box *x* into box *y,* P_x is productivity in box x, and vol_x is the box volume (m^3):

Equation 6.1

$$\frac{dC_x}{dt} = \frac{(C_y . f_{y\rightarrow x} - C_x . f_{x\text{-}y} + P_x)}{vol_x}$$

Tracer concentrations (C_x) in intermediate and deep boxes were calculated according to Equation 6.2:

Equation 6.2

$$\frac{dC_x}{dt} = \frac{(C_y . f_{y\rightarrow x} - C_x . f_{x\text{-}y} + R_x)}{vol_x}$$

Where C_y is the tracer concentration in box *y*, $f_{y\rightarrow x}$ is the flux from box *y* into box *x*, $f_{x\rightarrow y}$ is the flux from box *x* into box *y,* R_x is tracer remineralisation in box x, and vol_x is the box volume (m^3). Total water fluxes were calculated by [*Matsumoto et al.*, 2002], and were therefore given to our model as input conditions.

Production of organic carbon in the original model was driven by restoring the input of nitrate into the Low Latitude box to its original value. The production and remineralisation of organic matter was assumed to occur in the stoichiometric ratio of P:N: C_{org}:-O_2 = 1:16:117:170 [*Anderson and Sarmiento*, 1994]. The large flux term *flm* (Figure 6.1), determined by inverse modelling, ensured that the Low Latitude box accounted for 56% (2.84 Gt C yr^{-1}) of total primary productivity [*Matsumoto et al.*, 2002]. Remineralisation of organic matter in box x (R_{Corg_X}) proceeded according to the relationship below, after [*Yamanaka and Tajika*, 1997]:

Equation 6.3

$$R_{Corg_X} = \left(\frac{z}{\mathbf{100}_{\,m}}\right)^{\mathbf{-0.9}}$$

Where z is the depth in the water column (in metres), and 100 m is the length scale for remineralisation in the Low Latitude box (the same as box depth), representing complete dissolution of POM below the euphotic zone [*Yamanaka and Tajika*, 1997]. The settling speed of POM is assumed to be 100m/day [*Suess*, 1980], much faster than horizontal advection, which is assumed to be negligible [*Yamanaka and Tajika*, 1997]. In the high-latitude (Continental Margin, Subantarctic, Polar and North) boxes, the box depth (250 m) is used as the length scale of remineralisation. However, it was found when this POM remineralisation profile was used, the model's NO_3^- concentrations no longer matched those of Matsumoto *et al*. [2002], hence the remineralisation depth was adjusted to match tracer concentrations between the models.

Production of $CaCO_3$ in each box was a function of the fraction of non-diatoms in each box (calculated by subtracting the fraction of diatoms assigned to each box by Matsumoto *et al*. [2002], from 1, see Table 6.1), nitrate export, and a ratio of $CaCO_3$:nitrate in non-diatom producers. The $CaCO_3$:nitrate ratio was set to ensure that the global interglacial control $CaCO_3$:C_{org} has a value ~0.1 [*Sarmiento et al.*, 2002]. The remineralisation of $CaCO_3$ (R_{CaCO3}) proceeded according to the relationship below [*Yamanaka and Tajika*, 1996]. For a lack of information, Matsumoto *et al*. [2002] use the same remineralisation profile for opal, which was also used in the new model, with a remineralisation depth of 3800 m (closest to the model of Matsumoto *et al*. [2002]):

Equation 6.4

$$R_{CaCO3} = \exp\left(\frac{-\boldsymbol{z}}{\boldsymbol{d}}\right)$$

Where *z* is water depth (in metres), and *d* is an e-folding length scale of calcite flux, which is assumed to be 1500 m (calcite shallow profile), 2500 m, 3500 m (calcite control profile), or 5500 m (calcite deep profile), see [*Yamanaka and Tajika*, 1996] for more information. In the new model the calcite control profile (3500 m) was used.

Alkalinity in surface box x (C_{Alk_x}) was calculated in the following way, assuming that each mole of sinking $CaCO_3$ exported removes one mole of dissolved inorganic carbon (DIC), and two equivalent moles of alkalinity [*Broecker and Peng*, 1987]. Each mole of nitrate exported was assumed to add one mole of alkalinity:

Equation 6.5

$$\frac{dC_{Alk_x}}{dt} = \frac{(CAlk_y . f_{y\rightarrow x} - CAlk_x . f_{x\text{-}y} - 2.(CaCO_{3_exp_x}) + Nexp)}{vol_x}$$

Where $CaCO_{3_exp_x}$ is the export flux of calcite, and N_{exp} is the export of nitrate from surface boxes. Calculation of total inorganic carbon (ΣCO_2) (otherwise known as DIC) in surface boxes was carried out using the following equation:

Equation 6.6

$$\frac{dC_{\Sigma CO2_x}}{dt} = \frac{(C_{\Sigma CO2_y_ocean} . f_{y\rightarrow x} - CC_{\Sigma CO2_x_ocean} . f_{x\text{-}y} - (CaCO_{3_exp_x}) + C_{\Sigma CO2_atm})}{vol_x}$$

Where $C_{\Sigma CO2_x_ocean}$ is the ΣCO_2 concentration in the surface ocean box x, $C_{\Sigma CO2_y_ocean}$ is the ΣCO_2 concentration in the surface ocean box y and $C_{\Sigma CO2_atm}$ is the ΣCO_2 content of the atmosphere. The model atmosphere exchanges carbon with the atmosphere, driven by the pCO_2 gradient across the air-sea interface, and uses a "piston velocity" of 3 m day^{-1}, after [*Toggweiler and Sarmiento*, 1985; *Matsumoto et al.*,

2002]. See below for calculation of pCO_2 in the surface ocean boxes and the model atmosphere.

ΣCO_2 for the intermediate and deep boxes was calculated in the following way:

Equation 6.7

$$\frac{dC_{\Sigma CO2_x}}{dt} = \frac{(C_{\Sigma CO2_y_ocean} \cdot f_{y\rightarrow x} - CC_{\Sigma CO2_x_ocean} \cdot f_{x+} R_{POM+} R_{CaCO3})}{vol_x}$$

Where R_{POM} is all POM remineralisation that occurs in the box (according to Equation 6.3), and R_{CaCO3} is all $CaCO_3$ remineralisation that occurs in that box (according to Equation 6.4).

The partial pressure of CO_2 in equilibrium with seawater (pCO_2) (see Equation 6.8) was calculated using an algorithm developed by Zeebe and Wolf-Gladrow [2001], see case 15, appendix B, pp 277 in Zeebe and Wolf-Gladrow [2001]:

Equation 6.8

$$pCO_2 = \frac{[DIC]}{K_0} \frac{[H^+]^2}{[H^+]^2 + K_1[H^+] + K_1K_2}$$

Equation 6.8 was derived by rearranging and substituting the concentration definitions (DIC, Alk, TB) as defined below [*Sarmiento and Gruber*, 2006]:

Equation 6.9

$$DIC = [H_2CO_3^*] + [HCO_3^-] + [CO_3^{2-}]$$

Equation 6.10

$$Alk = [HCO_3^-] + 2[CO_3^{2-}] + [OH^-] + [H^+] + [B(OH)_4^-]$$

Equation 6.11

$$\text{Total Borate (TB)} = [B(OH)_4^-] + [H_3BO_3]$$

K_0, K_1, K_2, K_w and K_b are the equilibrium constants for the following equilibrium series:

Equation 6.12

$$CO_{2(gas)} + H_2O \overset{}{\underset{K0}{\rightleftarrows}} H_2CO_3^*$$

Equation 6.13

$$H_2CO_3^* \overset{}{\underset{K1}{\rightleftarrows}} H^+ + HCO_3^-$$

Equation 6.14

$$HCO_3^- \overset{}{\underset{K2}{\rightleftarrows}} + H^+ + CO_3^{2-}$$

Equation 6.15

$$H_2O \overleftrightarrow{KW} H^+ + OH^-$$

Equation 6.16

$$H_3BO_3 + H_2O \overleftrightarrow{KB} H^+ + B(OH)_4^-$$

Equation 6.17

$$K_0 = \frac{[H_2CO_3^*]}{pCO_2}$$

Equation 6.18

$$K_1 = \frac{[H^+][HCO_3^-]}{[H_2CO_3^*]}$$

Equation 6.19

$$K_2 = \frac{[H^+][CO_3^{2-}]}{[HCO_3^-]}$$

Equation 6.20

$$K_w = [H^+][OH^-]$$

Equation 6.21

$$K_b = \frac{[H^+][B(OH)_4^-]}{[H_3BO_3]}$$

* H_2CO_3 is a hypothetical species, as it is difficult to analytically distinguish between the two species $CO_{2(aq)}$ and H_2CO_3 [*Stumm and Morgan*, 1981; *Dickson and Goyet*, 1994]. Equilibrium constants are then calculated as follows [*Sarmiento and Gruber*, 2006]:

The equations used to calculate seawater equilibrium constants are the same as those set out in Table 8.2.2 in [*Sarmiento and Gruber*, 2006], where *T* = temperatures (in ° Kelvin), and *S* = salinity on the practical salinity scale (psu). For the purposes of our model we use a salinity of 35 psu, after Matsumoto et al. [2002].

Equation 6.22 – Solubility of CO_2 (mol kg^{-1} atm^{-1}) [*Weiss*, 1974]

$$ln\,K0 = -60.2409 + 93.4517\left(\frac{100}{T}\right) + 23.3585\,ln\left(\frac{T}{100}\right) + S\left(0.023517 - 0.023656\left(\frac{T}{100}\right) + 0.0047036\left(\frac{T}{100}\right)2\right)$$

Equation 6.23 – Dissociation constant (K_1) of $CO_2^{\dagger}$ (mol kg^{-1}) [*Mehrbach et al.*, 1973] as refitted by [*Dickson and Millero*, 1987].

$$-\log K_1 = -62.008 + \frac{3670.7}{T} + 9.7944 \ln(T) - 0.0118\ S + 0.000116\ S^2$$

Equation 6.24 - Dissociation constant (K_2) of $CO_2^{\dagger}$ (mol kg^{-1}) [*Mehrbach et al.*, 1973] as refitted by [*Dickson and Millero*, 1987].

$$-\log K_2 = +4.777 + \frac{1394.7}{T} - 0.0184\ S + 0.000118\ S^2$$

†All dissociation constants are stated with respect to the seawater pH scale [*Dickson*, 1993].

Equation 6.25 – Dissociation constant of $H_2O^{\dagger}$ [(mol kg^{-1})^2] [*Millero*, 1995]

$$\ln K_w = 148.96502 + \frac{-13847.26}{T} - 23.6521 \ln(T) + S^2 \left(-5.977 + \frac{118.67}{T} + 1.0495 \ln(T)\right) - 0.01615\ S$$

Equation 6.26 – Borate dissociation constant (mol kg^{-1}) [*Dickson*, 1990]

$$\ln K_b = \frac{1}{T} - (-8966.9 - 2890.53\ S^{0.5} - 77.942\ S = 1.728\ S^{1.5} - 0.0996\ S^2) + 148.0248$$
$$+ 137.1942\ S^{0.5} + 1.62142\ S + 0.053105\ S^{0.5}\ T + \ln(T)\ (-24.4344 - 25.085\ S^{0.5} - 0.2474\ S)$$

Equation 6.27 – Total boron (TB) equation (µmol kg^{-1}) [*Uppström*, 1974]

$$TB = 11.88\ .\ S$$

The change in pCO_2 of the model atmosphere over time was calculated as a function of air-sea gas flux assuming a "piston velocity" of 3 m day^{-1}, after Toggweiler and Sarmiento [1985] and Matsumoto *et al*. [2002], box surface area, CO_2 solubility (Equation 6.22) and surface ocean pCO_2 (Equation 6.8). The total pCO_2 from all surface boxes was mixed uniformly into an atmosphere with a molar volume of 1.773 x 10^{20} moles [*Toggweiler*, 1999]:

Equation 6.28

$$\frac{dC_{pCO2_atm}}{dt} = \frac{((pCO_{2_ocean} - pCO_{2_atm})\ .\ GF.\ A_{surf_box})}{vol_{atm}}$$

Where pCO_{2_ocean} is the combined pCO_2 of all surface boxes, pCO_{2_atm} is the atmospheric pCO_2, GF is the gas flux ("piston velocity"), $A_{surf\text{-}box}$ is the combined surface area of the surface oceanic boxes and vol_{atm} is the volume of the atmosphere (in moles).

To account for changes in the depth of the calcite lysocline, we couple the output from our model to a simple sedimentary model, following the approach to Matsumoto *et al*. [2002]. The model simulates the accumulation and dissolution of calcite on the seafloor, and allows the model system to be "open" with respect to the carbonate alkalinity budget. The depth of the calcite lysocline mediates the distribution of $CaCO_3$ burial by depth, and is controlled primarily by the calcite saturation depth, the point at which the carbonate ion concentration saturated with respect to calcite is equal to the bottom water carbonate ion concentration [CO_3^{2-}] (see Chapter 1.4).

Calcite dissolution is driven in the sediment model according to the parameterisation of Sigman et al [1998], where dissolution is given in units of µmol $CaCO_3$ cm^{-2} yr^{-1}, carbonate ion concentrations are in units of mol kg^{-1} and $F_{calcite}$ is the fraction of calcite in the sediment mixed layer:

Equation 6.29

$$d = 20.36 \times 10^{12}([CO_3^{2-}]_{saturation} - [CO_3^{2-}]_{bottom\ water})^{2.35} \cdot \sqrt{F_{calcite}}$$

This simple model does not account for respiratory dissolution of calcite, and is based on the sediment geochemistry model of [*Martin and Sayles*, 1996] using a calcite dissolution rate of 30 day^{-1} [*Keir*, 1980], see Sigman *et al.* [1998] for a full description.

The dissolution equation is applied in the 8 box geochemical model to sediments >1500 m, which constitutes ~90% of the total area below sea level. The sediments are partitioned into 12 depth ranges, with the area of seafloor covered by each depth range determined by ocean hypsometry [*Menard and Smith*, 1966]. The bottom water carbonate ion concentrations are those calculated for the Deep box. Unlike Matsumoto *et al*. [2002], we do not define Atlantic sediments in our model as we felt that the highly parameterised nature of the model did not allow distinction of separate ocean basins.

Following Matsumoto *et al*. [2002], the saturation concentration at each bin depth (mid-point of each depth range) is calculated using the apparent solubility product of calcite in seawater at 1 atm pressure [*Ingle et al.*, 1973], modified to account for temperature and pressure effects [*Millero*, 1995]. Sedimentary density was

assumed to be 2.7 g cm^{-3} with no porosity [*Emerson*, 1985]. The [CO_3^{2-}] supply from rivers was 6 x 10^{18} µmol, and was chosen to match interglacial $CaCO_3$ burial. The riverine [CO_3^{2-}] supply remained constant in a glacial SALH scenario.

6.1.4 Test of the new model against the Matsumoto et al. [2002] model

This investigation re-created the model of Matsumoto *et al*. [2002], using MATLAB. The new model uses identical input parameters for box areas, depths and volumes, gas flux, diatom fraction, Si:N export ratio, and total inventories of all nutrients (Tables 6.1 and 6.2). The model also used the same water fluxes and estimates of primary productivity (Table 6.3) obtained by Matsumoto *et al*. [2002] through inverse modelling, see paper for more details.

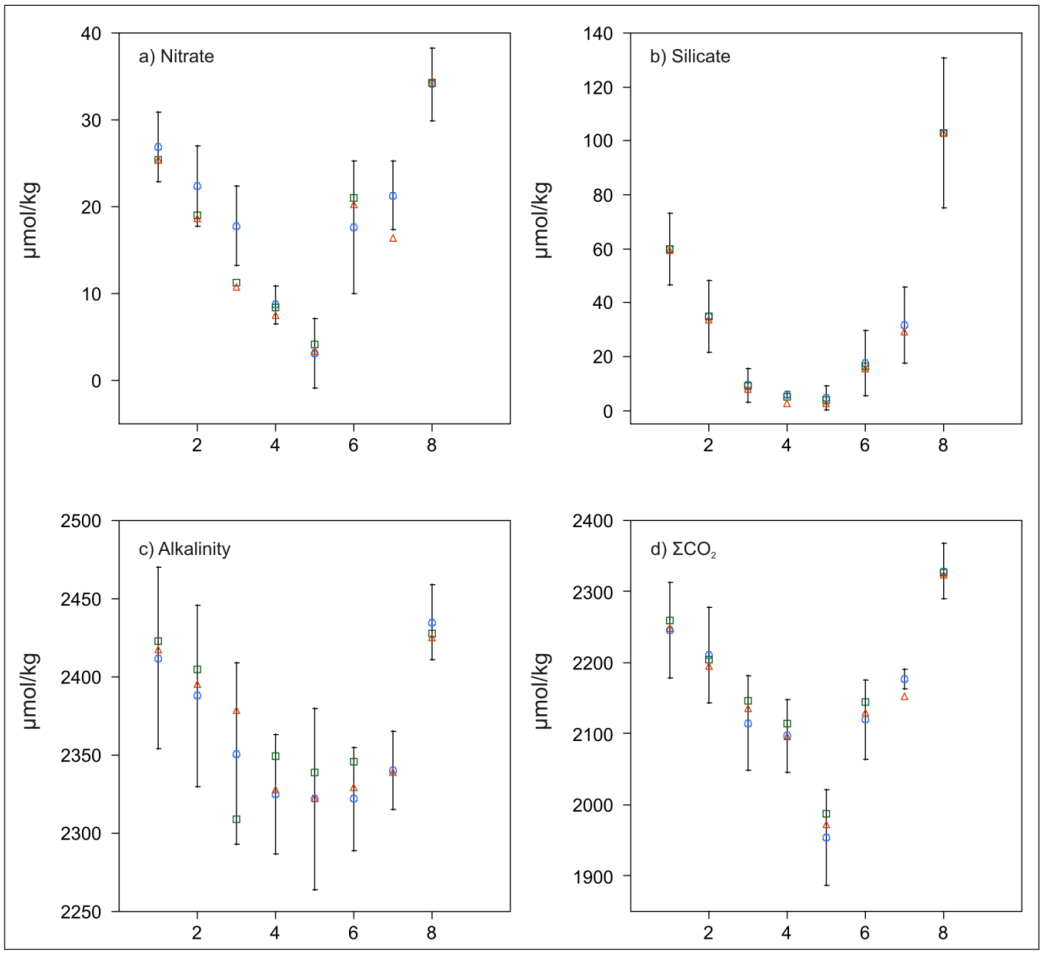

Figure 6.2 – Comparison of preindustrial state corresponding to the 8-box model of Matsumoto *et al*. [2002] (open blue circles), the data estimates of Matsumoto *et al*. [2002] (open green squares), and the model used in this study (open red triangles). Error bars represent the first standard deviation of the mean data values for each of the 8 boxes, see Table 2 in Matsumoto *et al*. [2002]. Box numbers are on the x-axis, see Table 6.1 for box names.

The new model was not constrained with $\Delta^{14}C$, as Matsumoto *et al*. [2002] found a mismatch of their value of atmospheric $\Delta^{14}C$ of 9.9 ‰, obtained through

inverse modelling, to the target value of 0 ‰. Matsumoto *et al*. [2002] note that some mismatch of variables to target values is inevitable in simplified box models.

In any case, $\Delta^{14}C$ was used by Matsumoto *et al*. [2002] as a tracer of ocean ventilation, and all the same water and gas fluxes are used in the new model. Similarly $\delta^{13}C$ was also calculated in the new model, but the comparison between the new model and that of Matsumoto *et al*. [2002] is not shown, because this is also designed to test realistic model circulation.

A key model parameter is the global $CaCO_3$:C_{org} ratio [*Matsumoto and Sarmiento*, 2008]. The global $CaCO_3$:C_{org} ratio is 0.1 in the interglacial control of the new model, which is consistent with a current estimate [*Sarmiento et al.*, 2002]. The interglacial value of atmospheric pCO_2 of 276.1 ppm in the new model is consistent with that of Matsumoto *et al*.'s [2002] model.

The performance of the new model (represented in by open red triangles) with that of Matsumoto *et al*. [2002] (represented by open blue circles, with error bars in black) is shown in Figure 6.2. For data sources see Matsumoto *et al*. [2002]. Generally, the new model model replicates the distribution of nitrate, silicate, pCO_2, alkalinity and ΣCO_2 in the Matsumoto *et al*. [2002] model within the error defined by the first standard deviation of the mean data values for each of the boxes (Figure 6.2).

Some mismatch in nitrate concentrations exist between data estimates and both models in box 3 (Subantarctic) possibly due to small differences in remineralisation profiles for sinking organic matter. Box 7 (Atlantic) in the new model differs from data estimates (blue markers in Figure 6.2), again possibly due to remineralisation depth differences between the model and measured data estimates.

Note that data for the Atlantic box in the interglacial control run of Matsumoto *et al*. [2002] is not provided in their paper. The atmospheric pCO_2 produced by the new model was 276.1 ppm compared to 277.2 ppm produced by the model of Matsumoto *et al*. [2002] (Table 6.4).

6.2 Results

6.2.1 Model comparisons

The 'non-SALH scenario' and 'SALH scenario' simulated by Matsumoto *et al*. [2002], was replicated using the new model. The results of the new model runs, reducing the High Latitude Si:N in increments of 0.5 each time, are shown in Figure 6.3 and Table 6.4.

The consumption of excess silicic acid by diatoms in the Low Latitude box is simulated in the new model by adjusting the Low Latitude diatom fraction to use the excess silicic acid, thereby returning the silicic acid concentration in the Low Latitude box to its original value (2.62 µmol kg^{-1}). Note that Figure 6.3 represents simulation of a

SALH scenario in a "closed" system which does not take carbonate compensation into account.

Simulation of silica leakage in the new model closely matches that of Matsumoto *et al*. [2002], in terms of changes in Low Latitude $Si(OH)_4$ and diatom fraction.

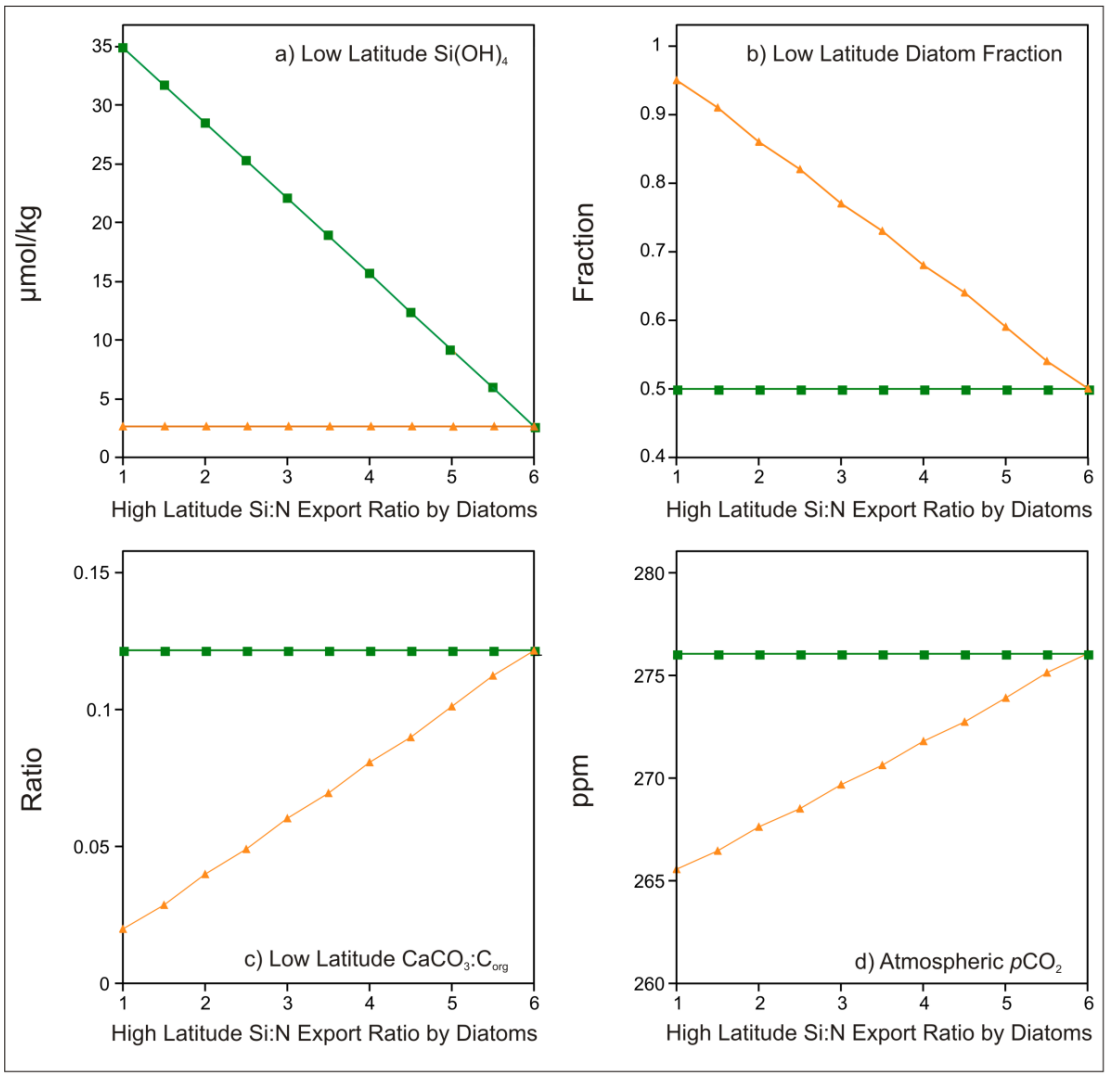

Figure 6.3 – Results of model runs, with a 'non-SALH scenario' (no consumption of excess silicic acid in the Low Latitude box) represented by green squares, and a 'SALH scenario' represented by orange triangles.

Slight differences in the response of pCO_2 to changes in the Low Latitude $CaCO_3$:C_{org} 'rain ratio' between the models is probably due to slight differences in the remineralisation depths of $CaCO_3$ and C_{org}; with the model of Matsumoto *et al*. [2002] producing a 1.46 ppm decrease in pCO_2 per 0.01 decrease in the Low Latitude rain

ratio, and the new model producing a decrease of 1.05 ppm per 0.01 decrease in the Low Latitude rain ratio.

Table 6.4 – Comparison of the new model from this study, with that of Matsumoto *et al*. (2002) (M02), for extremes of silicic acid leakage. A high-latitude Si:N of 6 represents no excess leakage (interglacial scenario), to an Si:N of 1 (maximum glacial Si leakage). Under a non-SALH scenario the excess silicic acid is not consumed and accumulates in the low latitude box (columns 2 and 3). Under a SALH scenario, this excess is consumed by diatoms, and they subsequently increase in the Low-Latitude box (columns 4-9).

High Lat Si:N	LL $Si(OH)_4$ (M02) (non-SALH)	LL $Si(OH)_4$ (this study) (non-SALH)	LL diatom frac (M02) (SALH)	LL diatom frac (this study) (SALH)	Global $CaCO_3$:C_{org} export (M02) (SALH)	Global $CaCO_3$:C_{org} export (this study) (SALH)	pCO_2 (ppm) (M02) (SALH)	pCO_2 (ppm) (this study) (SALH)
6	3.70	2.62	0.50	0.50	0.10	0.12	277.2	276.1
1	34.80	34.81	0.95	0.95	0.03	0.02	267.0	265.6

6.2.2 Model pCO_2 sensitivity

The pCO_2 sensitivity of the new model to changing the depth of $CaCO_3$ remineralisation is illustrated by Figure 6.4. The model has greater pCO_2 sensitivity if the $CaCO_3$ remineralisation depth is varied between 500-1500 m, probably due to most $CaCO_3$ remineralisation occurring in the Deep box, which is less well able to communicate with the surface compared with the Middle and Atlantic boxes. A remineralisation depth of 3800 m is used in the new model to obtain the best match to the alkalinity and ΣCO_2 values of Matsumoto *et al*. [2002].

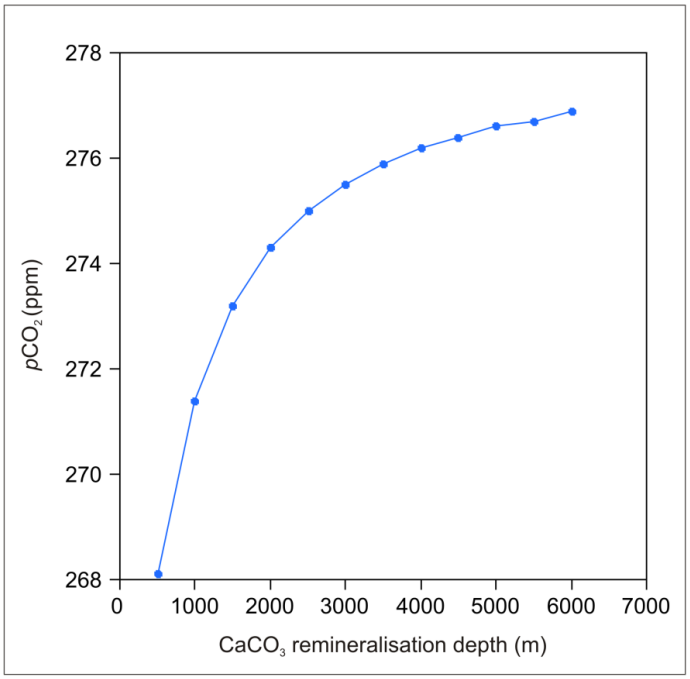

Figure 6.4 – Model pCO2 sensitivity to changing $CaCO_3$ remineralisation depth. The model uses a $CaCO_3$ remineralisation depth of 3800 m in the interglacial control run.

6.2.3 Differences in modelling approach from new data constraints

Measurement of opal flux rates suggests that the opal burial rate increased by an average ~100% from opal burial rate of ~2.5 Gt/ka in MIS 5a to ~5 Gt in MIS 4 (see Chapter 3). When the new model was run with a simulated maximum silica excess (high southern latitude Si:N export ratio =1), it produced an increase in Si export of ~2.43 x 10^{19} µmol, a doubling of the previous value when the model was run with a high southern latitude Si:N export ratio was 6 (i.e. no silica excess). Providing that opal dissolution rates remained similar during MIS 5a and MIS 4, a doubling of Si export could produce an approximate doubling of opal burial in MIS 4 relative to MIS 5a. The original model of Matsumoto *et al*. [2002] assumes that diatoms contribute 50% of primary productivity in the low latitude box, when no excess silica from high southern latitudes is consumed. This would of course mean that, using this initial diatom fraction, $CaCO_3$ production would have stopped entirely during MIS 4 if the diatom fraction increased by 100%, which is not supported by my data (see Chapter 4). The initial value of diatom contribution in the Low Latitude box suggested by Matsumoto *et al*. [2002] is a simple composite of diatom productivity in oligotrophic oceans (35%) and coastal zones (75%) [*Nelson et al.*, 1995].

It was proposed instead that an initial diatom fraction of 0.38 be used in the Low Latitude box of the new model. The oligotrophic areas of the world ocean have been identified through spectral reflectance data from satellite ocean colour sensors, and include the North and South Pacific gyres, the North and South Atlantic gyres, and the South Indian gyre [*Morel et al.*, 2010] (Figure 6.5). These areas total approximately 36% of the total area of the ocean [*Ryther*, 1969]. Measured values of the contribution of diatoms to total export productivity vary between 15-30% in oligotrophic areas [*Nelson et al.*, 1995; *Nelson and Brzezinski*, 1997], and therefore a median value of 22.5 % is assumed for diatom contribution to productivity in these areas.

The areas of coastal upwelling and adjacent areas of high offshore primary productivity comprise approximately 10% of the total area of the ocean [*Ryther*, 1969]. Upper estimates of the diatom contribution to productivity are around 75 % [*Nelson et al.*, 1995; *Tréguer et al.*, 1995]. In the open ocean regions that constitute the remaining 46% of the area of the surface ocean, an intermediate value of 48.5% was assumed to represent the diatom contribution to primary productivity. Weighting each diatom contribution by fractional area I calculated an initial diatom fraction of 0.38. Values of 3-20 % for the diatom contribution to productivity for an ‘intermediate’ area of the eastern equatorial Atlantic (non-oligotrophic, non-coastal upwelling) suggests that perhaps this initial diatom fraction could be lower still [*Lange et al.*, 1994]. Therefore, assuming a doubling of opal export and burial, I propose that the maximum diatom fraction that

may be supported in the Low Latitude box is 0.76, which corresponds to a high latitude Si:N export ratio of ~3 (Figure 6.3).

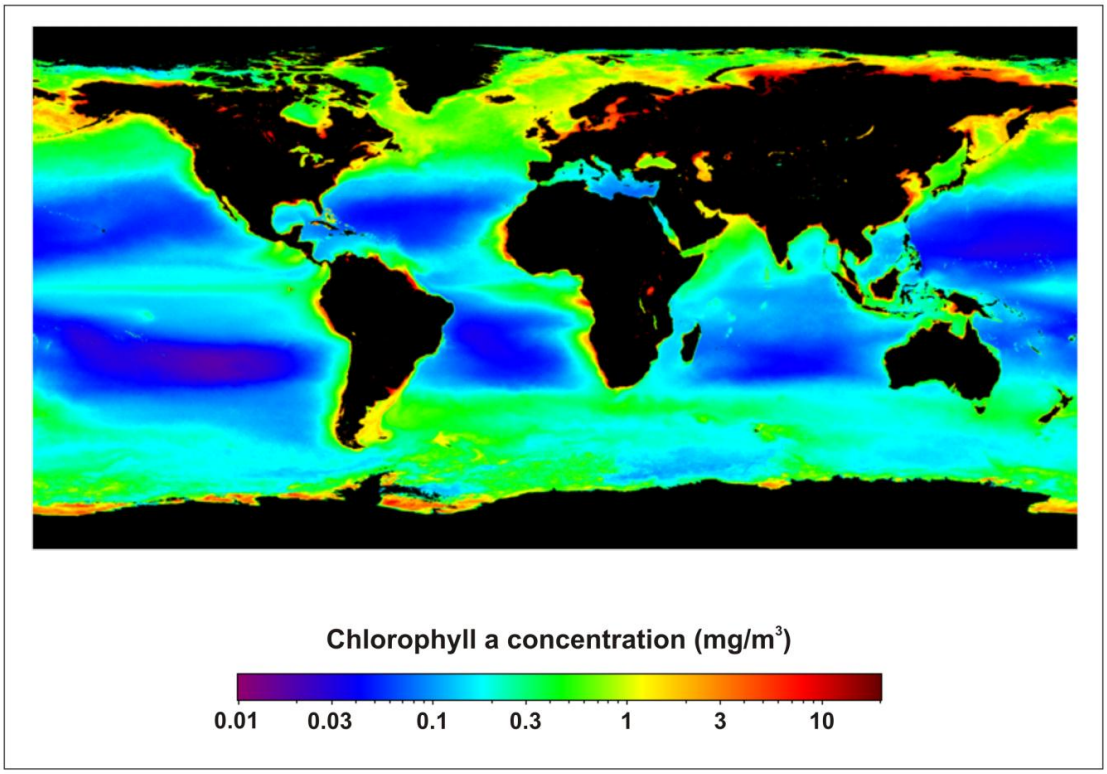

Figure 6.5 - Chlorophyll data are the entire mission composite SeaWiFS (1997-2010) from http://oceancolor.gsfc.nasa.gov. The blue areas are oligotrophic (<0.3 mg/m^3 chlorophyll a), and constitute ~ 36% of the total area of the ocean [*Ryther*, 1969]. The areas of coastal upwelling and near-shore high productivity zones are coloured red and yellow (>1 mg/m^3 chlorophyll a), and comprise ~10% of the total area of the ocean [*Ryther*, 1969].

The second data constraint proposes that overall productivity increased in the Low Latitude box during MIS 4. In the eastern equatorial Atlantic, productivity during MIS 4 was at least ~50% higher than in MIS 5a [*Sarnthein et al.*, 1992], which is supported qualitatively by results from this study (see Chapter 3), and others [*Verardo and McIntyre*, 1994; *Flores et al.*, 2000]. Productivity may have also increased by ~70-100 % in the equatorial Pacific [*Paytan et al.*, 1996; *Zhang et al.*, 2007], although a study from the eastern equatorial Pacific indicated that glacial productivity was lower [*Loubere et al.*, 2003]. Glacial productivity may also have increased by a similar amount in the Indian Ocean [*Schulte and Bard*, 2003], although other work suggests that productivity was highest in the equatorial Indian Ocean during MIS 5 [*Piotrowski et al.*, 2009].

Given that the new model has no separate ocean basins, and taking into account the inherent uncertainty and spatial heterogeneity of palaeoproductivity

records, a conservative 50 % increase in low latitude productivity during MIS 4 is assigned to the new model and used in subsequent simulations. This scenario will be tested in the model by combining it with silicic acid leakage, and also in a control case where the Low Latitude diatom fraction is maintained at the interglacial value of 0.38 (Table 6.5).

6.2.4 Glacial boundary conditions

As noted by Matsumoto *et al*. [2002], the achievement of glacial levels of pCO_2 is made more difficult by the implementation of appropriate glacial boundary conditions. The new model was ran based on estimates of glacial boundary conditions for MIS 4, including addition of ~ 500 Gt of terrestrial carbon to the ocean [*Shackleton*, 1977], cooling of 3-5°C in low latitudes [*CLIMAP*, 1981; *Schneider et al.*, 1999], and cooling of 3°C in high latitudes inferred from deep sea cooling [*Shackleton*, 2000]. A salinity increase of 2 % is assumed in the global ocean (making glacial ocean salinity ~35.7 psu), based on a sea level estimate from coral records of -81 m relative to modern during MIS 4 [*Cutler et al.*, 2003].

By imposing glacial (MIS 4) boundary conditions on the model, the pCO_2 of the model atmosphere was raised to 296.7 ppmv, which is a similar result as Matsumoto *et al*. [2002] achieved for the Last Glacial Period (~28-18 ka). The addition of 500 Gt (4.167×10^{16} moles) of terrestrial carbon raises pCO_2 by 42 ppmv, and a 2% saltier ocean caused by an 81 m lowering of sea level raises pCO_2 by an additional 12 ppmv. Reducing temperatures in the high latitude (Continental Margin, Polar, Subantarctic and North) boxes by 3°C, and by 4°C (average cooling estimate) in the Low Latitude box lowers pCO_2 by 33 ppmv.

6.2.5 Modelling a glacial SALH with new data constraints

First, the new model was ran with a diatom fraction of 0.38 in a 'non-SALH' scenario (high southern latitude Si:N = 6), to test whether the model still produces a reasonable value of interglacial pCO_2. The same amount of Low Latitude productivity as Matsumoto *et al*. [2002] was assumed, and the new model was also ran with the decreased Low Latitude diatom fraction, which resulted in a pCO_2 of 308.2 ppmv, due to increased Low Latitude $CaCO_3$ export productivity. The Low Latitude $CaCO_3$:C_{org} ratio in this simulation was 0.1486. The effect of a SALH scenario was tested (high southern latitude Si:N = 3.0, Low Latitude diatom fraction = 0.76) relative to this new initial fraction, and a pCO_2 of 266.7 ppmv and a Low Latitude $CaCO_3$:C_{org} ratio of 0.0628 was calculated, a relative decrease in pCO_2 of ~13.5% due to the effect of silica leakage.

As the initial pCO_2 of 308.2 ppmv was too high to be realistic, the $CaCO_3$ remineralisation depth was adjusted until a more realistic pCO_2 of 281.2 ppmv was achieved when running an interglacial 'non-SALH' scenario (high southern latitude Si:N = 6.0, Low Latitude diatom fraction = 0.38). The simulated Low Latitude $CaCO_3$:C_{org} ratio in this case was again 0.1486. The model was ran with sediments "open" to account for the effects of carbonate compensation on pCO_2.

Second, the model SALH scenario was ran again (high southern latitude Si:N = 3.0, Low Latitude diatom fraction = 0.76), and a pCO_2 of 242.8 ppmv was obtained, and a Low Latitude $CaCO_3$:C_{org} ratio of 0.0628. The relative decrease in pCO_2 was 13.7 %, very similar to the relative pCO_2 decrease from the previous simulations. This result therefore argues for a relative pCO_2 decrease of 13.6 % from interglacial values due to a SALH scenario (see Table 6.5).

Table 6.5 – Input parameters (Si:N, Low Latitude box diatom fraction and Low Latitude box Productivity) and output (Low Latitude $CaCO_3$:C_{org} and atmospheric pCO_2) for tests of the new model using new data-based constraints.

High-lat Si:N	Low Lat Diatom fraction	Low Lat Prod. (Gt C yr^{-1})	Low-lat $CaCO_3$:C_{org}	pCO_2 (ppm)
6	0.38	2.84	0.1486	281.18
3	0.76	2.84	0.0628	266.65
3	0.76	4.26	0.0626	229.58
6	0.38	4.26	0.1551	271.80

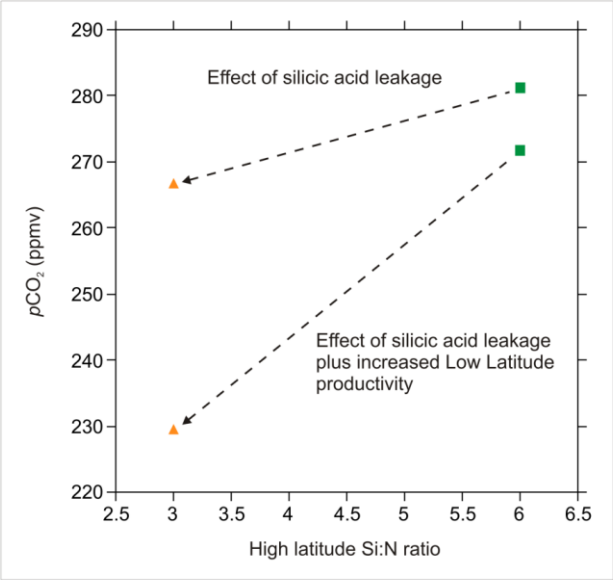

Figure 6.6 – A comparison of the different model scenarios outlined in Table 6.5. A scenario of silicic acid leakage to the Low Latitude surface box is represented by green squares, and interglacial control scenario represented by orange triangles.

The last new test of the model simulated a SALH scenario with a high latitude Si:N ratio of 3, a diatom fraction of 0.76, and a 50% increase of Low Latitude production rate from the value of 2.84 Gt C yr^{-1} used by Matsumoto *et al*. [2002], to 4.26 Gt C yr^{-1}, by multiplying the original productivity calculated by the inverse modelling method of Matsumoto *et al*. [2002] by 1.5. The results of all simulations are shown in Table 6.5 and Figure 6.6:

The scenario of Low Latitude productivity coupled with enhanced silicic acid leakage has the potential to account for all of the 47 ppmv MIS 4 pCO_2 drawdown [*Ahn and Brook*, 2008]. This result, however, may occur largely because of a large increase in the Low Latitude DIC gradient [*Ridgwell*, 2003], rather than a decrease in $CaCO_3$ production and export (see Chapter 4).

6.3 Discussion

The scenario of consumption of excess silicic acid in the subantarctic zone modelled by Matsumoto *et al*. [2002] is consistent with data from this study, in that it still predicts leakage of silicic acid from the subantarctic zone when the diatom fraction there saturates. It has been demonstrated in this investigation that the silicic acid supply rate to low latitudes was increased during MIS 4 (see Chapter 5), so that scenarios of increased glacial diatom productivity in the subantarctic zone [*Chase et al.*, 2001] do not preclude silicic acid leakage to low latitudes. Assuming, then, that an increased silicic acid delivery to the low latitudes by AAIW/SAMW took place during MIS 4; changes in the Low Latitude diatom fraction as a response to increasing Low Latitude silicic acid were simulated. To improve on the estimate of pCO_2 drawdown that may have occurred in this scenario made by Matsumoto *et al*. [2002], additional model constraints based on the new geochemical data in this thesis were imposed.

The first model constraint (a reduction of the initial Low Latitude diatom fraction) was based on the observation of a ~100% increase in opal burial in a suite of cores from the equatorial Atlantic (Chapter 3). The assertion that a 100% increase in opal burial in the equatorial Atlantic represented a 100% increase in diatom export productivity was based on the assumption that rates of opal dissolution remained reasonably constant across the MIS 5a/4 transition [*Pokras*, 1986]. Another study of an eastern equatorial Atlantic core found that changes in diatom assemblage in sediment reflected overlying hydrographic conditions despite a burial rate of 2% [*Treppke et al.*, 1996].

However, work by Nelson *et al*. [1995] indicates that the burial rate of biogenic opal may vary between 2 and 25 % depending on the magnitude of opal export. If extreme cases are considered, when opal accumulation was high during MIS 4, a

change in opal burial of 100 % may only represent a small fractional increase in opal export due to greatly increased opal preservation rates. In this case, diatoms would contribute very little to export productivity and argue for a diminished contribution of the SALH mechanism to pCO_2. Further work is needed to relate rates of opal burial to diatom export productivity, along with new proxies for opal dissolution, as highlighted by Ragueneau *et al.* [2000].

When a SALH scenario (high southern latitude Si:N = 3.0, Low Latitude diatom fraction = 0.76) was imposed on the model from an initial pCO_2 of 281.18, the model reduced the value of pCO_2 to 266.65 ppmv, a relative decrease of 13.7%. It can be argued that this is realistic given that a very similar relative pCO_2 drawdown was also achieved from a starting pCO_2 of 308.2 ppmv, ruling out the effect of the $CaCO_3$ remineralisation depth on pCO_2.

The second data constraint, that of increased glacial productivity, is suggested by a number of studies (see 6.2.3), but is nonetheless subject to very large uncertainty. The use of an estimate of overall glacial productivity increase (50 %) is at the lower end of these estimates. An increase of 1.42 Gt C yr^{-1} would require an increase in the supply rate of NO_3^- of 1.61 x 10^{19} µmol yr^{-1}, assuming stoichiometry of $16N:117C_{org}$ [*Anderson and Sarmiento*, 1994]. This could be achieved by a 50 % increase in the Low Latitude upwelling term *flm* (see Figure 6.1), provided that sufficient replenishment of N could occur from deeper waters. An increase in low latitude upwelling during MIS 4 is supported qualitatively in the Atlantic [*Abrantes*, 2000; *Flores et al.*, 2000], but not the Pacific [*Loubere et al.*, 2003]. This modelled simulation assumes an average productivity increase across a vast area of ocean represented by the Low Latitude box (279.2 x 10^{12} m^2), equivalent to 80 % of the total ocean surface area, which may or may not be supported by future data.

It may be reasonable to model an increase in Low Latitude productivity of 50 % based on the suggestion that the glacial NO_3^- inventory is thought to have been increased by up to 25 % in glacial periods due to reduced bacterial denitrification in oxygen minimum zones [*Altabet et al.*, 1995; *Ganeshram et al.*, 1995]. If this increase is applied to the N inventory of the model (4.01 x 10^{16} moles) [*Levitus et al.*, 1993], it is more than sufficient to fuel the modelled increase in productivity in the Low Latitude box. Without this glacial increase, a 50 % increase in Low Latitude productivity cannot be sustained by available nitrate in the Low Latitude box.

However, Matsumoto *et al*. [2002] note that the optimal organic carbon production of their box model is 5 Gt C yr^{-1}, far less than the calculated global value of ~11 Gt C yr^{-1} derived from a pelagic food web model [*Laws et al.*, 2000], which can also be supported by GCMs [*Yamanaka and Tajika*, 1997; *Archer et al.*, 2000a]. If box models are forced to support similar levels of maximum productivity to GCMs, deep

ventilation must become unrealistically high [*Matsumoto et al.*, 2002]. By increasing the Low Latitude productivity 50 % to 4.26 Gt C yr^{-1}, the global productivity is increased to 6.45 Gt C yr^{-1}, which is greater than the optimum value identified by Matsumoto *et al*. [2002].

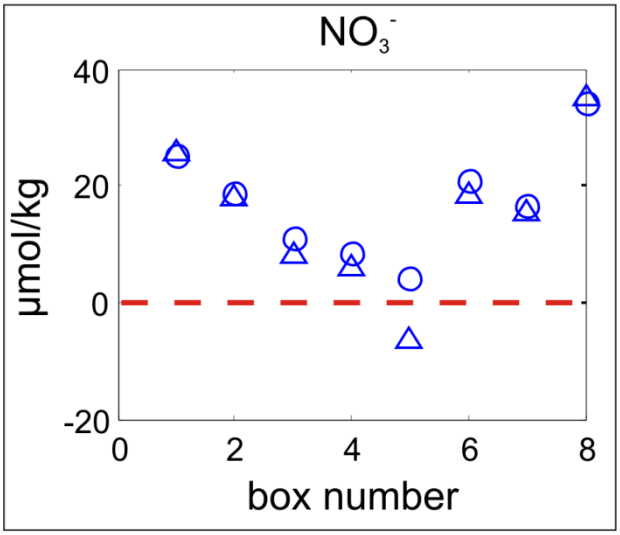

Figure 6.7 – Nitrate (NO_3^-) concentrations in the simulation of a 50 % increase in productivity in the Low Latitude box (number 5). The circles represent the model of Matsumoto *et al*. [2002], and the triangles represent this model. The red line marks the nitrate concentration threshold 0 µmol/kg, which is exceeded by our model if a nitrate inventory of 4.01×10^{16} moles is used [*Levitus et al.*, 1993]. Data suggests that this inventory may increase by ~25 % in glacial periods, however, which would allow a 50 % increase in the Low Latitude box without completely depleting Low Latitude nitrate [*Altabet et al.*, 1995; *Ganeshram et al.*, 1995].

This change could be compensated for by reducing the productivity of high latitude boxes by ~35 %, but data from the region suggests that glacial productivity in the Atlantic subantarctic zone (south of 40°S) increased [*Chase et al.*, 2001] or remained roughly similar to interglacial levels [*Frank et al.*, 2000]. Therefore, the inability of box models to support productivity higher than 5 Gt C yr^{-1} is an inherent limitation of this approach, and advocates the use of a GCM.

As highlighted by Matsumoto *et al*. [2002], the use of a climate model which has a greater sensitivity to low latitude nutrient dynamics, such as a GCM, may better represent the real ocean. The HBEI index (see 6.1.2) as defined by [*Broecker et al.*, 1999] is lower for box models than GCMs, meaning that gas exchange processes dominate thermohaline circulation in box models; which leads to the cold, high-latitude surface ocean having a much larger effect on pCO_2 than the warm, low latitude ocean [*Broecker et al.*, 1999]. Therefore, any tendency to change the CO_2 partial pressure of the low latitude surface ocean through changes in nutrient dynamics and productivity would be compensated by CO_2 transport from the high latitude ocean. If GCMs do indeed represent the real ocean better than box models, a greater pCO_2 drawdown via the SALH mechanism is potentially achievable.

The box modelling exercise presented here predicts a maximum pCO_2 drawdown of ~50 ppmv (including the effects of "open system" carbonate compensation) with a combined mechanism involving silicic acid leakage and a 50% increase in Low Latitude productivity. This combined drawdown is only achievable by a significant increase in the global nitrate inventory [*Ganeshram et al.*, 1995]. It also assumes that diatoms contribute around 38% to Low Latitude primary productivity on average, which may be revised downwards by future sediment trap studies. I suggest the likelihood that more modest changes in productivity occurred, given the ambiguity in palaeoproductivity studies in the low latitude oceans [*Sarnthein et al.*, 1992; *Loubere et al.*, 2003; *Schulte and Bard*, 2003; *Piotrowski et al.*, 2009], suggesting that the most likely contribution of the SALH to pCO_2 drawdown during MIS 4 was somewhere between 35 and 50 ppmv, but probably on the lower end of this estimate. The greater change was achieved largely by enhancing the Low Latitude biological pump, and increasing the DIC gradient [*Ridgwell*, 2003], rather than significant decreases in $CaCO_3$ production and export (Chapter 4). In the scenario where the preservation of exported opal increased greatly in MIS 4, as suggested by Nelson et al. [1995], the change in Low Latitude productivity alone would draw down pCO_2 by ~10 ppmv (Table 6.5). Further quantitative studies of past and present oceanic productivity will help to improve modelled estimates of the effect of the SALH.

6.4 Conclusions

Using a very similar box model to that of Matsumoto *et al.* [2002], a simulated maximum 50 ppmv glacial pCO_2 drawdown was achieved by invoking a SALH scenario, coupled with increased productivity; based on data constraints of a 100% increase in diatom burial (interpreted as a 100% increase in diatom productivity). I propose that the initial Low Latitude diatom fraction of 0.5 used by Matsumoto *et al*. [2002] in their model simulations is too high, and suggest reducing it to 0.38. Imposition of this constraint reduced pCO_2 by ~35 ppmv, assuming a value of 260 ppmv in MIS 5a [*Ahn and Brook*, 2008]. This result was achieved on the assumption that opal preservation did not vary significantly between MIS 5a and MIS 4. In the scenario where the preservation of exported opal did increase significantly in MIS 4, the change in pCO_2 associated with Low Latitude productivity would be more modest, at ~10 ppmv.

Using a further constraint of increased productivity, it was found that pCO_2 drawdown associated with the SALH coupled to increased low latitude productivity is ~ 50 ppmv, however, the applicability of a glacial increase in productivity of 50 % to the whole low latitude ocean (80 % of total ocean area) remains debatable, and may only be supported by an increase of 25 % in the global nitrate inventory [*Ganeshram et al.*, 1995]. With these new constraints, the maximum pCO_2 drawdown achieved under a

SALH scenario may account for a significant proportion of the MIS 4 pCO_2, taking into account glacial boundary conditions.

Based on this modelling exercise, the rapid pCO_2 decrease recorded during MIS 4 at ~ 71-69 ka [*Ahn and Brook*, 2008] could have been significantly contributed to by a SALH mechanism; in combination with a number of other physical oceanographic mechanisms, with further significant contributions from marine biota [*Hain et al.*, 2010; *Sigman et al.*, 2010].

Chapter 7 – summary and overall conclusions

This thesis has investigated the Silicic Acid Leakage Hypothesis (SALH) as a potential cause of the 47 ppm CO_2 drawdown observed from Antarctic ice core data that occurred ~71-69 ka (Ahn and Brook, 2008). The three main predictions of the SALH have been tested by reconstructing sediment geochemistry in a suite of cores from the equatorial Atlantic spanning ~40-100 ka. The first prediction of the SALH tested was that levels of sedimentary opal would have increased in the glacial (MIS 4) core sections, relative to the interglacial (MIS 5a) sections if a SALH scenario occurred. It was found that average levels of thorium-normalised sedimentary opal accumulation during MIS 4 exceeded those during MIS 5a by ~100%, which is in agreement with the SALH.

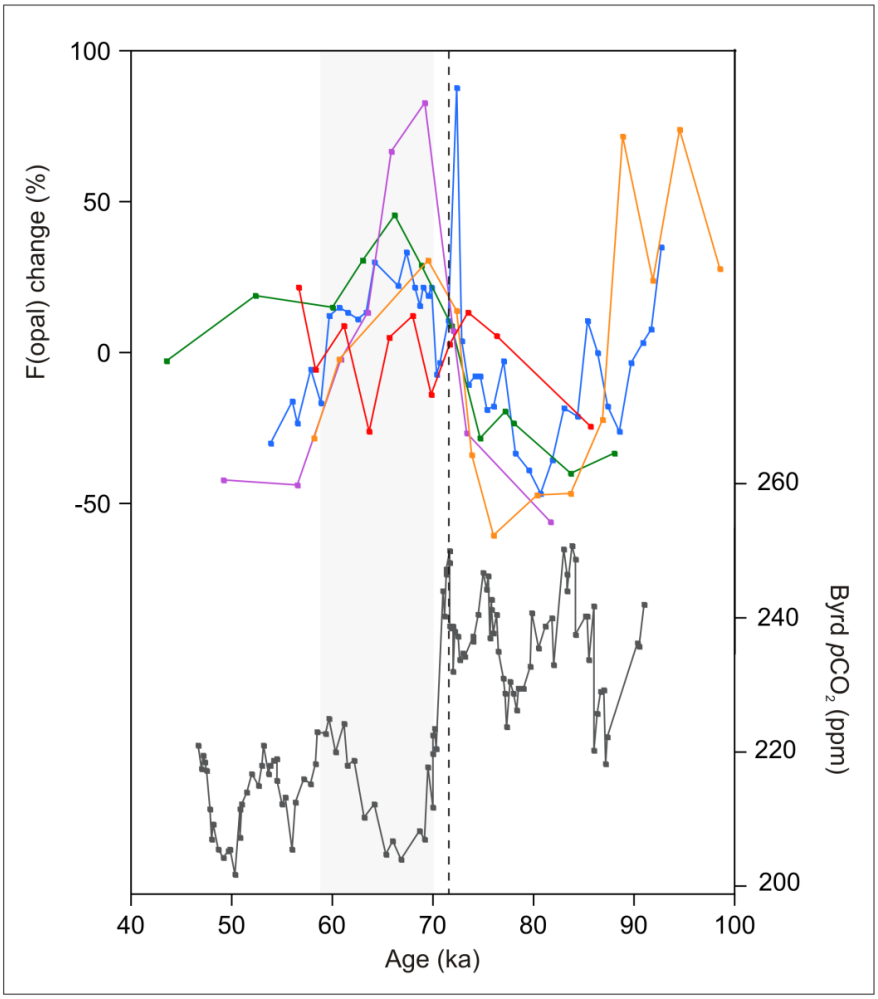

Figure 7.14 – A plot of the relative changes in opal accumulation (in g/cm^2/ka), relative to the long term mean of the core. RC16-66 is shown in red, VM30-40 in orange, RC24-01 in green, ODP 663A in blue and VM19-926 in violet. The cores are arranged chromatically from west (red) to east (violet). The Antarctic *p*CO_2 is plotted on the age scale of (Ahn and Brook, 2008), and the grey shaded area represents MIS 4 (~70-59 ka).

Additional measurements of other palaeo-productivity proxies (U_{auth}, TOC, TN) compared to the opal accumulation records also show, in general, coincident changes that reflect those of the opal accumulation, giving confidence that the flux records are primarily driven by shifts in opal productivity, rather than opal preservation or other processes.

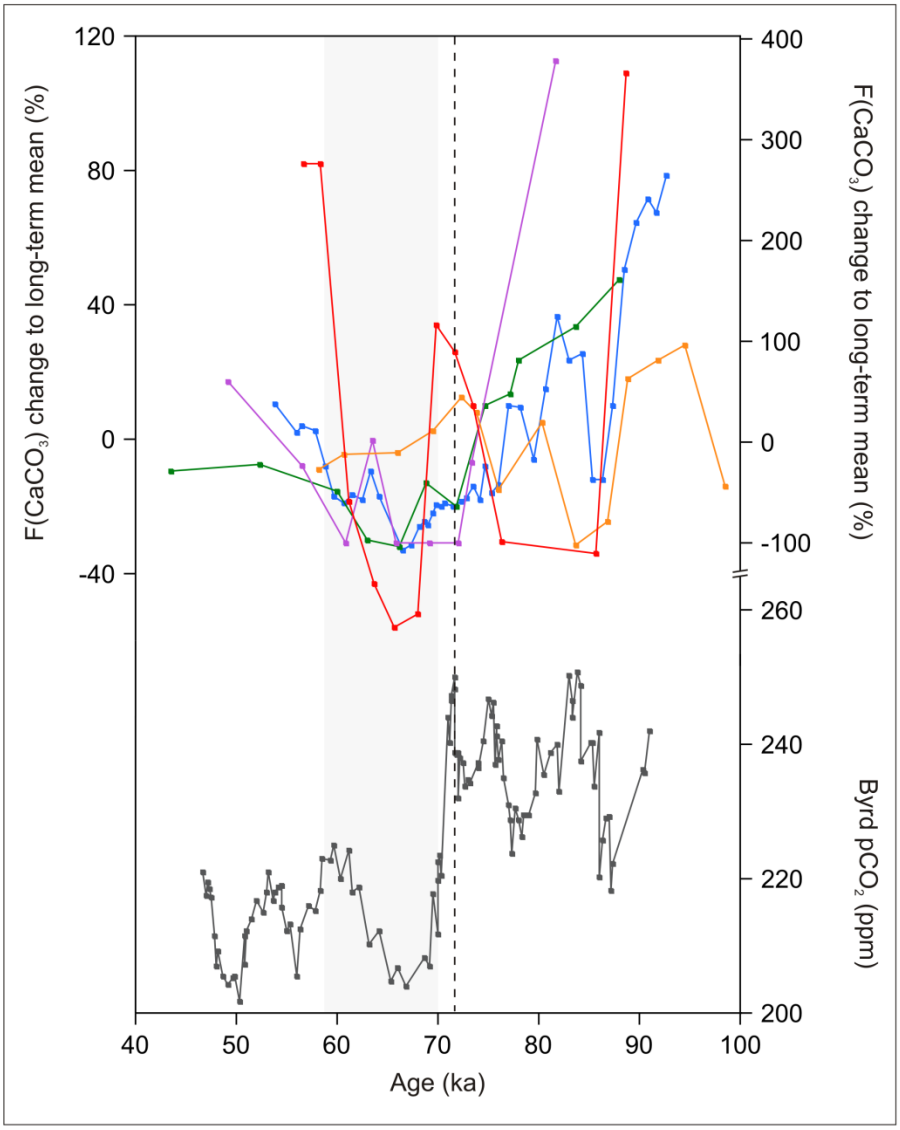

Figure 7.15 - A plot of the relative changes in $CaCO_3$ accumulation (in g/cm^2/ka), relative to the long term mean of the core (note separate scale on the left which only applies to VM19-296). RC16-66 is shown in red, VM30-40 in orange, RC24-01 in green, ODP 663A in blue and VM19-926 in violet. The cores are arranged chromatically from west (red) to east (violet). The Antarctic pCO_2 is plotted on the age scale of (Ahn and Brook, 2008), and the grey shaded area represents MIS 4 (~70-59 ka).

The second prediction of the SALH is as a corollary to the increased contribution of opal (diatoms) to primary productivity there would have been a corresponding decrease in $CaCO_3$ productivity and export. Thorium-normalised

$CaCO_3$ accumulation rates measured in the same core sections as those used to measure opal accumulation rate show that $CaCO_3$ accumulation rate did decrease significantly during MIS 4. However, the change in $CaCO_3$ accumulation rate are complicated by the fact that they could have been accounted for solely by changes in dissolution, given constraints on the glacial-interglacial change in carbonate ion concentration in the Atlantic [*Anderson and Archer*, 2002, *Broecker and Clark*, 2002, *Yu et al*., 2008]. This suggests that the decrease in $CaCO_3$ export productivity may have been more modest than suggested by these previous studies.

The SALH predicts that an increased contribution of opal to primary productivity caused a decline in $CaCO_3$ export by coccolithophorids, subsequently lowering pCO_2 through changes in surface- and whole-ocean alkalinity. Comparing the measured opal and $CaCO_3$ accumulation records to the Byrd pCO_2 record (Ahn and Brook, 2008) (Figures 7.1 & 7.2) suggests that the opal accumulation increase in the equatorial Atlantic took place over an extended ~15,000 yr interval, between ~80-65 ka, and that was no corresponding rapid decrease in $CaCO_3$ accumulation occurred during the rapid decrease in pCO_2. It is therefore concluded that the SALH is unlikely to have been the direct cause of the pCO_2 decrease, but rather that it could have provided a contribution to lower glacial pCO_2. Notably, in a scenario where an increase in diatom productivity promoted more efficient transfer of POC to the sediment than pico- or nannoplankton, significant drawdown of pCO_2 is still possible due to an increase in the DIC gradient [*Ridgwell*, 2003]. The third prediction of the SALH is that it would produce a change in the silicic acid content of SAMW and AAIW, which constitute the main conduit for the transport of preformed nutrients from the SAZ to the low latitudes [*Sarmiento et al*., 2004]. If a SALH scenario lead to the formation of a glacial silicic acid excess in the SAZ, as has been suggested by data [*Brzezinski et al*., 2002], then this would be manifest in a reconstruction of SAMW/AAIW chemistry at the MIS 5-4 transition.

Utilising neodymium isotopic ratios and silicon isotopic ratios of sponge spicules demonstrated an increased influence of silicic acid- enriched AAIW in the western tropical Atlantic (Figure 7.3). The timing of the increased silicic acid-enriched AAIW with increases in equatorial Atlantic and Bermuda Rise opal accumulation (see Chapter 5.2.2) is compelling, and strongly suggests that

changes in the supply of silicic acid drove an ecosystem shift towards diatom production at this time. Although the physical mechanism that might have brought AAIW from depth of 400-800 m to the surface in the western tropical Atlantic is currently unknown, if glacial silicic acid-enriched SAMW was also present and able to mix into shallower depths then this may explain the MIS 4 opal accumulation pattern.

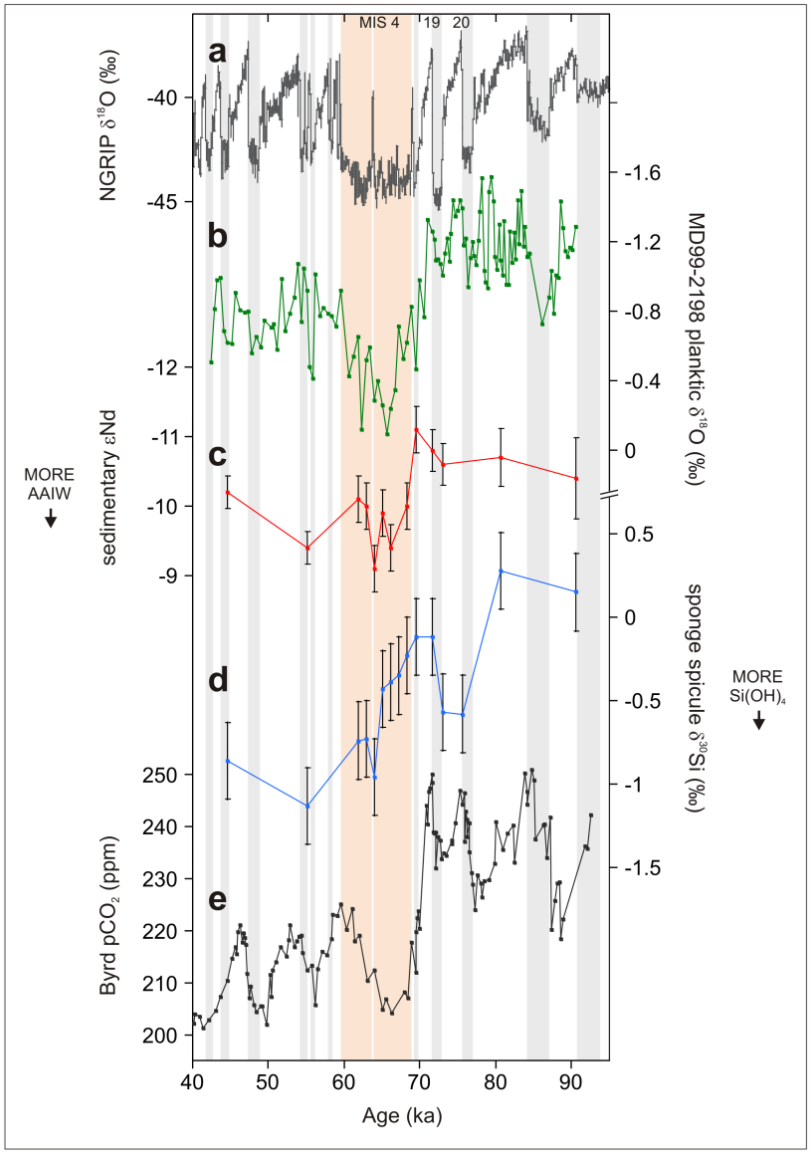

Figure 7.16 - (a) NGRIP $\delta^{18}O$ (‰), placed on an absolute age scale (see information on age model development); (b) MD99-2198 planktic $\delta^{18}O$; (c) MD99-2198 sedimentary ε_{Nd}; (d) MD99-2198 sponge spicule $\delta^{30}Si$; (e) Byrd (Antarctica) ice core pCO_2 (Ahn and Brook, 2008). Cold periods are marked by grey bands, and MIS 4 (orange shading), and cold D/O 19 and 20 are annotated.

In order to quantitatively assess the impact that a SALH scenario may have had on pCO_2, the results of the geochemical reconstructions have been used as new constraints on an 8-box geochemical model sensitivity experiment. Using the model approach of Matsumoto *et al*. [2002] a reduced initial fraction

of diatoms was applied representing the low latitude ocean, to better reflect sediment trap data [*Wefer and Fischer*, 1993; *Treppke et al*., 1996], and additionally impose a 50% increase in low latitude primary productivity on the model to reflect proxy evidence for increased low latitude productivity [*Sarnthein et al.*, 1992; *Verardo and McIntyre*, 1994; *Flores et al.*, 2000]. These simulations indicate a pCO_2 drawdown of 35-50 ppmv, given that the new constraints can realistically be applied across the whole latitude ocean.

Overall the results of this study support many of the testable predictions of the SALH and suggest that silicic acid does leak from the SAZ and may plausibly increase low latitude diatom productivity. While it is difficult to discern the quantitative effect that this may have had on $CaCO_3$ export productivity, it does allow for the possibility that the SALH contributed up to 35-50 ppmv of pCO_2 drawdown during glacial MIS 4.

It is often said that good research raises more questions than it answers, and while not exhaustive, in order to further develop the findings of this study, further work is suggested below:

1. Further detailed palaeoproductivity records from the 'low latitude' ocean (all areas equatorward) of ~50°S and 50°N are needed to address whether export productivity increased or decreased during MIS 5/4. As shown in Chapter 6, the modelling of significantly increased low latitude productivity, alongside a SALH scenario, has a large impact on pCO_2.

2. More work is needed to address uncertainty in the relationship of opal accumulation to diatom export productivity, as highlighted by Ragueneau *et al*. [2000]. Knowledge of the factors which control opal dissolution in the water column could be improved by further sediment trap studies in a range of oceanographic settings, (for example, oligotrophic areas vs. coastal upwelling sites). In addition, a better understanding of opal accumulation to diatom export productivity could aid palaeoceanographic interpretation of records of opal accumulation, in order to assess to what extent they are the result of increased productivity or increased dissolution. Development of opal dissolution proxies such as the preservation state of the vellum of the diatom *Azpeitia nodulifer* [*Warnock et al*., 2007] may also aid further investigation of the SALH.

3. Further studies are required to quantitatively determine past levels of carbonate dissolution. Proxies such as the *Globorotalia menardii* Fragmentation Index (MFI) [*Mekik et al*., 2010] have to potential to allow palaeoceanographers to determine whether past decreases in $CaCO_3$ accumulation, but only in areas where *G. menardii* shells are found. The development of similar proxies, perhaps utilised alongside biomarker reconstructions, could give valuable quantitative information on past levels of $CaCO_3$ export productivity and how they may have been affected by increased low latitude diatom productivity. This could then allow more precise determination of pCO_2 changes due to carbonate compensation in models, in response to a SALH scenario.

4. More palaeo-nutrient reconstructions, such as those from this study (Chapter 5) and Brzezinski *et al*. [2002] are needed from both the SAZ and low latitude oceans to determine the amount and areal extent of glacial silicic acid leakage. It would also be beneficial research to have $\delta^{30}Si$ records from low latitude diatoms, as evidence of enhanced silicic acid uptake relative to nitrate by diatoms in the low latitude ocean would further support the SALH.

5. If new constraints on low latitude diatom and coccolithophorid productivity become available, it would be instructive to run a SALH scenario in an EMIC or GCM, to firstly determine whether previous assumptions made in box modelling exercises were appropriate; and secondly to determine whether an EMIC or GCM is better suited to modelling the pCO_2 drawdown associated with a SALH scenario than a box model [*Broecker et al*., 1999; *Matsumoto et al.,* 2002].

References

Abouchami, W., and M. Zabel (2003), Climate forcing of the Pb isotope record of terrigenous input into the Equatorial Atlantic, *Earth and Planetary Science Letters*, *213*(3–4), 221-234.

Abouchami, W., S. L. Goldstein, S. J. G. Gazer, A. Eisenhauer, and A. Mangini (1997), Secular changes of lead and neodymium in central Pacific seawater recorded by a Fe-Mn crust, *Geochimica et Cosmochimica Acta*, *61*(18), 3957-3974.

Abrantes, F. (2000), 200,000 yr diatom records from Atlantic upwelling sites reveal maximum productivity during LGM and a shift in phytoplankton community structure at 185,000 yr, *Earth and Planetary Science Letters*, *176*(1), 7-16.

Abrantes, F. (2001), Assessing the Ethmodiscus ooze problem: new perspective from a study of an eastern equatorial Atlantic core, *Deep-Sea Research Part I-Oceanographic Research Papers*, *48*(1), 125-135.

Abrantes, F. (2003), A 340,000 year continental climate record from tropical Africa – news from opal phytoliths from the equatorial Atlantic, *Earth and Planetary Science Letters*, *209*(1–2), 165-179.

Acker, J. G., R. Byrne, S. Ben-Yaakov, R. A. Feely, and P. R. Betzer (1987), The effect of pressure on aragonite dissolution rates in seawater, *Geochimica et Cosmochimica Acta*, *51*(8), 2171-2175.

Adegbie, A. T. (2001), Reconstruction of paleoenvironmental conditions in equatorial Atlantic and the Gulf of Guinea basins for the last 245,000 years, *Issue 178 of Berichte aus dem Fachbereich Geowissenschaften der Universität Bremen, Universität (Bremen). Fachbereich Geowissenschaften*.

Adkins, J. F., K. McIntyre, and D. P. Schrag (2002), The Salinity, Temperature, and $\delta^{18}O$ of the Glacial Deep Ocean, *Science*, *298*(5599), 1769-1773.

Ahn, J., and E. J. Brook (2008), Atmospheric CO_2 and Climate on Millennial Time Scales During the Last Glacial Period, *Science*, *322*(5898), 83-85.

Altabet, M. A., R. Francois, D. W. Murray, and W. L. Prell (1995), Climate-related variations in denitrification in the Arabian Sea from sediment 15N/14N ratios, *Nature*, *373*(6514), 506-509.

Amakawa, H., D. S. Alibo, and Y. Nozaki (2000), Nd isotopic composition and REE pattern in the surface waters of the eastern Indian Ocean and its adjacent seas, *Geochimica et Cosmochimica Acta*, *64*(10), 1715-1727.

Amakawa, H., K. Sasaki, and M. Ebihara (2009), Nd isotopic composition in the central North Pacific, *Geochimica et Cosmochimica Acta*, *73*(16), 4705-4719.

Andersen, K. K., et al. (2007), Greenland Ice Core Chronology 2005 (GICC05) and 20 year means of oxygen isotope data from ice core NGRIP., *Pangaea*, doi:10.1594/PANGAEA.586838.

Anderson, D. M., and D. Archer (2002), Glacial-interglacial stability of ocean pH inferred from foraminifer dissolution rates, *Nature*, *416*(6876), 70-73.

Anderson, L. A., and J. L. Sarmiento (1994), Redfield ratios of remineralization determined by nutrient data analysis, *Global Biogeochem. Cycles*, *8*(1), 65-80.

Anderson, R. F. (1982a), Concentration, vertical flux, and remineralization of particulate uranium in seawater, *Geochimica et Cosmochimica Acta*, *46*(7), 1293-1299.

Anderson, R. F. (1987), Redox behavior of uranium in an anoxic marine basin, *Uranium*, *3*, 145-164.

Anderson, R. F., and A. P. Fleer (1982), Determination of natural actinides and plutonium in marine particulate material, *Analytical Chemistry*, *54*(7), 1142-1147.

Anderson, R. F., M. P. Bacon, and P. G. Brewer (1983a), Removal of ^{230}Th and ^{231}Pa from the open ocean, *Earth and Planetary Science Letters*, *62*(1), 7-23.

Anderson, R. F., M. P. Bacon, and P. G. Brewer (1983b), Removal of ^{230}Th and ^{231}Pa at ocean margins, *Earth and Planetary Science Letters*, *66*(0), 73-90.

Anderson, R. F., N. Kumar, R. A. Mortlock, P. N. Froelich, P. Kubik, B. Dittrich-Hannen, and M. Suter (1998), Late-Quaternary changes in productivity of the Southern Ocean, *Journal of Marine Systems*, *17*(1-4), 497-514.

Anderson, R. F., S. Ali, L. I. Bradtmiller, S. H. H. Nielsen, M. Q. Fleisher, B. E. Anderson, and L. H. Burckle (2009), Wind-Driven Upwelling in the Southern Ocean and the Deglacial Rise in Atmospheric CO_2, *Science*, *323*(5920), 1443-1448.

Aoki, S., M. Hariyama, H. Mitsudera, H. Sasaki, and Y. Sasai (2007), Formation regions of Subantarctic Mode Water detected by OFES and Argo profiling floats, *Geophys. Res. Lett.*, *34*(10), L10606.

Archer, D. (1991), Modeling the Calcite Lysocline, *J. Geophys. Res.*, *96*(C9), 17037-17050.

Archer, D. (1996), A data-driven model of the global calcite lysocline, *Global Biogeochem. Cycles*, *10*(3), 511-526.

Archer, D., and E. Maier-Reimer (1994), Effect of deep-sea sedimentary calcite preservation on atmospheric CO_2 concentration, *Nature*, *367*(6460), 260-263.

Archer, D., S. Emerson, and C. Reimers (1989), Dissolution of calcite in deep-sea sediments: pH and O2 microelectrode results, *Geochimica et Cosmochimica Acta*, *53*(11), 2831-2845.

Archer, D., M. Lyle, K. Rodgers, and P. Froelich (1993), What Controls Opal Preservation in Tropical Deep-Sea Sediments?, *Paleoceanography*, *8*(1), 7-21.

Archer, D., A. Winguth, D. Lea, and N. Mahowald (2000a), What caused the glacial/interglacial atmospheric pCO_2 cycles?, *Rev. Geophys.*, *38*(2), 159-189.
Archer, D. E., G. Eshel, A. Winguth, W. Broecker, R. Pierrehumbert, M. Tobis, and R. Jacob (2000b), Atmospheric pCO_2 sensitivity to the biological pump in the ocean, *Global Biogeochem. Cycles*, *14*(4), 1219-1230.
Arellano-Torres, E., L. E. Pichevin, and R. S. Ganeshram (2011), High-resolution opal records from the eastern tropical Pacific provide evidence for silicic acid leakage from HNLC regions during glacial periods, *Quaternary Science Reviews*, *30*(9–10), 1112-1121.
Armstrong, H. A., and M. D. Brasier (2005), *Microfossils*, Blackwell.
Bacon, M. P. (1984), Glacial to interglacial changes in carbonate and clay sedimentation in the Atlantic Ocean estimated from 230Th measurements, *Chemical Geology*, *46*(2), 97-111.
Bacon, M. P., and R. F. Anderson (1982), Distribution of Thorium Isotopes Between Dissolved and Particulate Forms in The Deep Sea, *J. Geophys. Res.*, *87*(C3), 2045-2056.
Bacon, M. P., and J. N. Rosholt (1982), Accumulation rates of Th-230, Pa-231, and some transition metals on the Bermuda Rise, *Geochimica et Cosmochimica Acta*, *46*(4), 651-666.
Bard, E., F. Rostek, J.-L. Turon, and S. Gendreau (2000), Hydrological Impact of Heinrich Events in the Subtropical Northeast Atlantic, *Science*, *289*(5483), 1321-1324.
Barker, S. (2006), Dissolution of deep-sea carbonates, *Paleoceanography, Physical and Chemical Proxies*, 1710-1722.
Barker, S., J. A. Higgins, and H. Elderfield (2003), The future of the carbon cycle: review, calcification response, ballast and feedback on atmospheric CO_2, *Phil. Trans. R. Soc. Lond.*, *361*, 1977-1999.
Barker, S., P. Diz, M. J. Vautravers, J. Pike, G. Knorr, I. R. Hall, and W. S. Broecker (2009), Interhemispheric Atlantic seesaw response during the last deglaciation, *Nature*, *457*(7233), 1097-1102.
Barker, S., G. Knorr, R. L. Edwards, F. Parrenin, A. E. Putnam, L. C. Skinner, E. Wolff, and M. Ziegler (2011), 800,000 Years of Abrupt Climate Variability, *Science*, *334*(6054), 347-351.
Barnes, C. E., and J. K. Cochran (1990), Uranium removal in oceanic sediments and the oceanic U balance, *Earth and Planetary Science Letters*, *97*(1–2), 94-101.
Barry, R. G., and R. J. Chorley (1987), *Atmosphere, Weather and Climate*, 5th ed., Routledge, London.
Bayon, G., C. R. German, R. M. Boella, J. A. Milton, R. N. Taylor, and R. W. Nesbitt (2002), An improved method for extracting marine sediment fractions and its application to Sr and Nd isotopic analysis, *Chemical Geology*, *187*(3–4), 179-199.
Beaufort, L., T. de Garidel-Thoron, A. C. Mix, and N. G. Pisias (2001), ENSO-like Forcing on Oceanic Primary Production During the Late Pleistocene, *Science*, *293*(5539), 2440-2444.
Behrenfeld, M. J., and P. G. Falkowski (1997), A consumers guide to phytoplankton primary production models, *Limnology & Oceanography*, *42*, 1479-1491.
Belyayeva, T. V. (1970), Abundance of Ethmodiscus in Pacific plankton, *Oceanol. Acad. Sci. USSR (translation by the American Geophysical Union)*, *10*, 672-675.
Berger, W. H. (1970), Planktonic Foraminifera: Selective solution and the lysocline, *Marine Geology*, *8*(2), 111-138.
Berger, W. H., and H. Herguera (1992), Reading the sedimentary record of the ocean's productivity., in *Primary productivity and biogeochemical cycles in the sea.*, edited by P. G. Falkowski and A. Woodhead, pp. 455-486, Plenum, New York.
Berner, R. A. (2004), *The Phanerozoic Carbon Cycle: CO2 and O2*, Oxford University Press, New York.
Berner, R. A., A. C. Lasaga, and R. M. Garrels (1983), The carbonate-silicate geochemical cycle and its effect on atmospheric carbon dioxide over the past 100 million years, *American Journal of Science*, *283*(7), 641-683.
Bertram, C. J., and H. Elderfield (1993), The geochemical balance of the rare earth elements and neodymium isotopes in the oceans, *Geochimica et Cosmochimica Acta*, *57*(9), 1957-1986.
Bickert, T., G. Wefer, and P. J. Müller (1999), Stable isotopes and sedimentology of core GeoB1105, *Pangaea*, doi:10.1594/PANGAEA.58768.
Bintanja, R., and R. S. W. van de Wal (2008), North American ice-sheet dynamics and the onset of 100,000-year glacial cycles, *Nature*, *454*(7206), 869-872.
Bishop, J. K. B., J. M. Edmond, D. R. Ketten, M. P. Bacon, and W. B. Silker (1977), The chemistry, biology, and vertical flux of particulate matter from the upper 400 m of the equatorial Atlantic Ocean, *Deep Sea Research*, *24*(6), 511-548.
Blunier, T., and E. J. Brook (2001), Timing of Millennial-Scale Climate Change in Antarctica and Greenland During the Last Glacial Period, *Science*, *291*(5501), 109-112.
Blunier, T., et al. (1998), Asynchrony of Antarctic and Greenland climate change during the last glacial period, *Nature*, *394*(6695), 739-743.
Bond, G., W. Showers, M. Elliot, M. Evans, R. Lotti, I. Hajdas, G. Bonani, and S. Johnson (1999), The North Atlantic's 1-2 kyr Climate Rhythm: Relation to Heinrich Events, Dansgaard/Oeschger Cycles and

the Little Ice Age in *Mechanisms of Global Climate Change at Millennial Timescales*, edited by P. U. Clark, R. S. Webb and L. D. Keigwin.
Bond, G., et al. (1992), Evidence for massive discharges of icebergs into the North Atlantic ocean during the last glacial period, *Nature*, *360*, 245-249.
Bond, G. C., and R. Lotti (1995), Iceberg Discharges into the North Atlantic on Millennial Time Scales During the Last Glaciation, *Science*, *267*(5200), 1005-1010.
Borole, D. V. (1993), Late pleistocene sedimentation: a case study of the central Indian Ocean Basin, *Deep Sea Research Part I: Oceanographic Research Papers*, *40*(4), 761-775.
Bourles, B., R. L. Molinari, E. Johns, W. D. Wilson, and K. D. Leaman (1999), Upper layer currents in the western tropical North Atlantic (1989-1991), *J. Geophys. Res.*, *104*(C1), 1361-1375.
Bowles, F. A. (1975), Paleoclimatic significance of quartz/illite variations in cores from the eastern equatorial north Atlantic, *Quaternary Research*, *5*(2), 225-235.
Bowles, F. A., and P. Fleischer (1985), Orinoco and Amazon River sediment input to the eastern Caribbean Basin, *Marine Geology*, *68*(1–4), 53-72.
Bradtmiller, L. I., R. F. Anderson, M. Q. Fleisher, and L. H. Burckle (2006), Diatom productivity in the equatorial Pacific Ocean from the last glacial period to the present: A test of the silicic acid leakage hypothesis, *Paleoceanography*, *21*(4), PA4201.
Bradtmiller, L. I., R. F. Anderson, M. Q. Fleisher, and L. H. Burckle (2007), Opal burial in the equatorial Atlantic Ocean over the last 30 ka: Implications for glacial-interglacial changes in the ocean silicon cycle, *Paleoceanography*, *22*(4), PA4216.
Bradtmiller, L. I., R. F. Anderson, M. Q. Fleisher, and L. H. Burckle (2009), Comparing glacial and Holocene opal fluxes in the Pacific sector of the Southern Ocean, *Paleoceanography*, *24*(2), PA2214.
Brewer, P. G., Y. Nozaki, D. W. Spencer and A. P. Fleer (1980), Sediment trap experiments in the deep north Atlantic: isotopic and elemental fluxes, *Journal of Marine Research*, *38*, 703-728.
Broecker, W., and E. Clark (2001), A dramatic Atlantic dissolution event at the onset of the last glaciation, *Geochem. Geophys. Geosyst.*, *2*(11).
Broecker, W., J. Lynch-Stieglitz, D. Archer, M. Hofmann, E. Maier-Reimer, O. Marchal, T. Stocker, and N. Gruber (1999), How strong is the Harvardton-Bear Constraint?, *Global Biogeochem. Cycles*, *13*(4), 817-820.
Broecker, W. S. (1982), Glacial to interglacial changes in ocean chemistry, *Progress In Oceanography*, *2*, 151-197.
Broecker, W. S. (1991), The Great Ocean Conveyer, *Oceanography*, *4*(2), 79-90.
Broecker, W. S. (1998), Paleocean Circulation during the Last Deglaciation: A Bipolar Seesaw?, *Paleoceanography*, *13*(2), 119-121.
Broecker, W. S. (2008), A need to improve reconstructions of the fluctuations in the calcite compensation depth over the course of the Cenozoic, *Paleoceanography*, *23*(1), PA1204.
Broecker, W. S., and T. Takahashi (1978), The relationship between lysocline depth and in situ carbonate ion concentration, *Deep Sea Research*, *25*, 65-95.
Broecker, W. S., and T.-H. Peng (1982), *Tracers of the Sea*, Lamont-Doherty Geological Observatory New York.
Broecker, W. S., and T.-H. Peng (1987), The role of CaCO3 compensation in the glacial to interglacial atmospheric CO2 change, *Global Biogeochem. Cycles*, *1*(1), 15-29.
Broecker, W. S., and E. Clark (2002), Carbonate ion concentration in glacial-age deep waters of the Caribbean Sea, *Geochem. Geophys. Geosyst.*, *3*(3), 1021.
Broecker, W. S., and E. Clark (2003), CaCO3 dissolution in the deep sea: Paced by insolation cycles, *Geochem. Geophys. Geosyst.*, *4*(7), 1059.
Broecker, W. S., S. Blanton, W. M. Smethie, Jr., and G. Ostlund (1991), Radiocarbon decay and oxygen utilization in the Deep Atlantic Ocean, *Global Biogeochem. Cycles*, *5*(1), 87-117.
Broecker, W. S., E. Clark, J. Lynch-Stieglitz, W. Beck, L. D. Stott, I. Hajdas, and G. Bonani (2000), Late glacial diatom accumulation at 9 degrees S in the Indian Ocean, *Paleoceanography*, *15*(3), 348-352.
Brovkin, V., A. Ganopolski, D. Archer, and S. Rahmstorf (2007), Lowering of glacial atmospheric CO_2 in response to changes in oceanic circulation and marine biogeochemistry, *Paleoceanography*, *22*(4), PA4202.
Brzezinski, M. A. (1985), The Si:C:N Ratio of Marine Diatoms: Interspecific Variability and the Effect of Some Environmental Variables, *Journal of Phycology*, *21*(3), 347-357.
Brzezinski, M. A., and D. M. Nelson (1995), The annual silica cycle in the Sargasso Sea near Bermuda, *Deep Sea Research Part I: Oceanographic Research Papers*, *42*(7), 1215-1237.
Brzezinski, M. A., D. M. Nelson, V. M. Franck, and D. E. Sigmon (2001), Silicon dynamics within an intense open-ocean diatom bloom in the Pacific sector of the Southern Ocean, *Deep Sea Research Part II: Topical Studies in Oceanography*, *48*(19-20), 3997-4018.

Brzezinski, M. A., C. J. Pride, V. M. Franck, D. M. Sigman, J. L. Sarmiento, K. Matsumoto, N. Gruber, G. H. Rau, and K. H. Coale (2002), A switch from $Si(OH)_4$ to NO_3^- depletion in the glacial Southern Ocean, *Geophys. Res. Lett.*, *29*(12), 1564-1567.
Brzezinski, M. A., et al. (2011), Co-limitation of diatoms by iron and silicic acid in the equatorial Pacific, *Deep Sea Research Part II: Topical Studies in Oceanography*, *58*(3-4), 493-511.
Bub, F. L., and W. S. Brown (1996), Intermediate layer water masses in the western tropical Atlantic Ocean, *J. Geophys. Res.*, *101*(C5), 11903-11922.
Cardinal, D., L. Y. Alleman, J. de Jong, K. Ziegler, and L. Andre (2003), Isotopic composition of silicon measured by multicollector plasma source mass spectrometry in dry plasma mode, *Journal of Analytical Atomic Spectrometry*, *18*(3), 213-218.
Cardinal, D., L. Y. Alleman, F. Dehairs, N. Savoye, T. W. Trull, and L. André (2005), Relevance of silicon isotopes to Si-nutrient utilization and Si-source assessment in Antarctic waters, *Global Biogeochem. Cycles*, *19*(2), GB2007.
Carr, M.-E. (2001), Estimation of potential productivity in Eastern Boundary Currents using remote sensing, *Deep Sea Research Part II: Topical Studies in Oceanography*, *49*(1–3), 59-80.
Castañeda, I. S., J. P. Werne, T. C. Johnson, and L. A. Powers (2011), Organic geochemical records from Lake Malawi (East Africa) of the last 700 years, part II: Biomarker evidence for recent changes in primary productivity, *Palaeogeography, Palaeoclimatology, Palaeoecology*, *303*(1–4), 140-154.
Charles, C. D., P. N. Froelich, M. A. Zibello, R. A. Mortlock, and J. J. Morley (1991), Biogenic Opal in Southern Ocean Sediments Over the Last 450,000 Years: Implications for Surface Water Chemistry and Circulation, *Paleoceanography*, *6*(6), 697-728.
Chase, Z., R. F. Anderson, and M. Q. Fleisher (2001), Evidence from Authigenic Uranium for Increased Productivity of the Glacial Subantarctic Ocean, *Paleoceanography*, *16*(5), 468-478.
Chase, Z., R. F. Anderson, M. Q. Fleisher, and P. W. Kubik (2002), The influence of particle composition and particle flux on scavenging of Th, Pa and Be in the ocean, *Earth and Planetary Science Letters*, *204*(1-2), 215-229.
Chase, Z., R. F. Anderson, M. Q. Fleisher, and P. W. Kubik (2003), Accumulation of biogenic and lithogenic material in the Pacific sector of the Southern Ocean during the past 40,000 years, *Deep Sea Research Part II: Topical Studies in Oceanography*, *50*(3-4), 799-832.
Cheng, H., R. L. Edwards, J. Hoff, C. D. Gallup, D. A. Richards, and Y. Asmerom (2000), The half-lives of uranium-234 and thorium-230, *Chemical Geology*, *169*(1–2), 17-33.
Chérubin, L. M., and P. L. Richardson (2007), Caribbean current variability and the influence of the Amazon and Orinoco freshwater plumes, *Deep Sea Research Part I: Oceanographic Research Papers*, *54*(9), 1451-1473.
Chester, R., and M. Hughes (1967), A chemical technique for the separation of ferro-manganese minerals, carbonate minerals and adsorbed trace elements from pelagic sediments *Chemical Geology*, *2*, 249-262.
Chiang, J. C. H., M. Biasutti and D. S. Battisti (2003), Sensitivity of the Atlantic Intertropical Convergence Zone to Last Glacial Maximum boundary conditions, *Paleoceanography*, *18*(4), 1094.
Chung, S. N., K. Lee, R. A. Feely, C. L. Sabine, F. J. Millero, R. Wanninkhof, J. L. Bullister, R. M. Key, and T. H. Peng (2003), Calcium carbonate budget in the Atlantic Ocean based on water column inorganic carbon chemistry, *Global Biogeochem. Cycles*, *17*(4), 1093.
Clegg, S. L., and M. Whitfield (1990), A generalized model for the scavenging of trace metals in the open ocean—I. Particle cycling, *Deep Sea Research Part A. Oceanographic Research Papers*, *37*(5), 809-832.
CLIMAP (1976), The Surface of the Ice-Age Earth, *Science*, *191*(4232), 1131-1137.
CLIMAP (1981), Seasonal reconstructions of the Earth's surface at the Last Glacial Maximum, *1-18*.
Coale, K. H., et al. (1996), A massive phytoplankton bloom induced by an ecosystem-scale iron fertilization experiment in the equatorial Pacific Ocean, *Nature*, *383*(6600), 495-501.
Coale, K. H., et al. (2004), Southern Ocean Iron Enrichment Experiment: Carbon Cycling in High- and Low-Si Waters, *Science*, *304*(5669), 408-414.
Cochran J. K. (1992) The oceanic chemistry of the uranium and thorium series nuclides. In *Uranium-series disequilibrium; Applications to earth, marine, and environmental sciences* (eds. M. Ivanovich and R. S. Harmon), OUP, pp. 334-395.
Coradin, T., and P. J. Lopez (2003), Biogenic Silica Patterning: Simple Chemistry or Subtle Biology?, *ChemBioChem*, *4*(4), 251-259.
Cox, P. M., R. A. Betts, C. D. Jones, S. A. Spall, and I. J. Totterdell (2000), Acceleration of global warming due to carbon-cycle feedbacks in a coupled climate model, *Nature*, *408*(6809), 184-187.
Crosta, X., C. Beucher, K. Pahnke, and M. A. Brzezinski (2007), Silicic acid leakage from the Southern Ocean: Opposing effects of nutrient uptake and oceanic circulation, *Geophysical Research Letters*, *34*(13).
Crowley, T. J. (1983), Calcium-carbonate preservation patterns in the central North Atlantic during the last 150,000 years, *Marine Geology*, *51*(1–2), 1-14.

Crowley, T. J. (1992), North Atlantic Deep Water Cools the Southern Hemisphere, *Paleoceanography*, *7*(4), 489-497.

Crusius, J., and J. Thomson (2000), Comparative behavior of authigenic Re, Mo and U during reoxidation and subsequent long-term burial in marine sediments, *Geochimica et Cosmochimica Acta*, *64*, 2233–2243.

Cruz, F. W., S. J. Burns, I. Karmann, W. D. Sharp, M. Vuille, A. O. Cardoso, J. A. Ferrari, P. L. Silva Dias, and O. Viana (2005), Insolation-driven changes in atmospheric circulation over the past 116,000 years in subtropical Brazil, *Nature*, *434*(7029), 63-66.

Curry, W. B., and G. P. Lohmann (1986), Late Quaternary carbonate sedimentation at the Sierra Leone Rise (eastern equatorial Atlantic Ocean), *Marine Geology*, *70*(3-4), 223-250.

Curry, W. B., and D. W. Oppo (2005), Glacial water mass geometry and the distribution of δ13C of TCO2 in the western Atlantic Ocean, *Paleoceanography*, *20*(1), PA1017.

Cutler, K. B., R. L. Edwards, F. W. Taylor, H. Cheng, J. Adkins, C. D. Gallup, P. M. Cutler, G. S. Burr, and A. L. Bloom (2003), Rapid sea-level fall and deep-ocean temperature change since the last interglacial period, *Earth and Planetary Science Letters*, *206*(3–4), 253-271.

Dannenmann, S., B. K. Linsley, D. W. Oppo, Y. Rosenthal, and L. Beaufort (2003), East Asian monsoon forcing of suborbital variability in the Sulu Sea during Marine Isotope Stage 3: Link to Northern Hemisphere climate, *Geochem. Geophys. Geosyst.*, *4*(1), 1001.

Dansgaard, W., et al. (1993), Evidence for general instability of past climate from a 250-kyr ice-core record, *Nature*, *364*(6434), 218-220.

de Baar, H. J. W., J. T. M. de Jong, D. C. E. Bakker, B. M. Loscher, C. Veth, U. Bathmann, and V. Smetacek (1995), Importance of iron for plankton blooms and carbon dioxide drawdown in the Southern Ocean, *Nature*, *373*(6513), 412-415.

De La Rocha, C. L. (2003), Silicon isotope fractionation by marine sponges and the reconstruction of the silicon isotope composition of ancient deep water, *Geology*, *31*(5), 423-426.

de Ruijter, W. P. M., A. Biastoch, S. S. Drijfhout, J. R. E. Lutjeharms, R. P. Matano, T. Pichevin, P. J. van Leeuwen, and W. Weijer (1999), Indian-Atlantic interocean exchange: Dynamics, estimation and impact, *J. Geophys. Res.*, *104*(C9), 20885-20910.

de Souza, G. F., B. C. Reynolds, J. Rickli, M. Frank, M. A. Saito, L. J. A. Gerringa, and B. Bourdon (2012), Southern Ocean control of silicon stable isotope distribution in the deep Atlantic Ocean, *Global Biogeochem. Cycles*, *26*(2), GB2035.

Delworth, T. L., et al. (2011), Simulated Climate and Climate Change in the GFDL CM2.5 High-Resolution Coupled Climate Model, *Journal of Climate*, *25*(8), 2755-2781.

DeMaster, D. J. (1981), The supply and accumulation of silica in the marine environment, *Geochimica et Cosmochimica Acta*, *45*(10), 1715-1732.

DeMaster, D. J., W. O. Smith Jr, D. M. Nelson, and J. Y. Aller (1996), Biogeochemical processes in Amazon shelf waters: chemical distributions and uptake rates of silicon, carbon and nitrogen, *Continental Shelf Research*, *16*(5-6), 617-643.

DeMaster, D. J., B. A. McKee, W. S. Moore, D. M. Nelson, W. J. Showers, and W. O. Smith Jr (1991), Geochemical processes occurring at the Amazon River/ocean boundary, *Oceanography*, *4*, 15-20.

deMenocal, P. B., W. F. Ruddiman, and E. M. Pokras (1993), Influences of High- and Low-Latitude Processes on African Terrestrial Climate:Pleistocene Eolian Records from Equatorial Atlantic Ocean Drilling Program Site 663, *Paleoceanography*, *8*(2), 209-242.

Dickson, A. G. (1990), Thermodynamics of the dissociation of boric acid in synthetic seawater from 273.15 to 318.15 K, *Deep Sea Research Part A. Oceanographic Research Papers*, *37*(5), 755-766.

Dickson, A. G. (1993), The measurement of sea water pH, *Marine Chemistry*, *44*(2–4), 131-142.

Dickson, A. G., and F. J. Millero (1987), A comparison of the equilibrium constants for the dissociation of carbonic acid in seawater media, *Deep Sea Research Part A. Oceanographic Research Papers*, *34*(10), 1733-1743.

Dickson, A. G., and C. Goyet (1994), *Handbook of Methods for the Analysis of the Various Parameters of the Carbon Dioxide System in Seawater*, Version 2, A. G. Dickson & C. Goyet, eds. ORNL/CDIAC-74.

DiTullio, G. R., and W. O. Smith Jr (1995), Relationship between dimethylsulfide and phytoplankton pigment concentrations in the Ross Sea, Antarctica, *Deep Sea Research Part I: Oceanographic Research Papers*, *42*(6), 873-892.

Dobson, D. M., G. R. Dickens, and D. K. Rea (1997), Terrigenous Sedimentation at Ceara Rise, in *Proceedings of the Ocean Drilling Program Scientific Results*, edited by N. J. Shackleton, W. B. Curry, C. Richter and T. J. Bralower, pp. 465-473, Ocean Drilling Program.

Dubois, N., M. Kienast, S. Kienast, S. E. Calvert, R. François, and R. F. Anderson (2010), Sedimentary opal records in the eastern equatorial Pacific: It is not all about leakage, *Global Biogeochem. Cycles*, *24*(4), GB4020.

Dugdale, R. C., and F. P. Wilkerson (1998), Silicate regulation of new production in the equatorial Pacific upwelling, *Nature*, *391*(6664), 270-273.
Dunne, J. P., J. L. Sarmiento, and A. Gnanadesikan (2007), A synthesis of global particle export from the surface ocean and cycling through the ocean interior and on the seafloor, *Global Biogeochem. Cycles*, *21*(4), GB4006.
Duplessy, J. C., N. J. Shackleton, R. G. Fairbanks, L. Labeyrie, D. Oppo, and N. Kallel (1988), Deepwater Source Variations During the Last Climatic Cycle and Their Impact on the Global Deepwater Circulation, *Paleoceanography*, *3*(3), 343-360.
Egge, J. K., and D. L. Aksnes (1992), Silicate as regulating nutrient in phytoplankton competition, *Marine Ecology Progress Series*, *83*, 281-289.
Elmore, A. C., E. L. Sikes, M. S. Cook, B. Schiraldi, and T. Guilderson (2011), Enhanced Southern Ocean Ventilation Through the Last Deglaciation., paper presented at American Geophysical Union Fall Meeting San Francisco, California.
Emerson, S. (1985), Organic carbon preservation in marine sediments, in *The carbon cycle and atmospheric CO_2: Natural variations Archean to Present*, edited by E. T. Sundquist and W. S. Broecker, pp. 78-88, American Geophysical Union, Washington D. C.
Emerson, S., and M. J. Bender (1981), Carbon fluxes at the sediment-water interface of the deep-sea: calcium carbonate preservation, *Journal of Marine Research*, *39*, 139-162.
EPICA (2006), One-to-one coupling of glacial climate variability in Greenland and Antarctica, *Nature*, *444*(7116), 195-198.
Fairbanks, R. G. (1989), A 17,000-year glacio-eustatic sea level record: influence of glacial melting rates on the Younger Dryas event and deep-ocean circulation, *Nature*, *342*(6250), 637-642.
Fleisher, M. Q., and R. F. Anderson (2003), Assessing the collection efficiency of Ross Sea sediment traps using ^{230}Th and ^{231}Pa, *Deep Sea Research Part II: Topical Studies in Oceanography*, *50*(3-4), 693-712.
Flores, J. A., M. A. Bárcena, and F. J. Sierro (2000), Ocean-surface and wind dynamics in the Atlantic Ocean off Northwest Africa during the last 140,000 years, *Palaeogeography, Palaeoclimatology, Palaeoecology*, *161*(3–4), 459-478.
Foster, G. L., D. Vance, and J. Prytulak (2007), No change in the neodymium isotope composition of deep water exported from the North Atlantic on glacial-interglacial time scales, *Geology*, *35*(1), 37-40.
Franck, V. M., M. A. Brzezinski, K. H. Coale, and D. M. Nelson (2000), Iron and silicic acid concentrations regulate Si uptake north and south of the Polar Frontal Zone in the Pacific Sector of the Southern Ocean, *Deep Sea Research Part II: Topical Studies in Oceanography*, *47*(15-16), 3315-3338.
Francois, R., M. P. Bacon, and D. O. Suman (1990), Thorium-230 Profiling in Deep-Sea Sediments: High-Resolution Records of Flux and Dissolution of Carbonate in the Equatorial Atlantic During the Last 24,000 Years, *Paleoceanography*, *5*(5), 761-787.
Francois, R., M. Frank, M. M. Rutgers van der Loeff, and M. P. Bacon (2004), ^{230}Th normalization: An essential tool for interpreting sedimentary fluxes during the late Quaternary, *Paleoceanography*, *19*(1), PA1018.
Francois, R., M. A. Altabet, E.-F. Yu, D. M. Sigman, M. P. Bacon, M. Frank, G. Bohrmann, G. Bareille, and L. D. Labeyrie (1997), Contribution of Southern Ocean surface-water stratification to low atmospheric CO_2 concentrations during the last glacial period, *Nature*, *389*(6654), 929-935.
Frank, M. (2002), Radiogenic isotopes: Tracers of past ocean circulation and erosional input, *Rev. Geophys.*, *40*(1), 1001.
Frank, M., R. Gersonde, M. R. van der Loeff, G. Bohrmann, C. C. Nürnberg, P. W. Kubik, M. Suter, and A. Mangini (2000), Similar Glacial and Interglacial Export Bioproductivity in the Atlantic Sector of the Southern Ocean: Multiproxy Evidence and Implications for Glacial Atmospheric CO2, *Paleoceanography*, *15*(6), 642-658.
Ganeshram, R. S., T. F. Pedersen, S. E. Calvert, and J. W. Murray (1995), Large changes in oceanic nutrient inventories from glacial to interglacial periods, *Nature*, *376*(6543), 755-758.
Ganopolski, A., and S. Rahmstorf (2001), Rapid changes of glacial climate simulated in a coupled climate model, *Nature*, *409*(6817), 153-158.
Gardner, J. V., and L. H. Burckle (1975), Upper Pleistocene Ethmodiscus rex oozes from the eastern equatorial Atlantic, *Micropaleontology*, *21*(2), 236-242.
Garzoli, S. L., and A. L. Gordon (1996), Origins and variability of the Benguela Current, *J. Geophys. Res.*, *101*(C1), 897-906.
Gasse, F. (2000), Hydrological changes in the African tropics since the Last Glacial Maximum, *Quaternary Science Reviews*, *19*(1–5), 189-211.
Geibert, W., and R. Usbeck (2004), Adsorption of thorium and protactinium onto different particle types: experimental findings, *Geochimica et Cosmochimica Acta*, *68*(7), 1489-1501.
Georg, R. B., B. C. Reynolds, M. Frank, and A. N. Halliday (2006), New sample preparation techniques for the determination of Si isotopic composition using MC-ICPMS, *Chemical Geology*, *235*, 95-104.

Gherardi, J. M., L. Labeyrie, J. F. McManus, R. Francois, L. C. Skinner, and E. Cortijo (2005), Evidence from the Northeastern Atlantic basin for variability in the rate of the meridional overturning circulation through the last deglaciation, *Earth and Planetary Science Letters*, *240*(3–4), 710-723.

Gil, I. M., L. D. Keigwin, and F. G. Abrantes (2009), Deglacial diatom productivity and surface ocean properties over the Bermuda Rise, northeast Sargasso Sea, *Paleoceanography*, *24*(4), PA4101.

Goldstein, S. L., and S. R. Hemming (2003), Long-lived Isotopic Tracers in Oceanography, Paleoceanography, and Ice-sheet Dynamics, in *Treatise on Geochemistry*, edited by D. H. Heinrich and K. T. Karl, pp. 453-489, Pergamon, Oxford.

Goldstein, S. L., R. K. O'Nions, and P. J. Hamilton (1984), A Sm-Nd isotopic study of atmospheric dusts and particulates from major river systems, *Earth and Planetary Science Letters*, *70*(2), 221-236.

Goldstein, S. L., N. T. Arndt, and R. F. Stallard (1997), The history of a continent from U-Pb ages of zircons from Orinoco River sand and Sm-Nd isotopes in Orinoco basin river sediments, *Chemical Geology*, *139*(1–4), 271-286.

Govin, A., E. Michel, L. Labeyrie, C. Waelbroeck, F. Dewilde, and E. Jansen (2009), Evidence for northward expansion of Antarctic Bottom Water mass in the Southern Ocean during the last glacial inception, *Paleoceanography*, *24*(1), PA1202.

Gregg, W. W., M. E. Conkright, P. Ginoux, J. E. O'Reilly, and N. W. Casey (2003), Ocean primary production and climate: Global decadal changes, *Geophys. Res. Lett.*, *30*(15), 1809.

Grützner, J., et al. (2002), Astronomical age models for Pleistocene drift sediments from the western North Atlantic (ODP Sites 1055–1063), *Marine Geology*, *189*(1–2), 5-23.

Gueguen, C., and L. Guo (2002), Thorium and protactinium sorption on silica, *Geochimica et Cosmochimica Acta*, *66*(S1), A295.

Guerzoni, S., Molinaroli, E. and R. Chester (1997), Saharan dust inputs to the western Mediterranean Sea: depositional patterns, geochemistry and sedimentological implications, *Deep-Sea Res.II*, *44*, 631-654.

Guihou, A., S. Pichat, S. Nave, A. Govin, L. Labeyrie, E. Michel, and C. Waelbroeck (2010), Late slowdown of the Atlantic Meridional Overturning Circulation during the Last Glacial Inception: New constraints from sedimentary (^{231}Pa/^{230}Th), *Earth and Planetary Science Letters*, *289*(3-4), 520-529.

Guilderson, T. P., R. G. Fairbanks, and J. L. Rubenstone (1994), Tropical Temperature Variations Since 20,000 Years Ago: Modulating Interhemispheric Climate Change, *Science*, *263*(5147), 663-665.

Gutjahr, M., M. Frank, C. H. Stirling, L. D. Keigwin, and A. N. Halliday (2008), Tracing the Nd isotope evolution of North Atlantic Deep and Intermediate Waters in the western North Atlantic since the Last Glacial Maximum from Blake Ridge sediments, *Earth and Planetary Science Letters*, *266*(1–2), 61-77.

Gutjahr, M., M. Frank, C. H. Stirling, V. Klemm, T. van de Flierdt, and A. N. Halliday (2007), Reliable extraction of a deepwater trace metal isotope signal from Fe-Mn oxyhydroxide coatings of marine sediments, *Chemical Geology*, *242*(3-4), 351-370.

Haddad, G. A., and A. W. Droxler (1996), Metastable $CaCO_3$ Dissolution at Intermediate Water Depths of the Caribbean and Western North Atlantic: Implications for Intermediate Water Circulation During the Past 200,000 Years, *Paleoceanography*, *11*(6), 701-716.

Hain, M. P., D. M. Sigman, and G. H. Haug (2010), Carbon dioxide effects of Antarctic stratification, North Atlantic Intermediate Water formation, and subantarctic nutrient drawdown during the last ice age: Diagnosis and synthesis in a geochemical box model, *Global Biogeochem. Cycles*, *24*(4), GB4023.

Hales, B. (2003), Respiration, dissolution, and the lysocline, *Paleoceanography*, *18*(4), 1099.

Hales, B., and S. Emerson (1997), Calcite dissolution in sediments of the Ceara Rise: In situ measurements of porewater O_2, pH, and CO_2(aq), *Geochimica et Cosmochimica Acta*, *61*(3), 501-514.

Haley, B. A., G. P. Klinkhammer, and J. McManus (2004), Rare earth elements in pore waters of marine sediments, *Geochimica et Cosmochimica Acta*, *68*(6), 1265-1279.

Hanawa, K., and L. D. Talley (2001), Mode Waters, in *Ocean Circulation and Climate*, edited by G. Siedler and J. Church, pp. 373-386, Academic Press, International Geophysics Series, San Diego.

Hansen, J., M. Sato, and R. Ruedy (1995), Long-term changes of the diurnal temperature cycle: implications about mechanisms of global climate change, *Atmospheric Research*, *37*(1–3), 175-209.

Hansen, J., D. Johnson, A. Lacis, S. Lebedeff, P. Lee, D. Rind, and G. Russell (1981), Climate Impact of Increasing Atmospheric Carbon Dioxide, *Science*, *213*(4511), 957-966.

Heath, G. R. (1974), Dissolved silica and deep-sea sediments, in *Soc. Econ. Paleont. Mineral. Spec. Publ.*, edited by W. W. Hay, pp. 77-93.

Heinrich, H. (1988), Origin and consequences of cyclic ice rafting in the Northeast Atlantic Ocean during the past 130,000 years, *Quaternary Research*, *29*(2), 142-152.

Henderson, G. M., and R. F. Anderson (2003), The U-series Toolbox for Paleoceanography, *Reviews in Mineralogy and Geochemistry*, *52*(1), 493-531.

Henderson, G. M., C. Heinze, R. F. Anderson, and A. M. E. Winguth (1999), Global distribution of the ^{230}Th flux to ocean sediments constrained by GCM modelling, *Deep Sea Research Part I: Oceanographic Research Papers*, *46*(11), 1861-1893.

Hendry, K. R., R. B. Georg, R. E. M. Rickaby, L. F. Robinson, and A. N. Halliday (2010), Deep ocean nutrients during the Last Glacial Maximum deduced from sponge silicon isotopic compositions, *EPSL*, *292*, 290-300.
Hendry, K. R., M. J. Leng, L. F. Robinson, H. J. Sloane, J. Blusztjan, R. E. M. Rickaby, R. B. Georg and A. N. Halliday (2011), Silicon isotopes in Antarctic sponges: an interlaboratory comparison, *Antarctic Science*, *23*(1), 34-42.
Hendry, K. R., and L. F. Robinson (2012), The relationship between silicon isotope fractionation in sponges and silicic acid concentration: modern and core-top studies of biogenic opal, *Geochimica et Cosmochimica Acta*, *81*, 1-12.
Herwitz, S. R., D. R. Muhs, J. M. Prospero, S. Mahan, and B. Vaughn (1996), Origin of Bermuda's clay-rich Quaternary paleosols and their paleoclimatic significance, *J. Geophys. Res.*, *101*(D18), 23389-23400.
Higginson, M. J., and M. A. Altabet (2004), Initial test of the silicic acid leakage hypothesis using sedimentary biomarkers, *Geophys. Res. Lett.*, *31*(18), L18303.
Hinnov, L. A., M. Schulz, and P. Yiou (2002), Interhemispheric space–time attributes of the Dansgaard–Oeschger oscillations between 100 and 0 ka, *Quaternary Science Reviews*, *21*(10), 1213-1228.
Hodell, D. A., K. A. Venz, C. D. Charles, and U. S. Ninnemann (2003), Pleistocene vertical carbon isotope and carbonate gradients in the South Atlantic sector of the Southern Ocean, *Geochem. Geophys. Geosyst.*, *4*(1), 1004.
Hofmann, E. E., J. M. Klinck, C. M. Lascara, and D. A. Smith (1996), Water mass distribution and circulation west of the Antarctic Peninsula and including Bransfield Strait, in *Foundations for ecological research west of the Antarctic Peninsula*, *Antarctic Research Series*, edited by E. E. Hofmann, R. M. Ross and L. B. Quetin, pp. 61-80, American Geophysical Union, Washington D.C.
Hofmann, M., and H.-J. Schellnhuber (2009), Oceanic acidification affects marine carbon pump and triggers extended marine oxygen holes, *Proceedings of the National Academy of Sciences*, *106*(9), 3017-3022.
Höll, C., B. Karwath, C. Rühlemann, K. A. F. Zonneveld, and H. Willems (1999), Palaeoenvironmental information gained from calcareous dinoflagellates: the late Quaternary eastern and western tropical Atlantic Ocean in comparison, *Palaeogeography, Palaeoclimatology, Palaeoecology*, *146*(1–4), 147-164.
Honjo, S. (1976), Coccoliths: Production, transportation and sedimentation, *Marine Micropaleontology*, *1*(0), 65-79.
Honjo, S. (1980), Material fluxes and modes of sedimentation in the mesopelagic and bathypelagic zones, *Journal of Marine Research*, *38*, 53-97.
Hüls, M., and R. Zahn (2000), Millennial-Scale Sea Surface Temperature Variability in the Western Tropical North Atlantic from Planktonic Foraminiferal Census Counts, *Paleoceanography*, *15*(6), 659-678.
Hurd, D. C., and F. Theyer (1977), Changes in the physical and chemical refractive index, density and water content of acid-cleaned samples, *American Journal of Science*, *277*, 1168-1202.
Hutchins, D. A., and K. W. Bruland (1998), Iron-limited diatom growth and Si:N uptake ratios in a coastal upwelling regime, *Nature*, *393*(6685), 561-564.
Hutchins, D. A., P. N. Sedwick, G. R. DiTullio, P. W. Boyd, B. Quéguiner, F. B. Griffiths, and C. Crossley (2001), Control of phytoplankton growth by iron and silicic acid availability in the subantarctic Southern Ocean: Experimental results from the SAZ Project, *J. Geophys. Res.*, *106*(C12), 31559-31572.
Iglesias-Rodriguez, M. D., R. Armstrong, R. Feely, R. Hood, J. Kleypas, J. D. Milliman, C. Sabine, and J. Sarmiento (2002), Progress made in study of ocean's calcium carbonate budget, *Eos Trans. AGU*, *83*(34).
Ikehara, M., K. Kawamura, N. Ohkouchi, M. Murayama, T. Nakamura, and A. Taira (2000), Variations of Terrestrial Input and Marine Productivity in the Southern Ocean (48°S) During the Last two Deglaciations, *Paleoceanography*, *15*(2), 170-180.
Ingle, S. E. (1975), Solubility of calcite in the ocean, *Marine Chemistry*, *3*(4), 301-319.
Ingle, S. E., C. H. Culberson, J. E. Hawley, and R. M. Pytkowicz (1973), The solubility of calcite in seawater at atmospheric pressure and 35% ‰ salinity, *Marine Chemistry*, *1*(4), 295-307.
Jacobsen, S. B. and G. J. Wasserburg (1980), Sm-Nd isotopic evolution of chondrites, *Earth and Planetary Science Letters*, *50*(1), 139-155.
Jaenicke, R., and L. Schütz (1978), Comprehensive Study of Physical and Chemical Properties of the Surface Aerosols in the Cape Verde Islands Region, *J. Geophys. Res.*, *83*(C7), 3585-3599.
Jahnke, R. A., and D. B. Jahnke (2004), Calcium carbonate dissolution in deep sea sediments: reconciling microelectrode, pore water and benthic flux chamber results, *Geochimica et Cosmochimica Acta*, *68*(1), 47-59.
Jansen, J. H. F., E. Ufkes, and R. R. Schneider (1996), Late Quaternary movements of the Angola-Benguela Front SE Atlantic and implications for advection in the equatorial ocean., in *The South Atlantic: Past and Present Circulation*, edited by G. Wefer, W. H. Berger, G. Siedler and D. J. Webb, pp. 553-575, Springer-Verlag, Berlin.

Jeandel, C. (1993), Concentration and isotopic composition of Nd in the South Atlantic Ocean, *Earth and Planetary Science Letters*, *117*(3-4), 581-591.
Jeandel, C., D. Thouron, and M. Fieux (1998), Concentrations and isotopic compositions of neodymium in the eastern Indian Ocean and Indonesian straits, *Geochimica et Cosmochimica Acta*, *62*(15), 2597-2607.
Jickells, T., Z. An, K. Andersen, A. Baker, G. Bergametti *et al*., (2005), Global iron connections between dust, ocean biogeochemistry and climate, *Science*, *308*, 67-71.
Jin, X., N. Gruber, J. P. Dunne, J. L. Sarmiento, and R. A. Armstrong (2006), Diagnosing the contribution of phytoplankton functional groups to the production and export of particulate organic carbon, $CaCO_3$, and opal from global nutrient and alkalinity distributions, *Global Biogeochem. Cycles*, *20*(2), GB2015.
Johnson, T. C. (1976), Controls on the Preservation of Biogenic Opal in Sediments of the Eastern Tropical Pacific, *Science*, *192*(4242), 887-890.
Kalu, A. E. (1979), *Saharan Dust: Mobilization, Transport, Deposition.*, John Wiley, New York.
Kameo, K., M. C. Shearer, A. W. Droxler, I. Mita, R. Watanabe, and T. Sato (2004), Glacial–interglacial surface water variations in the Caribbean Sea during the last 300 ky based on calcareous nannofossil analysis, *Palaeogeography, Palaeoclimatology, Palaeoecology*, *212*(1-2), 65-76.
Keigwin, L. D., and E. A. Boyle (2008), Did North Atlantic overturning halt 17,000 years ago?, *Paleoceanography*, *23*(1), PA1101.
Keir, R. S. (1980), The dissolution kinetics of biogenic calcium carbonates in seawater, *Geochimica et Cosmochimica Acta*, *44*(2), 241-252.
Keir, R. S. (1995), Is There a Component of Pleistocene CO_2 Change Associated with Carbonate Dissolution Cycles?, *Paleoceanography*, *10*(5), 871-880.
Kemp, A. E. S., R. B. Pearce, I. Grigorov, J. Rance, C. B. Lange, P. Quilty, and I. Salter (2006), Production of giant marine diatoms and their export at oceanic frontal zones: Implications for Si and C flux from stratified oceans, *Global Biogeochemical Cycles*, *20*(4).
Kienast, S. S., M. Kienast, S. Jaccard, S. E. Calvert, and R. François (2006), Testing the silica leakage hypothesis with sedimentary opal records from the eastern equatorial Pacific over the last 150 kyrs, *Geophys. Res. Lett.*, *33*(15), L15607.
Klaas, C., and D. E. Archer (2002), Association of sinking organic matter with various types of mineral ballast in the deep sea: Implications for the rain ratio, *Global Biogeochem. Cycles*, *16*(4), 1116.
Klinkhammer, G. P., and M. R. Palmer (1991), Uranium in the oceans: Where it goes and why, *Geochimica et Cosmochimica Acta*, *55*(7), 1799-1806.
Knauth, L. P., and S. Epstein (1982), The nature of water in hydrous silica, *American Mineralogist*, *67*, 510-520.
Knorr, G., and G. Lohmann (2003), Southern Ocean origin for the resumption of Atlantic thermohaline circulation during deglaciation, *Nature*, *424*(6948), 532-536.
Knorr, G., and G. Lohmann (2007), Rapid transitions in the Atlantic thermohaline circulation triggered by global warming and meltwater during the last deglaciation, *Geochem. Geophys. Geosyst.*, *8*(12), Q12006.
Kopp, G., and J. L. Lean (2011), A new, lower value of total solar irradiance: Evidence and climate significance, *Geophys. Res. Lett.*, *38*(1), L01706.
Koutavas, A., J. Lynch-Stieglitz, T. M. Marchitto, and J. P. Sachs (2002), El Niño-Like Pattern in Ice Age Tropical Pacific Sea Surface Temperature, *Science*, *297*(5579), 226-230.
Krause, J. W., M. W. Lomas, and D. M. Nelson (2009), Biogenic silica at the Bermuda Atlantic Time-series Study site in the Sargasso Sea: Temporal changes and their inferred controls based on a 15-year record, *Global Biogeochem. Cycles*, *23*(3), GB3004.
Ku, T.-L., K. G. Knauss, and G. G. Mathieu (1977), Uranium in open ocean: concentration and isotopic composition, *Deep Sea Research*, *24*(11), 1005-1017.
Kulongoski, J. T., D. R. Hilton, J. A. Izbicki, and K. Belitz (2009), Evidence for prolonged El Nino-like conditions in the Pacific during the Late Pleistocene: a 43 ka noble gas record from California groundwaters, *Quaternary Science Reviews*, *28*(23–24), 2465-2473.
Kumar, N., R. Gwiazda, R. F. Anderson, and P. N. Froelich (1993), $^{231}Pa/^{230}Th$ ratios in sediments as a proxy for past changes in Southern Ocean productivity, *Nature*, *362*(6415), 45-48.
Kumar, N., R. F. Anderson, R. A. Mortlock, P. N. Froelich, P. Kubik, B. Dittrich-Hannen, and M. Suter (1995), Increased biological productivity and export production in the glacial Southern Ocean, *Nature*, *378*(6558), 675-680.
Labeyrie, L. (1979), La composition isotopique de l'oxygene de la silice des valves de diatomees. Mise au point d'une nouveile methode de paleo-climatologie., *PhD thesis, University of Paris, Paris*.
Labeyrie, L., and R. Zahn (2005), Physical properties of sediment core MD99-2198., *Pangaea*, doi: 10.1594/PANGAEA.253083.
Lacan, F., and C. Jeandel (2005a), Acquisition of the neodymium isotopic composition of the North Atlantic Deep Water, *Geochem. Geophys. Geosyst.*, *6*(12), Q12008.

Lacan, F., and C. Jeandel (2005b), Neodymium isotopes as a new tool for quantifying exchange fluxes at the continent-ocean interface, *Earth and Planetary Science Letters*, *232*, 245-257.
Lacis, A. A., G. A. Schmidt, D. Rind, and R. A. Ruedy (2010), Atmospheric CO2: Principal Control Knob Governing Earth's Temperature, *Science*, *330*(6002), 356-359.
Laine, E. P., and C. D. Hollister (1981), Geological effects of the Gulf Stream System on the northern Bermuda Rise, *Marine Geology*, *39*(3-4), 277-310.
Lange, C. B., U. F. Treppke, and G. Fischer (1994), Seasonal Diatom Fluxes in the Giunea Basin and their Relationships to Trade Winds, Hydrography and Upwelling Events, *Deep-Sea Research Part 1 - Oceanographic Research Papers*, *41*(5-6), 859-878.
Laws, E. A., P. G. Falkowski, W. O. Smith, Jr., H. Ducklow, and J. J. McCarthy (2000), Temperature effects on export production in the open ocean, *Global Biogeochem. Cycles*, *14*(4), 1231-1246.
Le, J., and N. J. Shackleton (1992), Carbonate Dissolution Fluctuations in the Western Equatorial Pacific During the Late Quaternary, *Paleoceanography*, *7*(1), 21-42.
Le, J., A. C. Mix, and N. J. Shackleton (1995), Late Quaternary paleoceanography in the eastern equatorial Pacific Ocean from planktonic foraminifers: A high-resolution record from Site 846, in *Proceedings of the Ocean Drilling Program, Scientific Results*, edited by N. G. Pisias, L. A. Mayer, T. R. Janacek, A. Palmer-Julson and T. H. van Andel.
Lea, D. W., D. K. Pak, L. C. Peterson, and K. A. Hughen (2003), Synchroneity of Tropical and High-Latitude Atlantic Temperatures over the Last Glacial Termination, *Science*, *301*(5638), 1361-1364.
Leclerc, A. J., and L. Labeyrie (1987), Temperature dependence of the oxygen isotopic fractionation between diatom silica and water, *Earth and Planetary Science Letters*, *84*(1), 69-74.
Lee, K. (2001), Global net community production estimated from the annual cycle of surface water dissolved inorganic carbon, *Limnology & Oceanography*, *46*, 1287-1297.
Legrand, M., C. Feniet-Saigne, E. S. Sattzman, C. Germain, N. I. Barkov, and V. N. Petrov (1991), Ice-core record of oceanic emissions of dimethylsulphide during the last climate cycle, *Nature*, *350*(6314), 144-146.
Leuschner, D. C., and F. Sirocko (2000), The low-latitude monsoon climate during Dansgaard–Oeschger cycles and Heinrich Events, *Quaternary Science Reviews*, *19*(1–5), 243-254.
Levitus, S. (1982), *Climatological atlas of the world ocean*, U.S. Dept. of Commerce, National Oceanic and Atmospheric Administration.
Levitus, S., M. E. Conkright, J. L. Reid, R. G. Najjar, and A. Mantyla (1993), Distribution of nitrate, phosphate and silicate in the world oceans, *Progress In Oceanography*, *31*(3), 245-273.
Lewis, W., and J. Saunders (1989), Concentration and transport of dissolved and suspended substances in the Orinoco River, *Biogeochemistry*, *7*(3), 203-240.
Li, Y.-H., T. Takahashi, and W. S. Broecker (1969), Degree of Saturation of $CaCO_3$ in the Oceans, *J. Geophys. Res.*, *74*(23), 5507-5525.
Lippold, J., J. Grützner, D. Winter, Y. Lahaye, A. Mangini, and M. Christl (2009), Does sedimentary $^{231}Pa/^{230}Th$ from the Bermuda Rise monitor past Atlantic Meridional Overturning Circulation?, *Geophys. Res. Lett.*, *36*(12), L12601.
Lippold, J., S. Mulitza, G. Mollenhauer, S. Weyer, D. Heslop, and M. Christl (2012), Boundary scavenging at the East Atlantic margin does not negate the use of $^{231}Pa/^{230}Th$ to trace Atlantic overturning, *Earth and Planetary Science Letters*, *333-334*, 317-331.
Lisitzin, A. P. (1972), Sedimentation in the world ocean, in *Soc. Econ. Paleo. Min.*, edited, p. 218, Tulsa.
Loubere, P., M. Fariduddin, and R. W. Murray (2003), Patterns of export production in the eastern equatorial Pacific over the past 130,000 years, *Paleoceanography*, *18*(2), 1028.
Luo, S., T.-L. Ku, L. Wang, J. R. Southon, S. P. Lund and M. Schwartz (2001), ^{26}Al, ^{10}Be and U–Th isotopes in Blake Outer Ridge sediments: implications for past changes in boundary scavenging, *Earth and Planetary Science Letters*, *185*(1-2), 135-147.
Maher, B.A., J.M. Prospero, D. Mackie., D. Gaiero, P. P. Hesse and Y. Balkanski (2010), Global connections between aeolian dust, climate, and ocean biogeochemistry at the present day and at the last glacial maximum, *Earth-Science Reviews*, *99*, 61-97.
Mangini, A., C. Sonntag, G. Bertsch, and E. Muller (1979), Evidence for a higher natural uranium content in world rivers, *Nature*, *278*(5702), 337-339.
Marchal, O., R. François, T. F. Stocker, and F. Joos (2000), Ocean Thermohaline Circulation and Sedimentary $^{231}Pa/^{230}Th$ Ratio, *Paleoceanography*, *15*(6), 625-641.
Marchitto, T. M., and W. S. Broecker (2006), Deep water mass geometry in the glacial Atlantic Ocean: A review of constraints from the paleonutrient proxy Cd/Ca, *Geochem. Geophys. Geosyst.*, *7*(12), Q12003.
Marinov, I., M. Follows, A. Gnanadesikan, J. L. Sarmiento, and R. D. Slater (2008), How does ocean biology affect atmospheric pCO_2? Theory and models, *J. Geophys. Res.*, *113*(C7), C07032.
Marlowe, I. T., S. C. Brassell, G. Eglinton, and J. C. Green (1990), Long-chain alkenones and alkyl alkenoates and the fossil coccolith record of marine sediments, *Chemical Geology*, *88*(3–4), 349-375.

Marra, J., C. Ho, and C. C. Trees (2003), An Algorithm for Calculation of Primary Productivity from Remote Sensing Data*Rep.*, 27 pp. pp, Lamont-Doherty Earth Observatory, New York.
Martin, J. H. (1990), Glacial-Interglacial CO_2 Change: The Iron Hypothesis, *Paleoceanography*, *5*(1), 1-13.
Martin, J. H. (1992), *Iron as a limiting factor in oceanic productivity*, Plenum, New York.
Martin, W. R., and F. L. Sayles (1996), $CaCO_3$ dissolution in sediments of the Ceara Rise, western equatorial Atlantic, *Geochimica et Cosmochimica Acta*, *60*(2), 243-263.
Martínez-Méndez, G., R. Zahn, I. R. Hall, F. J. C. Peeters, L. D. Pena, I. Cacho, and C. Negre (2010), Contrasting multiproxy reconstructions of surface ocean hydrography in the Agulhas Corridor and implications for the Agulhas Leakage during the last 345,000 years, *Paleoceanography*, *25*(4), PA4227.
Martinson, D. G., N. G. Pisias, J. D. Hays, J. Imbrie, T. C. Moore Jr, and N. J. Shackleton (1987), Age dating and the orbital theory of the ice ages: Development of a high-resolution 0 to 300,000-year chronostratigraphy, *Quaternary Research*, *27*(1), 1-29.
Mashiotta, T. A., D. W. Lea, and H. J. Spero (1999), Glacial–interglacial changes in Subantarctic sea surface temperature and δ18O-water using foraminiferal Mg, *Earth and Planetary Science Letters*, *170*(4), 417-432.
Matsumoto, K., and J. L. Sarmiento (2008), A corollary to the silicic acid leakage hypothesis, *Paleoceanography*, *23*(2), PA2203.
Matsumoto, K., J. L. Sarmiento, and M. A. Brzezinski (2002), Silicic acid leakage from the Southern Ocean: A possible explanation for glacial atmospheric pCO_2, *Global Biogeochem. Cycles*, *16*(3), 1031.
McCartney, M. S. (1977), Subantarctic Mode Water, in *A Voyage of Discovery*, edited by M. Angel, pp. 103-119, Pergamon.
McManus, J. F., R. F. Anderson, W. S. Broecker, M. Q. Fleisher, and S. M. Higgins (1998), Radiometrically determined sedimentary fluxes in the sub-polar North Atlantic during the last 140,000 years, *Earth and Planetary Science Letters*, *155*, 29-43.
McManus, J. F., R. Francois, J. M. Gherardi, L. D. Keigwin, and S. Brown-Leger (2004), Collapse and rapid resumption of Atlantic meridional circulation linked to deglacial climate changes, *Nature*, *428*(6985), 834-837.
McManus, J., W. M. Berelson, G. P. Klinkhammer, D.E. Hammond, C. Holm (2005), Authigenic uranium: relationship to oxygen penetration depth and organic carbon rain, *Geochimica et Cosmochimica Acta*, *69*, 95–108.
Mehrbach, C., C. H. Culberson, and J. E. Hawley (1973), Measurement of the apparent dissociation constants of carbonic acid in seawater at atmospheric pressure., *Limnology & Oceanography*, *18*, 897-907.
Menard, H. W., and S. M. Smith (1966), Hypsometry of Ocean Basin Provinces, *J. Geophys. Res.*, *71*(18), 4305-4325.
Meredith, M. P., K. E. Grose, E. L. McDonagh, K. J. Heywood, R. D. Frew, and P. F. Dennis (1999), Distribution of oxygen isotopes in the water masses of Drake Passage and the South Atlantic, *J. Geophys. Res.*, *104*(C9), 20949-20962.
Mikkelsen, N. (1977), Origin of Ethmodiscus Ooze, *Marine Micropaleontology*, *2*(1), 35-46.
Millero, F. J. (1995), Thermodynamics of the carbon dioxide system in the oceans, *Geochimica et Cosmochimica Acta*, *59*(4), 661-677.
Milliman, J. D., and A. W. Droxler (1996), Neritic and pelagic carbonate sedimentation in the marine environment: Ignorance is not bliss., *Geologische Rundschau*, *85*, 496-504.
Mitchell, J. F. B. (1989), The "Greenhouse effect" and climate change, *Rev. Geophys.*, *27*(1), 115-139.
Molleri, G. S. F., E. M. L. d. M. Novo, and M. Kampel (2010), Space-time variability of the Amazon River plume based on satellite ocean color, *Continental Shelf Research*, *30*(3–4), 342-352.
Moore, J. K., S. C. Doney, and K. Lindsay (2004), Upper ocean ecosystem dynamics and iron cycling in a global three-dimensional model, *Global Biogeochem. Cycles*, 18:GB4028.
Morel, A., H. Claustre, and B. Gentili (2010), The most oligotrophic subtropical zones of the global ocean: similarities and differences in terms of chlorophyll and yellow substance, *Biogeosciences Discussions*, *7*, 5047-5079.
Moreno, A., I. Cacho, M. Canals, M. A. Prins, M. Sánchez-Goñi, amp, x, F. a, J. O. Grimalt, and G. J. Weltje (2002), Saharan Dust Transport and High-Latitude Glacial Climatic Variability: The Alboran Sea Record, *Quaternary Research*, *58*(3), 318-328.
Morford, J.L., A. D. Russell, S. Emerson (2001), Trace metal evidence for changes in the redox environment assocoated with the transition from terrigenous clay to diatomaceous sediments, Saanich Inlet, BC, *Marine Geology*, *174*, 355–369.
Mortlock, R. A., and P. N. Froelich (1989), A simple method for the rapid determination of biogenic opal in pelagic marine sediments, *Deep Sea Research Part A. Oceanographic Research Papers*, *36*(9), 1415-1426.

Mortlock, R. A., P. N. Froelich, R. A. Feely, G. J. Massoth, D. A. Butterfield, and J. E. Lupton (1993), Silica and germanium in Pacific Ocean hydrothermal vents and plumes, *Earth and Planetary Science Letters*, *119*(3), 365-378.
Mucci, A. (1983), The solubility of calcite and aragonite in seawater at various salinities, temperatures, and one atmosphere total pressure, *American Journal of Science*, *283*(7), 780-799.
Mudelsee, M. (2001), The phase relations among atmospheric CO_2 content, temperature and global ice volume over the past 420 ka, *Quaternary Science Reviews*, *20*(4), 583-589.
Negre, C., R. Zahn, A. L. Thomas, P. Masque, G. M. Henderson, G. Martinez-Mendez, I. R. Hall, and J. L. Mas (2010), Reversed flow of Atlantic deep water during the Last Glacial Maximum, *Nature*, *468*(7320), 84-88.
Nelson, D. M., and M. A. Brzezinski (1997), Diatom growth and productivity in an oligotrophic midocean gyre: A 3-yr record from the Sargasso Sea near Bermuda, *Limnology & Oceanography*, *43*, 473-486.
Nelson, D. M., P. Tréguer, M. A. Brzezinski, A. Leynaert, and B. Quéguiner (1995), Production and dissolution of biogenic silica in the ocean: Revised global estimates, comparison with regional data and relationship to biogenic sedimentation, *Global Biogeochem. Cycles*, *9*(3), 359-372.
Nozaki, Y., and D. S. Alibo (2003), Dissolved rare earth elements in the Southern Ocean, southwest of Australia: Unique patterns compared to the South Atlantic data, *Geochemical Journal*, *37*, 47-62.
Nozaki, Y., Y. Horibe, and H. Tsubota (1981), The water column distributions of thorium isotopes in the western North Pacific, *Earth and Planetary Science Letters*, *54*(2), 203-216.
Nozaki, Y., H.-S. Yang, and M. Yamada (1987), Scavenging of Thorium in the Ocean, *J. Geophys. Res.*, *92*(C1), 772-778.
Oeschger, H., J. Beer, U. Siegenthaler, B. Stauffer, W. Dansgaard, and C. C. Langway (1984), *Late Glacial Climate History from Ice Cores.*, 7 pp., American Geophysical Union, Washington D.C.
Oppo, D. W., and R. G. Fairbanks (1987), Variability in the deep and intermediate water circulation of the Atlantic Ocean during the past 25,000 years: Northern Hemisphere modulation of the Southern Ocean, *Earth and Planetary Science Letters*, *86*(1), 1-15.
Oppo, D. W., and S. J. Lehman (1993), Mid-Depth Circulation of the Subpolar North Atlantic During the Last Glacial Maximum, *Science*, *259*(5098), 1148-1152.
Orsi, A. H., G. C. Johnson, and J. L. Bullister (1999), Circulation, mixing, and production of Antarctic Bottom Water, *Progress In Oceanography*, *43*(1), 55-109.
Ott, S. T., A. Ott, D. W. Martin, and J. A. Young (1991), Analysis of a Trans-Atlantic Saharan Dust Outbreak Based on Satellite and GATE Data, *Monthly Weather Review*, *119*(8), 1832-1850.
Pahnke, K., and R. Zahn (2005), Southern Hemisphere Water Mass Conversion Linked with North Atlantic Climate Variability, *Science*, *307*(5716), 1741-1746.
Pahnke, K., S. L. Goldstein, and S. R. Hemming (2008), Abrupt changes in Antarctic Intermediate Water circulation over the past 25,000 years, *Nature Geoscience*, *1*, 870-874.
Paytan, A., M. Kastner, and F. P. Chavez (1996), Glacial to Interglacial Fluctuations in Productivity in the Equatorial Pacific as Indicated by Marine Barite, *Science*, *274*(5291), 1355-1357.
Peeters, F. J. C., R. Acheson, G.-J. A. Brummer, W. P. M. de Ruijter, R. R. Schneider, G. M. Ganssen, E. Ufkes, and D. Kroon (2004), Vigorous exchange between the Indian and Atlantic oceans at the end of the past five glacial periods, *Nature*, *430*(7000), 661-665.
Pelejero, C., J. O. Grimalt, M. Sarnthein, L. Wang, and J.-A. Flores (1999), Molecular biomarker record of sea surface temperature and climatic change in the South China Sea during the last 140,000 years, *Marine Geology*, *156*(1–4), 109-121.
Peterson, L. C., and G. H. Haug (2006), Variability in the mean latitude of the Atlantic Intertropical Convergence Zone as recorded by riverine input of sediments to the Cariaco Basin (Venezuela), *Palaeogeography, Palaeoclimatology, Palaeoecology*, *234*(1), 97-113.
Peterson, L. C., G. H. Haug, K. A. Hughen, and U. Röhl (2000), Rapid Changes in the Hydrologic Cycle of the Tropical Atlantic During the Last Glacial, *Science*, *290*(5498), 1947-1951.
Peterson, R. G., and L. Stramma (1991), Upper-level circulation in the South Atlantic Ocean, *Progress In Oceanography*, *26*(1), 1-73.
Petit, J. R., et al. (1999), Climate and atmospheric history of the past 420,000 years from the Vostok ice core, Antarctica, *Nature*, *399*(6735), 429-436.
Pichevin, L. E., B. C. Reynolds, R. S. Ganeshram, I. Cacho, L. Pena, K. Keefe, and R. M. Ellam (2009), Enhanced carbon pump inferred from relaxation of nutrient limitation in the glacial ocean, *Nature*, *459*(7250), 1114-1117.
Piepgras, D. J., and G. J. Wasserburg (1980), Neodymium isotopic variations in seawater, *Earth and Planetary Science Letters*, *50*(1), 128-138.
Piepgras, D. J., and G. J. Wasserburg (1982), Isotopic Composition of Neodymium in Waters from the Drake Passage, *Science*, *217*(4556), 207-214.

Piepgras, D. J., and G. J. Wasserburg (1983), Influence of the Mediterranean Outflow on the Isotopic Composition of Neodymium in Waters of the North Atlantic, *J. Geophys. Res.*, *88*(C10), 5997-6006.
Piepgras, D. J., and G. J. Wasserburg (1987), Rare earth element transport in the western North Atlantic inferred from Nd isotopic observations, *Geochimica et Cosmochimica Acta*, *51*(5), 1257-1271.
Piepgras, D. J., and S. B. Jacobsen (1988), The isotopic composition of neodymium in the North Pacific, *Geochimica et Cosmochimica Acta*, *52*(6), 1373-1381.
Piola, A. R., and D. T. Georgi (1982), Circumpolar properties of Antarctic intermediate water and Subantarctic Mode Water, *Deep Sea Research Part A. Oceanographic Research Papers*, *29*(6), 687-711.
Piola, A. R., and A. L. Gordon (1989), Intermediate waters in the southwest South Atlantic, *Deep Sea Research Part A. Oceanographic Research Papers*, *36*(1), 1-16.
Piotrowski, A. M., S. L. Goldstein, S. R. Hemming, and R. G. Fairbanks (2005), Temporal Relationships of Carbon Cycling and Ocean Circulation at Glacial Boundaries, *Science*, *307*(5717), 1933-1938.
Piotrowski, A. M., S. L. Goldstein, H. S. R, R. G. Fairbanks, and D. R. Zylberberg (2008), Oscillating glacial northern and southern deep water formation from combined neodymium and carbon isotopes, *Earth and Planetary Science Letters*, *272*(1-2), 394-405.
Piotrowski, A. M., V. K. Banakar, A. E. Scrivner, H. Elderfield, A. Galy, and A. Dennis (2009), Indian Ocean circulation and productivity during the last glacial cycle, *Earth and Planetary Science Letters*, *285*(1-2), 179-189.
Plant, J. A., P. R. Simpson, B. Smith, and B. F. Windley (1999), Uranium Ore Deposits - Products of the Radioactive Earth, in *Uranium: Mineralogy, Geochemistry and the Environment*, edited by P. C. Burns and R. Finch, The Mineralogical Society of America, Washington D.C.
Pokras, E. M. (1986), Preservation of fossil diatoms in Atlantic sediment cores: control by supply rate, *Deep Sea Research Part A. Oceanographic Research Papers*, *33*(7), 893-902.
Pondaven, P., O. Ragueneau, P. Treguer, A. Hauvespre, L. Dezileau, and J. L. Reyss (2000), Resolving the `opal paradox' in the Southern Ocean, *Nature*, *405*(6783), 168-172.
Pourmand, A., F. Marcantonio and H. Schulz (2004), Variations in productivity and eolian fluxes in the northeastern Arabian Sea during the past 110 ka, *Earth and Planetary Science Letters*, *221*(1-4), 39-54.
Prahl, F. G., R. B. Collier, J. Dymond, M. Lyle, and M. A. Sparrow (1993), A biomarker perspective on prymnesiophyte productivity in the northeast pacific ocean, *Deep Sea Research Part I: Oceanographic Research Papers*, *40*(10), 2061-2076.
Primeau, F. (2005), Characterizing Transport between the Surface Mixed Layer and the Ocean Interior with a Forward and Adjoint Global Ocean Transport Model, *Journal of Physical Oceanography*, *35*(4), 545-564.
Prospero, J. M., R. A. Glaccum, and R. T. Nees (1981), Atmospheric transport of soil dust from Africa to South America, *Nature*, *289*(5798), 570-572.
Prospero, J. M. (1996), Saharan dust transport over the North Atlantic Ocean and Mediterranean: an overview, in *The Impact of Desert Dust Across the Mediterranean*, eds. S. Guerzoni and R. Chester, Dordrecht, Neth.: Kluwer Acad., 133-151.
Ragueneau, O., et al. (2000), A review of the Si cycle in the modern ocean: recent progress and missing gaps in the application of biogenic opal as a paleoproductivity proxy, *Global and Planetary Change*, *26*(4), 317-365.
Rampen, S. W., B. A. Abbas, S. Schouten, and J. S. Sinninghe Damsté (2010), A comprehensive study of sterols in marine diatoms (Bacillariophyta): Implications for their use as tracers for diatom productivity, *Limnology & Oceanography*, *55*(1), 91-105.
Rattray, J. (1890), A revision of the genus Coscinodiscus and some allied genera, *Proceedings of the Royal Society of Edinburgh*, *16*, 449-692.
Raymont, J. E. G. (1980), Plankton and productivity in the oceans., in *Phytoplankton*, edited, p. 489, Pergamon, New York.
Rea, D. K., N. G. Pisias, and T. Newberry (1991), Late Pleistocene Paleoclimatology of the Central Equatorial Pacific: Flux Patterns of Biogenic Sediments, *Paleoceanography*, *6*(2), 227-244.
Richaud, M., P. Loubere, S. Pichat, and R. Francois (2007), Changes in opal flux and the rain ratio during the last 50,000 years in the equatorial Pacific, *Deep Sea Research II*, *54*, 762-771.
Ridgwell, A. J. (2003), An end to the rain ratio reign?, *Geochem. Geophys. Geosyst.*, *4*(6), 1051.
Ridgwell, A. J. and A. J. Watson (2002), Feedback between aeolian dust, climate and atmospheric CO_2 in glacial time, *Paleoceanography*, 17:1059.
Ridley, J. K., P. Huybrechts, J. M. Gregory, and J. A. Lowe (2005), Elimination of the Greenland Ice Sheet in a High CO_2 Climate, *Journal of Climate*, *18*(17), 3409-3427.
Robbins, L. L., M. E. Hansen, J. A. Kleypas, and S. C. Meylan (2010), CO2calc—A user-friendly seawater carbon calculator for Windows, Max OS X, and iOS (iPhone) *Rep.*, 17 pp, U.S. Geological Survey.
Robinson, L. F., and T. van de Flierdt (2009), Southern Ocean evidence for reduced export of North Atlantic Deep Water during Heinrich event 1, *Geology*, *37*(3), 195-198.

Rodger Harvey, H., J. H. Tuttle, and J. Tyler Bell (1995), Kinetics of phytoplankton decay during simulated sedimentation: Changes in biochemical composition and microbial activity under oxic and anoxic conditions, *Geochimica et Cosmochimica Acta*, *59*(16), 3367-3377.

Rogerson, M., P. P. E. Weaver, E. J. Rohling, L. J. Lourens, J. W. Murray, and A. Hayes (2006), Colour logging as a tool in high-resolution palaeoceanography, in *New Techniques in Sediment Core Analysis*, edited by R. G. Rothwell, pp. 99-112, Geological Society (Special Publications), London.

Rosenthal, Y., E. A. Boyle, L. Labeyrie, and D. Oppo (1995), Glacial Enrichments of Authigenic Cd And U in Subantarctic Sediments: A Climatic Control on the Elements' Oceanic Budget?, *Paleoceanography*, *10*(3), 395-413.

Rostek, F., E. Bard, L. Beaufort, C. Sonzogni, and G. Ganssen (1997), Sea surface temperature and productivity records for the past 240 kyr in the Arabian Sea, *Deep Sea Research Part II: Topical Studies in Oceanography*, *44*(6–7), 1461-1480.

Roy, T., L. Bopp, M. Gehlen, B. Schneider, P. Cadule, T. L. Frölicher, J. Segschneider, J. Tjiputra, C. Heinze, and F. Joos (2011), Regional Impacts of Climate Change and Atmospheric CO_2 on Future Ocean Carbon Uptake: A Multimodel Linear Feedback Analysis, *Journal of Climate*, *24*(9), 2300-2318.

Ruddiman, W. F. (2001), Earth's climate system today, in *Earth's climate: past and future*, edited by B. Salazar, pp. 18-53, W.H. Freeman and Company, New York.

Ruddiman, W. F., M. Sarnthein, and J. Baldauf (1986), Site 663, in *Proceedings of the Ocean Drilling Program, Part A (Initial Reports)*, edited by S. K. Stewart and W. D. Rose, pp. 557-619, ODP.

Rühlemann, C., M. Frank, W. Hale, A. Mangini, S. Mulitza, P. J. Müller, and G. Wefer (1996), Late Quaternary productivity changes in the western equatorial Atlantic: Evidence from ^{230}Th-normalized carbonate and organic carbon accumulation rates, *Marine Geology*, *135*(1–4), 127-152.

Rutberg, R. L., S. R. Hemming, and S. L. Goldstein (2000), Reduced North Atlantic Deep Water flux to the glacial Southern Ocean inferred from neodymium isotope ratios, *Nature*, *405*(6789), 935-938.

Ryther, J. H. (1969), Photosynthesis and Fish Production in the Sea, *Science*, *166*(3901), 72-76.

Sachs, J. P., and R. F. Anderson (2005), Increased productivity in the subantarctic ocean during Heinrich events, *Nature*, *434*(7037), 1118-1121.

Sarmiento, J. L., and N. Gruber (2006), *Ocean Biogeochemical Dynamics*, Princeton University Press, Princeton, N.J.

Sarmiento, J. L., N. Gruber, M. A. Brzezinski, and J. P. Dunne (2004), High-latitude controls of thermocline nutrients and low latitude biological productivity, *Nature*, *427*(6969), 56-60.

Sarmiento, J. L., J. Dunne, A. Gnanadesikan, R. M. Key, K. Matsumoto, and R. Slater (2002), A new estimate of the $CaCO_3$ to organic carbon export ratio, *Global Biogeochem. Cycles*, *16*(4), 1107.

Sarnthein, M., G. Tetzlaff, B. Koopmann, K. Wolter, and U. Pflaumann (1981), Glacial and interglacial wind regimes over the eastern subtropical Atlantic and North-West Africa, *Nature*, *293*(5829), 193-196.

Sarnthein, M., U. Pflaumann, R. Ross, R. Tiedemann, and K. Winn (1992), Transfer functions to reconstruct ocean palaeoproductivity: a comparison, in *Upwelling Systems: Evolution Since the Early Miocene*, edited by C. P. Summerhayes, W. L. Prell and K. C. Emeis, pp. 411-427, Geological Society Special Publication.

Sarnthein, M., K. Winn, S. J. A. Jung, J.-C. Duplessy, L. Labeyrie, H. Erlenkeuser, and G. Ganssen (1994), Changes in East Atlantic Deepwater Circulation Over the Last 30,000 years: Eight Time Slice Reconstructions, *Paleoceanography*, *9*(2), 209-267.

Sarnthein, M., et al. (2000), Fundamental Modes and Abrupt Changes in North Atlantic Circulation and Climate over the last 60 ky – Concepts, Reconstruction and Numerical Modeling, in *The Northern North Atlantic: A Changing Environment.*, edited by P. Schäfer, W. Ritzrau, M. Schlüter and J. Theide, pp. 365-410, Springer, Berlin.

Savage, P. S., R. B. Georg, R. M. G. Armytage, H. M. Williams, and A. N. Halliday (2010), Silicon isotope homogeneity in the mantle, *Earth and Planetary Science Letters*, *295*(1-2), 139-146.

Sawada, K., and Y. Shiraiwa (2004), Alkenone and alkenoic acid compositions of the membrane fractions of Emiliania huxleyi, *Phytochemistry*, *65*(9), 1299-1307.

Schefuß, E., G. J. M. Versteegh, J. H. F. Jansen, and J. S. Sinninghe Damsté (2004), Lipid biomarkers as major source and preservation indicators in SE Atlantic surface sediments, *Deep Sea Research Part I: Oceanographic Research Papers*, *51*(9), 1199-1228.

Scherer, R. P. (1994), A new method for the determination of absolute abundance of diatoms and other silt-sized sedimentary particles, *Journal of Paleolimnology*, *12*(2), 171-179.

Schlitzer, R. (2000), Electronic Atlas of WOCE Hydrographic and Tracer data now available, *Eos Trans AGU*, *81*.

Schmidt, M. W., M. J. Vautravers, and H. J. Spero (2006), Rapid subtropical North Atlantic salinity oscillations across Dansgaard-Oeschger cycles, *Nature*, *443*(7111), 561-564.

Schneider, R. R., P. J. Müller, and R. Acheson (1999), Atlantic Alkenone Sea Surface Temperature Records: Low versus Mid Latitudes and Differences Between Hemispheres, in *Reconstructing Ocean History: A Window into the Future*, edited by F. Abrantes and A. C. Mix, pp. 33-56, Plenum, New York.

Schneider, R. R., B. Price, P. J. Müller, D. Kroon, and I. Alexander (1997), Monsoon Related Variations in Zaire (Congo) Sediment Load and Influence of Fluvial Silicate Supply on Marine Productivity in the East Equatorial Atlantic During the Last 200,000 Years, *Paleoceanography*, *12*(3), 463-481.

Scholten, J. C., J. Fietzke, S. Vogler, M. M. Rutgers van der Loeff, A. Mangini, W. Koeve, J. Waniek, P. Stoffers, A. Antia, and J. Kuss (2001), Trapping efficiencies of sediment traps from the deep Eastern North Atlantic:: the 230Th calibration, *Deep Sea Research Part II: Topical Studies in Oceanography*, *48*(10), 2383-2408.

Scholz, C. A., et al. (2007), East African megadroughts between 135 and 75 thousand years ago and bearing on early-modern human origins, *Proceedings of the National Academy of Sciences*, *104*(42), 16416-16421.

Schouten, M. W., W. P. M. de Ruijter, P. J. van Leeuwen, and J. R. E. Lutjeharms (2000), Translation, decay and splitting of Agulhas rings in the southeastern Atlantic Ocean, *J. Geophys. Res.*, *105*(C9), 21913-21925.

Schrader, H.-J., and G. Schuette (1968), Marine diatoms, in *The Sea*, edited by C. Emiliani, pp. 1179-1231, Wiley, New York.

Schulte, S., and E. Bard (2003), Past changes in biologically mediated dissolution of calcite above the chemical lysocline recorded in Indian Ocean sediments, *Quaternary Science Reviews*, *22*(15–17), 1757-1770.

Schulte, S., K. Mangelsdorf, and J. Rullkötter (2000), Organic matter preservation on the Pakistan continental margin as revealed by biomarker geochemistry, *Organic Geochemistry*, *31*(10), 1005-1022.

Seidov, D., and M. Maslin (1999), North Atlantic deep water circulation collapse during Heinrich events, *Geology*, *27*(1), 23-26.

Seki, O., M. Ikehara, K. Kawamura, T. Nakatsuka, K. Ohnishi, M. Wakatsuchi, H. Narita, and T. Sakamoto (2004), Reconstruction of paleoproductivity in the Sea of Okhotsk over the last 30 kyr, *Paleoceanography*, *19*(1), PA1016.

Shackleton, N. J. (1977), Carbon-13 in Uvigerina: Tropical rain forest history and the equatorial Pacific carbonate dissolution cycle., in *The Fate of Fossil Fuel in the Oceans.*, edited by N. R. Andersen and A. Malahoff, pp. 401-427, Plenum, New York.

Shackleton, N. J. (2000), The 100,000-Year Ice-Age Cycle Identified and Found to Lag Temperature, Carbon Dioxide, and Orbital Eccentricity, *Science*, *289*(5486), 1897-1902.

Shimizu, H., K. Tachikawa, A. Masuda, and Y. Nozaki (1994), Cerium and neodymium isotope ratios and REE patterns in seawater from the North Pacific Ocean, *Geochimica et Cosmochimica Acta*, *58*(1), 323-333.

Shimmield, G. B., and N. B. Price (1988), The scavenging of U, ^{230}Th and ^{231}Pa during pulsed hydrothermal activity at 20°S, East Pacific Rise, *Geochimica et Cosmochimica Acta*, *52*(3), 669-677.

Sicre, M.-A., Y. Ternois, M. Paterne, P. Martinez, and P. Bertrand (2001), Climatic changes in the upwelling region off Cap Blanc, NW Africa, over the last 70 kyear: a multi-biomarker approach, *Organic Geochemistry*, *32*(8), 981-990.

Sicre, M.-A., Y. Ternois, M. Paterne, A. Boireau, L. Beaufort, P. Martinez, and P. Bertrand (2000), Biomarker stratigraphic records over the last 150 kyears off the NW African coast at 25°N, *Organic Geochemistry*, *31*(6), 577-588.

Sievers, H. A., and W. D. Nowlin, Jr. (1984), The Stratification and Water Masses at Drake Passage, *J. Geophys. Res.*, *89*(C6), 10489-10514.

Sigman, D. M., and E. A. Boyle (2000), Glacial/interglacial variations in atmospheric carbon dioxide, *Nature*, *407*(6806), 859-869.

Sigman, D. M., D. C. McCorkle, and W. R. Martin (1998), The calcite lysocline as a constraint on glacial/interglacial low-latitude production changes, *Global Biogeochem. Cycles*, *12*(3), 409-427.

Sigman, D. M., M. P. Hain, and G. H. Haug (2010), The polar ocean and glacial cycles in atmospheric CO_2 concentration, *Nature*, *466*(7302), 47-55.

Smayda, T. J. (1971), Normal and accelerated sinking of phytoplankton in the sea, *Marine Geology*, *11*(2), 105-122.

Spencer D. W., Bacon M. P., and Brewer P. G. (1981) Models of the distribution of ^{210}Pb in a section across the North Equatorial Atlantic Ocean, *Journal of Marine Research*, *39*(1): 119-137

Spivack, A. J., and G. J. Wasserburg (1988), Neodymium isotopic composition of the Mediterranean outflow and the eastern North Atlantic, *Geochimica et Cosmochimica Acta*, *52*(12), 2767-2773.

Stabell, B. (1986), Variations of Diatom Flux in the Eastern Equatorial Atlantic During the Last 400,000 Years (METEOR Cores 13519 and 13521), *Marine Geology*, *72*(3-4), 305-323.

Stephens, B. B., and R. F. Keeling (2000), The influence of Antarctic sea ice on glacial-interglacial CO_2 variations, *Nature*, *404*(6774), 171-174.

Stichel, T., M. Frank, J. Rickli, and B. A. Haley (2012), The hafnium and neodymium isotope composition of seawater in the Atlantic sector of the Southern Ocean, *Earth and Planetary Science Letters*, *317–318*(0), 282-294.

Stordal, M. C., and G. J. Wasserburg (1986), Neodymium isotopic study of Baffin Bay water: sources of REE from very old terranes, *Earth and Planetary Science Letters*, *77*(3-4), 259-272.
Stramma, L., and F. Schott (1999), The mean flow field of the tropical Atlantic Ocean, *Deep Sea Research Part II: Topical Studies in Oceanography*, *46*(1–2), 279-303.
Stumm, W., and J. J. Morgan (1981), *Aquatic Chemistry*, 2nd ed., Wiley and Sons, New York.
Suess, E. (1980), Particulate organic carbon flux in the oceans-surface productivity and oxygen utilization, *Nature*, *288*(5788), 260-263.
Suga, T., and L. D. Talley (1995), Antarctic Intermediate Water circulation in the tropical and subtropical South Atlantic, *Journal of Geophysical Research*, *100*(C7), 13441-13453.
Sultan, B., and S. Janicot (2000), Abrupt shift of the ITCZ over West Africa and intra-seasonal variability, *Geophys. Res. Lett.*, *27*(20), 3353-3356.
Suman, D. O., and M. P. Bacon (1989), Variations in Holocene sedimentation in the North American Basin determined from ^{230}Th measurements, *Deep Sea Research Part A. Oceanographic Research Papers*, *36*(6), 869-878.
Tachikawa, K., V. Athias, and C. Jeandel (2003), Neodymium budget in the modern ocean and paleo-oceanographic implications, *J. Geophys. Res.*, *108*(C8), 3254.
Tachikawa, K., M. Roy-Barman, A. Michard, D. Thouron, D. Yeghicheyan, and C. Jeandel (2004), Neodymium isotopes in the Mediterranean Sea: comparison between seawater and sediment signals, *Geochimica et Cosmochimica Acta*, *68*(14), 3095-3106.
Takeda, S. (1998), Influence of iron availability on nutrient consumption ratio of diatoms in oceanic waters, *Nature*, *393*(6687), 774-777.
Tanaka, T., et al. (2000), JNdi-1: a neodymium isotopic reference in consistency with LaJolla neodymium, *Chemical Geology*, *168*(3–4), 279-281.
Tans, P., and R. F. Keeling (2012), Recent Mauna Loa CO_2, NOAA/ESRL.
'The Ring Group'(1981), Gulf Stream Cold-Core Rings: Their Physics, Chemistry, and Biology, *Science*, *212*(4499), 1091-1100.
Thomas, A. L., G. M. Henderson, and L. F. Robinson (2006), Interpretation of the ^{231}Pa/^{230}Th paleocirculation proxy: New water-column measurements from the southwest Indian Ocean, *Earth and Planetary Science Letters*, *241*(3–4), 493-504.
Thomson, J., S. Nixon, C. P. Summerhayes, J. Schönfeld, R. Zahn, and P. Grootes (1999), Implications for sedimentation changes on the Iberian margin over the last two glacial/interglacial transitions from ($^{230}Th_{excess}$)$_0$ systematics, *Earth and Planetary Science Letters*, *165*(3–4), 255-270.
Thornalley, D. J. R., S. Barker, T. van de Flierdt, J. Becker, I. R. Hall and G. Knorr (2012), Abrupt changes in deep Atlantic circulation during the transition to full glacial conditions, *Paleoceanography*, submitted ms.
Thunell, R. C. (1982), Carbonate dissolution and abyssal hydrography in the Atlantic Ocean, *Marine Geology*, *47*(3–4), 165-180.
Thurman, H. V., and A. P. Trujillo (2002), *Essentials of oceanography*, 7 ed., Prentice Hall.
Timmermans, K. R., B. Van der Wagt, and H. J. W. De Baar (2004), Growth Rates, Half-Saturation Constants, and Silicate, Nitrate, and Phosphate Depletion in Relation to Iron Availability of Four Large, Open-Ocean Diatoms from the Southern Ocean, *Limnology & Oceanography*, *49*(6), 2141-2151.
Toggweiler, J. R. (1999), Variation of Atmospheric CO_2 by Ventilation of the Ocean's Deepest Water, *Paleoceanography*, *14*(5), 571-588.
Toggweiler, J. R., and J. L. Sarmiento (1985), Glacial to interglacial changes in atmospheric carbon dioxide: The critical role of ocean surface water in high latitudes., in *The carbon cycle and atmospheric CO_2: Natural Variations Archean to Present, Geophysical Monograph Series.*, edited by E. T. Sundquist and W. S. Broecker, pp. 163-184, American Geophysical Union, Washington, D.C.
Toggweiler, J. R., K. Dixon, and W. S. Broecker (1991), The Peru Upwelling and the Ventilation of the South Pacific Thermocline, *J. Geophys. Res.*, *96*(C11), 20467-20497.
Toggweiler, J. R., J. L. Russell, and S. R. Carson (2006), Midlatitude westerlies, atmospheric CO_2, and climate change during the ice ages, *Paleoceanography*, *21*(2), PA2005.
Tréguer, P., D. M. Nelson, A. J. Van Bennekom, D. J. DeMaster, A. Leynaert, and B. Quéguiner (1995), The silica balance in the world ocean: a reestimate, *Science*, *268*(5209), 375-379.
Treppke, U. F., C. B. Lange, and G. Wefer (1996), Vertical fluxes of diatoms and silicoflagellates in the eastern equatorial Atlantic, and their contribution to the sedimentary record, *Marine Micropaleontology*, *28*(1), 73-96.
Tribovillard, N., T. J. Algeo, T. Lyons and A. Riboulleau (2006), Trace metals as paleoredox and paleoproductivity proxies: An update, *Chemical Geology*, *232*, 12-32.
Tsuchiya, M. (1989), Circulation of the Antarctic Intermediate Water in the North Atlantic Ocean, *Journal of Marine Research*, *47*(4), 747-755.
UIC Coulometrics Ltd. (2008a), Operation manual for the CM5014 CO_2 Coulometer (version 3.00).
UIC Coulometrics Ltd. (2008b), Operation Manual for the CM5130 Acidification Module (version 2.00).

Uppström, L. R. (1974), The boron/chlorinity ratio of deep-sea water from the Pacific Ocean., *Deep Sea Research*, *21*, 161-162.
Uriz, M.-J., X. Turon, M. A. Becerro, and G. Agell (2003), Siliceous spicules and skeleton frameworks in sponges: Origin, diversity, ultrastructural patterns, and biological functions, *Microscopy Research and Technique*, *62*(4), 279-299.
van Aken, H. M., A. K. van Veldhoven, C. Veth, W. P. M. de Ruijter, P. J. van Leeuwen, S. S. Drijfhout, C. P. Whittle, and M. Rouault (2003), Observations of a young Agulhas ring, Astrid, during MARE in March 2000, *Deep Sea Research Part II: Topical Studies in Oceanography*, *50*(1), 167-195.
van de Flierdt, T., L. F. Robinson, J. F. Adkins, S. R. Hemming, and S. L. Goldstein (2006), Temporal stability of the neodymium isotope signature of the Holocene to glacial North Atlantic, *Paleoceanography*, *21*(4), PA4102.
Vance, D., A. E. Scrivner, P. Beney, M. Staubwasser, G. M. Henderson, and N. C. Slowey (2004), The use of foraminifera as a record of the past neodymium isotope composition of seawater, *Paleoceanography*, *19*(2), PA2009.
Verardo, D. J., and A. McIntyre (1994), Production and Destruction: Control of Biogenous Sedimentation in the Tropical Atlantic 0-300,000 years B.P, *Paleoceanography*, *9*(1), 63-86.
Villanueva, J., J. O. Grimalt, E. Cortijo, L. Vidal, and L. Labeyriez (1997), A biomarker approach to the organic matter deposited in the North Atlantic during the last climatic cycle, *Geochimica et Cosmochimica Acta*, *61*(21), 4633-4646.
Villareal, T. A. (1993), Abundance of the Giant Diatom Ethmodiscus in the Southwest Atlantic Ocean and Central Pacific Gyre, *Diatom Research*, *8*(1), 171-177.
Villareal, T. A., L. Joseph, M. A. Brzezinski, R. F. Shipe, F. Lipschultz, and M. A. Altabet (1999), Biological and chemical characteristics of the giant diatom Ethmodiscus (Bacillariophyceae) in the central North Pacific gyre, *Journal of Phycology*, *35*(5), 896-902.
Vital, H., and K. Stattegger (2000), Major and trace elements of stream sediments from the lowermost Amazon River, *Chemical Geology*, *168*(1-2), 151-168.
Volkman, J. K. (1986), A review of sterol markers for marine and terrigenous organic matter, *Organic Geochemistry*, *9*(2), 83-99.
Volkman, J. K., G. Eglinton, E. D. S. Corner, and T. E. V. Forsberg (1980), Long-chain alkenes and alkenones in the marine coccolithophorid Emiliania huxleyi, *Phytochemistry*, *19*(12), 2619-2622.
Volkman, J. K., S. M. Barrerr, S. I. Blackburn, and E. L. Sikes (1995), Alkenones in Gephyrocapsa oceanica: Implications for studies of paleoclimate, *Geochimica et Cosmochimica Acta*, *59*(3), 513-520.
von Blanckenburg, F. (1999), Tracing Past Ocean Circulation?, *Science*, *286*(5446), 1862-1863.
Vuille, M., R. S. Bradley, M. Werner, R. Healy, and F. Keimig (2003), Modeling $\delta^{18}O$ in precipitation over the tropical Americas: 1. Interannual variability and climatic controls, *J. Geophys. Res.*, *108*(D6), 4174.
Wagner, T. (2000), Control of Organic Carbon Accumulation in the Late Quaternary Equatorial Atlantic (Ocean Drilling Program Sites 664 and 663): Productivity Versus Terrigenous Supply, *Paleoceanography*, *15*(2), 181-199.
Walker, J. C. G., P. B. Hays, and J. F. Kasting (1981), A Negative Feedback Mechanism for the Long-Term Stabilization of Earth's Surface Temperature, *J. Geophys. Res.*, *86*(C10), 9776-9782.
Wallace, J. M., and P. V. Hobbs (2006), *Atmospheric Science - An Introductory Survey*, 2nd ed., Elsevier.
Wang, C.-H., and H.-W. Yeh (1984a), Oxygen isotope analysis of marine diatoms, *Bulletin of the Institute of Earth Sciences, Academia Sinica*, *4*, 131-140.
Wang, C.-H., and H.-W. Yeh (1984b), Water in biogenic silica and its effect on oxygen isotope values., *Bulletin of the Institute of Earth Sciences, Academia Sinica*, *4*, 141-147.
Wang, C.-H., and H.-W. Yeh (1985), Oxygen isotopic compositions of DSDP Site 480 diatoms: Implications and applications, *Geochimica et Cosmochimica Acta*, *49*(6), 1469-1478.
Wang, W. C., Y. L. Yung, A. A. Lacis, T. Mo, and J. E. Hansen (1976), Greenhouse Effects due to Man-Made Perturbations of Trace Gases, *Science*, *194*(4266), 685-690.
Wang, Y., H. Cheng, R. L. Edwards, X. Kong, X. Shao, S. Chen, J. Wu, X. Jiang, X. Wang, and Z. An (2008), Millennial- and orbital-scale changes in the East Asian monsoon over the past 224,000 years, *Nature*, *451*(7182), 1090-1093.
Wang, Y. J., H. Cheng, R. L. Edwards, Z. S. An, J. Y. Wu, C.-C. Shen, and J. A. Dorale (2001), A High-Resolution Absolute-Dated Late Pleistocene Monsoon Record from Hulu Cave, China, *Science*, *294*(5550), 2345-2348.
Warnock, J., R. Scherer, and P. Loubere (2007), A quantitative assessment of diatom dissolution and late quaternary primary productivity in the Eastern Equatorial Pacific, *Deep Sea Research Part II: Topical Studies in Oceanography*, *54*(5–7), 772-783.
Wefer, G., and G. Fischer (1993), Seasonal patterns of vertical particle flux in equatorial and coastal upwelling areas of the eastern Atlantic, *Deep Sea Research Part I: Oceanographic Research Papers*, *40*(8), 1613-1645.

Wefer, G., et al. (1996), Late Quaternary surface circulation of the South Atlantic: The stable isotope record and implications for heat transport and productivity, in *The South Atlantic: Present and Past Circulation*, edited by G. Wefer, W. H. Berger, G. Siedler and D. Webb, pp. 461-502, Springer, Berlin, Heidelberg.

Weiss, R. F. (1974), Carbon dioxide in water and seawater: the solubility of a non-ideal gas, *Marine Chemistry*, *2*(3), 203-215.

Weldeab, S., D. W. Lea, R. R. Schneider, and N. Andersen (2007), 155,000 Years of West African Monsoon and Ocean Thermal Evolution, *Science*, *316*(5829), 1303-1307.

Wilson, T. R. S. (1975), *Salinity and the major elements of sea water*, Academic Press, London.

Wilson, W. D., E. Johns, and R. L. Molinari (1994), Upper layer circulation in the western tropical North Atlantic Ocean during August 1989, *J. Geophys. Res.*, *99*(C11), 22513-22523.

Wiseman, J. D. H., and N. Ingram Hendey (1953), The significance and diatom content of a deep-sea floor sample from the neighbourhood of the greates oceanic depth, *Deep Sea Research (1953)*, *1*(1), 47-59.

Wong, A. P. S., N. L. Bindoff, and J. A. Church (1999), Large-scale freshening of intermediate waters in the Pacific and Indian oceans, *Nature*, *400*(6743), 440-443.

Wüst, G. (1964), Stratification and Circulation of the Antillean–Caribbean Basins: Part 1. Spreading and Mixing of the Water Types with an Oceanographic Atlas., *Columbia University Press, New York*.

Xie, R. C., F. Marcantonio, and M. W. Schmidt (2012), Deglacial variability of Antarctic Intermediate Water penetration into the North Atlantic from authigenic neodymium isotope ratios, *Paleoceanography* (in press).

Yamanaka, Y., and E. Tajika (1996), The role of the vertical fluxes of particulate organic matter and calcite in the oceanic carbon cycle: Studies using an ocean biogeochemical general circulation model, *Global Biogeochem. Cycles*, *10*(2), 361-382.

Yamanaka, Y., and E. Tajika (1997), Role of dissolved organic matter in the marine biogeochemical cycle: Studies using an ocean biogeochemical general circulation model, *Global Biogeochem. Cycles*, *11*(4), 599-612.

Yiou, P., and F. Vimeux (2001), Ice-age variability from the Vostok deuterium and deuterium excess records, *Journal of Geophysical Research - Atmospheres 106*(D23), 31875-31884.

You, Y. (1999), Dianeutral mixing, transformation and transport of Antarctic Intermediate Water in the South Atlantic Ocean, *Deep Sea Research Part II: Topical Studies in Oceanography*, *46*(1–2), 393-435.

Yu, E.-F., R. Francois, and M. P. Bacon (1996), Similar rates of modern and last-glacial ocean thermohaline circulation inferred from radiochemical data, *Nature*, *379*(6567), 689-694.

Yu, E. F., R. Francois, M. P. Bacon, and A. P. Fleer (2001a), Fluxes of ^{230}Th and ^{231}Pa to the deep sea: implications for the interpretation of excess ^{230}Th and ^{231}Pa/^{230}Th profiles in sediments, *Earth and Planetary Science Letters*, *191*(3-4), 219-230.

Yu, E. F., R. Francois, M. P. Bacon, S. Honjo, A. P. Fleer, S. J. Manganini, M. M. Rutgers van der Loeff and V. Ittekot (2001b), Trapping efficiency of bottom-tethered sediment traps estimated from the intercepted fluxes of ^{230}Th and ^{231}Pa, *Deep Sea Research Part I: Oceanographic Research Papers*, *48*(3), 865-889.

Yu, J., H. Elderfield, and A. M. Piotrowski (2008), Seawater carbonate ion-δ^{13}C systematics and application to glacial–interglacial North Atlantic ocean circulation, *Earth and Planetary Science Letters*, *271*(1–4), 209-220.

Zabel, M., T. Wagner, and P. B. deMenocal (2002), Terrigenous Signals in Sediments of the Low-Latitude Atlantic - Indications to Environmental Variations during the Late Quaternary: Part II: Lithogenic Matter, in *The South Atlantic in the Late Quaternary: Reconstruction of Material Budgets and Current Systems*, edited by G. Wefer, S. Mulitza and V. Ratmeyer, pp. 323-345, Springer, Berlin.

Zeebe, R. E., and D. Wolf-Gladrow (2001), CO_2 in seawater: equilibrium, kinetics, isotopes., 346 pp., *Elsevier, Amsterdam*.

Zhang, J., P. Wang, Q. Li, X. Cheng, H. Jin, and S. Zhang (2007), Western equatorial Pacific productivity and carbonate dissolution over the last 550 kyr: Foraminiferal and nannofossil evidence from ODP Hole 807A, *Marine Micropaleontology*, *64*(3–4), 121-140.

Zhao, M., L. Dupont, G. Eglinton, and M. Teece (2003), n-Alkane and pollen reconstruction of terrestrial climate and vegetation for N.W. Africa over the last 160 kyr, *Organic Geochemistry*, *34*(1), 131-143.

Zheng, Y., R. F. Anderson, A. van Geen, and M. Q. Fleisher (2002), Preservation of particulate non-lithogenic uranium in marine sediments, *Geochimica et Cosmochimica Acta*, *66*(17), 3085-3092.

Zhou, H., T. Li, G. Jia, Z. Zhu, B. Chi, Q. Cao, R. Sun, and P. a. Peng (2007), Sea surface temperature reconstruction for the middle Okinawa Trough during the last glacial–interglacial cycle using C37 unsaturated alkenones, *Palaeogeography, Palaeoclimatology, Palaeoecology*, *246*(2–4), 440-453.

Zonneveld, K. A. F., et al. (2010), Selective preservation of organic matter in marine environments; processes and impact on the sedimentary record., *Biogeosciences*, *7*, 483-511.

Zuo, H., A. C. Naveira Garabato, A. L. New, and A. Oschlies (2012), Mechanisms of subantarctic mode water upwelling in a hybrid-coordinate global GCM, *Ocean Modelling*, *45–46*(0), 59-80.

Table A1 - Weights of samples and spikes for all samples analysed for Pa and Th.

Sample identifier	Weight of 100µl of (2006-2) ^{236}U-^{229}Th (g)	Weight of 100µl of (2009-1a) ^{233}Pa (g)	Sample weight (g)
JG-1	0.1065	0.0800	0.1056
JG-2	0.1060	0.0806	0.1056
JG-3	0.1063	0.0804	0.1002
JG-4	0.1060	0.0804	0.1086
JG-5	0.1061	0.0803	0.1018
JG-6	0.1061	0.0800	0.1026
JG-7	0.1059	0.0802	0.1126
JG-8	0.1060	0.0803	0.1010
JG-9	0.1062	0.0803	0.1008
JG-10	0.1060	0.0799	0.1050
JG-11	0.1060	0.0805	0.1024
JG-12	0.1056	0.0801	0.1069
JG-13	0.1061	0.0811	0.1018
JG-14	0.1061	0.0806	0.1028
JG-15	0.1038	0.0803	0.1026
JG-16	0.1064	0.0806	0.1015
JG-17	0.1061	0.0778	0.1002
JG-18	0.1062	0.0810	0.1028
JG-19	0.1058	0.0800	0.1024
JG-20	0.1059	0.0804	0.1023
JG-21	0.1060	0.0800	0.1011
JG-22	0.1061	0.0802	0.1038
JG-23	0.1062	0.0782	0.1026
JG-24	0.1056	0.0804	0.1029
JG-25	0.1052	0.0804	0.1052
JG-26	0.1066	0.0803	0.1005
JG-27	0.1063	0.0802	0.1020
JG-28	0.1061	0.0799	0.1018
JG-29	0.1060	0.0804	0.1012
JG-30	0.1064	0.0804	0.1007
JG-31	0.1060	0.0804	0.1004
JG-32	0.1062	0.0802	0.1013
JG-33	0.1067	0.0803	0.1024
JG-34	0.1062	0.0801	0.1034
JG-35	0.1058	0.0800	0.1022
JG-36	0.1067	0.0802	0.1068
JG-37	0.1066	0.0803	0.1006

JG-12 (repeat #2)	0.1057	0.0800	0.1006
JG-45 (BLANK)	0.1066	0.0802	0.0000
JG-38	0.1031	0.1088	0.1102
JG-39	0.1099	0.1092	0.1067
JG-40	0.1033	0.1076	0.1117
JG-41	0.1070	0.1070	0.1143
JG-42	0.1239	0.1069	0.1045
JG-43	0.1062	0.1073	0.1086
JG-46	0.1021	0.1075	0.1043
JG-47	0.1066	0.1065	0.1079
JG-48	0.1025	0.1013	0.1020
JG-49	0.1082	0.1121	0.1023
JG-50	0.1067	0.1073	0.1182
JG-51	0.1067	0.1068	0.1107
JG-52	0.1068	0.1071	0.1030
JG-53	0.1067	0.1065	0.1038
JG-54	0.1025	0.1069	0.1021
JG-55	0.1104	0.1071	0.1002
JG-56	0.1067	0.1070	0.1104
JG-57	0.1174	0.1066	0.1052
JG-12 (repeat #3)	0.1368	0.1034	0.1116
JG-58 (BLANK)	0.1069	0.1065	0.0000
JG-12 (repeat #4)	0.1052	0.1306	0.1013
JG-59	0.1049	0.1317	0.1002
JG-60	0.1052	0.1303	0.1011
JG-61	0.1055	0.1311	0.1029
JG-62	0.1056	0.1305	0.1087
JG-63	0.1058	0.1318	0.1014
JG-64	0.1057	0.1304	0.1121
JG-65	0.1053	0.1303	0.1008
JG-66	0.1054	0.1304	0.1003
JG-67	0.1060	0.1308	0.1035
JG-68	0.1054	0.1302	0.1010
JG-69	0.1054	0.1316	0.1005
JG-70	0.1052	0.1304	0.1016
JG-71	0.1055	0.1303	0.1113
JG-72	0.1048	0.1312	0.1010
JG-73	0.1056	0.1304	0.1053
JG-74	0.1056	0.1304	0.1042
JG-75	0.1063	0.1303	0.1013

JG-76 (BLANK)	0.1066	0.1309	0.0000
JG-12 (repeat #5)	0.1044	0.1312	0.1025
JG-77	0.1055	0.1302	0.1097
JG-78	0.1052	0.1300	0.1022
JG-79	0.1040	0.1310	0.1066
JG-80	0.1055	0.1305	0.1041
JG-81	0.1054	0.1312	0.1034
JG-82	0.1057	0.1307	0.1032
JG-83	0.1051	0.1309	0.1055
JG-84	0.1052	0.1299	0.1039
JG-85	0.1051	0.1321	0.1140
JG-86	0.1051	0.1305	0.1021
JG-87	0.1053	0.1300	0.1033
JG-88	0.1055	0.1308	0.1020
JG-89	0.1059	0.1304	0.1031
JG-90	0.1052	0.1278	0.1046
JG-91	0.1052	0.1265	0.1032
JG-92	0.1056	0.1289	0.1018
JG-93	0.1056	0.1296	0.1022
JG-94	0.1057	0.1299	0.1020
JG-95 (BLANK)	0.1057	0.1296	0.0000

* Note that from JG-21 to JG-37 (plus JG-10, JG-12 repeat2 and JG-45), 75 µl of ^{233}Pa was added; and from JG-12 (repeat #4) onwards the amount of ^{233}Pa added was 125 µl, not 100 µl; to account for decay loss

Table A2 - Gamma counts for samples, column headings identify the geometry of the container and volume of acid. Note that only 'Batch 1' (JG-1 to JG-20). 'Batch 2' (JG-21 TO JG-37, plus JG-10, JG-12 repeat 2 and JG-45) and 'Batch 5' (JG-77 to JG-95, plus JG-12 repeat 5) were counted in either 6ml concentrated HNO_3^- in 15ml c-tube and 0.8ml concentrated HNO_3^- and 0.1 % HF in 7ml Savillex beaker.

Sample identifier	2ml concentrated HCl in 15ml Savillex beaker	6ml concentrated HCl in 15ml c-tube	6.1ml concentrated 8N HNO_3^- in 15ml c-tube	0.8ml concentrated HNO_3^- and 0.1 % HF in 7ml Savillex beaker
JG-1	1610	93	N/A	2922
JG-2	1578	77	N/A	3217
JG-3	1686	82	N/A	3230
JG-4	1616	82	N/A	3349
JG-5	1653	92	N/A	3184
JG-6	1610	82	N/A	3307
JG-7	1715	82	N/A	3114
JG-8	1693	64	N/A	2998
JG-9	1686	70	N/A	3316
JG-10	1413	80	558	N/A
JG-11	1655	93	N/A	3092
JG-12	1701	80	N/A	3206
JG-13	1659	75	N/A	3179
JG-14	1709	72	N/A	3276
JG-15	1658	87	N/A	3328
JG-16	1624	79	N/A	3159
JG-17	1537	82	N/A	3178
JG-18	1664	77	N/A	3203
JG-19	1652	69	N/A	3332
JG-20	1598	83	N/A	3282
Mix 2009-1a #1	3305	83	N/A	3287
Background	59	79	N/A	82
JG-12 (rpt #2)	1462	64	634	N/A
JG-21	1512	67	604	N/A
JG-22	1456	70	491	N/A
JG-23	578	94	284	N/A
JG-24	1421	108	439	N/A
JG-25	1430	86	468	N/A
JG-26	1415	67	501	N/A
JG-27	1460	120	432	N/A
JG-28	1400	79	512	N/A

JG-29	1420	124	653	N/A
JG-30	1429	102	487	N/A
JG-31	1453	84	668	N/A
JG-32	1399	81	433	N/A
JG-33	1452	75	564	N/A
JG-34	1393	107	486	N/A
JG-35	1452	99	619	N/A
JG-36	1455	74	559	N/A
JG-37	1457	101	622	N/A
Mix 2009-1a #2	2743	72	N/A	N/A
Background	66	79	75	N/A
JG-12 (rpt #3)	1438	86	N/A	N/A
JG-38	1475	82	N/A	N/A
JG-39	1517	72	N/A	N/A
JG-40	1552	77	N/A	N/A
JG-41	1504	81	N/A	N/A
JG-42	1518	87	N/A	N/A
JG-43	1596	75	N/A	N/A
JG-46	1498	92	N/A	N/A
JG-47	1558	95	N/A	N/A
JG-48	1442	99	N/A	N/A
JG-49	1531	91	N/A	N/A
JG-50	1579	77	N/A	N/A
JG-51	1504	95	N/A	N/A
JG-52	1544	90	N/A	N/A
JG-53	1606	74	N/A	N/A
JG-54	1496	76	N/A	N/A
JG-55	1532	106	N/A	N/A
JG-56	1529	79	N/A	N/A
JG-57	1467	73	N/A	N/A
JG-12 (rpt #4)	1569	66	N/A	N/A
Mix 2009-1a #3	2998	81	N/A	N/A
Background	91	81	N/A	N/A
JG-58	1491	99	N/A	N/A
JG-59	1567	93	N/A	N/A
JG-60	1538	86	N/A	N/A
JG-61	1578	86	N/A	N/A
JG-62	1468	80	N/A	N/A
JG-63	1613	58	N/A	N/A
JG-64	1545	75	N/A	N/A

JG-65	1552	85	N/A	N/A
JG-66	1596	95	N/A	N/A
JG-67	1618	81	N/A	N/A
JG-68	1594	69	N/A	N/A
JG-69	1507	79	N/A	N/A
JG-70	1547	88	N/A	N/A
JG-71	1598	75	N/A	N/A
JG-72	1542	79	N/A	N/A
JG-73	1615	99	N/A	N/A
JG-74	1585	71	N/A	N/A
JG-75	1637	92	N/A	N/A
JG-12 (rpt #5)	1319	91	530	N/A
JG-76 (BLANK)	1592	84	N/A	N/A
Mix 2009-1a #4	3121	97	N/A	N/A
Background	86	76	N/A	N/A
JG-77	1378	74	686	N/A
JG-78	1398	80	645	N/A
JG-79	1409	86	567	N/A
JG-80	1299	71	480	N/A
JG-81	1312	87	460	N/A
JG-82	1393	96	524	N/A
JG-83	1355	72	404	N/A
JG-84	1396	101	541	N/A
JG-85	1426	79	562	N/A
JG-86	1328	77	547	N/A
JG-87	1398	106	435	N/A
JG-88	1352	76	582	N/A
JG-89	1350	110	472	N/A
JG-90	1394	92	436	N/A
JG-91	562	76	194	N/A
JG-92	1368	91	545	N/A
JG-93	1403	83	443	N/A
JG-94	1366	89	537	N/A
JG-95	1274	77	359	N/A
Mix 2009-1a #5	2766	96	N/A	N/A
Background	70	71	83	N/A

Table A3 – MD99-2198 Nd isotopic ratio data (Chapter 5). All reported $^{143}Nd/^{144}Nd$ ratios have been normalised to the recommended JNdi value of Tanaka et al. (2000). Epsilon Nd values denote the deviation of measured $^{143}Nd/^{144}Nd$ values from the bulk Earth value of CHUR=0.512638 [*Jacobsen and Wasserburg,* 1980] in parts per 10,000. The external reproducibility (2σSD) is reported based on repeat JNd_i analyses of the day. For one sample (*), the ion beam was significantly smaller than for standards and hence a propagated error is reported to reflect this difference.

Depth (cm)	Age (ka)	$^{143}Nd/^{144}Nd$	2 σ S.E.	ε_{Nd}	2 σ S.D.
850-851	44.62	0.512116	0.000010	-10.2	0.2
950-951	55.09	0.512159	0.000012	-9.3	0.2
1016-1017	61.79	0.512121	0.000006	-10.1	0.3
1026-1027	62.88	0.512124	0.000010	-10.0	0.3
1036-1037	63.97	0.512174	0.000014	-9.1	0.3
1046-1047	65.06	0.512130	0.000010	-9.9	0.3
1056-1057	66.15	0.512155	0.000008	-9.4	0.3
1076-1077	68.33	0.512127	0.000012	-10.0	0.3
1086-1087	69.42	0.512072	0.000012	-11.0	0.3
1106-1107	71.60	0.512087	0.000020	-10.8	0.3
1131-1132	73.01	0.512097	0.000018	-10.6	0.3
1276-1277	80.68	0.512088	0.000012	-10.7	0.3
1421-1422 *	90.50	0.512103	0.000014	-10.4	0.6

Table A4 - MD99-2918 Si isotope data. External reproducibility for δ^{30}Si values is +/- 0.23 per mil. For calculation of δ^{30}Si values see Chapter 5 (Equation 5.2) and palaeo-Si (Equation 5.3).

Depth (cm)	Age (ka)	Mean δ^{30}Si (all analyses)	~[$Si(OH)_4$] (µM)
850-851	44.62	-0.86	11.6
950-951	55.09	-1.13	16.0
1016-1017	61.79	-0.74	9.8
1026-1027	62.88	-0.73	9.6
1036-1037	63.97	-0.96	13.1
1046-1047	65.06	-0.43	5.5
1056-1057	66.15	-0.39	5.0
1066-1067	67.24	-0.35	4.6
1076-1077	68.33	-0.23	3.1
1086-1087	69.42	-0.12	1.9
1106-1107	71.60	-0.12	1.8
1131-1132	73.01	-0.57	7.4
1176-1177	75.55	-0.58	7.5
1276-1277	80.68	0.28	-2.2
1421-1422	90.50	0.15	-1.0

Table A5 – Stable isotope measurements (VM30-40, RC24-01 and ODP 663A). Stable isotope data for VM19-296 and RC16-66 were not used in this investigation.

ODP 663A

Depth (cm)	Age (ka)	Sed. rate (cm/ka)	$\delta^{18}O$
229.5	48.300	2.86	-0.08
231.5	49.000	2.86	0.11
233.5	49.700	2.86	0.11
235.5	50.400	2.86	-0.30
237.5	51.100	2.86	-0.02
239.5	51.800	2.86	-0.48
243.5	53.200	2.86	-0.01
245.5	53.900	2.86	-0.11
247.5	54.600	3.58	-0.09
249.5	55.065	4.30	-0.21
251.5	55.530	4.30	-0.44
253.5	55.995	4.30	-0.12
255.5	56.459	4.30	-0.23
257.5	56.924	4.30	-0.24
259.5	57.389	4.30	0.27
261.5	57.854	4.30	0.17
263.5	58.319	4.30	-0.06
265.5	58.784	4.30	-0.18
267.5	59.249	4.30	0.10
269.5	59.714	4.30	-0.07
270.5	59.946	4.30	-0.09
271.5	60.178	4.30	0.07
272.5	60.411	4.30	0.28
273.5	60.643	4.30	0.14
274.5	60.876	4.30	0.13
275.5	61.108	4.30	0.33
276.5	61.341	4.30	0.23
277.5	61.573	4.30	-0.07
278.5	61.805	4.30	0.22
279.5	62.038	4.30	0.44
280.5	62.270	4.30	0.18
282.5	62.735	4.30	-0.03
283.5	62.968	4.30	0.21
284.5	63.200	4.55	0.04
285.5	63.409	4.79	0.12
286.5	63.617	4.79	0.05
287.5	63.826	4.79	0.22
288.5	64.035	4.79	-0.05
289.5	64.243	4.79	0.06
290.5	64.452	4.79	0.02
291.5	64.661	4.79	-0.07
292.5	64.870	4.79	-0.17
293.5	65.078	4.79	0.07
294.5	65.287	4.79	0.03
295.5	65.496	4.79	0.05
296.5	65.704	4.79	0.04
297.5	65.913	4.79	0.05
298.5	66.122	4.79	0.05
299.5	66.330	4.79	0.03
300.5	66.539	4.79	0.14
301.5	66.748	4.79	0.24
302.5	66.957	4.79	0.15

303.5	67.165	4.79	0.01
304.5	67.374	4.79	-0.06
305.5	67.583	4.79	-0.13
306.5	67.791	4.79	n/a
307.5	68.000	4.79	0.19
308.5	68.209	4.79	-0.10
309.5	68.417	4.79	-0.07
310.5	68.626	4.79	0.01
311.5	68.835	4.79	-0.26
312.5	69.043	4.79	-0.08
313.5	69.252	4.79	0.49
314.5	69.461	4.79	-0.07
315.5	69.670	4.79	0.00
316.5	69.878	4.79	-0.30
317.5	70.087	4.79	-0.13
318.5	70.296	4.79	-0.34
319.5	70.504	4.79	-0.34
320.5	70.713	4.79	-0.46
321.5	70.922	4.79	-0.37
322.5	71.130	4.79	-0.54
323.5	71.339	4.79	-0.55
324.5	71.548	4.79	-0.62
325.5	71.757	4.79	-0.26
326.5	71.965	4.79	-0.42
327.5	72.174	4.79	-0.65
328.5	72.383	4.79	-0.51
329.5	72.591	4.79	-0.54
330.5	72.800	3.94	-0.15
331.5	73.123	3.10	-0.26
332.5	73.446	3.10	-0.31
333.5	73.769	3.10	-0.62
334.5	74.092	3.10	-0.15
335.5	74.415	3.10	-0.50
336.5	74.738	3.10	-0.74
337.5	75.062	3.10	-0.24
338.5	75.385	3.10	-0.11
339.5	75.708	3.10	-0.65
340.5	76.031	3.10	-0.69
341.5	76.354	3.10	-0.68
343.5	77.000	3.19	-0.68
345.5	77.608	3.29	-0.53
347.5	78.217	3.29	-0.66
349.5	78.825	3.29	-0.74
351.5	79.433	3.29	-0.57
353.5	80.042	3.29	-0.67
355.5	80.650	3.29	-0.70
357.5	81.258	3.29	-0.81
359.5	81.867	3.29	-0.71
361.5	82.475	3.29	-0.87
363.5	83.083	3.29	-0.66
365.5	83.692	3.29	-1.00
367.5	84.300	3.58	-0.72
369.5	84.817	3.87	-0.58
371.5	85.333	3.87	-0.56
373.5	85.850	3.87	-0.37
375.5	86.367	3.87	-0.28
377.5	86.883	3.87	-0.37
379.5	87.400	3.70	-0.55

381.5	87.967	3.53	-0.47
383.5	88.533	3.53	-0.33
385.5	89.100	3.53	-0.56
387.5	89.667	3.53	-0.55
393.5	91.264	4.31	-0.13
395.5	91.728	4.31	-0.74
397.5	92.192	4.31	-0.70
399.5	92.655	4.31	-0.91
401.5	93.119	4.31	-0.82

RC24-01

Depth (cm)	Age (ka)	Sed. rate (cm/ka)	$\delta^{18}O$
284.5	43.451	1.006	0.44
286.5	45.440	1.006	0.71
287.5	46.434	1.006	0.12
289.5	48.423	1.006	0.26
291.5	50.412	1.006	0.16
293.5	52.401	1.006	0.08
294.5	53.395	1.006	-0.63
295.5	54.390	1.006	0.29
297.5	56.378	1.006	0.31
299.5	58.367	1.006	-0.30
302.5	59.988	2.588	0.34
309.5	62.693	2.588	0.43
310.5	63.079	2.588	-0.35
313.5	64.238	2.588	0.17
315.5	65.011	2.588	0.37
317.5	65.784	2.588	0.38
318.5	66.170	2.588	0.42
319.5	66.556	2.588	0.22
321.5	67.329	2.588	0.27
323.5	68.102	2.588	0.01
325.5	68.875	2.588	0.18
326.5	69.261	2.588	0.29
327.5	69.647	2.588	-0.64
329.5	70.420	2.588	-0.49
331.5	71.193	2.588	-0.38
333.5	71.836	3.884	-0.70
334.5	72.094	3.884	-0.62
335.5	72.351	3.884	-0.44
339.5	73.381	3.884	0.11
341.5	73.896	3.884	-0.20
342.5	74.154	3.884	-0.92
343.5	74.411	3.884	-0.49
344.5	74.669	3.884	-0.81
347.5	75.441	3.884	-0.73
349.5	76.232	2.152	-0.97
351.5	77.161	2.152	-0.74
353.5	78.090	2.152	-0.82
355.5	79.020	2.152	-0.63
357.5	79.949	2.152	-0.84
358.5	80.414	2.152	-0.97
361.5	81.807	2.152	-0.73
363.5	82.737	2.152	-0.90
365.5	83.666	2.152	-0.90

366.5	84.130	2.152	-0.70
367.5	84.634	1.813	-0.90
369.5	85.738	1.813	-0.63
371.5	86.841	1.813	-0.29
373.5	87.944	1.813	-0.45
375.5	89.048	1.813	-0.78
379.5	90.842	4.172	-0.67
381.5	91.322	4.172	-0.46

VM30-40

Depth (cm)	Age (ka)	Sed. rate (cm/ka)	$\delta^{18}O$
183.5	57.175	2.025	-0.06
184.5	57.669	2.025	-0.32
185.5	58.162	2.025	-0.30
187.5	59.150	2.025	-0.55
189.5	60.137	2.025	0.12
190.5	60.631	2.025	-0.23
192.5	61.618	2.025	-0.01
193.5	62.112	2.025	-0.19
195.5	63.100	2.025	-0.02
197.5	64.087	2.025	-0.08
199.5	65.075	2.025	0.06
200.5	65.568	2.025	-0.10
201.5	66.062	2.025	0.03
203.5	67.049	2.025	-0.07
205.5	68.037	2.025	-0.08
207.5	69.024	2.025	-0.28
208.5	69.518	2.025	-0.58
209.5	70.012	2.025	-0.55
211.5	70.999	2.025	-0.53
213.5	71.664	4.538	-0.41
215.5	72.105	4.538	-0.36
216.5	72.325	4.538	-0.75
217.5	72.545	4.538	-0.76
219.5	72.986	4.538	-0.79
221.5	73.427	4.538	-1.10
223.5	73.868	4.538	-0.81
224.5	74.088	4.538	-0.84
225.5	74.308	4.538	-0.89
227.5	74.749	4.538	-1.07
229.5	75.190	4.538	-0.98
231.5	75.631	4.538	-0.88
232.5	75.925	2.071	-0.73
233.5	76.407	2.071	-0.96
235.5	77.373	2.071	-1.45
237.5	78.338	2.071	-1.05
239.5	79.304	2.071	-1.13
240.5	79.787	2.071	-1.14
241.5	80.269	2.071	-1.31
243.5	81.235	2.071	-1.07
245.5	82.201	2.071	-1.30
247.5	83.166	2.071	-1.16
248.5	83.649	2.071	-1.12
249.5	84.102	2.982	-0.75

251.5	84.773	2.982	-0.80
253.5	85.443	2.982	-0.55
255.5	86.114	2.982	-0.99
256.5	86.449	2.982	-0.72
257.5	86.785	2.982	-0.78
259.5	87.455	2.982	-0.65
261.5	88.126	2.982	-0.85
263.5	88.796	2.982	-0.65
264.5	89.132	2.982	-0.75
265.5	89.467	2.982	-0.81
267.5	90.138	2.982	-1.02
269.5	90.810	2.962	-0.82
271.5	91.485	2.962	-0.50
272.5	91.823	2.962	-0.69
273.5	92.161	2.962	-0.69
275.5	92.836	2.962	-0.65
277.5	93.511	2.962	-0.88
279.5	94.186	2.962	-0.66
280.5	94.524	2.962	-0.77
281.5	94.861	2.962	-1.05
283.5	95.536	2.962	-0.71
285.5	96.212	2.962	-0.95
287.5	96.887	2.962	-0.95
288.5	97.224	2.962	-0.78
289.5	97.562	2.962	-1.27
291.5	98.237	2.962	-1.04
292.5	98.575	2.962	-1.12

Table A6 – $CaCO_3$ measurements (all cores)

VM19-296

Depth (cm)	Age (ka)	Sed. rate (cm/ka)	% $CaCO_3$
145.5	39.220	7.573	18.02
150.5	39.880	7.573	23.22
155.5	40.540	7.573	21.88
160.5	41.201	7.573	28.47
165.5	41.861	7.573	22.94
170.5	42.521	7.573	22.85
175.5	43.181	7.573	21.74
180.5	43.842	7.573	15.48
185.5	44.502	7.573	19.76
190.5	45.162	7.573	27.16
195.5	45.822	7.573	34.43
200.5	46.483	7.573	29.92
205.5	47.143	7.573	24.67
210.5	47.803	7.573	13.58
215.5	48.464	7.573	6.15
220.5	49.124	7.573	20.50
221.5	49.256	7.573	21.71
222.5	49.388	7.573	21.85
224.5	49.652	7.573	24.20
226.5	49.916	7.573	26.93
228.5	50.180	7.573	17.84
230.5	50.444	7.573	34.53
232.5	50.709	7.573	36.01
234.5	50.973	7.573	41.16
236.5	51.237	7.573	39.50
238.5	51.501	7.573	36.89
240.5	51.765	7.573	35.28
242.5	52.029	7.573	30.45
244.5	52.293	7.573	34.78
246.5	52.557	7.573	38.84
248.5	52.821	7.573	35.45
250.5	53.086	7.573	27.87
252.5	53.350	7.573	30.69
254.5	53.614	7.573	32.78
256.5	53.878	7.573	35.79
260.5	54.762	3.867	14.49
261.5	55.020	3.867	22.61
263.5	55.538	3.867	17.95
265.5	56.055	3.867	27.78
267.5	56.572	3.867	8.42
269.5	57.089	3.867	18.38
270.5	57.348	3.867	9.45
271.5	57.607	3.867	12.02
273.5	58.124	3.867	5.73
275.5	58.641	3.867	6.82
277.5	59.158	3.867	21.16
281.5	59.704	8.523	0.05
282.5	59.821	8.523	0.00
283.5	59.939	8.523	0.00
284.5	60.056	8.523	0.00
285.5	60.173	8.523	0.00
286.5	60.291	8.523	0.00
287.5	60.408	8.523	0.00
288.5	60.525	8.523	0.00

289.5	60.643	8.523	0.00
290.5	60.760	8.523	0.00
291.5	60.877	8.523	0.00
292.5	60.995	8.523	0.00
293.5	61.112	8.523	6.56
294.5	61.229	8.523	24.15
295.5	61.347	8.523	27.22
296.5	61.464	8.523	23.58
297.5	61.581	8.523	7.77
298.5	61.699	8.523	6.52
299.5	61.816	8.523	3.86
300.5	61.933	8.523	0.00
301.5	62.050	8.523	6.36
302.5	62.168	8.523	3.25
303.5	62.285	8.523	7.27
304.5	62.402	8.523	2.12
305.5	62.520	8.523	3.66
306.5	62.637	8.523	1.76
307.5	62.754	8.523	3.21
308.5	62.872	8.523	4.01
309.5	62.989	8.523	2.71
310.5	63.106	8.523	19.37
311.5	63.224	8.523	12.69
312.5	63.341	8.523	15.05
313.5	63.458	8.523	10.14
314.5	63.576	8.523	10.04
315.5	63.693	8.523	12.09
316.5	63.810	8.523	26.30
317.5	63.939	6.664	19.61
318.5	64.089	6.664	13.12
319.5	64.239	6.664	6.84
320.5	64.389	6.664	4.91
321.5	64.539	6.664	0.80
322.5	64.689	6.664	0.00
323.5	64.839	6.664	0.00
324.5	64.989	6.664	0.00
325.5	65.139	6.664	0.00
326.5	65.289	6.664	0.90
327.5	65.439	6.664	0.00
328.5	65.589	6.664	0.00
329.5	65.739	6.664	0.00
330.5	65.889	6.664	0.00
331.5	66.039	6.664	0.00
332.5	66.190	6.664	0.00
333.5	66.340	6.664	0.00
334.5	66.490	6.664	0.00
335.5	66.640	6.664	0.00
336.5	66.790	6.664	0.00
337.5	66.940	6.664	0.00
338.5	67.090	6.664	0.03
339.5	67.240	6.664	0.00
340.5	67.390	6.664	0.00
341.5	67.540	6.664	0.00
342.5	67.690	6.664	0.00
343.5	67.840	6.664	0.00
344.5	67.990	6.664	0.00
345.5	68.140	6.664	0.00
346.5	68.290	6.664	0.00
347.5	68.441	6.664	0.00
348.5	68.591	6.664	0.00

349.5	68.741	6.664	0.00
350.5	68.891	6.664	0.00
352.5	69.191	6.664	0.06
354.5	69.491	6.664	0.57
356.5	69.791	6.664	0.00
358.5	70.091	6.664	1.50
360.5	70.391	6.664	0.00
362.5	70.692	6.664	0.49
364.5	70.992	6.664	0.00
366.5	71.292	6.664	0.41
368.5	71.592	6.664	8.02
372.5	72.014	9.807	0.00
374.5	72.218	9.807	0.50
376.5	72.422	9.807	6.46
378.5	72.626	9.807	9.09
380.5	72.830	9.807	8.39
385.5	73.340	9.807	10.52
392.5	74.054	9.807	7.94
395.5	74.359	9.807	13.05
400.5	74.869	9.807	10.39
405.5	75.379	9.807	15.45
409.5	75.953	5.385	5.45
415.5	77.067	5.385	10.97
420.5	77.995	5.385	23.10
425.5	78.924	5.385	21.83
429.5	79.667	5.385	28.56
435.5	80.781	5.385	52.97
440.5	81.709	5.385	45.16
445.5	82.638	5.385	33.80
450.5	83.567	5.385	42.62

ODP 663A

Depth (cm)	Age (ka)	% $CaCO_3$
229.5	48.300	67.87
231.5	49.000	71.56
233.5	49.700	72.51
235.5	50.400	77.63
237.5	51.100	79.87
239.5	51.800	82.29
241.5	52.500	81.00
243.5	53.200	81.88
245.5	53.900	79.50
247.5	54.600	71.82
249.5	55.065	77.02
251.5	55.530	75.95
253.5	55.995	75.94
255.5	56.459	78.40
257.5	56.924	75.38
259.5	57.389	76.98
261.5	57.854	77.42
263.5	58.319	75.29
265.5	58.784	76.49
267.5	59.249	68.15
269.5	59.714	68.70
270.5	59.946	69.40

271.5	60.178	66.68
272.5	60.411	66.85
273.5	60.643	67.29
274.5	60.876	67.03
275.5	61.108	69.62
276.5	61.341	65.33
277.5	61.573	70.96
278.5	61.805	67.45
279.5	62.038	67.90
280.5	62.270	69.08
281.5	62.503	69.40
282.5	62.735	70.51
283.5	62.968	72.64
284.5	63.200	71.73
285.5	63.409	71.35
286.5	63.617	73.66
287.5	63.826	73.24
288.5	64.035	68.14
289.5	64.243	68.83
290.5	64.452	68.75
291.5	64.661	68.98
292.5	64.870	65.04
293.5	65.078	63.85
294.5	65.287	60.58
295.5	65.496	60.99
296.5	65.704	64.16
297.5	65.913	67.46
298.5	66.122	65.24
299.5	66.330	64.12
300.5	66.539	65.36
301.5	66.748	65.61
302.5	66.957	64.18
303.5	67.165	64.01
304.5	67.374	64.83
305.5	67.583	65.13
306.5	67.791	65.33
307.5	68.000	68.48
308.5	68.209	67.03
309.5	68.417	66.26
310.5	68.626	67.65
311.5	68.835	67.14
312.5	69.043	67.47
313.5	69.252	67.24
314.5	69.461	67.85
315.5	69.670	69.75
316.5	69.878	66.61
317.5	70.087	68.53
318.5	70.296	69.42
319.5	70.504	69.20
320.5	70.713	67.37
321.5	70.922	69.41
322.5	71.130	64.74
323.5	71.339	68.04
324.5	71.548	63.27
325.5	71.757	65.44
326.5	71.965	61.72
327.5	72.174	62.43
328.5	72.383	62.29

329.5	72.591	64.55
330.5	72.800	65.56
331.5	73.123	75.49
332.5	73.446	67.07
333.5	73.769	76.45
334.5	74.092	71.05
335.5	74.415	74.27
336.5	74.738	73.76
337.5	75.062	73.18
338.5	75.385	73.28
339.5	75.708	72.26
340.5	76.031	72.94
341.5	76.354	71.77
343.5	77.000	73.06
345.5	77.608	75.90
347.5	78.217	80.59
349.5	78.825	80.33
351.5	79.433	80.83
353.5	80.042	83.26
355.5	80.650	84.00
357.5	81.258	83.54
359.5	81.867	83.57
361.5	82.475	81.82
363.5	83.083	82.54
365.5	83.692	80.44
367.5	84.300	79.07
369.5	84.817	71.69
371.5	85.333	71.15
373.5	85.850	72.85
375.5	86.367	73.09
377.5	86.883	73.85
379.5	87.400	77.86
381.5	87.967	82.05
383.5	88.533	81.63
385.5	89.100	82.33
387.5	89.667	82.35
389.5	90.233	81.26
391.5	90.800	81.71
393.5	91.264	79.71
395.5	91.728	78.24
397.5	92.192	80.57
399.5	92.655	79.55

RC24-01

Depth (cm)	Age (ka)	% $CaCO_3$
284.5	43.451	58.90
286.5	45.440	60.25
287.5	46.434	59.67
289.5	48.423	51.43
291.5	50.412	50.90
293.5	52.401	61.88
294.5	53.395	58.40
295.5	54.390	61.02
297.5	56.378	67.43

299.5	58.367	63.10
302.5	59.988	54.28
309.5	62.693	55.37
310.5	63.079	53.80
313.5	64.238	56.88
315.5	65.011	56.82
317.5	65.784	51.23
318.5	66.170	46.01
319.5	66.556	55.21
321.5	67.329	57.12
323.5	68.102	47.93
325.5	68.875	57.41
326.5	69.261	58.76
327.5	69.647	59.10
329.5	70.420	60.28
331.5	71.193	60.30
333.5	71.836	49.54
334.5	72.094	47.84
335.5	72.351	53.81
339.5	73.381	50.77
341.5	73.896	65.42
342.5	74.154	67.97
343.5	74.411	69.73
344.5	74.669	67.72
347.5	75.441	71.25
349.5	76.232	66.42
350.5	76.697	68.21
351.5	77.161	71.30
353.5	78.090	69.90
355.5	79.020	79.33
357.5	79.949	78.15
358.5	80.414	77.29
361.5	81.807	78.87
363.5	82.737	75.99
365.5	83.666	77.77
366.5	84.130	70.70
367.5	84.634	66.21
369.5	85.738	65.87
371.5	86.841	70.31
373.5	87.944	78.49
375.5	89.048	80.58
379.5	90.842	79.92
381.5	91.322	81.10

VM30-40

Depth (cm)	Age (ka)	% $CaCO_3$
183.5	57.175	76.82
184.5	57.669	72.07
185.5	58.162	74.35
187.5	59.150	72.47
189.5	60.137	73.56
190.5	60.631	76.67
192.5	61.618	68.32
193.5	62.112	75.84
195.5	63.100	76.17

197.5	64.087	72.93
199.5	65.075	73.33
200.5	65.568	75.93
201.5	66.062	71.73
203.5	67.049	73.29
205.5	68.037	75.37
207.5	69.024	75.68
208.5	69.518	71.56
209.5	70.012	76.35
211.5	70.999	71.62
213.5	71.664	70.62
215.5	72.105	62.73
216.5	72.325	69.43
217.5	72.545	75.62
219.5	72.986	76.46
221.5	73.427	76.27
223.5	73.868	74.29
224.5	74.088	73.65
225.5	74.308	75.39
227.5	74.749	77.05
229.5	75.190	84.28
231.5	75.631	86.18
232.5	75.925	83.54
233.5	76.407	85.41
235.5	77.373	83.32
237.5	78.338	81.02
239.5	79.304	82.56
240.5	79.787	82.33
241.5	80.269	82.57
243.5	81.235	84.21
245.5	82.201	75.32
247.5	83.166	78.13
248.5	83.649	63.56
249.5	84.102	69.49
251.5	84.773	66.50
253.5	85.443	66.32
255.5	86.114	67.97
256.5	86.449	71.22
257.5	86.785	72.13
259.5	87.455	81.55
261.5	88.126	82.67
263.5	88.796	80.87
264.5	89.132	81.88
265.5	89.467	82.77
267.5	90.138	84.31
269.5	90.810	82.44
271.5	91.485	81.64
272.5	91.823	80.90
273.5	92.161	82.59
275.5	92.836	79.56
277.5	93.511	82.41
279.5	94.186	83.19
280.5	94.524	82.73
281.5	94.861	83.93
283.5	95.536	81.71
285.5	96.212	79.82
287.5	96.887	84.41
288.5	97.224	80.78

289.5	97.562	82.43
291.5	98.237	81.49
292.5	98.575	84.27

RC16-66

Depth (cm)	Age (ka)	Sed. rate (cm/ka)	% $CaCO_3$
281.5	56.632	3.517	26.86
282.5	56.917	3.517	37.11
284.5	57.485	3.517	38.68
286.5	58.054	3.517	26.82
287.5	58.338	3.517	27.32
292.5	59.760	3.517	27.84
294.5	60.328	3.517	13.83
297.5	61.181	3.517	14.21
302.5	62.603	3.517	13.31
304.5	63.171	3.517	14.92
306.5	63.740	3.517	12.85
308.5	64.308	3.517	12.12
310.5	64.877	3.517	10.85
312.5	65.446	3.517	9.53
313.5	65.730	3.517	8.95
314.5	66.014	3.517	10.34
316.5	66.583	3.517	8.92
318.5	67.151	3.517	8.47
321.5	68.004	3.517	10.04
322.5	68.288	3.517	9.98
324.5	68.857	3.517	12.20
326.5	69.426	3.517	12.07
328.5	69.853	4.833	22.50
329.5	70.060	4.833	21.36
332.5	70.680	4.833	18.58
334.5	71.094	4.833	16.85
336.5	71.508	4.833	19.72
337.5	71.715	4.833	19.46
338.5	71.922	4.833	8.78
342.5	73.181	3.166	22.36
343.5	73.497	3.166	19.17
344.5	73.813	3.166	16.10
346.5	74.444	3.166	26.17
348.5	75.076	3.166	24.87
352.5	76.339	3.166	13.04
353.5	77.058	0.917	37.40
354.5	78.148	0.917	31.58
356.5	80.328	0.917	38.35
358.5	82.508	0.917	38.56
361.5	85.680	0.917	13.07
362.5	86.118	0.917	36.52
364.5	86.996	0.917	40.77
366.5	87.873	0.917	35.06
368.5	88.750	0.917	41.49
372.5	90.505	0.917	33.96

Table A7 – Percent opal and opal accumulation/flux [F(opal)] measurements for all cores. Note that 'n/a' represents intervals where radionucliude measurements were not made due to time and budget constraints.

VM19-296

Depth (cm)	Age (ka)	% opal	F(opal) (g/cm^2/ka)
145.5	39.220	15.60	n/a
150.5	39.880	20.44	n/a
155.5	40.540	31.36	n/a
160.5	41.201	20.66	n/a
165.5	41.861	19.63	n/a
170.5	42.521	21.93	n/a
175.5	43.181	19.19	n/a
180.5	43.842	18.92	n/a
185.5	44.502	23.46	n/a
190.5	45.162	18.91	n/a
195.5	45.822	14.56	n/a
200.5	46.483	24.04	n/a
205.5	47.143	15.87	n/a
210.5	47.803	16.56	n/a
215.5	48.464	20.37	n/a
220.5	49.124	17.85	0.128
221.5	49.256	15.38	n/a
222.5	49.388	17.62	n/a
224.5	49.652	20.73	n/a
226.5	49.916	11.02	n/a
228.5	50.180	13.12	n/a
230.5	50.444	11.47	n/a
232.5	50.709	11.13	n/a
234.5	50.973	12.15	n/a
236.5	51.237	10.86	n/a
238.5	51.501	11.24	n/a
240.5	51.765	10.29	n/a
242.5	52.029	10.67	n/a
244.5	52.293	10.94	n/a
246.5	52.557	10.85	n/a
248.5	52.821	10.84	n/a
250.5	53.086	15.54	n/a
252.5	53.350	12.20	n/a
254.5	53.614	15.31	n/a
256.5	53.878	11.60	n/a
258.5	54.244	16.24	n/a
260.5	54.762	11.90	n/a
261.5	55.020	12.81	n/a
262.5	55.279	15.27	n/a
263.5	55.538	18.31	n/a
264.5	55.796	15.62	n/a
265.5	56.055	15.74	n/a
266.5	56.313	16.05	n/a
267.5	56.572	14.77	0.125
268.5	56.831	13.58	n/a
269.5	57.089	12.75	n/a
270.5	57.348	19.57	n/a
271.5	57.607	15.97	n/a
272.5	57.865	16.63	n/a
273.5	58.124	15.22	n/a
275.5	58.641	18.75	n/a
277.5	59.158	15.22	n/a

281.5	59.704	21.29	n/a
282.5	59.821	26.11	n/a
283.5	59.939	22.61	n/a
284.5	60.056	23.01	n/a
285.5	60.173	26.00	n/a
286.5	60.291	27.81	n/a
287.5	60.408	25.40	n/a
288.5	60.525	26.78	n/a
289.5	60.643	23.79	n/a
290.5	60.760	24.51	0.217
291.5	60.877	26.82	n/a
292.5	60.995	23.58	n/a
293.5	61.112	21.81	n/a
294.5	61.229	19.82	n/a
295.5	61.347	22.86	n/a
296.5	61.464	24.42	n/a
297.5	61.581	28.76	n/a
298.5	61.699	25.64	n/a
299.5	61.816	26.85	n/a
300.5	61.933	19.40	n/a
301.5	62.050	27.82	n/a
302.5	62.168	26.75	n/a
303.5	62.285	27.73	n/a
304.5	62.402	36.47	n/a
305.5	62.520	37.83	n/a
306.5	62.637	39.63	n/a
307.5	62.754	33.90	n/a
308.5	62.872	33.41	n/a
309.5	62.989	28.09	n/a
310.5	63.106	37.95	n/a
311.5	63.224	26.44	n/a
312.5	63.341	23.39	n/a
313.5	63.458	27.40	n/a
314.5	63.576	26.87	0.251
315.5	63.693	32.06	n/a
316.5	63.810	26.87	n/a
317.5	63.939	26.44	n/a
318.5	64.089	26.82	n/a
319.5	64.239	26.67	n/a
320.5	64.389	26.57	n/a
321.5	64.539	31.24	n/a
322.5	64.689	27.61	n/a
323.5	64.839	30.44	n/a
324.5	64.989	34.15	n/a
325.5	65.139	36.30	n/a
326.5	65.289	36.33	n/a
327.5	65.439	33.29	n/a
328.5	65.589	32.11	n/a
329.5	65.739	34.28	n/a
330.5	65.889	33.57	0.370
331.5	66.039	35.64	n/a
332.5	66.190	30.67	n/a
333.5	66.340	34.56	n/a
334.5	66.490	33.76	n/a
335.5	66.640	34.46	n/a
336.5	66.790	33.07	n/a
337.5	66.940	29.36	n/a
338.5	67.090	27.23	n/a
339.5	67.240	26.87	n/a
340.5	67.390	31.77	n/a

341.5	67.540	28.31	n/a
342.5	67.690	25.64	n/a
343.5	67.840	29.92	n/a
344.5	67.990	29.48	n/a
345.5	68.140	27.66	n/a
346.5	68.290	19.91	n/a
347.5	68.441	22.54	n/a
348.5	68.591	24.11	n/a
349.5	68.741	29.64	n/a
350.5	68.891	34.52	n/a
352.5	69.191	35.27	0.406
354.5	69.491	29.91	n/a
356.5	69.791	23.25	n/a
366.5	71.292	23.62	n/a
368.5	71.592	26.16	n/a
372.5	72.014	25.73	0.238
374.5	72.218	26.19	n/a
376.5	72.422	23.90	n/a
378.5	72.626	23.17	n/a
380.5	72.830	21.73	n/a
385.5	73.340	23.25	0.163
392.5	74.054	18.96	n/a
395.5	74.359	20.81	n/a
400.5	74.869	19.94	n/a
405.5	75.379	17.32	n/a
409.5	75.953	15.68	n/a
415.5	77.067	19.41	n/a
420.5	77.995	14.05	n/a
425.5	78.924	15.74	n/a
429.5	79.667	17.56	n/a
435.5	80.781	13.36	n/a
440.5	81.709	10.05	0.098
445.5	82.638	12.30	n/a
450.5	83.567	11.47	n/a

ODP 663A

Depth (cm)	Age (ka)	% opal	F(opal) (g/cm^2/ka)
229.5	48.300	4.95	n/a
231.5	49.000	4.90	n/a
233.5	49.700	4.36	n/a
235.5	50.400	4.53	n/a
237.5	51.100	3.75	n/a
239.5	51.800	2.44	n/a
241.5	52.500	3.51	n/a
243.5	53.200	3.54	n/a
245.5	53.900	3.25	0.046
247.5	54.600	3.98	n/a
249.5	55.065	4.46	n/a
251.5	55.530	4.51	n/a
253.5	55.995	4.02	0.055
255.5	56.459	3.72	0.050
257.5	56.924	3.86	n/a
259.5	57.389	4.48	n/a
261.5	57.854	4.59	0.062
263.5	58.319	4.77	n/a

265.5	58.784	4.47	0.055
267.5	59.249	5.43	n/a
269.5	59.714	5.98	0.074
270.5	59.946	6.37	n/a
271.5	60.178	6.08	n/a
272.5	60.411	6.55	n/a
273.5	60.643	6.14	0.076
274.5	60.876	6.48	n/a
275.5	61.108	6.95	n/a
276.5	61.341	7.16	n/a
277.5	61.573	6.20	0.074
278.5	61.805	7.06	n/a
279.5	62.038	6.55	n/a
280.5	62.270	5.90	n/a
281.5	62.503	6.07	0.073
282.5	62.735	6.27	n/a
283.5	62.968	6.16	n/a
284.5	63.200	5.47	n/a
285.5	63.409	5.74	0.074
286.5	63.617	5.70	n/a
287.5	63.826	5.88	n/a
288.5	64.035	6.76	n/a
289.5	64.243	6.95	0.086
290.5	64.452	7.78	n/a
291.5	64.661	6.43	n/a
292.5	64.870	7.09	n/a
293.5	65.078	6.93	n/a
294.5	65.287	6.86	n/a
295.5	65.496	7.33	n/a
296.5	65.704	7.87	n/a
297.5	65.913	8.03	n/a
298.5	66.122	8.83	n/a
299.5	66.330	7.94	n/a
300.5	66.539	9.19	0.081
301.5	66.748	7.69	n/a
302.5	66.957	8.72	n/a
303.5	67.165	8.67	n/a
304.5	67.374	8.14	0.088
305.5	67.583	7.83	n/a
306.5	67.791	8.03	n/a
307.5	68.000	7.27	n/a
308.5	68.209	7.07	0.080
309.5	68.417	6.81	n/a
310.5	68.626	6.68	0.076
311.5	68.835	6.85	n/a
312.5	69.043	7.10	0.080
313.5	69.252	6.49	n/a
314.5	69.461	6.67	0.078
315.5	69.670	5.74	n/a
316.5	69.878	6.48	0.080
317.5	70.087	5.24	n/a
318.5	70.296	5.19	0.061
319.5	70.504	4.86	n/a
320.5	70.713	5.16	0.063
321.5	70.922	5.19	n/a
322.5	71.130	5.53	n/a
323.5	71.339	5.03	n/a
324.5	71.548	5.63	0.073

325.5	71.757	5.03	n/a
326.5	71.965	4.39	n/a
327.5	72.174	6.56	n/a
328.5	72.383	9.27	0.124
329.5	72.591	5.75	n/a
330.5	72.800	5.32	0.068
331.5	73.123	5.28	n/a
332.5	73.446	4.49	0.059
333.5	73.769	3.99	n/a
334.5	74.092	5.14	0.061
335.5	74.415	5.48	n/a
336.5	74.738	4.75	0.061
337.5	75.062	4.14	n/a
338.5	75.385	4.57	0.054
339.5	75.708	4.81	n/a
340.5	76.031	4.47	0.054
341.5	76.354	4.16	n/a
343.5	77.000	4.16	0.064
345.5	77.608	4.47	n/a
347.5	78.217	3.15	0.044
349.5	78.825	3.50	n/a
351.5	79.433	3.39	0.040
353.5	80.042	2.58	n/a
355.5	80.650	2.51	0.035
357.5	81.258	2.62	n/a
359.5	81.867	2.54	0.042
361.5	82.475	3.08	n/a
363.5	83.083	3.51	0.054
365.5	83.692	3.62	n/a
367.5	84.300	3.20	0.052
369.5	84.817	5.21	n/a
371.5	85.333	5.73	0.073
373.5	85.850	4.87	n/a
375.5	86.367	5.33	0.066
377.5	86.883	5.58	n/a
379.5	87.400	3.74	0.054
381.5	87.967	2.59	n/a
383.5	88.533	3.20	0.049
385.5	89.100	3.12	n/a
387.5	89.667	3.15	0.064
389.5	90.233	3.32	n/a
391.5	90.800	3.71	0.068
393.5	91.264	3.30	n/a
395.5	91.728	3.53	0.071
397.5	92.192	3.93	n/a
399.5	92.655	3.28	0.089

RC24-01

Depth (cm)	Age (ka)	% opal	F(opal) (g/cm^2/ka)
284.5	43.451	6.65	0.084
286.5	45.440	5.71	n/a
287.5	46.434	5.59	n/a
289.5	48.423	5.46	n/a
291.5	50.412	7.49	n/a
293.5	52.401	8.40	0.102

294.5	53.395	8.23	n/a
295.5	54.390	6.15	n/a
297.5	56.378	5.76	n/a
299.5	58.367	6.17	n/a
302.5	59.988	7.78	0.099
309.5	62.693	12.34	n/a
310.5	63.079	10.59	0.112
313.5	64.238	12.88	n/a
315.5	65.011	11.05	n/a
317.5	65.784	10.61	n/a
318.5	66.170	10.38	0.125
319.5	66.556	10.97	n/a
321.5	67.329	10.42	n/a
323.5	68.102	8.60	n/a
325.5	68.875	8.94	0.111
326.5	69.261	9.14	n/a
327.5	69.647	9.37	n/a
329.5	70.420	5.97	n/a
331.5	71.193	6.68	n/a
333.5	71.836	7.09	0.094
334.5	72.094	6.14	n/a
335.5	72.351	6.86	n/a
339.5	73.381	5.59	n/a
341.5	73.896	5.54	n/a
342.5	74.154	5.16	n/a
343.5	74.411	4.66	n/a
344.5	74.669	4.62	0.062
347.5	75.441	4.14	n/a
349.5	76.232	4.03	n/a
350.5	76.697	4.00	n/a
351.5	77.161	5.32	0.069
353.5	78.090	6.18	0.066
355.5	79.020	3.98	n/a
357.5	79.949	4.69	n/a
361.5	81.807	4.73	n/a
363.5	82.737	4.70	n/a
365.5	83.666	3.67	0.051
366.5	84.130	5.49	n/a
367.5	84.634	5.34	n/a
369.5	85.738	6.58	n/a
371.5	86.841	4.35	n/a
373.5	87.944	3.73	0.057
375.5	89.048	3.60	n/a
377.5	90.151	3.53	n/a
379.5	90.842	3.15	n/a
381.5	91.322	3.59	n/a

VM30-40

Depth (cm)	Age (ka)	% opal	F(opal) (g/cm^2/ka)
183.5	57.175	2.28	n/a
184.5	57.669	2.08	n/a
185.5	58.162	1.92	0.033
187.5	59.150	2.00	n/a
189.5	60.137	2.39	n/a

190.5	60.631	2.59	0.045
192.5	61.618	2.13	n/a
193.5	62.112	2.68	n/a
195.5	63.100	2.75	n/a
197.5	64.087	3.23	n/a
199.5	65.075	2.74	n/a
200.5	65.568	3.19	n/a
203.5	67.049	2.12	n/a
205.5	68.037	3.01	n/a
207.5	69.024	2.46	n/a
208.5	69.518	3.00	0.060
209.5	70.012	2.60	n/a
211.5	70.999	2.12	n/a
213.5	71.664	2.25	n/a
215.5	72.105	2.93	n/a
216.5	72.325	2.31	0.052
217.5	72.545	2.31	n/a
219.5	72.986	2.65	n/a
221.5	73.427	2.00	n/a
223.5	73.868	1.49	0.030
224.5	74.088	2.01	n/a
225.5	74.308	2.23	n/a
227.5	74.749	1.45	n/a
229.5	75.190	1.45	n/a
231.5	75.631	1.28	n/a
232.5	75.925	1.27	0.018
233.5	76.407	1.78	n/a
235.5	77.373	1.70	n/a
237.5	78.338	1.74	n/a
239.5	79.304	1.48	n/a
240.5	79.787	1.24	n/a
241.5	80.269	1.37	0.024
243.5	81.235	2.02	n/a
245.5	82.201	1.79	n/a
247.5	83.166	1.82	n/a
248.5	83.649	1.63	0.025
249.5	84.102	1.91	n/a
251.5	84.773	1.96	n/a
253.5	85.443	1.97	n/a
255.5	86.114	3.44	n/a
256.5	86.449	2.02	n/a
257.5	86.785	2.46	0.036
259.5	87.455	2.22	n/a
261.5	88.126	2.37	n/a
263.5	88.796	3.87	0.079
264.5	89.132	2.64	n/a
265.5	89.467	2.42	n/a
267.5	90.138	3.31	n/a
269.5	90.810	3.59	n/a
271.5	91.485	3.55	n/a
272.5	91.823	2.67	0.057
273.5	92.161	3.39	n/a
275.5	92.836	3.19	n/a
277.5	93.511	4.06	n/a
279.5	94.186	3.09	n/a
280.5	94.524	3.70	0.080
281.5	94.861	3.78	n/a
283.5	95.536	2.98	n/a

285.5	96.212	3.62	n/a
287.5	96.887	4.06	n/a
288.5	97.224	3.48	n/a
289.5	97.562	3.68	n/a
291.5	98.237	3.86	n/a
292.5	98.575	4.11	0.059

RC16-66

Depth (cm)	Age (ka)	% opal	F(opal) (g/cm^2/ka)
281.5	56.632	1.91	0.030
282.5	56.917	1.89	n/a
284.5	57.485	1.88	n/a
286.5	58.054	2.03	n/a
287.5	58.338	1.51	0.024
289.5	58.907	1.42	n/a
292.5	59.760	1.63	n/a
294.5	60.328	2.18	n/a
297.5	61.181	2.02	0.027
302.5	62.603	2.18	n/a
304.5	63.171	2.20	n/a
306.5	63.740	1.77	0.019
308.5	64.308	1.88	n/a
310.5	64.877	2.16	n/a
312.5	65.446	1.82	n/a
313.5	65.730	2.42	0.026
314.5	66.014	2.37	n/a
316.5	66.583	2.15	n/a
318.5	67.151	2.21	n/a
321.5	68.004	2.49	0.028
322.5	68.288	2.22	n/a
324.5	68.857	1.86	n/a
326.5	69.426	206.5	n/a
328.5	69.853	1.54	0.022
329.5	70.060	1.52	n/a
332.5	70.680	2.24	n/a
334.5	71.094	1.73	n/a
336.5	71.508	1.51	n/a
337.5	71.715	1.69	0.026
338.5	71.922	2.10	n/a
342.5	73.181	1.86	n/a
343.5	73.497	2.10	0.028
344.5	73.813	2.21	n/a
346.5	74.444	2.22	n/a
348.5	75.076	1.72	n/a
352.5	76.339	2.10	0.026
353.5	77.058	1.40	n/a
354.5	78.148	2.06	n/a
356.5	80.328	1.77	n/a
358.5	82.508	1.54	n/a
361.5	85.680	1.60	0.019
362.5	86.118	1.70	n/a
364.5	86.996	1.53	n/a
366.5	87.873	1.53	n/a

Table A8 – Pa. Th and U radionuclide measurements for all cores.

VM19-296

Depth (cm)	Age (ka)	$_{xs}(^{231}Pa/^{230}Th)_0$	U_{auth} (dpm/g)	$F(^{232}Th)$ (g/cm^2/ka)
220.5	49.124	0.074	2.964	1.349
267.5	56.572	0.261	2.617	1.308
290.5	60.760	0.067	1.685	1.562
314.5	63.576	0.065	2.799	1.722
330.5	65.889	0.080	1.002	1.635
352.5	69.191	0.061	4.284	2.239
372.5	72.014	0.079	0.923	2.222
385.5	73.340	0.081	0.764	1.459
440.5	81.709	0.104	0.851	0.962

ODP 663A

Depth (cm)	Age (ka)	$_{xs}(^{231}Pa/^{230}Th)_0$	U_{auth} (dpm/g)	$F(^{232}Th)$ (g/cm^2/ka)
245.5	53.900	0.054	3.434	0.581
253.5	55.995	0.061	3.250	0.717
255.5	56.459	0.059	3.684	0.628
261.5	57.854	0.065	3.519	0.659
265.5	58.784	0.064	3.693	0.639
269.5	59.714	0.066	3.166	0.852
273.5	60.643	0.063	2.985	0.925
277.5	61.573	0.057	2.608	0.858
281.5	62.503	0.057	2.894	0.812
285.5	63.409	0.058	3.051	0.768
289.5	64.243	0.059	3.085	0.782
300.5	66.539	0.071	4.389	0.741
304.5	67.374	0.068	4.557	0.758
308.5	68.209	0.069	4.605	0.782
310.5	68.626	0.072	4.242	n/a
312.5	69.043	0.068	4.252	0.804
314.5	69.461	0.072	4.298	0.825
316.5	69.878	0.060	4.077	0.905
318.5	70.296	0.069	4.199	0.843
320.5	70.713	0.071	4.000	0.969
324.5	71.548	0.066	3.233	1.192
328.5	72.383	0.058	3.050	1.341
330.5	72.800	0.058	3.281	1.073
332.5	73.446	0.073	2.788	1.022
334.5	74.092	0.064	3.179	0.951
336.5	74.738	0.079	2.797	0.765
338.5	75.385	0.076	2.826	0.773
340.5	76.031	0.071	2.734	0.823
343.5	77.000	0.066	2.229	0.889
347.5	78.217	0.064	2.362	0.588
351.5	79.433	0.075	2.300	0.487
355.5	80.650	0.064	1.801	0.458
359.5	81.867	0.053	1.398	0.511
363.5	83.083	0.054	1.124	0.585
367.5	84.300	0.048	0.843	0.703
371.5	85.333	0.061	0.550	0.823
375.5	86.367	0.056	0.532	0.816
379.5	87.400	0.053	0.571	0.769
383.5	88.533	0.048	0.696	0.651

387.5	89.667	0.053	0.717	0.686
391.5	90.800	0.045	0.960	0.754
395.5	91.728	0.048	1.003	0.749
399.5	92.655	0.033	1.639	0.827

RC24-01

Depth (cm)	Age (ka)	$_{xs}(^{231}Pa/^{230}Th)_0$	U_{auth} (dpm/g)	$F(^{232}Th)$ (g/cm^2/ka)
284.5	43.451	0.060	0.880	1.046
293.5	52.401	0.052	1.257	1.159
302.5	59.988	0.053	1.781	1.157
310.5	63.079	0.067	2.644	1.071
318.5	66.170	0.072	2.818	1.158
325.5	68.875	0.071	2.046	1.390
333.5	71.836	0.073	1.486	1.666
344.5	74.669	0.063	1.298	1.070
351.5	77.161	0.062	1.097	1.140
353.5	78.090	0.088	0.778	0.641
365.5	83.666	0.054	0.304	0.899
373.5	87.944	0.056	0.133	0.888

VM30-40

Depth (cm)	Age (ka)	$_{xs}(^{231}Pa/^{230}Th)_0$	U_{auth} (dpm/g)	$F(^{232}Th)$ (g/cm^2/ka)
185.5	58.162	0.049	-0.074	0.944
190.5	60.631	0.067	-0.209	1.703
201.5	66.062	0.060	-0.083	1.370
208.5	69.518	0.066	0.042	1.449
216.5	72.325	0.051	0.185	1.759
223.5	73.868	0.060	0.164	1.401
232.5	75.925	0.040	0.133	0.777
241.5	80.269	0.052	-0.006	0.866
248.5	83.649	0.061	-0.141	1.110
257.5	86.785	0.084	-0.173	1.196
263.5	88.796	0.059	-0.052	0.836
272.5	91.823	0.071	-0.005	0.820
280.5	94.524	0.071	0.045	0.804
292.5	98.575	0.068	0.147	0.657

RC16-66

Depth (cm)	Age (ka)	$_{xs}(^{231}Pa/^{230}Th)_0$	U_{auth} (dpm/g)	$F(^{232}Th)$ (g/cm^2/ka)
281.5	56.632	0.073	-0.512	4.017
287.5	58.338	0.075	-0.477	3.736
297.5	61.181	0.085	-0.652	4.253
306.5	63.740	0.068	-0.718	3.491
313.5	65.730	0.064	-0.688	3.549
321.5	68.004	0.070	-0.666	3.697
328.5	69.853	0.061	-0.570	3.997
337.5	71.715	0.063	-0.629	4.973
343.5	73.487	0.066	-0.607	4.134
352.5	76.339	0.065	-0.484	3.121
361.5	85.680	0.071	-0.508	3.238
368.5	88.750	0.060	-0.431	2.575

Table A9 – TOC, TN, F(TOC), F(TN) and biomarker measurements for all cores. The label n/a represents samples that could not be measured. The column 'biomarker ratio' in ODP 663A refers to the brassicasterol:alkenone ratio.

VM19-296

Depth (cm)	Age (ka)	% TOC	% TN	F(TOC) (g/cm^2/ka)	F(TN) (g/cm^2/ka)
220.5	49.124	3.19	0.185	0.026	0.0013
267.5	56.572	2.78	0.136	0.024	0.0011
290.5	60.760	1.70	0.267	0.016	0.0024
314.5	63.576	2.36	0.185	0.027	0.0017
330.5	65.889	1.56	0.224	0.018	0.0025
352.5	69.191	1.49	0.233	0.018	0.0027
372.5	72.014	1.55	n/a	0.018	n/a
385.5	73.340	2.31	0.164	0.016	0.0011
440.5	81.709	2.52	0.105	0.025	0.0010

ODP 663A

Depth (cm)	Age (ka)	% TOC	% TN	F(TOC) (g/cm^2/ka)	F(TN) (g/cm^2/ka)	Biomarker ratio (peak area)
229.5	48.300	2.48	0.10	n/a	n/a	n/a
243.5	53.200	1.63	0.07	n/a	n/a	n/a
245.5	53.900	1.16	0.11	0.016	0.0016	n/a
253.5	55.995	1.70	n/a	0.023	n/a	n/a
255.5	56.459	1.54	0.11	0.021	0.0015	n/a
257.5	56.924	1.92	0.08	n/a	n/a	n/a
261.5	57.854	2.07	n/a	0.028	n/a	n/a
265.5	58.784	1.72	0.15	0.021	0.0019	n/a
269.5	59.714	2.08	0.13	0.025	0.0017	n/a
273.5	60.643	2.05	0.13	0.025	0.0016	n/a
277.5	61.573	2.50	0.12	0.030	0.0014	n/a
281.5	62.503	2.01	0.13	0.024	0.0016	n/a
284.5	63.200	2.78	0.09	n/a	n/a	n/a
285.5	63.409	2.45	0.15	0.032	0.0019	n/a
289.5	64.243	2.35	0.12	0.029	0.0014	1.06e-2
291.5	64.661	2.97	0.10	n/a	n/a	n/a
300.5	66.539	2.72	n/a	0.029	n/a	n/a
304.5	67.374	2.84	0.14	0.031	0.0015	8.83e-2
308.5	68.209	2.19	0.09	0.025	0.0015	5.65e-3
310.5	68.626	2.37	0.14	0.027	0.0016	n/a
312.5	69.043	2.70	0.12	0.031	0.0014	8.57e-2
314.5	69.461	2.25	0.13	0.027	0.0016	n/a
316.5	69.878	2.18	n/a	0.027	n/a	5.37e-2
318.5	70.296	1.74	0.12	0.021	0.0014	n/a
320.5	70.713	2.82	n/a	0.035	n/a	2.31e-1
324.5	71.548	2.39	0.12	0.031	0.0015	n/a
326.5	71.965	2.93	0.09	n/a	n/a	n/a
328.5	72.383	2.34	0.11	0.032	0.0015	4.95e-2
330.5	72.800	2.67	n/a	0.035	n/a	8.16e-2
332.5	73.446	2.14	0.08	0.028	0.0014	n/a
333.5	73.769	2.12	0.08	n/a	n/a	n/a
334.5	74.092	2.69	0.12	0.032	0.0014	n/a
336.5	74.738	1.92	0.11	0.023	0.0015	n/a
338.5	75.385	1.10	0.10	0.013	0.0011	n/a

340.5	76.031	1.77	0.06	0.021	0.0012	n/a
343.5	77.000	1.69	0.09	0.026	0.0014	2.18e-2
347.5	78.217	2.29	0.02	0.032	0.0013	n/a
351.5	79.433	1.11	n/a	0.013	n/a	n/a
353.5	80.042	1.33	0.06	n/a	n/a	n/a
355.5	80.650	0.59	0.08	0.008	0.0011	n/a
359.5	81.867	0.59	0.06	0.010	0.0011	n/a
363.5	83.083	0.81	0.05	0.012	0.0008	6.92e-3
367.5	84.300	1.32	0.05	0.021	0.0009	n/a
371.5	85.333	1.37	0.06	0.017	0.0008	n/a
375.5	86.367	1.64	n/a	0.020	n/a	n/a
379.5	87.400	1.01	0.06	0.015	0.0009	n/a
383.5	88.533	1.06	0.05	0.020	0.0010	n/a
387.5	89.667	0.71	0.07	0.014	0.0015	n/a
391.5	90.800	0.95	0.07	0.020	0.0016	n/a
395.5	91.728	1.28	n/a	0.027	n/a	n/a
397.5	92.192	1.30	0.07	n/a	n/a	n/a
399.5	92.655	1.19	0.07	0.027	0.0015	n/a

RC24-01

Depth (cm)	Age (ka)	% TOC	% TN	F(TOC) ($g/cm^2/ka$)	F(TN) ($g/cm^2/ka$)
284.5	43.451	0.213	0.067	0.00269	0.00085
293.5	52.401	0.177	0.073	0.00216	0.00089
302.5	59.988	0.166	0.082	0.00211	0.00104
310.5	63.079	0.246	0.093	0.00261	0.00099
318.5	66.170	0.233	0.087	0.00280	0.00105
325.5	68.875	0.191	0.089	0.00237	0.00111
333.5	71.836	0.160	0.078	0.00212	0.00103
344.5	74.669	0.114	0.068	0.00152	0.00090
351.5	77.161	0.113	0.066	0.00147	0.00086
353.5	78.090	0.129	0.059	0.00172	0.00079
365.5	83.666	0.051	0.043	0.00072	0.00061
373.5	87.944	0.037	0.034	0.00056	0.00053

VM30-40

Depth (cm)	Age (ka)	% TOC	% TN	F(TOC) ($g/cm^2/ka$)	F(TN) ($g/cm^2/ka$)
185.5	58.162	0.78	0.040	0.013	0.00068
190.5	60.631	0.73	0.038	0.013	0.00066
201.5	66.062	1.23	0.043	0.023	0.00080
208.5	69.518	0.81	0.046	0.016	0.00093
216.5	72.325	1.20	0.048	0.027	0.00109
223.5	73.868	1.17	0.044	0.024	0.00090
232.5	75.925	0.39	0.030	0.006	0.00042
241.5	80.269	0.81	0.028	0.014	0.00050
257.5	86.785	1.33	0.035	0.019	0.00051
263.5	88.796	0.79	0.021	0.016	0.00043
280.5	94.524	1.22	0.071	0.026	0.00154
292.5	98.575	0.91	n/a	0.013	n/a

RC16-66

Depth (cm)	Age (ka)	% TOC	% TN	F(TOC) ($g/cm^2/ka$)	F(TN) ($g/cm^2/ka$)
281.5	56.632	0.089	0.097	0.00141	0.00154
287.5	58.338	0.096	0.084	0.00150	0.00131
297.5	61.181	0.132	0.099	0.00178	0.00134
306.5	63.740	0.179	0.090	0.00187	0.00094
313.5	65.730	0.151	0.097	0.00164	0.00106
321.5	68.004	0.147	0.090	0.00166	0.00102
328.5	69.853	0.059	0.088	0.00082	0.00123
337.5	71.715	0.009	0.091	0.00014	0.00138
343.5	73.487	0.068	0.096	0.00092	0.00130
352.5	76.339	0.091	0.102	0.00114	0.00128
361.5	85.680	0.109	0.093	0.00129	0.00110
368.5	88.750	0.087	0.077	0.00104	0.00091

Table A10 – Foraminiferal fragmentation index (FFI) for ODP 663A

Depth (cm)	Age (ka)	Fragmentation (%)
229.5	48.300	45.68
231.5	49.000	39.88
233.5	49.700	39.93
235.5	50.400	41.85
237.5	51.100	45.20
239.5	51.800	44.58
241.5	52.500	37.60
243.5	53.200	43.51
245.5	53.900	35.01
247.5	54.600	40.11
249.5	55.065	33.11
251.5	55.530	41.01
253.5	55.995	41.81
255.5	56.459	34.55
257.5	56.924	42.38
259.5	57.389	35.31
261.5	57.854	30.45
263.5	58.319	32.78
265.5	58.784	36.78
267.5	59.249	34.52
269.5	59.714	32.60
270.5	59.946	29.74
271.5	60.178	34.08
272.5	60.411	30.12
273.5	60.643	33.98
274.5	60.876	32.22
275.5	61.108	37.40
276.5	61.341	39.09
277.5	61.573	36.55
278.5	61.805	35.99
279.5	62.038	36.93
280.5	62.270	39.93
281.5	62.503	36.89
282.5	62.735	38.60
283.5	62.968	40.22
284.5	63.200	39.76
285.5	63.409	41.17
286.5	63.617	42.47
287.5	63.826	37.94
288.5	64.035	36.61
289.5	64.243	33.87
290.5	64.452	38.13
291.5	64.661	38.13
292.5	64.870	36.91
300.5	66.539	46.53
301.5	66.748	42.68
302.5	66.957	41.34
303.5	67.165	47.99
304.5	67.374	37.54
305.5	67.583	42.41
306.5	67.791	42.63
307.5	68.000	39.19
308.5	68.209	46.30
309.5	68.417	44.47
310.5	68.626	43.02

311.5	68.835	46.63
312.5	69.043	46.11
313.5	69.252	43.08
314.5	69.461	42.64
315.5	69.670	47.19
316.5	69.878	38.60
317.5	70.087	42.99
318.5	70.296	34.60
319.5	70.504	43.09
320.5	70.713	41.78
321.5	70.922	36.98
322.5	71.130	37.44
323.5	71.339	36.35
324.5	71.548	41.59
325.5	71.757	32.89
326.5	71.965	39.14
327.5	72.174	36.44
328.5	72.383	35.16
329.5	72.591	42.25
330.5	72.800	41.80
331.5	73.123	35.44
332.5	73.446	42.98
333.5	73.769	35.30
334.5	74.092	36.83
335.5	74.415	33.70
336.5	74.738	38.95
337.5	75.062	36.46
338.5	75.385	33.17
339.5	75.708	34.93
340.5	76.031	27.20
341.5	76.354	26.46
343.5	77.000	32.21
345.5	77.608	29.86
347.5	78.217	27.58
349.5	78.825	28.18
351.5	79.433	30.34
353.5	80.042	25.84
355.5	80.650	21.71
357.5	81.258	22.85
359.5	81.867	20.73
361.5	82.475	22.40
363.5	83.083	21.02
365.5	83.692	22.74
367.5	84.300	26.87
369.5	84.817	33.64
371.5	85.333	38.85
373.5	85.850	35.68
375.5	86.367	41.71
377.5	86.883	43.08
379.5	87.400	41.15
381.5	87.967	35.64
383.5	88.533	33.50
385.5	89.100	34.72
387.5	89.667	37.20
389.5	90.233	32.72
391.5	90.800	38.27
393.5	91.264	40.07
395.5	91.728	36.41

397.5	92.192	35.08
399.5	92.655	39.52
401.5	93.119	33.91